

Copyright Undertaking

This thesis is protected by copyright, with all rights reserved.

By reading and using the thesis, the reader understands and agrees to the following terms:

- 1. The reader will abide by the rules and legal ordinances governing copyright regarding the use of the thesis.
- 2. The reader will use the thesis for the purpose of research or private study only and not for distribution or further reproduction or any other purpose.
- 3. The reader agrees to indemnify and hold the University harmless from and against any loss, damage, cost, liability or expenses arising from copyright infringement or unauthorized usage.

IMPORTANT

If you have reasons to believe that any materials in this thesis are deemed not suitable to be distributed in this form, or a copyright owner having difficulty with the material being included in our database, please contact lbsys@polyu.edu.hk providing details. The Library will look into your claim and consider taking remedial action upon receipt of the written requests.

WEARABLE FLEXIBLE HEALTHCARE DEVICESPRESSURE SENSATION TECHNOLOGY AND PHOTOBIOMODULATION

MA KIT MING

PhD

The Hong Kong Polytechnic University

2025

The Hong Kong Polytechnic University
School of Fashion and Textiles
Wearable flexible healthcare devices- Pressure sensation technology and photobiomodulation
Ma Kit Ming
A thesis submitted in partial fulfilment of the requirements for the degree of Doctor of
Philosophy
August 2024

CERTIFICATE OF ORIGINALITY

I hereby declare that this thesis is my own work that, to the best of my knowledge and belief, it reproduces no material previously published or written, nor material that has been accepted for the award of any other degree or diploma, except where due acknowledgement has been made in the text.

Ma Kit Ming (Name of student)

__(Signed)

Abstract

Wearable flexible healthcare devices have the potential to provide real-time, continuous, and remote monitoring, and/or treatment, thereby alleviating the medical system burden, and reducing the need for patient hospital visits. Flexible, comfortable, and safe wearable healthcare devices, including both monitoring devices, and treatment devices, are preferred for their seamless, and accurate functionality. However, the performance of the current pressure sensation device is significantly influenced by the environment, such as temperature, and relative humidity, due to its material, and mechanism. This variability poses a challenge to maintain sensation fidelity. Furthermore, there is often a discrepancy between the sensor performance, and the specific requirement of the application, particularly in terms of the pressure sensation range, which varies across different needs. This increases the requirement for the sensor performance, like sensor linearity, sensitivity, and a wide dynamic range. To address these challenges, it is necessary to develop specific health monitoring devices to reduce the sensor performance requirement. It also can reduce the time for data processing, and energy consumption. On the other hand, there is a notable scarcity of wearable healthcare treatment devices. Current research predominantly focuses on wearable drug delivery, rather than energytreatment. Adopting energy-treatment devices in wearable format would be highly valuable, as it can significantly enhance patient care.

To address the above problems, a novel mechanoreceptor was designed, wherein the pressure threshold can be controlled through adopting the structure parameters, and materials. The interrelationship between the pressure threshold, and structural parameters was comprehensively studied. By increasing the material filling rate of the insulation cavity, the pressure threshold can be controlled in the range of 3 kPa to 297 kPa. In addition, by increasing

the height of the PDMS, the pressure threshold can be controlled in the range of 54.84 kPa to 1466.78 kPa. Moreover, the pressure thresholds can also be modulated by altering the material modulus, compression area, and the size of the mechanoreceptor. Given the diversity of controllable dimensions, the processing requirements associated with any particular dimension can be reduced by leveraging synergies across multiple dimensions. This broadens the application potential. In addition, the introduction of PDMS structure into the insulation layer of the mechanoreceptors allows for an excellent on-off ratio, exceeding eight orders to magnitudes, comparable to commercial HMI interface. Otherwise, this mechanoreceptor also shows good reliability under repeated compressions (>40000 compression cycles), and laundries (20 laundry cycles). It is capable of functioning under 1 kHz compressions. The response time, and recovery time of the mechanoreceptor was only around 43 ms. Overall, this mechanoreceptor exhibits good mechanical, electrical, and textile properties, making it a promising candidate for advanced wearable healthcare devices.

Additionally, a corresponding spiral mechanoreceptor array was designed, and fabricated, containing a total of 16 mechanoreceptors in series connection with flexible resistors. This array was developed to enhance data processing, and wearable connection, and features only two output electrodes for data processing, and power. It can be used for position identification based on different resistance output values. The resistance value of the mechanoreceptor was in the range of 1Ω to $50~k\Omega$, in which the resistance difference between mechanoreceptors was approximately 3.226 k Ω . This array's on-off resistance value remains stable across different environments, including high temperature (50 °C), low temperature (-40°C), cyclic temperature, underwater conditions (1 m depth), and under maximum mechanical load (100 N). Furthermore, this array also can function effectively under bending with good comfort. Finally, this novel mechanoreceptor, and the corresponding

mechanoreceptor array were integrated into different wearable products to explore its potential in wearable applications with different pressure sensation requirements, like plantar pressure sensation (~250 kPa), and gait analysis (~30 kPa). Moreover, a pressure sensation platform was developed to detect both pressure, and position, potentially simulating the human skin's pressure sensation mechanism. This advancement may pave the way for more sophisticated pressure sensation technology with stable performance across different environments.

For the wearable energy treatment device, a comprehensive photobiomodulation evaluation system was established to assess the performance of the PBM devices from different aspects, including peak wavelength, wavelength shifting at different currents, systematic electrical properties, LED IV curve, irradiance, system irradiance distribution, and temperature variation throughout treatment. Two different types of commercial photobiomodulation devices were studied with the system to understand their functionality, and performance. Moreover, this help to establish the relationship between the effective photobiomodulation parameters, and the device settings/ design. This also provides a valuable insight into the challenge associated with developing wearable photobiomodulation devices, and even other energy-based treatment devices.

A flexible photobiomodulation panel was developed with an appropriate LED light source to treat the radioactive dermatitis of the breast cancer patient. A group of LEDs was evaluated from different aspects, including wavelength, irradiance, voltage, and current to ensure optimal selection for photobiomodulation. Moreover, the design of the LED array was studied through simulation, and experiments to achieve the best configuration. The panel adopted a fabric-making pattern to realize good conformability onto the human body contour. Besides this, a study was conducted on the light efficiency of the wearable treatment device.

This flexible photobiomodulation panel can be seamlessly integrated into the underwear for comfort, and convenience. This work illustrates a feasible pathway to transform energy-based treatment devices into wearable formats.

Overall, this work comprehensively studied wearable healthcare devices, including pressure sensation techniques, and photobiomodulation devices. It deeply investigates the current challenges, and limitations of these devices, and explores potential solutions to address these issues.

Publications and Patent

Related Journal Publications

- 1) Pu, J., Ma, K., Luo, Y., Tang, S., Liu, T., Liu, J., ... & Tao, X. (2023). Textile electronics for wearable applications. International Journal of Extreme Manufacturing.
- 2) Li, J., Xiong, Y., Yang, B., **Ma**, **K**., & Tao, X. Asymmetric Flexible Electroadhesive Clutches. Available at SSRN 3931629.
- 3) Fang, B., Yan, J., Chang, D., Piao, J., **Ma, K**. M., Gu, Q., ... & Tao, X. (2022). Scalable production of ultrafine polyaniline fibres for tactile organic electrochemical transistors. Nature communications, 13(1), 2101.
- 4) Liu, S., **Ma, K.**, Yang, B., Li, H., & Tao, X. (2020). Textile Electronics for VR/AR Applications. Advanced Functional Materials, 2007254.
- 5) Yang, B., Xiong, Y., **Ma, K**., Liu, S., & Tao, X. (2020). Recent advances in wearable textile-based triboelectric generator systems for energy harvesting from human motion. EcoMat, 2(4), e12054.

Paper in preparation

1) Reliable bio-mimicking fabric mechanoreceptor array with tunable pressure threshold for human-machine interaction.

Patent

1) Tao, X. & Kit ming Ma. (in Chinese). Durable fabric electric switch arrays with tunable pressure thresholds. Accepted in April 2024.

Acknowledgements

I would like to express my deepest appreciation to my chief supervisor, Prof. TAO Xiao Ming for her long-term support, invaluable patience, and great encouragement. Over the past four years, I have gained a wealth of scientific knowledge, research experience, and valuable skills in planning, critical thinking, communication, mental resilience, interpersonal relationships, and collaboration. These are all invaluable assets that will continue to benefit me throughout my life.

In addition, I appreciate the great help from our group members: Miss Ma Linlin, Ms Yang Jing, Ms Piao Jinli, Dr. Liu Su, Dr. Fang Bo, Dr. Li Jun, Dr. Lin Shuping, Dr. Zhang Lisa, Dr. Zhu Renbo, Dr. Xiong Ying, and other team members for their valuable assistance, and collaboration. Additionally, I extend my heartfelt thanks to all the scientific officers, and technicians at the School of fashion, and textiles, the Hong Kong Polytechnic University, for their generous help with instrument operations.

I also would like to express my sincere appreciation to the panels for their commitment to efforts, and reviews in this process. I would like to thank The Hong Kong Polytechnic University for a postgraduate scholarship.

Last but not least, I am immensely grateful to my family for their patience, unwavering trust, and constant support. Their presence has been a source of strength, and comfort throughout the challenges, and frustrations of my postgraduate studies.

Table of Contents

Abstract	t	I
Publicat	ions and	d PatentV
Acknow	ledgem	entsVII
Table of	Conter	ntsVIII
List of F	igures.	XVII
List of T	ables	XXVI
List of A	Abbrevi	ations and SymbolsXXVIII
Chapter	1. Intro	duction1
	1.1.	Background1
	1.2.	Problem statement
	1.3.	Objectives6
	1.4.	Methodology7
	1.5.	Originality and Significance
	1.6.	Structure of the thesis
	1.7.	References
Chapter	2 Litera	ature review
	2.1.	Introduction
	2.2.	Introduction of pressure sensation
	2.2	.1. Requirements of flexible pressure sensation device/interface
	2.2	.2. Developments of flexible pressure sensitive devices

2.2.2.1. Pressure sensor	7
2.2.2.2. Other flexible input device	16
2.2.3. Materials, and Fabrication techniques of flexible input devices	18
2.2.4. Study of human sensation, and perception system	20
2.2.5. Wearable applications of flexible input devices	24
2.3. Introduction of radiation dermatitis	27
2.3.1. Pathology of radiation dermatitis	29
2.3.2. Radiation dermatitis in breast cancer patients	30
2.4. Introduction of Photobiomodulation	32
2.4.1. Mechanism of the photobiomodulation	33
2.4.2. Photobiomodulation light source	35
2.4.3. Parameters of photobiomodulation	36
2.4.3.1. Wavelength	36
2.4.3.2. Dose rate	40
2.4.3.3. Photobiomodulation device configuration	44
2.4.4. Development of flexible photobiomodulation device	46
2.4.5. Photobiomodulation for radioactive dermatitis	49
2.5. Summary and Perspectives	51
2.6. References	53
Chapter 3. Bioinspired mechanoreceptors with turnable pressure threshold	65
3.1. Introduction	65

3.2. Exp	erimental Design	65
3.3. Prel	iminary study	66
3.3.1. D	Design of the mechanoreceptor	69
3.4. Exp	eriment	71
3.4.1. M	Materials and Tools	72
3.4.2. Fa	abrication of the mechanoreceptor	73
3.4.3. St	urface and structural characterization	74
3.4.4. E	valuation of the mechanoreceptor	75
3.4.5. R	eliability test with laundry cycles	76
3.5. Resu	ults and Discussion	77
3.5.1. P	DMS structure evaluation	77
3.5.2. M	Mechanism of the mechanoreceptor	80
3.5.3. O	n-off ratio	83
3.5.4. R	esponse time and Recovery time	84
3.5.5. Fi	requency response	85
3.5.6. R	eliability of mechanoreceptor	86
3.5.6.1	. Repeated compressions	86
3.5.6.2	2. Laundry	89
	actors influencing mechanoelectrical characterization of	90
3.5.7.1	. Material filling rate	91
3.5.7.2	2. Stencil thickness	93

	3.5.	8. Hardness of PDMS	96
	3.6.	Conclusion	98
	3.7.	References	99
Chapter 4	1. Texti	ile-based mechanoreceptor-synaptic array	101
	4.1.	Introduction	101
	4.2.	Experimental Design	102
	4.2.	Study of commercial flexible keypad	102
	4.2.	2. Textile-based sensor-synaptic array design	104
	4.2	3. Preliminary study	106
	4.3.	Experiment	108
	4.3.	1. Materials	108
	4.3.	2. Textile-based sensor-synaptic array fabrication	110
	4.3	3. Characterization	111
	4.	.3.3.1. Electrical characterization	111
	4.	.3.3.2. Bending performance of the array	112
	4.	.3.3.3. Water immersion test	113
	4.	.3.3.4. Temperature test	114
	4.	.3.3.5. Mechanical stability of the textile array	114
	4.	.3.3.6. Usabiliy	115
	4.4.	Result and discussion	115
	4.4.	Textile-based array resistance	115

4.4.2. Bending performance of the textile-based sensor-synaptic array 119
4.4.3. Water immersion test
4.4.4. Environmental stability test
4.1.1.1. Cyclic temperature test
4.1.1.2. Low temperature test
4.1.1.3. High temperature test
4.4.5. Longevity of the resistive keyboard
4.4.6. Mechanical stability of the sensor-synaptic array
4.4.7. Pressing by different people
4.5. Conclusion
4.6. References
Chapter 5 Integration of mechanoreceptors for wearable application
5.1. Introduction
5.2. Design of the wearable products
5.3. Preliminary experiment
5.4. Experiment
5.4.1. Materials
5.4.2. Fabrication process of the prototype
5.4.3. Testing
5.4.3.1. Material Testing
5.4.3.2. Mechanoreceptors testing

5.4.3.3. User experience improvement
5.5. Results and discussion
5.5.1. Material tensile properties
5.5.2. Interrelationship between pressure thresholds, and other factors 158
5.5.3. Testing of diabetic foot pressure monitoring system
5.5.4. Testing of Parkinson gait analysis system
5.5.5. Pressure sensation platform
5.5.6. Improvement on user experience
5.6. Conclusions
5.7. References
Chapter 6. Evaluation system for wearable PBM device
6.1. Introduction
6.2. Experimental design
6.3. Characterization
6.3.1. Electrical characterization
6.3.2. Optical Characterization
6.3.3. Wavelength and irradiance measurement
6.3.4. Irradiance distribution measurement
6.3.5. LED viewing angle measurement
6.3.6. Temperature measurement
6.3.7. Textile properties measurement

6.4. Result and discussion
6.4.1. PBM panel
6.4.1.1. Structure and component of the PBM panel
6.4.1.2. Near-infrared LED (850 nm)
6.4.2. RED light LED (660nm)
6.4.2.1. Secondary optical design of LED
6.4.2.2. PBM panel irradiance properties
6.4.2.3. Temperature measurement
6.4.3. Wearable PBM system
6.4.3.1. Structure and component of the wearable PBM
6.4.3.2. Wearable PBM panel wavelength
6.4.3.3. Wearable PBM LED electric properties
6.4.4. Wearable PBM irradiance properties
6.4.4.1. Temperature measurement
6.4.4.2. Textile properties
6.4.5. Comparison and conclusion
6.5. Conclusion
6.6. References
Chapter 7. Development of the wearable flexible photobiomodulation panel for breast cancer
patients
7.1. Introduction
7.2. Experiment design

7.3.	Е	xperiment	231
7.3	3.1.	Material	231
7.4.	T	esting	232
,	7.4.	1.1. LED irradiance distribution measurement	233
,	7.4.	1.2. LED wavelength measurement	233
,	7.4.	1.3. LED electrical, and irradiance characterization	234
,	7.4.	1.4. LED viewing angle measurement	234
7.4	1.2.	Design of the shape of the flexible PBM panel	235
7.4	1.3.	Secondary optical system design	237
7.5.	R	esults and discussion	238
7.5	5.1.	LED selection	238
,	7.5.	1.1. Irradiance distribution of LED chips at different sizes	238
,	7.5.	1.2. LED wavelength	240
,	7.5.	1.3. LED IV properties, and corresponding irradiance	244
7.5	5.2.	LED viewing angle measurement	247
7.5	5.3.	LED array design	249
7.5	5.4.	Wearable panel shape design	256
7.5	5.5.	LED array circuit design	259
7.5	5.6.	Optical study for the flexible PBM	266
7.5	5.7.	Integration of the flexible PBM	267
7.6.	C	onclusion	268

	7.7.	References	269
Chapter	8. Con	clusions and Future work	270
	8.1.	Conclusions	270
	8.2	Future work	272

List of Figures

Figure 1-1. Classification of WHDs.	2
Figure 2-1. Overview of human-machine interface framework.	3
Figure 2-2 A schematic illustration of the mechanism of common flexible sensors. (a))
Piezoresistive sensor. (b) Capacitive sensor. (c) Piezoelectric sensor. (d) Piezoelec	tric
sensor	8
Figure 2-3. A schematic diagram of stretchable resistive pressure sensor with micro-pyr	amid
structure.	9
Figure 2-4. Porous capacitive sensor fabrication process. (a) A schematic diagram of the	e
fabrication process. (b-j) Digital image of the porous structure	11
Figure 2-5. Fiber-based piezoelectric nanogenerator	12
Figure 2-6. Textile-based triboelectric nanogenerator array for sleep monitoring. (a) A	
schematic diagram of the design of the bedding. (b) Digital image of the TENG. (c	;)
Photo of the TENG	14
Figure 2-7. Overview of key issues of flexible sensors.	15
Figure 2-8. A pressure sensitive inkjet-printed resistor. (a) A schematic illustration of the	ne
fabrication process of the pressure sensitive resistor. (b) Chemical structure of the	ink.
(d) Photo of the inkjet-printed resistor. (d) Mechanism of the inkjet-printed resistor	r 17
Figure 2-9. Overview of (a) human tactile perception system, and (b) mechanism	21
Figure 2-10. A schematic illustration of skin anatomy with cutaneous sensory receptors	22
Figure 2-11. Subtypes mechanoreceptors properties, and function	23
Figure 2-12. Designed insole system for diabetic foot	26
Figure 2-13. Image about grades of radioactive dermatitis in hair, and dark pigment skin	1 29
Figure 2-14. A schematic illustration of the mechanism of photobiomodulation	34
Figure 2-15. A schematic illustration of light penetration depth of skin with different	

wavelength36
Figure 2-16. Absorption spectrum of different melanin, and haemoglobin
Figure 2-17. Arnt Schulz model of dose rate[121]
Figure 2-18. Dose/response curve. (A) Proliferation of HFF-1 lineage fibroblasts after 72 h
of irradiation at different fluences. (B) Photomicrographs of the cell proliferation at 72 h
after irradiation41
Figure 2-19 In vitro studies with lower volume of mitochondria (a) Effective studies (b)
Ineffective studies (c) Combination of effective studies, and ineffective studies 42
Figure 2-20. A schematic diagram of inverse square law
Figure 2-21. Three types of LEDs light distribution.(a) Lambertian lens. (b) Batwing lens. (c)
side emitting lens
Figure 2-22. Attachable μLEDs photobiomodulation panel. (a) Design concept of the PBM
panel. (b) A schematic illustration of the fabrication process of the PBM panel. (c-e)
Digital image of the panel. (f-g) Measured power density of the panel with or without
loading. (h) Electrical properties of the panel
Figure 2-23. OLED photobiomodulation patch. (a) Design concept of the OLED panel. (b-c,
e-f) Digital images of the OLED panel. (d) A schematic illustration of the structure of
the panel
Figure 3-1. Research framework
Figure 3-2. Image of the printed PDMS pattern. 67
Figure 3-3. Image of the fabric-based mechanoreceptor on-off resistance
Figure 3-4. Interrelationship between PDMS material filling rate, and measured pressure
threshold
Figure 3-5. A schematic illustration of the structure of textile-based mechanoreceptor 71
Figure 3-6. A schematic illustration of the fabrication of the textile-based mechanorecentor

74
Figure 3-7. A schematic diagram of the experiment set-up of the electromechanical
characterization
Figure 3-8. Image of the deformed mechanoreceptor. 79
Figure 3-9. A schematic diagram about the cross-section of the mechanoreceptor, and the
corresponding electric diagram
Figure 3-10. (a) On-off resistance of the mechanoreceptor (Insulation resistance tester). (b)
Image of the off resistance of the mechanoreceptor under pressing
Figure 3-11. (a) Response time, and recovery time of the pressure mechanoreceptor,, and (b)
corresponding Instron compression data
Figure 3-12. Frequency response of the mechanoreceptor
Figure 3-13. Voltage of the mechanoreceptor under 40000 compressions
Figure 3-14. Voltage response at 1-10 cycles
Figure 3-15. Voltage response at 20000 cycles
Figure 3-16. Voltage response at 39550 cycles
Figure 3-17. Voltage response of cycle 1, cycle 20001, and cycle 39551
Figure 3-18. Off-state resistance of the mechanoreceptor throughout 20 washing cycles 89
Figure 3-19. Electromechanical performance of the mechanoreceptor throughout 20 washing
cycles90
Figure 3-20. Voltage response of the mechanoreceptor versus different material filling rate
(0.1 mm in Height, DS 20)
Figure 3-21. Interrelationship between material filling rate, and the pressure threshold of
mechanoreceptor (0.1 mm in Height, DS 20)
Figure 3-22. Voltage response of the mechanoreceptor versus different height of stencil (Area
material filling rate: 33.33%, DS 20).

Figure 3-23. Interrelationship between stencil thickness, and the pressure threshold of
mechanoreceptor (Area material filling rate: 33.33%, DS 20)
Figure 3-24. Voltage response of the mechanoreceptor versus different modulus PDMS 96
Figure 3-25. Interrelationship between the pressure threshold, and PDMS modulus (0.1mm in
height, Area material filling rate: 44.44%)
Figure 4-1. Photo of the rubber keypad
Figure 4-2. Photo of the membrane keypad
Figure 4-3. Deformation of the membrane keypad
Figure 4-4. Pressure threshold of the membrane keypad
Figure 4-5. Electric diagram of the textile sensor-synaptic array
Figure 4-6. Exploded structure of the textile-based sensor-synaptic array
Figure 4-7. Fabrication process of the textile-based mechanoreceptors array
Figure 4-8. Experimental set up of water immersion test
Figure 4-9. Photo of the textile mechanoreceptors array
Figure 4-10. Textile-based sensor-synaptic array resistance
Figure 4-11. Resistance different between keys
Figure 4-12. Bending curve of the textile sensor-synaptic array
Figure 4-13. Bending force of three textile-based sensor-synaptic array samples
Figure 4-14. Sensor-synaptic array key resistance variation before, and after the water
immersion test
Figure 4-15. Resistance difference between keys before, and after the water immersion test.
Figure 4-16. Sensor-synaptic array key resistance before, and after the cyclic temperature
test
Figure 4-17. Resistance difference between keys before, and after the cyclic temperature test.

Figu	are 4-18. Sensor-synaptic array key resistance before, and after low temperature test 126
Figu	are 4-19. Resistance difference between keys before, and after the low temperature test.
6.	Figure 4-20. Sensor-synaptic array key resistance before, and after the high temperature
	test
8.	Figure 4-21. Resistance difference between keys before, and after the high temperature
	test
Figu	are 4-22. Key resistance of sensor-synaptic array at 1 min and 100000 min
Figu	are 4-23. Resistance difference between keys at 1 min and 100000 min
Figu	are 4-24. Key 4, 8, 12, and 16 resistance variation along time
Figu	are 4-25. Resistance measurement of mechanoreceptors array under maximum mechanical
	force
Figu	are 4-26. Actual resistance of the textile array under different tester pressing
Figu	are 4-27. Resistance difference between keys under different tester pressing
Figu	re 5-1. Electric diagram of the diabetic foot sock
Figu	are 5-2. Overall design of the sock pressure monitoring system
Figu	are 5-3. Mechanism, and design of the sock for Parkinson patient
Figu	are 5-4. Cross-section of the pressure sensation platform
Figu	are 5-5. Electric diagram of the pressure sensation platform
Figu	are 5-6. Mechanism of the pressure sensation platform
Figu	are 5-7. A schematic illustration of the serpentine circuit design
Figu	are 5-8. Photo of the flexible stretchable circuit
Figu	are 5-9. Photo of the electronic yarn
Figu	are 5-10. A schematic diagram of the connection of the pressure sensation platform 149

2. Figure 5-11. Experiment set-up of the pressure measurement	153
Figure 5-12. Tensile properties of the bandage.	155
Figure 5-13. Tensile properties of the encapsulated bandage.	155
Figure 5-14. Cyclic tensile properties of the bandage	156
Figure 5-15. Cyclic tensile properties of the laminated bandage	157
Figure 5-16. Resistance change of the serpentine circuit(strain rate: 30%)	158
Figure 5-17. Pressure threshold of the mechanoreceptors with different sizes	158
Figure 5-18. Pressure thresholds of the mechanoreceptors with different compr	ression area.
	158
Figure 5-19. Voltage response of the mechanoreceptors under compression	165
Figure 5-20. Pressure threshold of the mechanoreceptors.	165
Figure 5-21. Mannequin wearing the sock for diabetic patients. Left: LED is in	ı off-state.
Right: LED is in on-state.	166
Figure 5-22. Voltage response of the mechanoreceptor for Parkinson patient	167
Figure 5-23. Pressure threshold of the mechanoreceptor for Parkinson patient	167
Figure 5-24. Photo of the sock for gait analysis.	168
Figure 5-25. Photo of the measurement of the sock when the users in sitting	169
Figure 5-26. Photo of the pressure sensation platform.	169
Figure 5-27. Response of the pressure sensation platform. (a) Resistance of the	;
mechanoreceptor. (b) Enlarged of the resistance of the mechanoreceptor a	at position 2, 3,
and 4. (c) Instron compression data	170
Figure 5-28. Bending rigidity of the mechanoreceptor array.	174
Figure 6-1. A multidisciplinary framework for wearable PBM device	179
Figure 6-2. Overview of evaluation system for the wearable PBM system	180
Figure 6-3. Experiment set-up for irradiance measurement	183

Figure 6-4. Photo of the KES-F8 air permeability tester.	185
Figure 6-5. Photo of the components of the PBM panel.	187
Figure 6-6. Electric circuit diagram of the PBM panel.	188
Figure 6-7. Photo of the working mode of the PBM panel. Left: 850 nm LED is	on. Right:
650 nm LED is on.	188
Figure 6-8. Wavelength shift of 850 nm LED at different current	189
Figure 6-9. 850 nm LEDs systematic IV curve.	190
Figure 6-10. Individual 850 nm LED IV curve.	191
Figure 6-11. 850 nm LED IV curve.	192
Figure 6-12. Wavelength shift of 660 nm LED.	195
Figure 6-13. 660 nm LEDs system IV curve.	196
Figure 6-14. Individual 660 nm LED IV curve.	196
Figure 6-15. 660 nm LED average IV curve.	197
Figure 6-16. Irradiance of the panel with or without lens.	200
Figure 6-17. 850 nm LED irradiance distribution.	201
Figure 6-18. 850 nm LED viewing angle.	202
Figure 6-19. 650 nm LED irradiance distribution.	203
Figure 6-20. 650 nm LED viewing angle.	204
Figure 6-21. Irradiance distribution of the panel (Horizontal).	205
Figure 6-22. Irradiance distribution of the panel (Vertical).	205
Figure 6-23. Irradiance of the panel during treatment time	206
Figure 6-24. Photo of the wearable PBM panel.	209
Figure 6-25. Optical image of the 5050 LED.	210
Figure 6-26. Working mode of the wearable PBM panel.	210
Figure 6-27. Photo of the wearable PBM circuit.	211

Figure 6-28. Circuit design of the wearable PBM.	211
Figure 6-29. Electric diagram of the wearable PBM panel.	212
Figure 6-30. Wavelength spectrum of the wearable PBM panel.	213
Figure 6-31. Wavelength shift of the 850 nm emitter.	214
Figure 6-32. Wavelength shift of the 650 nm emitter.	215
Figure 6-33. LED voltage of the wearable PBM device.	216
Figure 6-34. IV curve of the LED.	217
Figure 6-35. Irradiance of the wearable PBM panel.	218
Figure 6-36. Irradiance distribution of wearable PBM (Horizontal).	219
Figure 6-37. Irradiance distribution of wearable PBM (vertical).	220
Figure 6-38. Irradiance variation of the panel throughout treatment.	220
Figure 6-39. Bending rigidity of the wearable PBM circuit.	223
Figure 7-1. Research framework of the wearable PBM panel	230
Figure 7-2. Actual irradiance distribution of different sizes of LEDs	239
Figure 7-3. Relative irradiance distribution of different sizes of LEDs	239
Figure 7-4. Irradiance distribution of the LEDs.	248
Figure 7-5. Viewing angle of the LEDs in relative intensity	248
Figure 7-6. A schematic diagram of the simulated array.	249
Figure 7-7. Simulated central irradiance distribution of LEDs with different distance	251
Figure 7-8. Simulated irradiance distribution of LEDs with different distances (Middle	
position).	252
Figure 7-9. Simulated irradiance distribution of the LEDs with different arrangement	253
Figure 7-10. Simulated irradiance distribution of the LEDs with different arrangement	254
Figure 7-11. Irradiance distribution of the LED array with 30 mm interdistan5ce	255
Figure 7-12. Irradiance distribution of the LED array with 15 mm interdistance	255

Figure 7-13. Fabric pattern of the underwear.	257
Figure 7-14. Shape of the flexible PBM panel, and corresponding LED positions	258
Figure 7-15. Circuit design of the PBM panel pattern 1.	259
Figure 7-16. Circuit design of the PBM panel pattern 2.	260
Figure 7-17. Photo of the PBM panel pattern 1.	260
Figure 7-18. Photo of the PBM panel pattern 2.	260
Figure 7-19. Irradiance distribution of the flexible PBM panel in horizontal direction	261
Figure 7-20. Irradiance distribution of the flexible PBM panel in vertical direction	262
Figure 7-21. Irradiance variation of the flexible PBM panel throughout treatment	263
Figure 7-22. Conformabiltiy of the flexible PBM panel	264
Figure 7-23. LED irradiance distribution with different light diffuser.	266
Figure 7-24. Integration of the flexible PBM panel into the underwear.	267

List of Tables

Table 2-1. Table about the recent flexible photobiomodulation device
Table 3-1. Materials and tools.
Table 3-2. Design, and optical image of the PDMS structure
Table 3-3. Optical image of the cross-section of mechanoreceptor with or without loading. 83
Table 3-4. Parameters of the PDMS, and corresponding material filling rate
Table 3-5. Thickness measurement of the PDMS.
Table 4-1. Materials and Tools.
Table 4-2. Functionality of the sensor-synaptic array under bending
Table 4-3. Optical image of the sensor-synaptic array
Table 4-4. Off-state resistance of the keyboard before, and after cyclic temperature test 12:
Table 4-5. Off-state resistance of the keyboard before, and after low temperature test 12
Table 4-6. Off-state resistance of the keyboard before and after high temperature test 129
Table 5-1. Position of the mechanoreceptors for diabetic foot
Table 5-2. Experiment design about the compression area, and size
Table 5-3. Interrelationship between the pressure threshold, and the mechanoreceptor size 16
Table 5-4. Interrelationship between the pressure threshold, and compression area 163
Table 5-5. Design of the mechanoreceptor array
Table 5-6. Thickness measurement of the mechanoreceptor array
Table 5-7. Pressure measurement of mechanoreceptors (6 cm)
Table 5-8. Pressure measurement of mechanoreceptors (4 cm)
Table 6-1. 850 nm LED IV curve in relation to irradiance
Table 6-2. Individual 660 nm LED IV curve, and irradiance
Table 6-3. Temperature measurement of the PBM panel

Table 6-4. IV, and irradiance of the LEDs in wearable PBM	. 217
Table 6-5. Temperature measurement of wearable PBM	. 221
Table 6-6. Comparison between PBM panel, and wearable PBM.	. 223
Table 7-1. Parameter of the LEDs	. 231
Table 7-2. Specification of the diffusers.	. 232
Table -7-3. Cup size	. 235
Table 7-4. Size of the bra.	. 237
Table 7-5. Wavelength variation of the LEDs at different current	. 242
Table 7-6. LED IV curve, and corresponding irradiance.	. 246
Table 7-7. Size of the flexible PBM panel	. 258
Table 7-8. Temperature measurement of the flexible PBM panel	. 265

List of Abbreviations and Symbols

ATP	Adenosine triphosphate
AlInGaP	Aluminium gallium indium phosphide
BaTiO ₃	Barium Titante
CNT	Carbon nanotube
Cox	Cyclooxygenase
FCB	Flexible circuit board
HMI	Human machine interface
InGaN	Indium gallium nitride
LED	Light emitting diode
μLED	Micro light emitting diode
OLED	Organic light emitting diode
PVDF-TrFE	Poly(vinylidene fluoride-trifluoroethylene)
PAN	Polyacrylonitrile
PBM	Photobiomodulation
PZT	Lead Zirconium Titanate
PDMS	Polydimethylsiloxane
PET	polyethylene terephthalate
TENG	Triboelectric sensor
TPU	Thermoplastic polyurethane
UV	Ultraviolet light
SNR	Signal-to-noise ratio
WHD	Wearable healthcare devices

ZnO	Zinc Oxide
3D	Three-dimensional
ROS	Reactive oxygen species

Chapter 1. Introduction

1.1. Background

In recent years, tremendous research has focused on developing different wearable healthcare products to improve the life quality of people/patients, like smart watches[1], headset,[2] ring[3], and shoes[4]. The development, and utilization of wearable healthcare products also can relieve the burden on the medical system, particularly in the context of the global aging problem. These devices can provide real-time, continuous, and remote monitoring to allow early detection of the disease, and reduce the requirement for frequent doctor visits[5], [6]. In addition, it can track the condition of the patient, promoting high adherence to treatment regimens, and making prompt adaption to patient care plans, especially for chronic disease[7]. On the other hand, the wearable devices also can provide remote, and tailored treatment adopting different patient conditions, reducing the demand for hospital visits. Overall, developing wearable healthcare devices is important in understanding the human body, and providing new ways to prevent, and treat disease.

Healthcare products can be simply classified into monitoring devices, and treatment devices. The classification of healthcare devices is demonstrated in Figure 1-1[8]. Monitoring devices can be used to monitor body signals, like heartbeat[9], blood pressure[10], and biomarkers[11], [12], to evaluate the health condition of the users to prevent diseases or damage. The development of wearable health monitoring devices can be generally classified as textile-based or tattoo-based based on the contact way. Textile-based devices are integrated into clothing or accessories, while tattoo-based devices direct contact with human skin. Textile-based devices offer advantages in terms of comfort, flexibility, and reusability for long-term monitoring, enabling seamless integration into the user's daily life. It is the ideal option for

extended use. However, the performance of the textile-based device deteriorates with usage, and the signal fidelity is affected by the contact. In summary, it is valuable to develop textile-based monitoring devices for long-term usage.

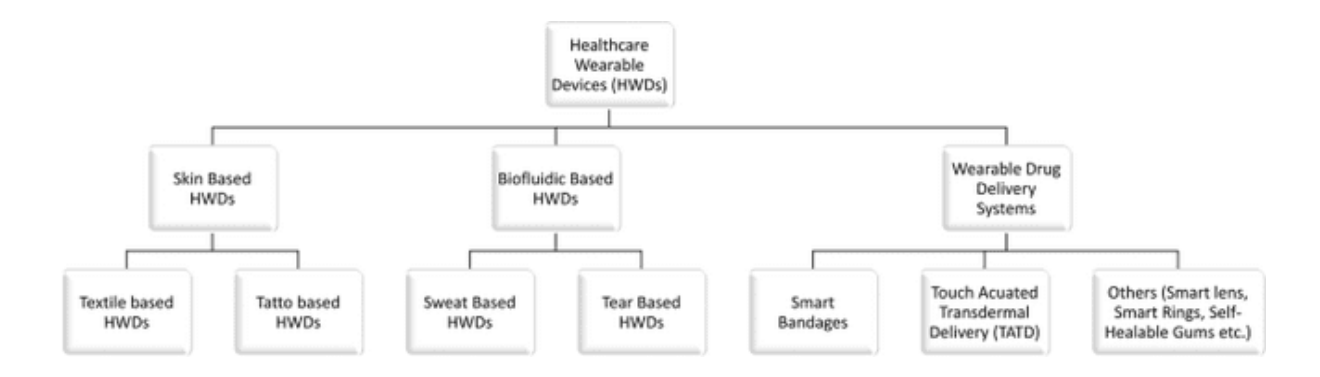


Figure 1-1. Classification of WHDs.

Pressure is a critical human parameter that represents the interaction between human skin, and the outdoor environment. At present, the usage of pressure sensors is the predominating method to monitor human pressure. The monitoring is significantly influenced by environmental factors, like temperature, relative humidity, electric field, and users's skin condition. The unstable performance of these sensors challenges the reliability of the sensation[13], [14], [15], [16], thereby limiting its practical application. Given these limitations, it is valuable to study the pressure sensation mechanism of human skin to develop emulated mechanoreceptors that can improve the reliability, and stability of pressure sensation. Another consideration is the diversity of the pressure sensation range and usage conditions in health monitoring applications. For instance, plantar pressure can be in the range of dozens to several hundred or even thousands of kilopascals[17], [18]. The pressure for nerve sensation loss was around 250 kPa[19], while the pressure to detect gait was around 20 or 30 kPa depending on the wearers' weight, and foot size[20]. The diverse pressure sensation range requirements also indicate that some pressure sensation range is not essential to specific health monitoring conditions. Eliminate a certain range of pressure sensations can reduce the data processing, and

decrease the sensation errors. Therefore, a novel pressure sensation device with thresholds for health monitoring is highly demanded.

Wearable treatment devices typically deliver drugs or energy to the human body via different formats, like bandages, lenses, and rings. These developments seek to minimize the treatment inconvenience to shorten the distance in time, and space. Current researches mainly focus on the drug deliverable system[21], [22], and only a few attentions are drawn to the energy deliverable device. In the realm of energy-based treatment, photobiomodulation is historically to treat diverse diseases. The treatment scope can be covered in skin rejuvenation[23], hair loss[24], skin improvement (reduce wrinkles, and skin laxity), and oral dermatitis[25]. However, PBM is not prevalent because of the time characteristic of treatment, and the applicability of the devices. Patients often need to conduct several times of PBM in a month, which one treatment usually lasts from seconds to twenty minutes depending on the dose rate, power of the light source, and working mode of the PBM devices[26]. This places a burden on the medical system and patients. To address this issue, developing an effective, wearable, lightweight, and remote PBM device is vital. For effective treatment, the treatment distance, energy of the light source, and other parameters are critical. There is no general guideline about the requirement of a PBM device for efficient photobiomodulation. Additionally, the existing PBM device is not suitable for conducting remote PBM at home. Commercial PBM panels are difficult to control at home, especially in terms of the treatment distance, while wearable PBM systems are still in an embryotic stage. The comfort, comfortability, light source, and irradiance still need further research. Overall, there is a clear demand for a remote wearable PDM system to effectively conduct, and monitor the treatment condition.

Cancer has become one of the leading causes of death around the world. In addition to

treating the tumor, improving the cancer patient's life quality also is vital to their survival rate[27], [28]. Supportive care is drawn much attention in helping patients to monitor the associated symptoms and side effects. Among the side effects, radioactive dermatitis is a serious consequence of the radiotherapy. Currently, there is no effective method to relieve the radioactive dermatitis[29], and there are several clinical studies proved that conducting photobiomodulation can reduce the severity of symptoms of radioactive dermatitis[30], [31]. However, this treatment is still relatively new, and there are limited devices available due to factors such as price, form factor, and adaptability. For example, in the case of breast cancer patients, the treated area is not flat, and photobiomodulation needs to conform to the contours of the breast, with a larger treatment area being preferred. Therefore, the development of a wearable photobiomodulation device that conforms to the human body's contours as a supportive care system for cancer patients would be highly valuable.

1.2. Problem statement

As stated in the background, stable, reliable, comfortable, and wearable healthcare systems for healthcare monitoring, and treatment are still limited. The major research problems about the wearable pressure sensation devices for health monitoring, and wearable photobiomodulation systems involve the following aspects:

Health monitoring device - pressure sensation:

1. Poor stability, and reliability of pressure sensation: In health monitoring, the use of different sensors to detect pressure sensation is common, but their performance is highly influenced by environmental factors, such as temperature, relative humidity, and electric fields. This challenges the pressure sensor signal fidelity, and necessitates additional calibration, and the incorporation of another

sensor, like temperature sensors. Therefore, a novel type of mechanoreceptors should be designed, and fabricated with stable performance across different environments. This will ensure consistent, and reliable pressure sensation in health monitoring applications.

2. Diverse requirements on pressure sensation range for various applications: Pressure sensation requirements in health monitoring are diverse because of the different sensation purpose, and sensation location. Using the same sensor for all applications necessitates complicated algorithms for decision-making, resulting in higher, and time consumption. On the other hand, it indicates that there is no need for pressure sensation in certain ranges. For sensation accuracy, time, and energy efficiency, the mechanoreceptors should be equipped with a pressure threshold to specify the range of pressure sensation.

Wearable photobiomodulation device:

- 3. Unknown interrelationship between the photobiomodulation treatment parameters, and the design PBM device: To conduct effective photobiomodulation, the PBM device needs to emit light with appropriate optical properties, matching the pathology of the radioactive dermatitis. However, the pathology of radioactive dermatitis and the mechanism of the photobiomodulation are not fully understood. It is vital to establish an evaluation system to study existing commercial photobiomodulation devices 'performance to identify their capability, merits, and challenges. Furthermore, this evaluation could serve as a benchmark for the development of wearable photobiomodulation devices for breast cancer patients.
- 4. Limited wearable photobiomodulation panel conforming body contour for

remote treatment: Existing commercial photobiomodulation is not applicable to conduct remote photobiomodulation due to their form factor, size, and limited flexibility. The control of the treatment is not precise, bringing challenges to the effectiveness, and the popularity of photobiomodulation. It is demanding to develop a novel photobiomodulation device capable of conforming human contour, particularly the shape of the breast, to conduct effective photobiomodulation.

Despite addressing distinct functions, both stable pressure sensation and effective wearable photobiomodulation face fundamental hurdles related to conformability and consistent interface performance on the dynamic human body. Maintaining reliable skin-device contact is critical for both accurate pressure signal acquisition and efficient light delivery, yet body contours, movement, and natural variations in skin properties (e.g., moisture, texture) pose significant challenges. This necessitates novel material strategies and device designs that ensure stable, conformal adhesion/alignment across complex and changing surfaces like limbs or the breast, without compromising user comfort during extended wear. Furthermore, both technologies require robustness against environmental variables (e.g., temperature fluctuations, humidity) and user-induced perturbations (motion artifacts, pressure changes) to guarantee data fidelity for monitoring or treatment efficacy for therapy, moving beyond controlled lab conditions into real-world use. Overall, there is a need to develop devices that meet these challenges.

1.3. Objectives

To address the challenges, this study focuses on developing mechanoreceptors with novel structured to have stable performance, through the design, utilization of the materials. The detailed objectives are listed as follows:

- 1) To design, develop, and characterize a novel pressure sensation device with stable performance in different environments to enhance the reliability of pressure sensation for wearable health monitoring devices.
- 2) To study the controllability of the pressure thresholds in the mechanoreceptors, exploring their correlation with various structural parameters to enable precise control the pressure thresholds through multiple factors, thus broadening the design potential for wearable applications.
- 3) To develop a mechanoreceptor array for positioning, streamlining the data processing, and connection for wearable applications, and explore the integration of corresponding devices on different wearable applications.
- 4) To establish a comprehensive evaluation system for wearable photobiomodulation systems from the aspect of electrical properties, optical properties, and textile properties to study the device parameters in relation to efficient photobiomodulation.
- 5) To design, and develop a flexible photobiomodulation panel to relieve the radioactive dermatitis of breast cancer patients, as a pathway for the conversion of rigid health treatment devices to a wearable, and flexible format.

1.4. Methodology

The thesis mainly focuses on the study of pressure sensation for healthcare and the photobiomodulation. For the pressure sensation part, this thesis mainly focuses on the controllability of the pressure threshold adopting different wearable applications through the utilization of the PDMS structure, materials, and device design. In the context of

photobiomodulation, it focuses on the transforming of efficient photobiomodulation devices into wearable format.

Pressure health monitoring device:

Firstly, a comprehensive literature review will be conducted on the human-machine interface, especially the mechanical sensation. It will provide insight to understand the priority of pressure sensor parameters, different types of pressure sensors, and the corresponding fabrication techniques. Human skin pressure sensation and perception will be studied to study its efficiency as the basis for mechanoreceptor design to assess the challenges in pressure sensation.

Then, a novel mechanoreceptor structure will be designed, fabricated, and characterized. The interrelationship between the pressure threshold of the mechanoreceptors and the structural parameters will be studied. Furthermore, the controllability of the pressure thresholds of the mechanoreceptors from different aspects will be explored to broaden the potential of design freedom. The mechanoreceptor's performance on the response time, frequency, and reliability also will be evaluated.

Next, a novel mechanoreceptor array will be designed, and fabricated with simpler connection, and data processing. The interconnection, and assembly of the novel mechanoreceptors will be investigated to explore the challenges associated with flexible textile electronics assembly. The array performance at different environments will be characterized, and compared to the commercial product.

Finally, we will explore the integration of the mechanoreceptor and its array into the clothing or accessories for various wearable applications. The performance of the

mechanoreceptors in different applications will be characterized will be studied to examine the adaptability of mechanoreceptor and their potential for widespread use.

Wearable photobiomodulation panel:

Firstly, we will conduct a literature review about the mechanism of photobiomodulation, and pathology of radioactive dermatitis, and investigate their interconnection. It will provide insight into the treatment requirement of photobiomodulation, including wavelength, and irradiance, as well as the current research gap on the photobiomodulation device. Additionally, different types of wearable photobiomodulation systems will be examined to discuss their merits, and challenges.

Next, an evaluation system for the photobiomodulation device will be established to study the commercial photobiomodulation device from electrical properties, optical properties, and textile properties. Two commercial photobiomodulation devices will be evaluated via the system to study the device parameters to the treatment efficiency. This study will explore the connection between the treatment parameter, and device properties as a basis for PBM device design. The evaluation system will also serve as a framework for the further evaluation of the flexible PBM.

Finally, a flexible photobiomodulation panel for breast cancer patients will be designed, fabricated, and characterized. In detail, the appropriate LEDs will be selected through various measurements from the aspect of electrical, and optical properties, and the arrangement, and the interdistance between LEDs will be studied through simulation. The panel's shape will be tailored to conform to the breast anatomy, and the circuit will be adapted to fit this design. Additionally, sizing variations for different users will be addressed.

1.5. Originality and Significance

The novelty of this thesis lies in the following aspects:

- 1. A novel fabric-based mechanoreceptor was designed in which the pressure threshold can be controlled through various parameters, including PDMS material filling rate, height of PDMS structure, PDMS material modulus, compression area, and size of the mechanoreceptors. This design allows pressure thresholds ranging from several kPa to MPa, making it adaptable to a wide range of wearable applications. Given the multiplicity of controllable dimensions, the processing requirement associated with any specific dimension can be reduced by exploiting the synergistic effects of multiple dimensions. The response time of the mechanoreceptor was only 40 ms, and it can function under 1 kHz compression frequency. Additionally, this novel structure endows the mechanoreceptors with a high on-off ratio (>10⁻⁸), and maintains good reliability under repeated compressions (>40000 compressions), and laundry cycles (20 laundry cycles).
- 2. A novel mechanoreceptor spiral array containing a total of 16 mechanoreceptors was developed, in which the connection between the data processing unit, and the array becomes simpler (2 output electrodes), and the data processing becomes faster and more efficient. The identification of the mechanoreceptors can be realized through the resistance difference between keys. The resistance of mechanoreceptors is in the range of 0.01 kΩ to 48.4 kΩ, and the resistance difference between mechanoreceptors is around 3.226 kΩ. The entire fabrication process and materials of the mechanoreceptor are based on textile substrates, including the mechanoreceptor, and the flexible resistor, without the addition of bulky, and rigid components. This leads to a fabric-based pressure-sensitive array seamlessly integrated into textile products. Additionally, the

mechanoreceptor's on-off resistance value can be maintained stable at the high temperature (50°C for 72 hours), the low temperature (-40°C for 72 hours), water immersion test (1 m), a lifespan of 10000 mins, and under maximum mechanical load (100 N).

- 3. The mechanoreceptor, and its array are developed based on the textile or flexible materials, which can be seamlessly integrated into socks, and other clothing for 3D plantar pressure sensation, fall detection, and pressure sensation for various wearable applications.
- 4. A comprehensive evaluation system was established to evaluate the photobiomodulation device on the aspects of electrical properties, optical properties, and textile properties. This system was utilized to evaluate two commercial photobiomodulation devices, with a focus on how LED selection influences treatment performance, including wavelength, IV, irradiance, and system power. The evaluation successfully established the connection between the PBM treatment parameter and the device design.
- 5. A flexible wearable photobiomodulation panel was developed to conform to the human contour based on the underwear pattern. This innovation provides a guideline for transforming rigid health treatment devices into wearable formats that conform to the human contour, addressing sizing issues.

1.6. Structure of the thesis

The thesis focuses on fabric-based mechanoreceptors and wearable PBM devices for breast cancer patients. It consists of eight chapters, and the detailed content of the thesis is described as follows:

Chapter 1 provides a brief introduction to the background of wearable healthcare devices, and corresponding challenges. The detailed research objectives about the fabric-based mechanoreceptors, and the flexible PBM are stated. The originality, and significance of this research are summarized.

Chapter 2 comprehensively reviews different human-machine interface technology and photobiomodulation techniques. Regarding HMI technology, it discusses the important parameters of pressure sensation, different pressure sensation techniques, and the corresponding fabrication techniques. This provides a guideline for further design on the design, and fabrication techniques of the fabric-based mechanoreceptors. In the context of PBM, it explores the mechanism of the PBM, important parameters for the efficient PBM, and different wearable PBM techniques. This exploration helps to determine the development pathway of the flexible wearable PBM device.

Chapter 3 introduces a novel type of mechanoreceptors, in which the pressure threshold can be controlled with the structural parameters. The interrelationship between the mechanoreceptor pressure threshold and different structural parameters is examined. The mechanoreceptors were characterized from different aspects, including frequency response, time response, reliability under repeated compressions, and laundries.

Chapter 4 presents a corresponding serpentine mechanoreceptor array with a simpler connection and more efficient data processing. The position of the mechanoreceptors can be identified simply through the resistance variation of the output. The array stability was characterized by different conditions, including temperature variation, mechanical load, water immersion, and others.

Chapter 5 explores the potential of the mechanoreceptors and its array for different

wearable applications. Mechanoreceptors with different pressure thresholds are developed based on the previous research. The mechanoreceptors are then integrated into clothing and accessories. Additionally, the design of the mechanoreceptors was improved for better user experience and comfortability.

Chapter 6 depicted the establishment of an evaluation system for PBM, from the aspect of electric properties, optical properties, and textile properties. Furthermore, two different types of commercial PBM devices were evaluated using this system. This provides insight into identifying the challenges and problems in the development of wearable flexible PBM systems.

Chapter 7 presents the development of the flexible photobiomodulation panel for breast cancer patients. It covers the LED selection, array design, optical design, panel shape design, panel sizing, and integration of the panel to underwear. This helps to identify the limitations, and challenges of the development of wearable PBM devices.

Chapter 8 summarizes the work on the mechanoreceptors and the flexible photobiomodulation device. It also discusses the limitations, and insufficiencies of current studies, and prospects for further studies.

1.7. References

- [1] B. Reeder and A. David, 'Health at hand: A systematic review of smart watch uses for health and wellness', *J. Biomed. Inform.*, vol. 63, pp. 269–276, Oct. 2016, doi: 10.1016/j.jbi.2016.09.001.
- [2] M. R. Golab, P. J. Breedon, and M. Vloeberghs, 'A wearable headset for monitoring electromyography responses within spinal surgery', *Eur. Spine J.*, vol. 25, no. 10, pp. 3214–3219, Oct. 2016, doi: 10.1007/s00586-016-4626-x.
- [3] 'Smart ring: a wearable device for hand hygiene compliance monitoring at the point-of-need | Microsystem Technologies'. Accessed: Aug. 16, 2024. [Online]. Available: https://link.springer.com/article/10.1007/s00542-018-4268-5

- [4] N. Surantha, P. Atmaja, David, and M. Wicaksono, 'A Review of Wearable Internet-of-Things Device for Healthcare', *Procedia Comput. Sci.*, vol. 179, pp. 936–943, Jan. 2021, doi: 10.1016/j.procs.2021.01.083.
- [5] Z. Lou, L. Wang, K. Jiang, Z. Wei, and G. Shen, 'Reviews of wearable healthcare systems: Materials, devices and system integration', *Mater. Sci. Eng. R Rep.*, vol. 140, p. 100523, Apr. 2020, doi: 10.1016/j.mser.2019.100523.
- [6] X. Wang, Z. Liu, and T. Zhang, 'Flexible sensing electronics for wearable/attachable health monitoring', *Small*, vol. 13, no. 25, p. 1602790, 2017.
- [7] T. Kamei, T. Kanamori, Y. Yamamoto, and S. Edirippulige, 'The use of wearable devices in chronic disease management to enhance adherence and improve telehealth outcomes: A systematic review and meta-analysis', *J. Telemed. Telecare*, vol. 28, no. 5, pp. 342–359, Jun. 2022, doi: 10.1177/1357633X20937573.
- [8] S. M. A. Iqbal, I. Mahgoub, E. Du, M. A. Leavitt, and W. Asghar, 'Advances in healthcare wearable devices', *Npj Flex. Electron.*, vol. 5, no. 1, pp. 1–14, 2021, doi: 10.1038/s41528-021-00107-x.
- [9] Y. H. Kwak, W. Kim, K. B. Park, K. Kim, and S. Seo, 'Flexible heartbeat sensor for wearable device', *Biosens. Bioelectron.*, vol. 94, pp. 250–255, Aug. 2017, doi: 10.1016/j.bios.2017.03.016.
- [10] J. Kim, E.-F. Chou, J. Le, S. Wong, M. Chu, and M. Khine, 'Soft wearable pressure sensors for beat-to-beat blood pressure monitoring', *Adv. Healthc. Mater.*, vol. 8, no. 13, p. 1900109, 2019.
- [11] J. Kim *et al.*, 'Noninvasive Alcohol Monitoring Using a Wearable Tattoo-Based Iontophoretic-Biosensing System', *ACS Sens.*, vol. 1, no. 8, pp. 1011–1019, Aug. 2016, doi: 10.1021/acssensors.6b00356.
- [12] C. Song, B. Yang, Y. Zhu, Y. Yang, and L. Wang, 'Ultrasensitive sliver nanorods array SERS sensor for mercury ions', *Biosens. Bioelectron.*, vol. 87, pp. 59–65, 2017.
- [13] B. Aksoy, Y. Hao, G. Grasso, K. M. Digumarti, V. Cacucciolo, and H. Shea, 'Shielded soft force sensors', *Nat. Commun.*, vol. 13, no. 1, p. 4649, 2022.
- [14] V. Nguyen and R. Yang, 'Effect of humidity and pressure on the triboelectric nanogenerator', *Nano Energy*, vol. 2, no. 5, pp. 604–608, Sep. 2013, doi: 10.1016/j.nanoen.2013.07.012.
- [15] M. Aryafar, M. Hamedi, and M. M. Ganjeh, 'A novel temperature compensated piezoresistive pressure sensor', *Measurement*, vol. 63, pp. 25–29, Mar. 2015, doi: 10.1016/j.measurement.2014.11.032.

- [16] R. B. Mishra, N. El-Atab, A. M. Hussain, and M. M. Hussain, 'Recent Progress on Flexible Capacitive Pressure Sensors: From Design and Materials to Applications', *Adv. Mater. Technol.*, vol. 6, no. 4, p. 2001023, 2021, doi: 10.1002/admt.202001023.
- [17] J.-L. Chen *et al.*, 'Plantar Pressure-Based Insole Gait Monitoring Techniques for Diseases Monitoring and Analysis: A Review', *Adv. Mater. Technol.*, vol. 7, no. 1, p. 2100566, 2022, doi: 10.1002/admt.202100566.
- [18] A. H. A. Razak, A. Zayegh, R. K. Begg, and Y. Wahab, 'Foot plantar pressure measurement system: A review', *Sensors*, vol. 12, no. 7, pp. 9884–9912, 2012.
- [19] L. Shu *et al.*, 'Monitoring diabetic patients by novel intelligent footwear system', in *2012 International Conference on Computerized Healthcare (ICCH)*, 2012, pp. 91–94. doi: 10.1109/ICCH.2012.6724478.
- [20] B. Yang *et al.*, 'Intelligent wearable system with accurate detection of abnormal gait and timely cueing for mobility enhancement of people with Parkinson's disease', *Wearable Technol.*, vol. 3, p. e12, 2022.
- [21] A. Kar, N. Ahamad, M. Dewani, L. Awasthi, R. Patil, and R. Banerjee, 'Wearable and implantable devices for drug delivery: Applications and challenges', *Biomaterials*, vol. 283, p. 121435, Apr. 2022, doi: 10.1016/j.biomaterials.2022.121435.
- [22] J. Di *et al.*, 'Stretch-Triggered Drug Delivery from Wearable Elastomer Films Containing Therapeutic Depots', *ACS Nano*, vol. 9, no. 9, pp. 9407–9415, Sep. 2015, doi: 10.1021/acsnano.5b03975.
- [23] G. E. Glass, 'Photobiomodulation: a systematic review of the oncologic safety of low-level light therapy for aesthetic skin rejuvenation', *Aesthet. Surg. J.*, vol. 43, no. 5, pp. NP357–NP371, 2023.
- [24] A. E. Torres and H. W. Lim, 'Photobiomodulation for the management of hair loss', *Photodermatol. Photoimmunol. Photomed.*, vol. 37, no. 2, pp. 91–98, 2021.
- [25] R.-J. Bensadoun, M. A. Bollet, X. Liem, K. Cao, and N. Magné, 'New photobiomodulation device for prevention and cure of radiotherapy-induced oral mucositis and dermatitis: results of the prospective Safe PBM study', *Support. Care Cancer*, pp. 1–9, 2022.
- [26] L. Gavish and N. N. Houreld, 'Therapeutic Efficacy of Home-Use Photobiomodulation Devices: A Systematic Literature Review', *Photobiomodulation Photomed. Laser Surg.*, vol. 37, no. 1, pp. 4–16, Jan. 2019, doi: 10.1089/photob.2018.4512.
- [27] R. Sanson-Fisher *et al.*, 'The unmet supportive care needs of patients with cancer', *Cancer*, vol. 88, no. 1, pp. 226–237, 2000, doi: 10.1002/(SICI)1097-0142(20000101)88:1<226::AID-CNCR30>3.0.CO;2-P.

- [28] J. Armes *et al.*, 'Patients' Supportive Care Needs Beyond the End of Cancer Treatment: A Prospective, Longitudinal Survey', *J. Clin. Oncol.*, vol. 27, no. 36, pp. 6172–6179, Dec. 2009, doi: 10.1200/JCO.2009.22.5151.
- [29] E. B. Ferreira *et al.*, 'Topical interventions to prevent acute radiation dermatitis in head and neck cancer patients: a systematic review', *Support. Care Cancer*, vol. 25, pp. 1001–1011, 2017.
- [30] J. Robijns *et al.*, 'Photobiomodulation therapy for the prevention of acute radiation dermatitis in head and neck cancer patients (DERMISHEAD trial)', *Radiother. Oncol.*, vol. 158, pp. 268–275, 2021.
- [31] S. Censabella, S. Claes, J. Robijns, P. Bulens, and J. Mebis, 'Photobiomodulation for the management of radiation dermatitis: the DERMIS trial, a pilot study of MLS® laser therapy in breast cancer patients', *Support. Care Cancer*, vol. 24, pp. 3925–3933, 2016.

Chapter 2 Literature review

2.1. Introduction

This chapter conducts a comprehensive literature review on pressure sensation technique, radioactive dermatitis, and photobiomodulation to explore current problems in the field and identify potential solutions.

In the pressure sensation section, we discussed the existing pressure sensation limitations, recent advancements in flexible pressure sensation devices, and their fabrication techniques to identify their constraints. Additionally, we also studied the advanced mechanisms of human perception and examined related work that mimic human skin perceptions for efficient, and precise pressure sensation. This aims to explore new approaches to develop flexible input device that mimics human skin for efficient pressure sensation or communication between the environment, and the human.

Cancer patients often suffer serious side effects from radiotherapy, one of which is radioactive dermatitis. The skin is characterized by a range of symptoms from mild redness, and itching to several ulceration, and pain. This may reduce the physiology, and psychology of cancer patients, resulting in lower life quality. The pathology of the radioactive dermatitis, and related treatment to solve the pain and inconvenience were studied in order to develop new supportive care solutions, such as wearable supportive care systems for cancer patients.

In the photobiomodulation session, we first investigated the mechanism of photobiomodulation and then studied the impact of the device's parameter or treatment parameter on the efficient treatment. Based on this, we elucidated the interrelationship between

photobiomodulation parameters and the mechanism for efficient treatment. Furthermore, we summarized and analyzed current flexible photobiomodulation devices' structure, and fabrication techniques to identify their limitations. Otherwise, we tried to explore the potential of using photobiomodulation to treat radioactive dermatitis from the pathology, clinical studies, and device applicability.

Overall, this chapter aims to conduct a review of the development of pressure sensation, radioactive dermatitis, and photobiomodulation, address the problems within the field, and to search potential solutions for further research.

2.2. Introduction of pressure sensation

Pressure sensation is a typical technique used for human-machine interface (HMI), which is a user interface that connect user, and machine, enabling users to control, monitor, communicate with machines, systems or processes. It is valuable to start with the development of flexible HMI to review pressure sensation. HMI is normally composed of input, user/human, data processing, and output device, as shown in **Figure 2-1**[1]. User generate an input signal, which is received, and transmit to electrical signal via input device, data processing unit analysis the signal, and generate signal for output, the output unit response. The primary objective of the HMI is simplifying the inherent complexity of the automated operations. Consequently, HMI design, and materials must be tailored to fit usage habit in the related scenario. In details, the design needs to be user-cantered, considering the user's need, and behaviour in the specified scenario. For example, in sport monitoring, users prefer wearable devices to free their hand for comfort, and convenience. Conventional input devices, typical keyboard, and mouse, are rigid, and bulky, which can limit their suitability for certain applications, especially wearable applications. In wearable applications, such as fitness

trackers, smart clothing, or augmented reality devices, the input devices need to integrate into users' attire or accessories. Additionally, the integration of the input device needs to be seamless, indicating that the textile properties, and comfort need to similar to the attire or accessories[2]. Therefore, the input device needs to be flexible, lightweight, and capable of deforming to the contours of human body.

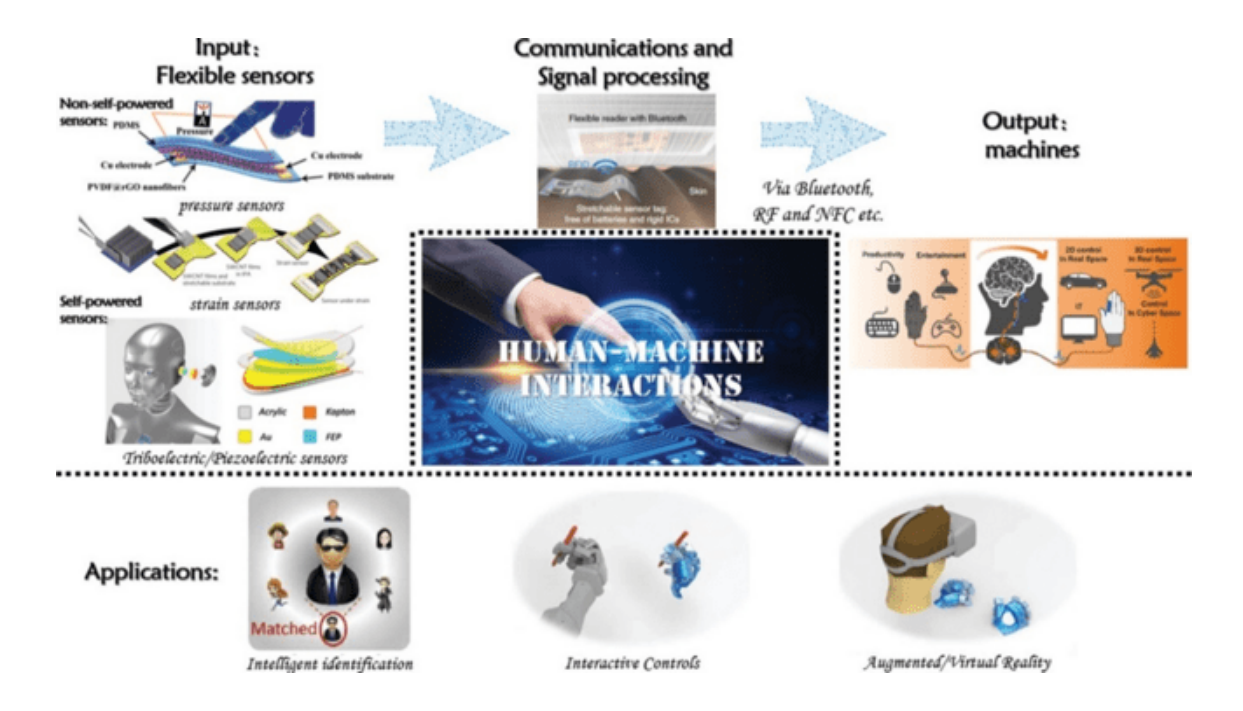


Figure 2-1. Overview of human-machine interface framework.

To enhance better user experience of HMI for wearable applications, it is essential to define the requirement of HMI. These requirements of the HMI are important parameter for the selection of the material, and designing the structure of the input device that is both flexible, and comfortable. In the following session, we are going to discuss the parameters of the flexible pressure input device.

2.2.1. Requirements of flexible pressure sensation device/interface

For wearable applications, the materials, and design of the wearable pressure sensation devices need to be sufficiently flexible to conform to the contour of human body, or integrate

seamlessly with clothing, thereby enhance a closer interaction between system, and the user. However, the flexibility, and deformability of the wearable pressure sensation cannot compromise the input device performance. Additionally, these characteristics can enhance its performance. To ensure the basic functionality of the flexible pressure input device, the detailed parameter of the flexible input device is defined, and elaborated in the following session.

Sensitivity: Sensitivity is interpreted as the device ability to detect, and respond to the environment stimuli or user interaction. It is a basic indicator to ensure the device to detect the stimuli, and its requirements may varied significantly depend on the usage scenario. In addition, the measurement of the sensitivity among different types of device are different. For instance, pressure sensor sensitivity refers to the quantitative response of the sensor to the output compression pressure. Switch sensitivity is elaborated as its actuation point, also termed as pressure threshold. It is defined as the minimum requirement to the output signal for the activation of the device. Higher sensitivity may detect minimized pressure signals, it is not universally advantageous. The application scenario, and pressure detection range need to be considered. In the case of plantar pressure monitoring, a sensor with very high sensitivity can lead to the pressure sensation being highly influenced by the environment, requiring complicated algorithms to filter out the noise. Higher sensitivity can increase the data processing time, and the energy consumption. Therefore, flexible pressure device needs appropriate sensitivity, fitting to the wearable applications.

Reliability: Sensitivity assure the functionality of the device, while reliability assure the accuracy, and credibility of the function. It defined as the probability of the device operating without failure under a specific set of usage condition. Reliability is complicated, and comprehensive concept, involving the measurement of the impacts of many factors on device performance[3]. For example, the sensor signal stability needs to be measured at the

different environment, like temperature, humidity, and sunshine[4]. Based on this, it is preferred to select functional materials with minimum responses to different temperature, and relative humidity. If the sensor is highly influenced, additional calibration unit, and process are required. On the other hand, the effect of the environmental electric field to the sensor signal need to be measured as signal-to-noise ratio (SNR), which is defined as the ratio of signal power to noise power. Besides environment, the integration of the flexible input device may involve exposure to different mechanical forces, like bending, stretching, and torture. Longevity of the device are also crucial part of the reliability, especially for wearable applications. In the case of wearable pressure sensor, number of compressions, laundry cycles, and maximum mechanical load need to measure to ensure the device long-term performance.

Time response: In addition to assess the function, and reliability of device, it is essential to test the time response of device to ensure the respond of the device on time with limited time delay. The time response of the input devices includes two main aspects- response time, and recovery time. Response time is defined as the time it takes for the sensor to change its output signal for the initial state to a certain percentage of the final value. The most common definition uses 90% of the final response, but sometimes 50% is also found in the literature[5]. Recovery time is defined as the interval between when an output signal change, and the time required for the device reaches a specified percentage from its final value. The most common definition is 10% of the maximum value[6].

Frequency Responses: In consideration of the application, the signal generated to the device may occur at various frequencies. For instance, the human heartbeat commonly falls within the frequency range of 0.6 Hz to 1 Hz, whereas body movement frequency is typically very low[7]. It is essential to measure the frequency response of the device, which represents the variation of the ratio between input variance, and output variance with the input frequency.

This analysis can verify that the flexible input device functions effectively across different frequencies.

Comfort: In addition to the electrical functionality, the textile properties of the flexible input device also need to be considered for comfort, and integration. One important consideration is the bending rigidity of the input device, which refers to the force required to bend or deform the device to a certain degree. Furthermore, the functionality of the device under bending, stretching, or other forms of deformation needs to be evaluated. In terms of comfort, it is also essential to measure the water permeability, and air permeability of the materials used. Water permeability assesses the ability of a fabric to allow perspiration in its vapor or liquid form to pass through[8], while air permeability is defined as the rate of airflow passing perpendicularly through a known area under a prescribed air pressure differential between the two surfaces of a material[9]. These properties play a crucial role in determining the balance of heat, and water vapor between the human body, and clothing, thereby contributing to comfort in different weather conditions.

Water proof: Water proof is a critical consideration to ensure the safety, and functionality of the flexible input device, particularly in wearable applications that involve the exposure to sweat, and laundry process. Due to this, the electric circuit, and the flexible switch need to be encapsulated to prevent the current leakage. The encapsulation material needs to be flexible with no deterioration to the functionality of the device. In addition, the applicability of the encapsulation methods to the device material, and fabrication are need to investigated. The testing method can refer to the standard from electrical encapsulation.

2.2.2. Developments of flexible pressure sensitive devices

In the previous section, we studied flexible pressure input device parameters, and

established a basic requirement in the material selection, and structure of the device. In the following section, we are going to investigated current flexible pressure input device, and compare their performance to the requirement in previous section to study its limitation. In recent years, there are numerous types of flexible input device in the recent years for different applications. From the mechanism of the input devices, the flexible pressure input device can be commonly categorized as two types- sensor based or others.

2.2.2.1. Pressure sensor

Sensor is defined as a device or instrument that detects, and measures certain physical signal from the environment, in response in electrical signals or other forms of signal for processing, and control. Flexible sensors can conform to the human contour to acquire biological signals, like blood pressure, respiration rate, and body movement to sense the movement in the interactions[10]. Using sensor as input device for HMI has got great attention in recent years. The common sensors mechanism includes piezoresistive, piezocapacitive, piezoelectric, and triboelectric, as shown in **Figure 2-2**[11]. Different types of sensor characterize with different advantages, and disadvantages for different applications. In the following section, different types of pressure sensor mechanism, materials, and development for flexible HMI was reviewed.

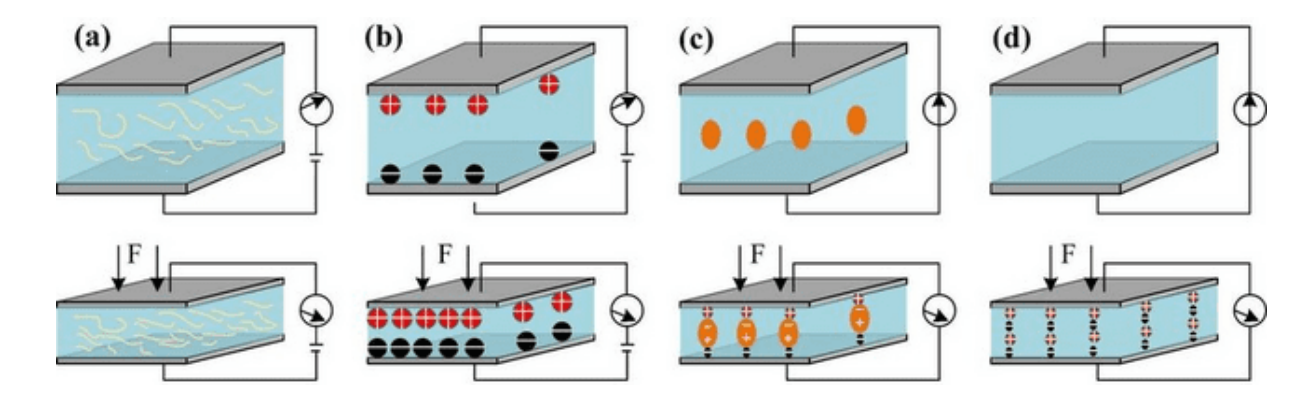


Figure 2-2. A schematic illustration of the mechanism of common flexible sensors. (a) Piezoresistive sensor. (b) Capacitive sensor. (c) Piezoelectric sensor. (d) Piezoelectric sensor.

Piezoresistive sensor changes in response of resistance or current to the external forces. It is usually employing a conductive elastomer embedding between two electrodes[12]. The active material should provide sufficient charge transport paths for electrical current flows. The change of the resistance is based on the contact resistance between the electrode, and conductive elastomer, and the conducting layers resistance variation under pressing. The common development approach is developing composite material containing conductive filler in the elastic matrix. An example is the piezoresistive sensor made up of compositing multiwalled-carbon nanotubes in PDMS to realize elastomer deformation under pressing[13]. Besides compositing elastomer materials, another approach is using conductive material to fabricate porous structure to maximize the deformation under pressing. A sensitive film in porous structure made up of reduced graphene oxide/MXene/ reduced graphene oxide was fabricated with the technique of thermally induced foaming. The introduction of porous structure increases the sensitivity of the sensor to 0.918 kPa⁻¹ in the range of 0-0.9 kPa[14]. Besides material development, it is common to fabricate different structure on the electrode or active material to improve the sensitivity of the sensor. A stretchable resistive pressure sensor wit micro-pyramid PDMS structure was fabricated with the sensitivity of 10.3 kPa⁻¹ under 40% stretching, as depicted in Figure 2-3[15]. This sensor can be used to detect pulse rate. Another

resistive pressure sensor was fabricated with screen-printed interdigital electrode with a carbonized crepe paper showing high sensitivity 2.56-5.67 kPa⁻¹ in the range of 0-2.53 kPa[16]. Resistive sensor takes the advantages of simple preparation, low energy consumption, and excellent sensitivity. However, piezoresistive sensor using conductive material as the core is highly influenced by the temperature, as the electrical charge may vibrate more at high temperature.

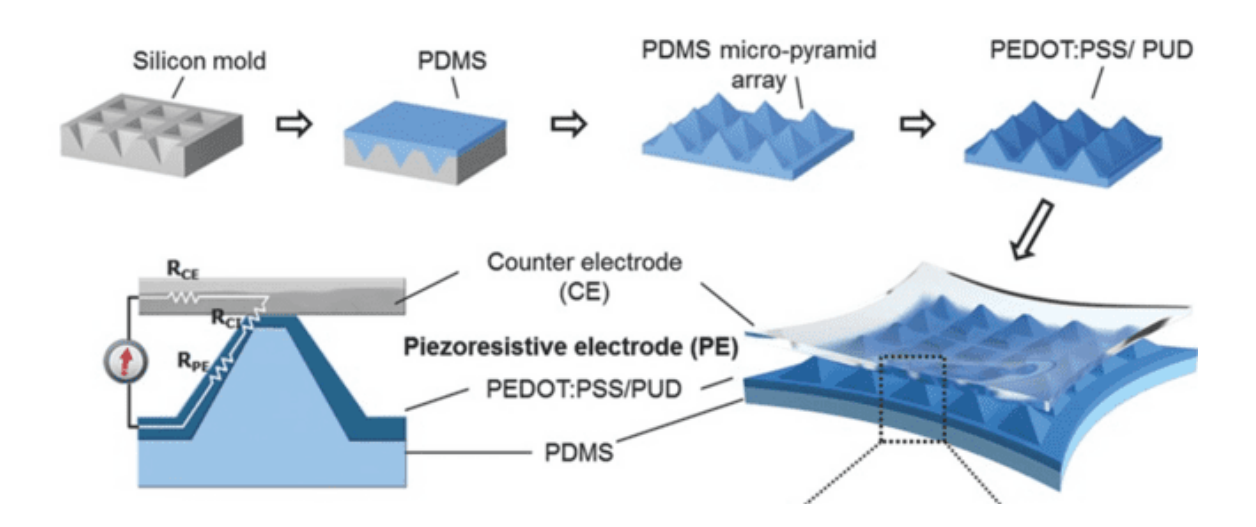


Figure 2-3. A schematic diagram of stretchable resistive pressure sensor with micro-pyramid structure.

Capacitive sensor changes in capacitance in response to the deformation of the dielectric material. It is normally composed of a pair of electrodes with a dielectric layer locating between them[17], [18]. Dielectric material is a poor conductor of electricity, storing electrical charges to generate an electric field for functionality[19]. It is characterized with the term of dielectric constant, and dielectric loss. Dielectric constant is described as the amount of stored charges/electric energy in the field, dielectric loss refers to the dissipation of energy in the form of heat or others[20]. From the mechanism of capacitive sensor, its sensitivity is mainly determined by the changes of thickness, contact area, and dielectric constant under pressing. Based on this, using elastic materials with low modulus as the matrix of dielectric

material is preferred as first approach. The second approach is fabricating microstructure in the dielectric layer to improve the performance of sensor[21]. Fabricating microstructure introduces the air as types of dielectric material to lower the initial dielectric constant, and increases the contact area between electrodes, and dielectric material. An example is one capacitive sensor fabricated with the micropattern from the lotus leave [22]. Its sensitivity is 0.815 kPa⁻¹, and the response time is only 38 ms. A capacitive pressure sensor with porous structure was fabricated via embedding the distilled water droplet into the PDMS to form a controllable porous structure. This sensor sensitivity can be higher to 0.86 kPa⁻¹, and the detection range can be up to 100 kPa[23]. The fabrication process, and the optical image of the porous structure was illustrated in Figure 2-4. Among sensor, capacitive sensor exhibits high pressure sensitivity, and less reactive to temperature drift. However, the introduction of air in the dielectric air brings another challenge to sensor stability. The dielectric constant of air varies with the relative humidity, while the dielectric constant of wet air is higher [24]. Since the sensation of the capacitive sensor is relied on monitoring variation of the electric field under pressing, the sensation is highly influenced by the outside environment, especially the electric field from other devices. Capacitive pressure sensor requires encapsulation to isolate the effects from environment, except the input pressure. A shield soft capacitive sensor was developed with a silver shielding layer, and liquid metal as electrode, which capacitance signal is not influenced by the outside environment to confirm the signal stability[25]. This field about the encapsulation of flexible capacitive sensor still requires further research to realize practical application of the sensors.

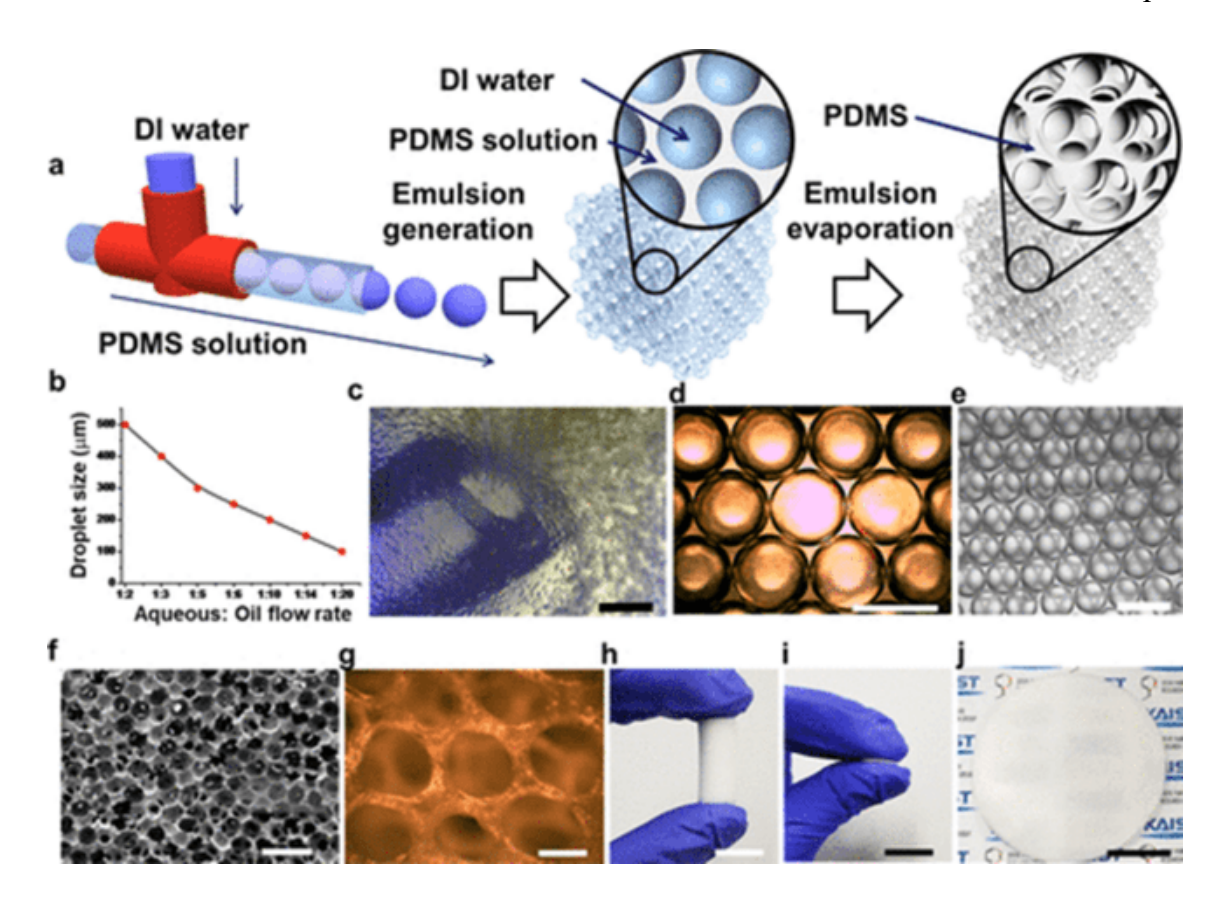


Figure 2-4. Porous capacitive sensor fabrication process. (a) A schematic diagram of the fabrication process. (b-j) Digital image of the porous structure

Piezoelectric sensor is based on piezoelectric effect, in which the input mechanical forces can be converted to electrical energy[26]. In details, the electric dipole moment becomes shorter, and generates corresponding positive, and negative charges on the relative electrode surface[27]. The contrary displacement of cations relative to anions leads to the generation of piezoelectric potential. Finally, the electrons may go through the external circuity to conduct a piezo potential release to reach a new electric balance. Piezoelectric sensor is normally composed of a number of piezoelectric materials with electrodes. Piezoelectric materials can be classified as piezoceramics (like BaTiO₃, ZnO, and ZnO), piezopolymers (like PVDF-TrFE, PAN, and PLLA), and piezocomposites[28]. Piezoceramics exhibits high piezoelectric coefficient, but these materials are stiff, and brittle. Piezopolymers are preferred due to good conformability, and flexibility[29]. One limitation is that the piezoelectric coefficient of

piezoelectric polymer is smaller than that of ceramic types. Many studies tried to develop the piezocomposite with both high piezoelectric coefficient, and good flexibility[30]. An example is the microstructure fiber consisting of polycarbonate core, and cladding. The cladding consists of alternating layers of piezoelectric composites, which introduces BaTiO3, PZT, or CNT into polyvinylidene, and conductive polymer, as shown in **Figure 2-5** [31]. The fiber can be integrated into the woven structure using dobby loom. Similar to the previous sensors, micro-engineering can be used to improve the performance of the sensor. A piezoelectric nanogenerator using ZnO embossed hollow hemispheres thin films as active layer generates 7 mA cm⁻² at normal force of 30 N[32]. One unique advantage of piezoelectric sensor is its multiple application, acting as a sensor or actuator. Piezoelectric sensor does not require power source for sensation, it is suitable for dynamic sensing[33]. It is not applicable to static sensing because the sensor generated output voltage is impulsive. One of the limitations is about the temperature sensitivity, and higher drift in response over time.

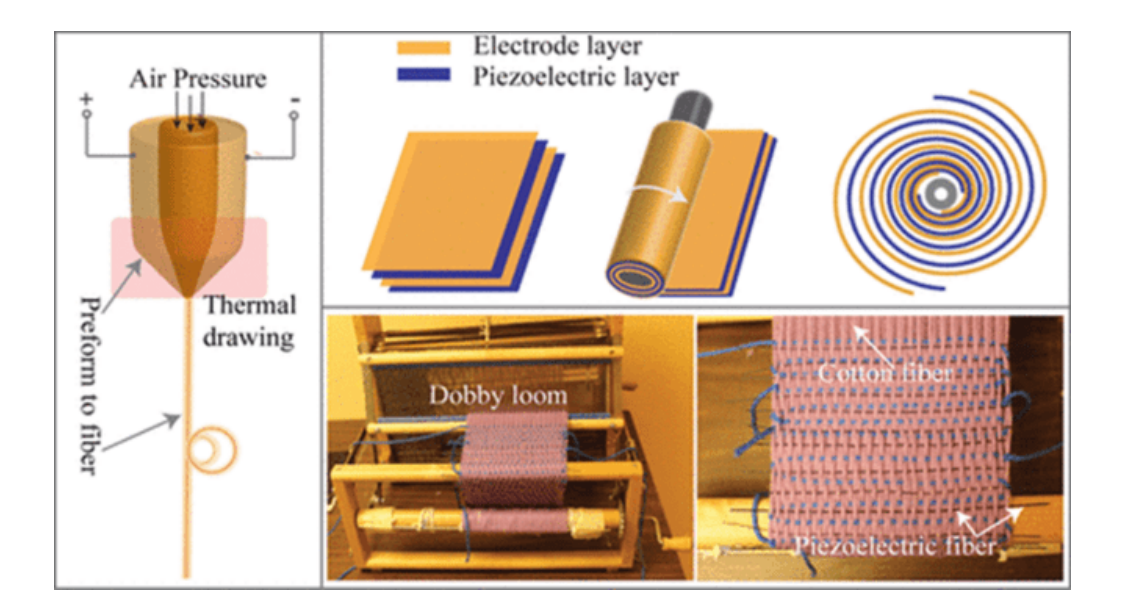


Figure 2-5. Fiber-based piezoelectric nanogenerator.

Triboelectric sensor (TENG) is emerging sensor, which mechanism is relied on the triboelectricity, and electrostatic induction. When two types of materials with different

triboelectric coefficients contact each other, electrostatic charges are generated on the material surface to create an electric potential for charge flow. TENG can be summarized into four types: vertical-contact separation, single electrode mode, lateral sliding mode, and freestanding mode[34], [35]. Vertical contact separation, and single electrode modes are common for pressure sensor design, while the other two are more applicable to rotation or translational motion. A triboelectric pressure sensor, composed of activated carbon/polyurethane as positive triboelectric material, PTFE as negative triboelectric material, and microsphere array electrodes (Single electrode- mode), was fabricated as part of vamp lining to detect the shape, and stress of the foot for the comfort of shoes [36]. The detection range of the shoe can be higher to 7.27 MPa, and the voltage can be reaches to 9.7 V with 10 mm compression. Another textilebased triboelectric nanogenerator arrays was fabricated from one wavy shape PET embedding between two conductive fabrics, as illustrated in Figure 2-6 [37]. This textile array can be used a bedsheet to monitor the sleep behaviour, and sleep quality in real-time. Differ to piezoelectric sensor, triboelectric sensor can be used for both static, and dynamic pressure sensation, depended on the measurement tactics. For static pressure sensation, open circuit voltage with transferred charge density is employed. For dynamic pressure detection, pulse like short circuit currents peaks are employed. One limitation of the triboelectric sensor is easily influenced by the environment, like sweat, and salt.

Besides the above four common types of pressure sensor, there are also some other sensors for pressure sensation. Photoelectric sensor is based on the photoelectric effect, which uses the photoelectric effect to convert mechanical pressure into an electrical signal. When pressure is applied, the photosensitive materials may generate an electrical charge to cause electric field strength variation, influencing the current. An example is flexible difunctional sensor made up of graphene/ZnO nanowire array show 1.7 nA kPa⁻¹ pressure sensitivity[38]. However, this type of sensors can be influenced by the ambient light, leading to reduce

reliability, and stability.

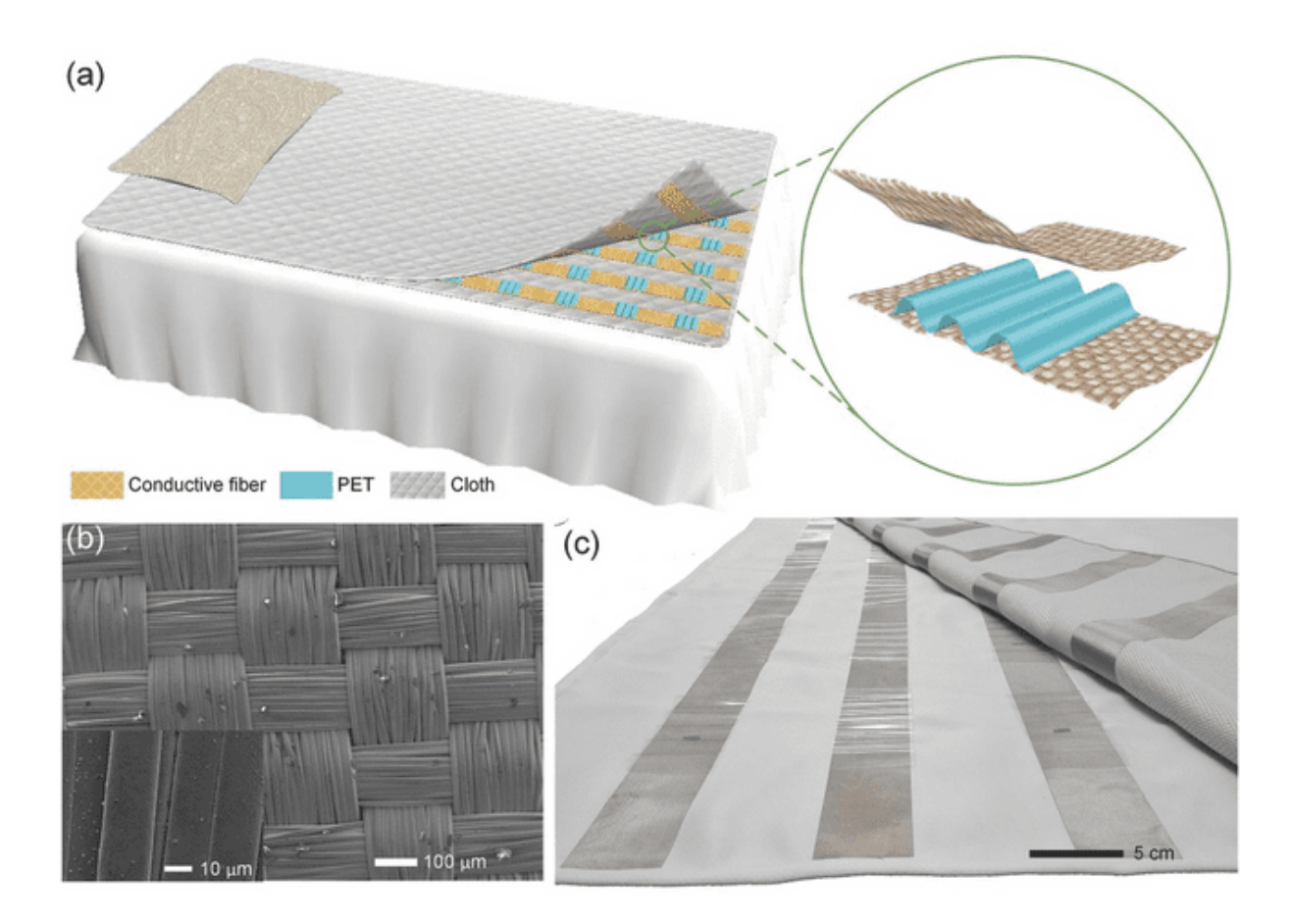


Figure 2-6. Textile-based triboelectric nanogenerator array for sleep monitoring. (a) A schematic diagram of the design of the bedding. (b) Digital image of the TENG. (c) Photo of the TENG.

From above searching, it can find out that the structure, format, and materials of the sensor was improved to realize advanced performance in the aspects of high sensitivity, wide detection range, multimodal sensation. However, there are still many limitations in the practical applications. These limitations, and challenges can be categorized into three aspects, as shown in **Figure 2-7**[39]. The first field is related to the basic metrics, like sensitivity, stability, and linearity, and the second filed is about the mechanical performance, like bending rigidity, elasticity, and fatigue resistance, and final field is the array performance. Above searching elaborates many challenges about the basic metric, and mechanical performance of the sensors,

while there is limited exploration about the array performance.

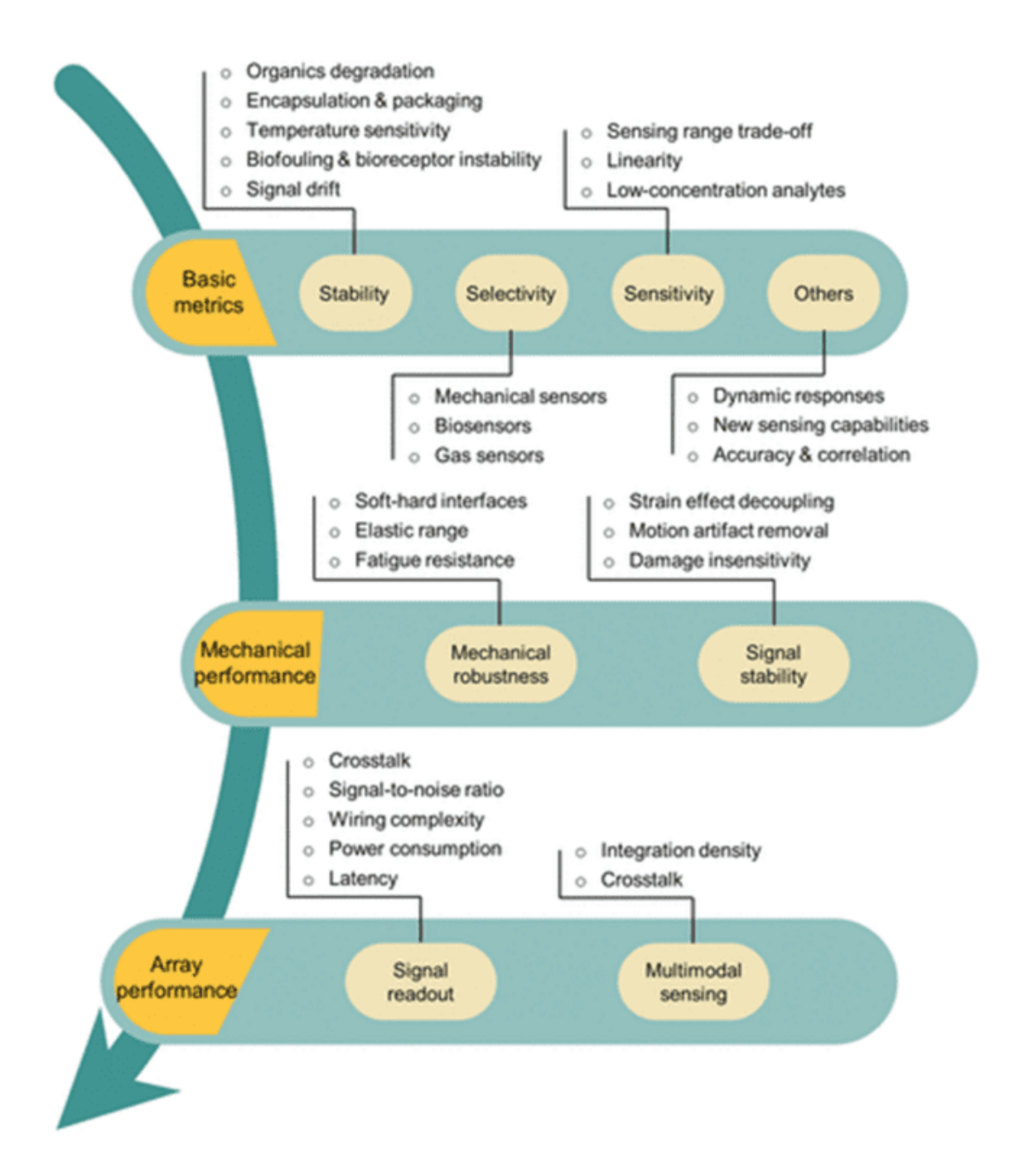


Figure 2-7. Overview of key issues of flexible sensors.

HMI necessitates multiple sensors to assemble together for effective interactions, in which the cross-talk, and the wiring complexity are critical challenges to the wearable applications. Cross-talk describes the interference between multiple sensor operating in close

proximity. Cross-talk between sensors may generate undesired current paths, which limits signal fidelity. This can be tackled by complex readout circuits for scanning, and filtering. However, this solution of using complex readout circuit may introduce another challenge-wiring complexity. Complex wiring between the sensors, and the signal processing modules requires a more reliable connection method, which electrical impedance needs to be small to avoid overheating. In addition, the connection needs to be durable to withstand the corresponding mechanical deformation in the usages without performance deterioration. These may bring higher requirements to the materials, structure, and fabrication process of the connection materials.

The effective integration of flexible input device in wearable applications presents many challenges. In light of these challenges, the development of wearable HMI system requires multidisciplinary approach that encompasses not only electrical engineering but also material science, mechanical engineering, and human factors.

2.2.2. Other flexible input device

In addition to sensor type device, there are also some other types of pressure sensitive device. The most classical type is switching input device, like membrane keyboard, and mouse. The membrane keyboard is normally composed of one PET film with perforations, embedding between two screen-printed silver circuit board. In addition to sensor type device, there are also some other types of pressure input device. The most classical type is switching input device, like membrane keyboard, and mouse. The membrane keyboard is normally composed of one PET film with perforations, embedding between two screen-printed silver circuit board. One important parameter for switch-based input device is actuation force, which can be influenced by the membrane thickness, spacer thickness, spacer aperture diameter, and the base plate

curvature[40]. In addition, temperature, and humidity effect the rate of aging of the screenprinted circuit board[41]. In terms of the material rigidity of the membrane keyboard, the membrane keyboard is not applicable to wearable applications because the printed circuit board can be easily damaged by water, abrasion, and other wears.

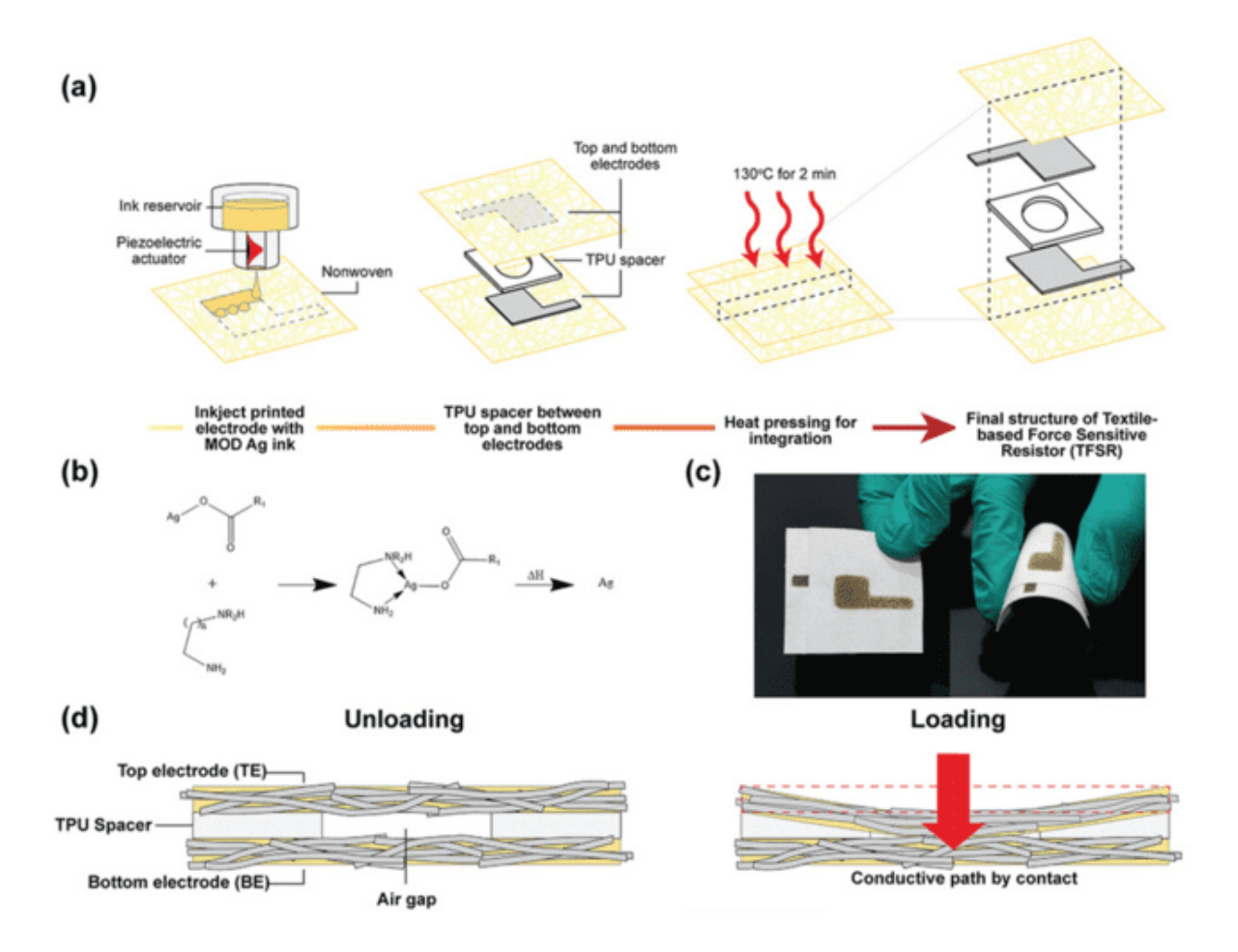


Figure 2-8. A pressure sensitive inkjet-printed resistor. (a) A schematic illustration of the fabrication process of the pressure sensitive resistor. (b) Chemical structure of the ink. (d) Photo of the inkjet-printed resistor. (d) Mechanism of the inkjet-printed resistor

Some studies were conducted to explore the usage of other textile conductive material, and fabrication technique to address the inherent limitation of the membrane keyboard, and develop a switch input device for wearable applications. An example is a pressure switch conductive keyboard made up of conductive yarn, and non-conductive yarn in knitting structure, while its threshold force, and the performance of the keyboard can be influenced by the

stretching[42]. In order to accommodate a wide range of wearable products in wearable applications, researchers explored the structure, and materials to control the switching-based device performance fitting the application requirement, like laundry, pressure threshold, and bending. An inkjet-printed pressure sensitive resistor was developed, in which TPU was used as spacer between two printed circuit, as shown in **Figure 2-8**. The pressure threshold of the resistors can be controlled in the range of 4.9 kPa to 7.1 MPa through adapting the layers of TPU spacers, and different hole diameters[43]. Although this pressure sensitive resistors pressure threshold can be controlled, the controllability is limited, offering only several options for applications. In addition, the long-term reliability of the device remains a challenge.

In summary, we have searched different pressure input device for HMI, and pressure sensation, including mechanism studies, analysis of their limitations, and explorations of the potential solutions. In the following section, our focus shifts to the fabrication techniques of functional materials, and device structure, which is crucial to the development of HMI devices.

2.2.3. Materials, and Fabrication techniques of flexible input devices

There are several methods available for fabricating different types of flexible input devices. Specifically, the fabrication technique can be categorized into two main parts for the elements of the pressure input device: materials fabrication, and structure technique. These two components are essential in the development of flexible input devices, and play a significant role in their overall functionality, and performance.

Materials: For material fabrications, these techniques can be categorized into conductive material or non-conductive elastic composite. For conductive material parts, electrode fabrication can be divided into two ways: One is using conductive material in different textile format, such as conductive yarn or fabric. These electrodes show good

textile properties, like flexibility, air permeability, and comfortability. In details, the conductive textile also can be categorized as intrinsic conductive textile or additive manufactured conductive textile. The intrinsic conductive textile only includes conductive polymer yarn or fiber, like PANI, PPY, and PEDOT:PSS, and carbonized textile, like carbon fiber[44]. Additive manufactured methods involve coating, plating, printing, chemical vapor depositions, and others. The additive manufacturing method needs to consider the material applicability between substrates, and the conductive materials, as well as the chemicals used in the production techniques. For other non-conductive functional materials, like insulation material, dielectric material, and encapsulation material, the fabrication method varies due to its applications. Among them, PDMS are widely used as the matrix for composition due to its flexibility, biocompatibility, and the resistance to moisture, and chemicals. Its shapability also endows its potential for different application. In addition to PDMS, other materials such as styrene-butadiene-styrene (SBS), polyurethane, and nylon are also preferred for their specific properties, and suitability for diverse applications.

Structure: Previous studies explored many techniques to assemble the functional materials together in different format or structure to improve the performance of the devices. These techniques can be summarized into two directions: First, the device fabrication techniques is using traditional textile techniques to fabricate textiles structure, like weaving, knitting, and braiding. The device fabrication can be integrated into the textile production, enhancing large-scale production, and the comfortability of the wearable accessories or products. However, existing textile production may limit the usage of materials, and structural developments, potentially leading to suboptimal device performance. The second direction involve using other industrial techniques to fabricate microstructure for the device, which are then integrated the device or material into the wearable products in later production. For microstructure, material moulding is the most common method. Moulding also can be

categorized based on the controllability of the structure. One approach is using existing mould, from natural (such as leaf or petals) or synthetic products (like sandpaper). Another approach entails fabricating mould, like lithographic techniques or 3D printing. The first method is advantageous in terms of ease of fabrication, and lower cost, but it may exhibit significant quality variation, making its not suitable for large-scale production. The second offer more control on structure design, and quality, typically involve higher costs.

Overall, there are diverse fabrication techniques for different purposes. It is crucial to analyse the requirement/applications of the devices in order to select appropriate materials, and fabrication techniques.

2.2.4. Study of human sensation, and perception system

Human sensation, and perception are two important process for human to interact with the environment for survival, navigation, communication, learning, and others. Sensation is the process by which the sensory organ detecting the external stimuli, and transform to the neurological impulse for processing, while perception refers to the brans' selection, and the interpretation the sensation information[45]. In **Figure 2-9**, human tactile perception can be categorized with four process: 1) sensory neuron to detect the external tactile signal, 2) neurons transmit the electrical signal from sensory neuron, 3) part of the brain for sensory perception, and 4) muscle activation as feedbacks [46]. Human sensation system is an efficient, and complex system capable of detecting different types of external stimuli, with high resolution, and high sensitivity. For perception, our brain contains 10¹¹ neurons, and 10¹⁵ synapses for information processing, but the power consumption is only 20 watts[47]. Its energy consumption is quite smaller than computer. This highlights the advance of the human sensory, and perception system. In the following section, we are going to elaborate the mechanism, and

functionality of the different sensory organs in order to explore the potential for mimicking in technological, and scientific advancements.

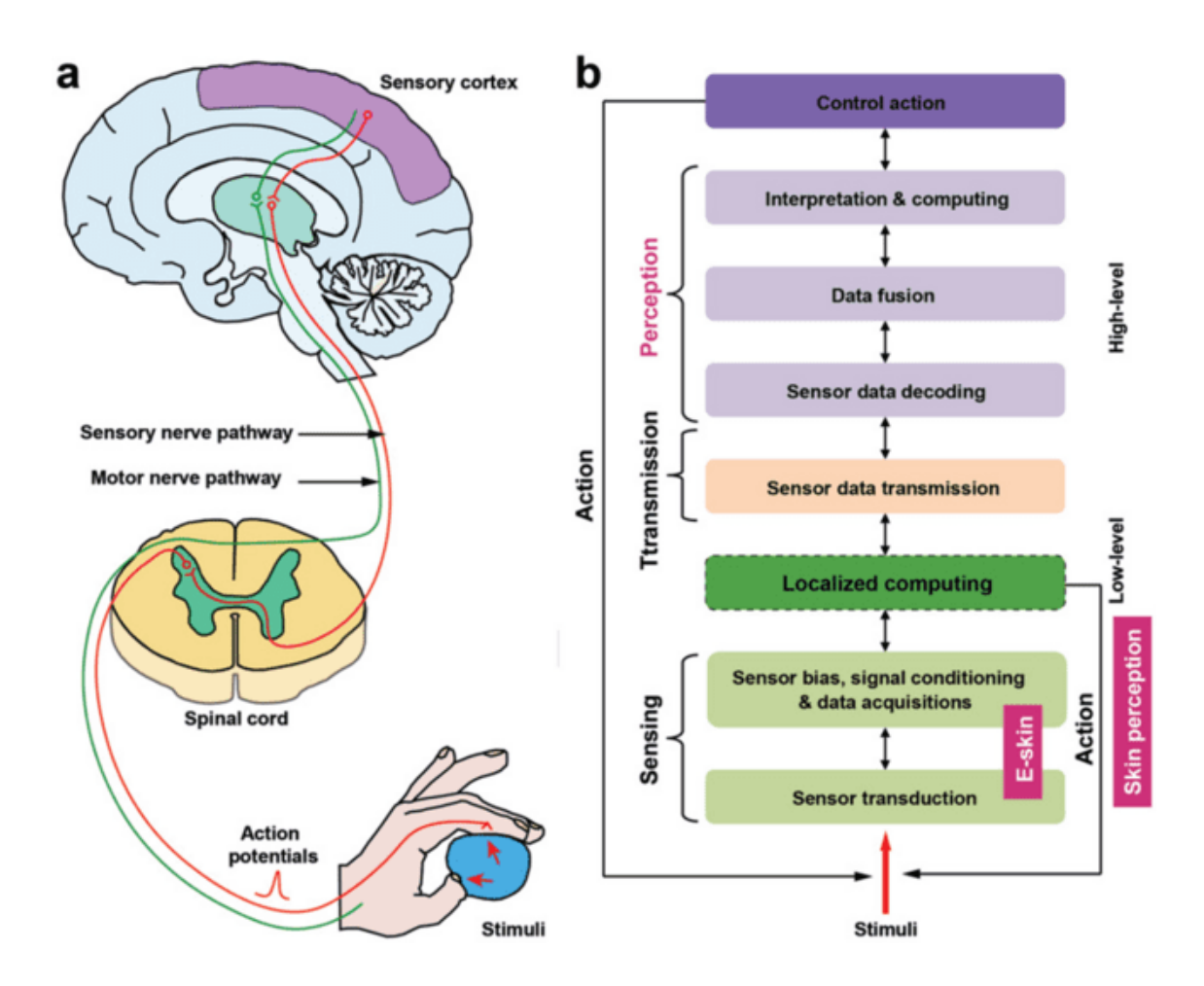


Figure 2-9. Overview of (a) human tactile perception system, and (b) mechanism.

Human skin is the largest are organ of the human body, normally cover around 2m^{2, and} weighs around 4 kg[48]. The human skin is normally covered with different sensory receptors from the epidermis layer to the hypodermis layer to provide precise detection, and protection to human from the environment, as depicted in **Figure 2-10**[49]. The receptors include mechanoreceptors (for pressure/vibration), thermoreceptors (for temperature), nociceptors (for pain/damage), and proprioceptors (for position/movement). In this review, we focus on the mechanoreceptors.

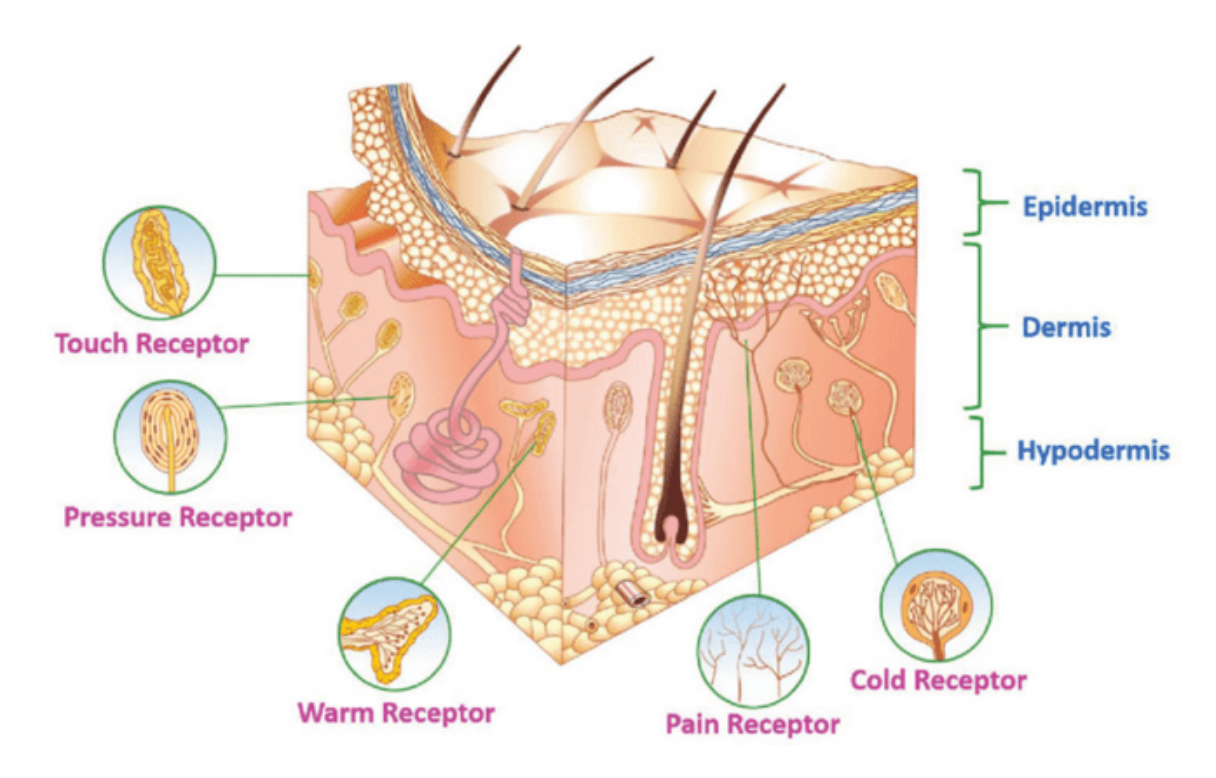


Figure 2-10. A schematic illustration of skin anatomy with cutaneous sensory receptors

Human skin contains over 45 thousand mechanoreceptors, comprising Meissners' Corpuscles, Merkel Disks, Ruffini Organs, and Pacinian Corpuscles, free nerve ending, and others[50]. The functionality of mechanoreceptor relied on mechanotransduction, which refers to the conversion of mechanical stimulus to a biological response. Cutaneous mechanoreceptors localize in different layers of the skin with varying ranges of mechanical stimuli detection[51]. Meissner's corpuscles are encapsulated neuron between the dermal papillae under the epidermis of the glabrous skin; Pacinian corpuscles are located in the subcutaneous tissue; Merkel's disk is aligned within the papillae that lie under the dermal ridges; and Ruffini's corpuscle are located deep in the skin, ligaments, and tendons.

These mechanoreceptors contribute to complex tactile information transferred to the brain. The mechanoreceptors range sensing divides into two groups: low-threshold mechanoreceptors (LTMRs), and high-threshold mechanoreceptors (HTMRs). LTMRs react to light, benign pressure (0.5- 2 mN) [52], [53], [54], while HTMRs react to stronger, harmful,

mechanical pressure. LTMR can be categorized into four types, as type I, and type II of slowly adapting receptors (SAI, and SAII), and type I, and type II of rapidly adapting receptors (RA, and RAII)[55]. SAI, and SAII are difference in the regularity of their static-phase firing rates, in which SAII exhibits a higher degree of regularity. The differentiation between RAI, and RAII is the size of receptive field, and their frequency vibrations, with RAI frequency response is 1-10 Hz, while RAII is 80-300 Hz. For example, Meissner's corpuscles elicit the sensation of light touch or flutter (10-60 Hz), while Pacinian corpuscles are sensitive to acceleration, and vibration of 70-1000 Hz[56]. The subtypes of cutaneous mechanoreceptors details were listed up in Figure 2-11. From current studies about the mechanoreceptors, it can find out that the different types of mechanoreceptors characterizing with different rate of adaptation to stimuli, the location within the skin, the mean receptive areas, the spatial resolution, the response frequency rate, and others. These help to the achievement of different tactile perception properties or purpose. It is important to note that no any single mechanoreceptor is capable of encompassing the entire spectrum of human tactile perception.

Physiological subtype	Associated fiber (conduction velocity ¹)	Skin type	End organ/ending type	Location	Optimal Stimulus ⁴	Response properties
SAI-LTMR	Aβ (16-96m/s)	Glabrous Hairy	Merkel cell Merkel cell (touch dome)	Basal Layer of epidermis Around Guard hair follicles	Indentation	
SAII-LTMR	Aβ (20-100m/s)	Glabrous	Ruffini ² unclear	Dermis ³ unclear	Stretch	/
RAI-LTMR	Aβ (26-91m/s)	Glabrous Hairy	Meissner corpuscle Longitudinal lanceolate ending	Dermal papillae Guard/Awl-Auchene hair follicles	Skin movement Hair follicle deflection	*
RAII-LTMR	Aβ (30-90m/s)	Glabrous	Pacinian corpuscle	Deep dermis	Vibration	#
Aδ-LTMR	Αδ (5-30m/s)	Hairy	Longitudinal lanceolate ending	Awl-Auchene/ Zigzag hair follicles	Hair follicle deflection	
C-LTMR	C (0.2-2m/s)	Hairy	Longitudinal lanceolate ending	Awl-Auchene/ Zigzag hair follicles	Hair follicle deflection	
HTMR	Αβ/Αδ/C (0.5-100m/s)	Glabrous Hairy	Free nerve ending	Epidermis/Dermis	Noxious mechanical	

Figure 2-11. Subtypes mechanoreceptors properties, and function.

Besides mechanoreceptors, nerves or neuron connecting to the mechanoreceptors play a critical role in human tactile perception. The nerves types can be classified as A-beta-, A- delta- or C-fibers based on their action potential conduction velocities. The neuron connecting to the receptor is termed as primary sensory neuron. It is responsible to build up the connection between the skin, and the central nervous system through axon. Differ to normal neuron, it is lack of dendrites, and synaptic contacts, containing axon terminals, and receptor terminals. The cell bodies of sensory neuron are located within dorsal root ganglia (DRG), and cranial sensory ganglia[57]. DRG neuron axonal branch extend to the peripherical, and another branch extend to the spinal cords, and form synapses to the second-order neurons in the grey matter of spinal cord. There are two different types of synapses - chemical synapse, and electrical synapse. The chemical synapse is a small extracellular space that is about 20-30 nm across, while electrical synapse gap is narrower (2-4 nm)[58]. The surface of the axon terminal where is contact the neuron is presynaptic membrane, the specialized surface of the neuron that receive the terminal is postsynaptic membrane. When a stimulus forms the environment is applied to human skin, the receptor may generate a potential, which magnitude is proportional to the intensity of the applied stimulus[59]. If the receptor potential is over certain threshold, an action potential developed in the axon of the sensory neuron, and transduces from the receptor terminal to the axonal terminal [60]. The membrane potential at the axon terminal needs to be balanced. The arrival of an action potential may disturb the balance of the membrane potential, leading to the opening of calcium channels as a local depolarizing response of the axon membrane. The influx of calcium ions may result in the movement of vesicles containing neurotransmitters towards the presynaptic membrane. When vesicles arrived the neuronal membrane, the neurotransmitter will be released to the synaptic space[61]. The protein receptors in the postsynaptic membrane will then be activated or inhabited depend on the functionality of the neurotransmitter.

2.2.5. Wearable applications of flexible input devices

The human body senses external pressure, and respond to pressure is fundamental to

our interaction with the environment. The flexible pressure-based input device allows the HMI to be more convenience, efficient, and with good user experience. In addition, Pressure generated by human body are important parameter for the people's health condition. The flexible input device can be attached to human body to capture different physiological signal in real time for early detection, and diagnosis. In the following section, we are going to discuss several usages of pressure sensations in health monitoring.

Diabetic foot plantar pressure measurement: Diabetic foot ulcer affects more than 18.6 million in the world [62]. Diabetic foot ulcers develop as a result of diabetic sensory, motor, and autonomic neuropathy[63]. The initiation of the diabetic foot ulcer is the formation of superficial callus due to the lack of abnormal pressure sensation on the foot. The inflammation, and/or minor trauma from impact may result in haemorrhage beneath the callus. After the removal of the callus, the ulcer may extend through the epidermis, and dermis layer into the subcutaneous layer [64]. The potential risk for diabetic foot ulcer includes tight shoes, foot deformities, decreased sweating, drying skin, decreased lower extremity perfusion, and others. The clinic suggests that people at risk of diabetic foot ulcer should receive education about the proper foot care, and appropriate footwear[65]. For the diabetic foot patients, their footwear needs to be custom-made, which requires appropriate foot shape, and extra-depth shoe for pressure relieve [66]. Considering the semi-quantitative test of sensory loss, a monofilament with a given force was applied to human skin to evaluate the sensation loss. The plantar threshold for diminished protective sensation is around 244 kPa[67]. To develop appropriate footwear, and monitoring the plantar pressure in daily life, previous studies mainly focus on the development of smart insole with sensor to monitoring the planar pressure, as demonstrated in Figure 2-12[68], [69]. However, these insoles cannot comprehensive monitoring the pressure for diabetic ulcer because the regions where the most ulcer occurrence is the hallux[70], in which the side pressure from the sock, and footwear cannot be measured[71].



Figure 2-12. Designed insole system for diabetic foot.

Parkinson patient fall detection: Gait analysis, as with blood pressure, and body temperature, can reflect the health status, and pathological features of the human body from different angles[72]. Gait analysis can be applied in sport training, patient healing, medical knee osteoarthritis identification, Parkinson patient monitoring, and others[73]. Parkinson disease is a group of neurological disorders characterized with movement problems or other neurodegenerative disease, such as rigidity, slowness, tremor, and progressive supranuclear palsy[74]. One significant risk for individuals with Parkinson's disease is the occurrence of falls. Thirty-eight percent of parkinsonian patients fell, and 13% fell more than once a week[75]. The patient falls is associated with freezing of gaits (FoG). FoG is a short-lasting episodic inability to generate effective stepping in the absence of any known cause other than parkinsonism or high-level gait disorders. It is most commonly experienced during turning, and step initiation, and also when the patient is faced with spatial constraints, stress, and distraction[76]. Previous researches focus on monitoring different symptoms to identify, and monitor Parkinson diseases, like FoG, tremor, rigidity, depression, and others. An intelligent wearable system was developed to detect FoG, and provide timely cue to enhance patients' mobility[77]. The pressure sensation threshold is determined by the weight of users, and the foot size. For FoG, and gait disturbance monitoring, it is common to use inertial sensors

attaching to the limb, ankles, necklace to calculate the angle, velocity, orientation, gravitational force of the users[78]. These systems are very complicated, and may be more suitable for the usage in Lab or clinics.

Skin pressure measurement: In addition to the pressure generated from the human body, our skin also detects the pressure from the environment. Pressure is also an important parameter for comfort, and the monitoring of treatment efficiency. For example, in the case of varicose veins, it is common to wear compression stocking or compression bandage as a general treatment to help the reflow of blood, and lymph from the limbs[79], [80]. For level 2 compression stockings, the pressure of the stocks needs to maintain in the range of 23 mmHg to 32 mmHg to optimize the treatment effect. Besides compression stocking, it is common to apply pressure through massage to help the recovery, and well-being of the massage, in which the pressure needs to be controlled well to avoid damage, like bone fracture or tissue damage. The pressure interface between human skin, and garment/wearable device is critical to the comfort. The pressure threshold that causes discomfort is 5.88-9.8 kPa[81]. It is essential to monitor the interface pressure between human skin, and the garments/wearable accessories to select appropriate materials for functionality, and comfort.

In the preceding section, we conducted a comprehensive review of flexible Human-Machine Interface (HMI), encompassing the advancement of flexible input devices, associated fabrication techniques, human skin tactile perception mechanisms, and their relevance to wearable applications.

2.3. Introduction of radiation dermatitis

Cancer is a leading cause of death worldwide, accounting for nearly 10 million deaths in 2020[82]. The treatment for cancer usually includes surgery, radiotherapy, and/or systemic

therapy (chemotherapy, hormonal treatments, targeted biological therapies). Among treatments, radiation therapy is a common, and effective way of using high dose of radiation to kill, and shrink tumours. There is ample evidence that roughly half of all patients diagnosed with cancer require at least one course of radiotherapy during their disease history. Despite its efficiency, radiation therapy is normally associated with a spectrum of serious side effect, like fatigue, loss of appetite, and radiation dermatitis. Radiation dermatitis, in particular, presents a significant clinical challenge. Radioactive dermatitis can be classified as acute or chronic, depending on the onset time, from several weeks to years. Acute radiodermatitis occurs within hours to weeks after starting radiotherapy, with an incidence of 98% in breast cancer patients[83]. In addition, about 80-90% patients with head, and neck cancer undergoing radiotherapy develop radiation dermatitis[84], whereas severe skin reactions occurs in approximately 25% of these patients[85]. Radioactive dermatitis is mainly caused by skin exposure to high energy radiation (usually dose level over 20-40 Gy), resulting in skin mucosal inflammatory damage[86]. The pattern of clinical manifestation is related to the radiation dose. At 6-20 Gy, faint or definite erythema, epilation, and hyperpigmentation occurs 1-3 weeks later. At doses over 20 Gy, there is a high possibility of dry or moist desquamation, and ulceration.

2.3.1. Pathology of radiation dermatitis

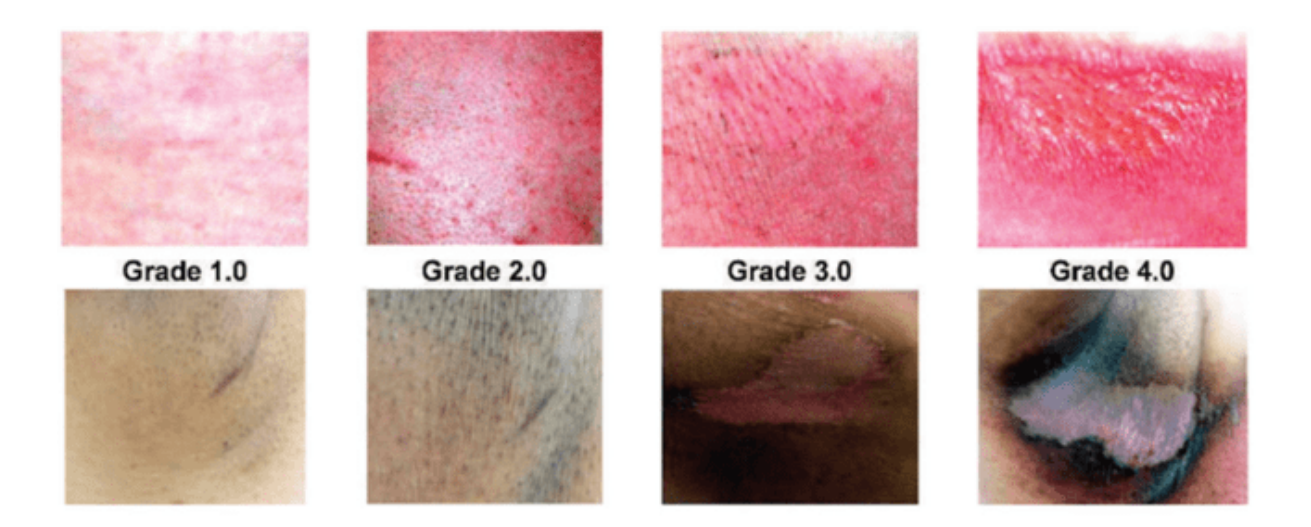


Figure 2-13. Image about grades of radioactive dermatitis in hair, and dark pigment skin

The pathology of the radioactive dermatitis is initiated by DNA damage caused by

radiation, and/or the secondary effect of radiation, which leads to the additional generation of ROS. These may cause damage on the basal cells of the epidermis, and the vascular endothelium. Radioactive dermatitis can be classified into four grades. Grade 1: presence of faint erythema/epilation/dry desquamation/decrease sweating; Grade 2: Presence of bright erythema/patchy moist desquamation/moderate edema; Grade 3: presence of confluent, moist desquamation at areas other than skin folds/presence of pitting edema; Grade 4: Presence of ulcer, necrosis or haemorrhage. In the aspect of the pathogenesis, the grade of the radioactive dermatitis depends on the survival of the actively proliferating basal cells in the epidermis.

Figure 2-13 illustrates different grades of radioactive dermatitis in hair, and dark pigment skin[87]. The skin may firstly develop an erythematous skin reaction by an increased vascular permeability, and vasodilation, followed by an inflammatory response. The inflammation may induce second erythematous reaction. Inflammation may stimulate the resident, and circulating immune cells. The irradiated skin cell may produce a wide range of cytokines, and chemokines[88]. These substances may upregulate the adhesion molecules of the affected skin

cells, which can facilitate the migration of circulatory immune cells to the irradiated skin. At the later stage, the skin then increases the rate of mitosis in the basal epidermal cell layer. If the turnover of news cells is faster than the shedding of old cells, it may form a thicken, dry, scaly skin. Most desquamation arises if all the stem cells in the basal layer are destroyed. If the turnover of new cell is lower than the shedding of old cells, it may cause a broken epidermis, skin blisters filled serous exudate, and substantial pain. For chronic radioactive dermatitis, inflammation cytokines may be generated to produce inflammation to cause tissue fibrosis[89]. Otherwise, the extended inflammation may induce skin atrophy, and necrosis via the accumulation, and activation of leucocytes at the irradiated area.

In summary, radioactive dermatitis manifests as erythema, epithelial shedding, skin ulcers, and pain. Sever causes may cause local or systemic infection. However, there is no standard or validated consensus approach to prevent, and treat radioactive dermatitis[90]. The common approach is using hydrogel membranes to enhance re-epithelialization, and accumulation of cytokine, and growth factor or applying moist exposed burn ointment to facilitate the expansion of partial blood vessels, and speed tissue metabolism, and repair of blood vessel endothelium[91], [92].

2.3.2. Radiation dermatitis in breast cancer patients

Among cancers, breast cancer is the leading cause of cancer death in women worldwide, accounting for 11.7% of all cases, and 6.9% of deaths[93]. Treatment for breast cancer is multimodal, and about 50% of patients will undergo radiotherapy at some stage of treatment planning[94]. For breast cancer patient, patients undergoing radiation treatment to the intact breast or chest wall with or without regional lymph nodes typically receive 4-6 weeks for treatment[95].

The incidence, and severity of radiation dermatitis in breast cancer patients are notably significant, attributable in part to the unique anatomical characteristics of the breast. Firstly, the radiation treatment dose rate for cancer patient is more uneven because of the shape, and contour of the breast, as well as radiation treatment set-up. The uneven distribution of the radiation dose increases the risk of skin toxicity. In addition, the size, and shape of the breast size may be influenced by the respiration, and body movement[96]. Since the radiation therapy last for months to years, this may cause inconsistency to the radiation treatment of the breasts throughout periods. This may exacerbate the unevenness of dose delivery. There is an evidence that the dose inhomogeneity of radiation treatment is greater than over 10%. Based on this, over 95% of breast cancer patients treated with radiotherapy exhibit different degrees of radioactive dermatitis[97]. The prevalence, and severity of radiation-induced dermatitis presents considerable challenges to breast cancer patients both psychologically, and physiologically, and even to the medical system

The severity variation of radiation dermatitis among breast cancer is large. The risk factor for the skin acute toxicity from radiation includes breast size, and body mass index[98]. Larger breast size was identified as a risk factor for acute toxicity. The main reason for this phenomenon is multifaceted. Larger breast size may increase the skin-to-skin contact. The increase contact may cause higher level of moisture, and friction, which are conducive to the development of dermatitis. Moreover, larger breast may cause higher difficulty in precisely targeting the cancer cells or tumour in the radiation, resulting in inhomogeneous dose rate. For patients with high BMI, the distribution of adipose tissue may change the contour, and density of the breast, causing more inhomogeneous dose distribution in the radiation. Therefore, the large variation in severity brings more challenge in the radiation dermatitis management, and treatment.

The treatment, and management of radiation dermatitis face many challenges due to the characteristic of breast. First, the skin over the breast is very sensitive. The higher sensitivity of the breast skin may result in greater propensity for skin reaction. This settle higher requirement in the treatment, and management. Second, the treatment area for breast cancer is not limited to the breast, also involve armpit. The larger area, and complexity of the human contour limit the applicability of the treatment methods, like the hydrogel dressing applications. Moreover, the under-breast area is particularly prone to sweating, and moisture. This may cause bacterial infection as second inflammation, and severely cause ulcer.

In summary, it is difficult, and challenge to manage, and treat radiation dermatitis among breast cancer patients. It is demand to explore effective treatment for radiation dermatitis, and the device or materials for the treatment need customize design fitting to the breast shape, and contour.

2.4. Introduction of Photobiomodulation

Photobiomodulation, also known as low-level light therapy, utilize non-ionizing light in the spectrum width of 600 nm- 1000 nm to the affected area to stimulate cellular function, and promote tissue repair, and promotion. It is an historical treatment for different disease, like reduce inflammation, oral mucositis, and pain management. Unlike other phototreatment, photobiomodulation do not generate any heat to the tissue. Hence, photobiomodulation has emerged as potential supportive care system due to its non-invasiveness, safe, and convenience. In this section, we are going to explore the mechanism of photobiomodulation, light source of photobiomodulation, photobiomodulation parameter, and current flexible photobiomodulation device.

2.4.1. Mechanism of the photobiomodulation

Many studies investigated the mechanism of the photobiomodulation, there are still many unknown aspects of its mechanism, particularly in relation to its cellular effects, and consequences. Furthermore, the correlation between specific diseases, and the impact of cellular effects from photobiomodulation also requires further study. Current research proved that the treatment effect of photobiomodulation is associated with the cyctochrome c oxidase (Cox) of the mitochondria. The absorption spectrum of the cellular proliferation is similar to the absorption spectrum of Cox[99]. Margaret (2005) conducted a biological experiment that the photobiomodulation effect may attenuate due to the presence of the inhibitor of Coxpotassium cyanide[100]. These proved that Cox is the photoreceptor of the photobiomodulation. Cox is the terminal enzyme of the respiration chains of the mitochondria. It catalyses electron transfer form Cox to molecule oxygen, reduce the latter to water as product. The election transfer is coupled to proton translocation across the membrane, resulting in a proton, and charge gradient. This can be employed to drive the protons back through the membrane to synthesise adenosine triphosphate (ATP) by the FOF1-ATPase. ATP is the mediate energy source for numerous process, including ion transport, muscle contraction, nerve impulse propagation, substrate phosphorylation, and chemical synthesis [101]. In addition, the increase of membrane potential may increase the generation of reactive oxygen species (ROS). Figure 2-14 briefly describes the photobiomodulation mechanism. ROS can be either beneficial or harmful due to its conditions[102]. ROS at normal level can mediate cellular responses, such as growth, and immunity. Excess ROS may lead to lipid peroxidation, DNA damage, and even induce cell death. Current mechanism studies only proved that the photobiomodulation mechanism is based on the absorption from Cox, while the interrelationship between the product (ATP, and ROS) as a consequence of the Cox absorption, and the treatment effect remains unknown.

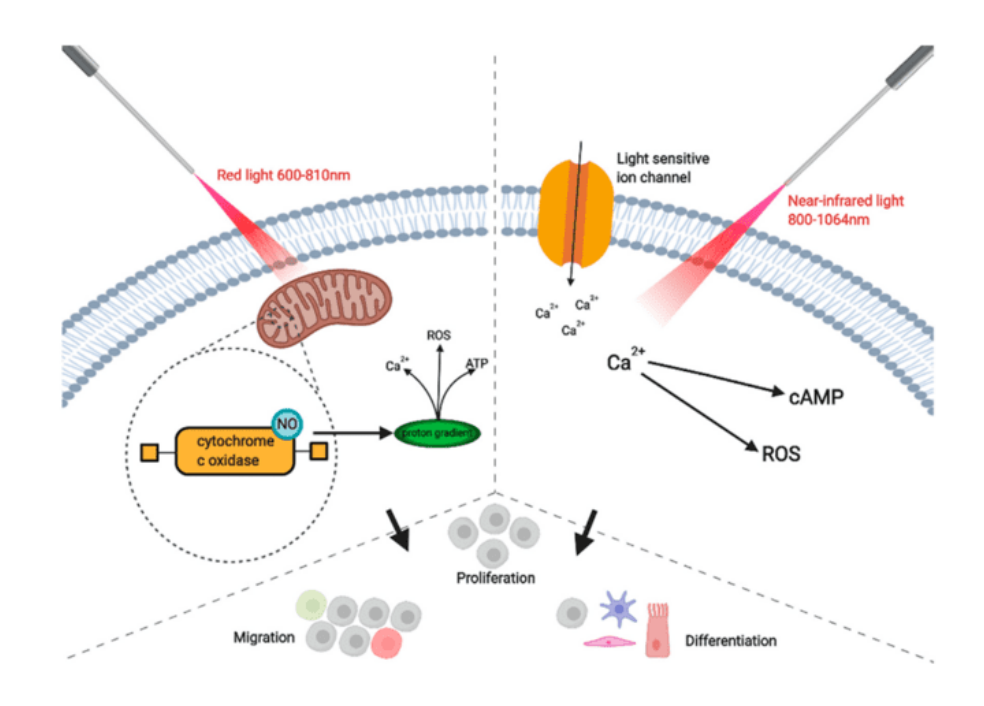


Figure 2-14. A schematic illustration of the mechanism of photobiomodulation

In addition to Cox, other photoreceptors, such as opsins, cryptochromes, and water molecules are also assumed to be the causes of the treatment effect of photobiomodulation. After treatment, opsin can be activated to facilitate the opening of the light-gated ion channels, and results in non-selective permeabilization to calcium, sodium, and magnesium. Cryptochromes, which are biological chromophores, can absorb green or yellow light, and play a crucial role in the regulation of the circadian clock[103]. Beyond the Cox absorption spectrum (>1000 nm), it is hypothesized that water molecules vibration may be increase to perturb the tertiary protein structure, results in the opening of the ion channels to module the intracellular calcium levels. However, the interrelationship between the photobiomodulation effects, and these photoreceptors still requires more evidence, and studies to explore their role in the anti-inflammation, wound healing, and tissue regeneration.

Considering the mechanism of the photobiomodulation, the selection of photobiomodulation parameter need to consider the content of the mitochondria of the treatment area, and the depth of the light penetration for treatment efficiency. In addition, the

number of mitochondria in cells varies widely, and it is strongly correlated with the metabolic requirement of the cell. This condition also determines the photobiomodulation treatment efficiency. These factors contribute to the complexity of achieving optimal photobiomodulation efficiency.

2.4.2. Photobiomodulation light source

Light is the core of the photobiomodulation. There are different light sources for photobiomodulation. Conventional light source for photobiomodulation is laser diode. Laser is light source utilize the physical phenomenon of stimulated emission to create a monochromatic, and coherent beam of light of low divergence [104]. LEDs are another common light source in recent years because it is cost-effective. It was based on the electroluminescence of semiconductors, like InGaN, and AlInGaP[105]. One significance difference to laser is LED bandwidth is wider. One serious problem of LED is the energy efficiency, in which only 20-30% electrical energy will be converted to light energy, while the other will be converted to heat energy. Based on this, if the LED array is in contact with human skin, the power of the LED needs to be controlled to avoid the heating problem. The main difference between the light of the laser diode, and the light of an LED is the coherence. Laser light is coherent, while LED light is non-coherent. However, many researches proved that coherence of light do not influence the photobiomodulation effects with the same parameters [106]. In recent years, there is a rising trend of using µLEDs, and organic light emitting diode(OLED) as light source for photobiomodulation techniques, while most are limited in small scale or lab due to the cost, and production complexity. The selection of light source technique is mainly depending on the production parameter, and device properties, like energy efficiency, flexibility, and scale of device, instead of the optical parameters from different techniques

2.4.3. Parameters of photobiomodulation

To study the effectiveness of the photobiomodulation, there are many factors influencing the effectiveness of the photobiomodulation, including wavelength, dose rate, treatment time, device configuration, and others. In the following section, we are going to elaborate the interrelationship between these factors, and the treatment efficiency.

2.4.3.1. Wavelength

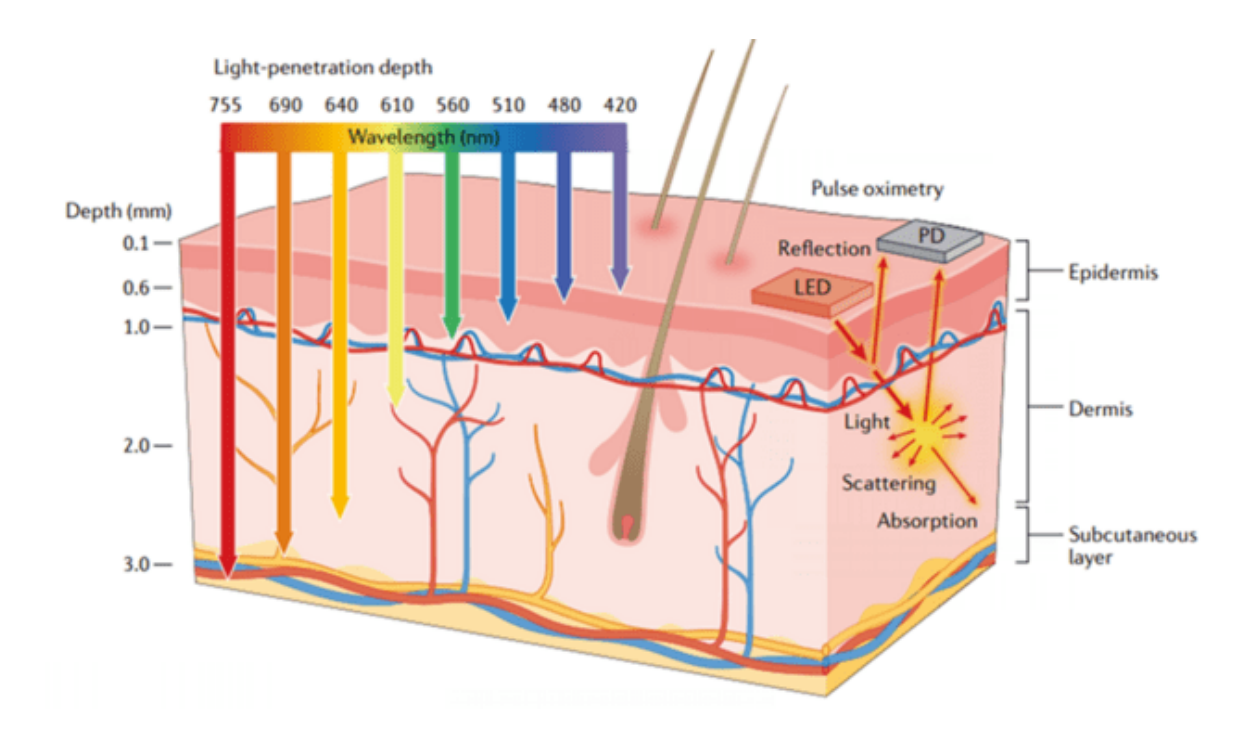


Figure 2-15. A schematic illustration of light penetration depth of skin with different wavelength.

Wavelength is an important indicator to the efficiency of the photobiomodulation. It influences the light penetration depth of the skin, and the biological interaction of human body. Firstly, the penetration depth increases with the number of wavelengths[107]. As shown in **Figure 2-15**, blue light with the wavelength of 480 nm only can penetrate to the epidermis layer, while red light with 750 nm wavelength can penetrate to the subcutaneous layer. Red

wavelength penetrates 0.5 to 1 mm, and near-infrared energy penetrates 2 mm before losing 37% of the intensity. Considering to the penetration depth, the selection of the light source needs to consider the lesions position. For example, child with neonatal jaundice treated with blue light with the range of 430 to 490 nm, which can penetrate to 0.07, and 1 mm[108]. The average thickness of epidermis is 0.1 mm[109]. Blue light can penetrate to the epidermis, and dermis layer containing haemoglobin as the source of bilirubin.

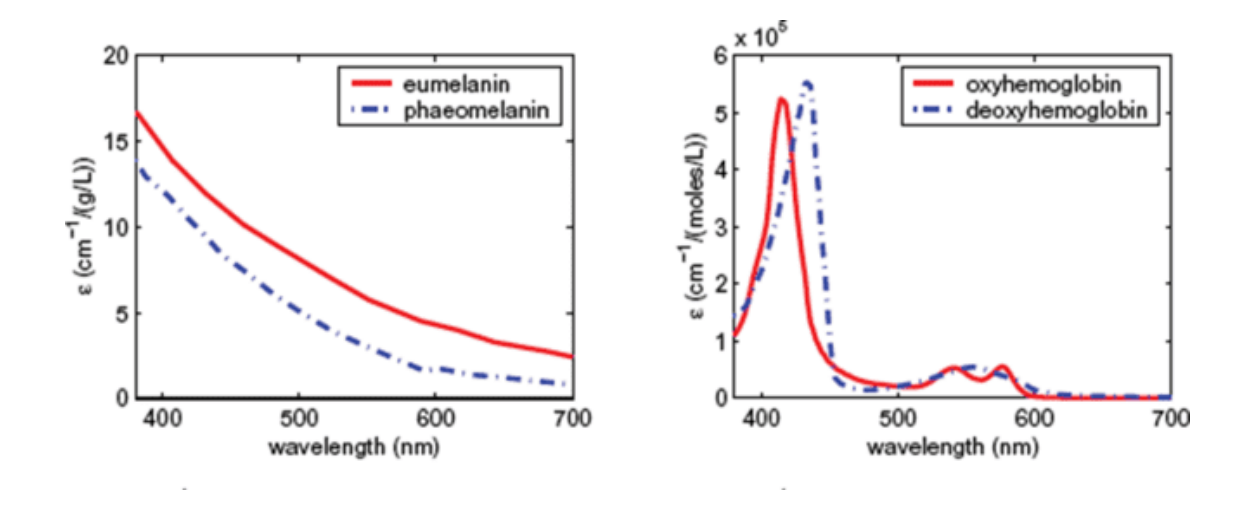


Figure 2-16. Absorption spectrum of different melanin, and haemoglobin

Secondly, the interaction between light, and the human tissue varies with the human body composition, and molecules. The interaction between light, and human skin can be summarized into two ways – absorption, and scattering. In details, approximately 5-7% of the incident light are reflected back to the environment, and the remaining light refracted into the skin. Human skin scattering includes surface, and subsurface scattering[110]. Surface scattering is influenced by the presence of folds in the stratum corneum, while subsurface scattering includes Mie, and Rayleigh scattering[111]. Mie scattering is related to the alignment of fibres, like collagen fibres. Rayleigh scattering is related to the smaller scale fibrils, and other micro-structures. Absorption indicates a reduction in light energy. The absorption of light in skin can be influenced by haemoglobin, and melanin, meaning that part of light will be

absorbed by these substances instead of by mitochondria[112]. Melanin includes red/yellow phaeomelanin or a brown/back eumelanin, which absorption spectrum is different, as depicted in **Figure 2-16**. In addition, the volume fraction of the epidermis occupied by melanosomes varies from 1.3% to 43% among people. Blood contain haemoglobin in the tissue also absorb part of light. In details, the oxygenated, and deoxygenated haemoglobin absorption spectrum varies, as shown **in Figure 2-16**[113].

Due to above research about the interaction between the human body, and light, the selection of the light wavelength needs to be carefully considered to treat different disease. Additionally, the understanding of the pathology of the radioactive dermatitis, and the mechanism of the photobiomodulation is limited. There is no consensus regarding specific substance that initiate the symptoms. It is challenged to identify to the penetration requirement of light to skin, so the selection of light wavelength is primarily based on clinical studies. In this section, we briefly summarize several light wavelengths for different disease.

UV light: UV light is composed of three types- UVA, UVB, and PUVA. UVB radiation have wavelength in the range of 290-320 nm, which is most popular used UV light for therapy. It is commonly used to treat psoriasis, parapsoriasis, and other skin disease[114]. The clinical effect of UVB is relied on the cell proliferation, and immune system[115]. However, there is a high risk of side effects by UV phototherapy because of its penetration, and energy level. The side effect includes sunburn, and higher risk of skin cancer[116]. However, using UV light in treatment belongs to phototherapy instead of photobiomodulation because the light power, and energy is high.

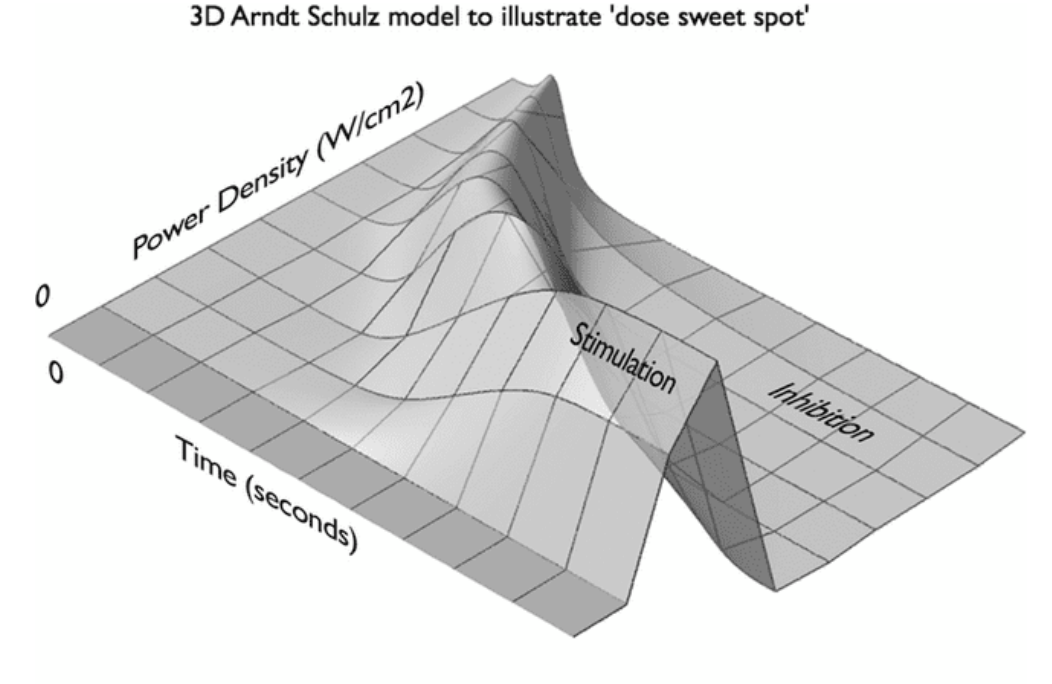
Blue light: The spectrum of blue light is in the range of 420 to 490 nm, while its peak wavelength is located between the range of 440 to 460 nm[117]. It is common to treat neonatal

jaundice, caused by the presence of bilirubin in skin. On the other hand, blue light also can be used to reduce inflammation in superficial tissue, promoting wound healing, and limit bacterial grown. However, blue light may side effect to human health[118]. A study showed that blue light decreased the transcription of the PER1 gene in keratinocytes, and results in the interfere of skin cells' nightly rhythm[119]. Based on this, the blue light photobiomodulation requires monitoring, and careful consideration.

Green light: The spectrum of the green light is normally in the range of 495 nm to 570 nm. Green light can be used to facilitate tissue repair, pain management, treating acne, reduce inflammation, and others[120].

Red light, and near infrared light: Red light, and near-infrared light have vast application to treat skin because its penetration depth is larger. The preferred wavelength of phototherapy, and infrared red light is in the range of 600-900 nm. The mechanism of red-light treatment is modifying molecular functions, prompting cell survival, increase the regeneration of disuse, and wound healing because it can penetrate to the subcutaneous layer of human skin. The common disease of using red light or near-infrared light include wound healing, radioactive dermatosis, inflammation, and oral mucositis[93]. For photobiomodulation, the clinic conducts a skin sensitivity test before treatment. Another problem is the treatment parameter is diverse because the disease, and condition of patient is varied. There is no general or standard treatment parameter, so it is necessary to consult clinics in the development of red light photobiomodulation device.

2.4.3.2. Dose rate



Too much power density and / or time may lead to inhibition

Figure 2-17. Arnt Schulz model of dose rate[121].

A dose rate refers to the quantity of radiation absorbed per unit of time. There is a primary consensus about the photobiomodulation dose rate – Arndt-Schultz law of biphasic dose response, as shown in **Figure 2-17**. This graph suggests that insufficient power density or too short a time will have no effect on the pathology, that too much power balance between power density, and time that produces a maximal beneficial effect. A study conducted 660 nm laser to oral mucositis hamster model with two sets of treatment parameter: one use 55 mW/cm² for 16 seconds, and another use 155 mW/cm² for 6 seconds with the same dose rate 0.9 J/cm² per point[122]. The results show that the clinical mucositis of 55 mW/cm² group was improved, while there is no any severity reduction in the group of 155 Mw/cm², compared to control. Another research is conducting photobiomodulation on human fibroblast, which results shows that the cell viability, and mitochondria activity is higher with lower doses than that of higher dose, as shown in **Figure 2-18**[123]. However, different wavelength, tissue types, redox states,

pulse parameter, and others may influence the dose rate absorbed by human body. This means that there is a great variation on the optimized dose rate for different diseases, and different body parts.

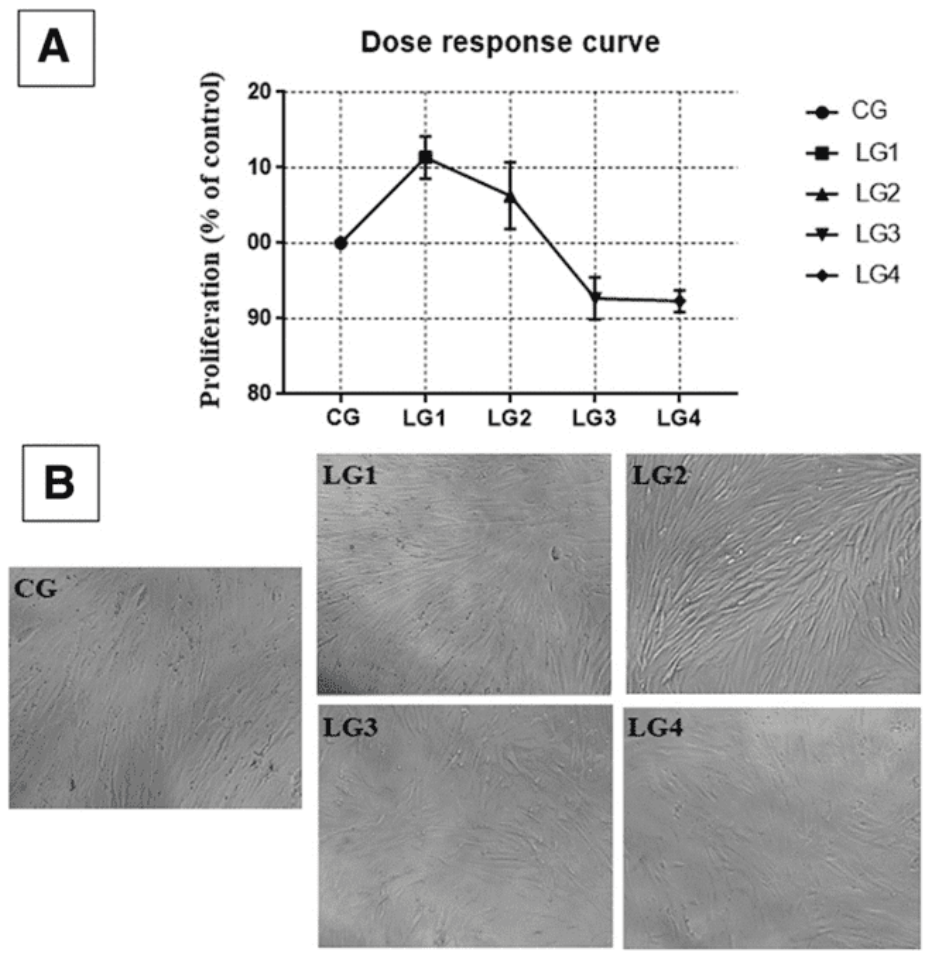


Figure 2-18. Dose/response curve. (A) Proliferation of HFF-1 lineage fibroblasts after 72 h of irradiation at different fluences. (B) Photomicrographs of the cell proliferation at 72 h after irradiation.

The dose rate is determined by power of the light source, and treatment time. The calculation for this is as follows:

Energy
$$(J)$$
 = Power $(W) * Time (s)$

From this equation, we can get the optimized dose rate by increasing the treatment time or increasing the power of the light source. However, it is important to notice that there is a

upper limit on the treatment time, and there is a lower limit on the power.

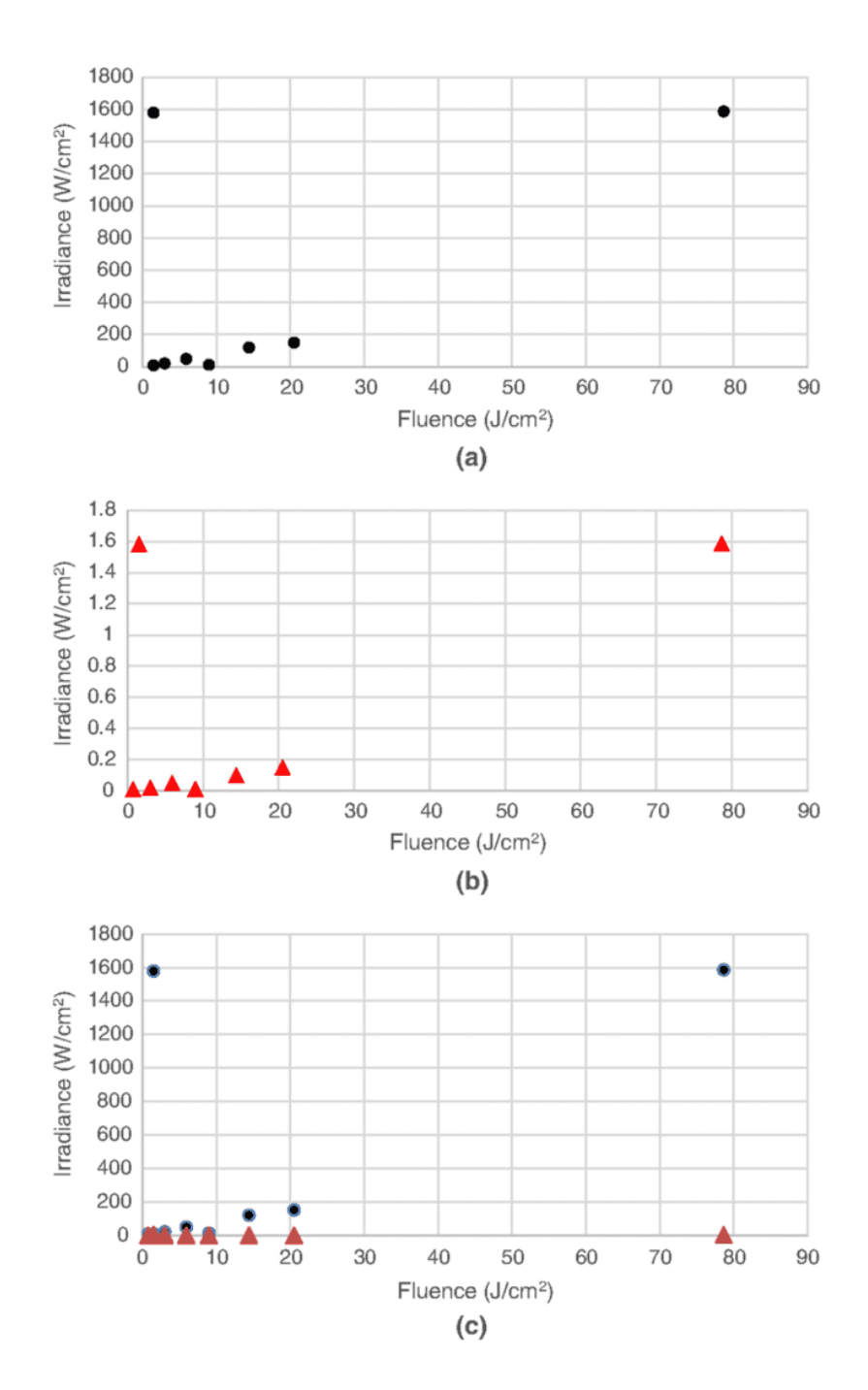


Figure 2-19.. In vitro studies with lower volume of mitochondria (a) Effective studies (b) Ineffective studies (c) Combination of effective studies, and ineffective studies.

Using low irradiance, and prolong the irradiance to achieve the ideal fluence, termed as the Bunsen-roscoe law of reciprocity, may not yield satisfactory result[124]. Therefore, the second law of photobiology is that Bunsen-roscoe law of reciprocity is not applicable to low

Chapter 3

incident power density. It points out that the power of the light source needs to maintain at

certain level. A comprehensive review was conducted about the photobiomodulation light

parameter, in which outline the effectiveness, and ineffectiveness of both in vivo, and in vitro

studies light parameters[125]. Figure 2-19 illustrates the summary of the in vitro studies: which

tissue contains lower volume of mitochondria. It can find out that even the total fluence is the

same, studies using low irradiance below 0.2 W/cm² may produce effective results. If the

irradiance is at the higher level, the treatment effect is positive. Another evidence is cell

viability with different treatment time. Shen (2013) conduct photobiomodulation on human

fibroblast, in which the energy density is fixed at 5 J/cm. Among five samples, only the sample

with lowest irradiance 0.1424 mW/cm² were death after 9.5 hrs treatment[126].

Besides the power density, and treatment time, there are also other terms related to the

light source of photobiomodulation, as follows:

Centre wavelength (nm): Centre wavelength, also called peak wavelength, is the

wavelength at which the spectral distribution reaches its largest value.

Spectral bandwidth: It refers to the width of the light spectrum

Irradiance: Irradiance, also termed as power density, is defined as the radiance flux

received by a surface per unit area. The standard unit for irradiance is the watt per square meter.

Operating mode: The operating mode of the light can be pulse or continuous. If the

beam is pulsed, the power is called as average power. Below is the equation:

Average Power (W)

= Peak Power (W) \times Pulse width (s) \times Pulse frequency (Hz)

43

Treatment Interval: It refers to the frequency of treatment, normally number of sessions per weeks.

2.4.3.3. Photobiomodulation device configuration

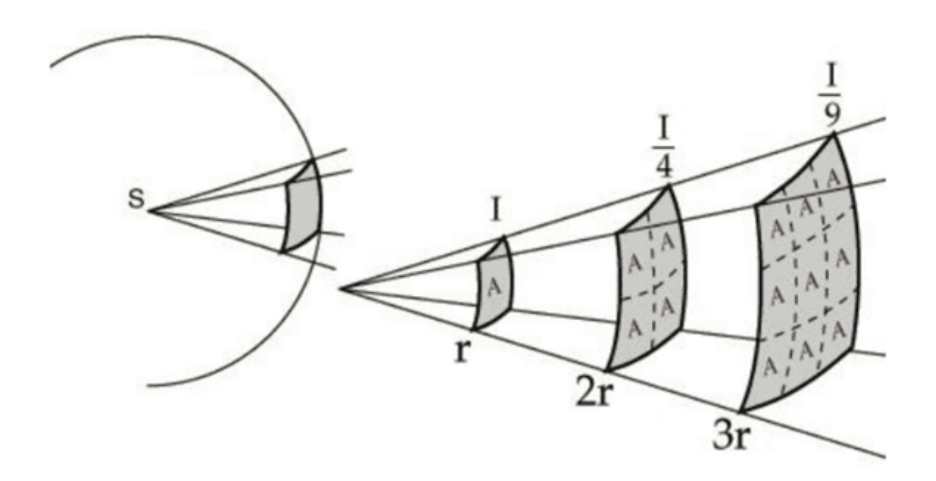


Figure 2-20. A schematic diagram of inverse square law.

Above section discusses the significance, and requirement of the light parameter for effective photobiomodulation. A critical parameter power is defined as the amount of light received by the skin in square of area. It is not equal to the power emitted from the light source. There are several factors influencing the power density on skin- treatment distance, and the spacing between point light sources.

Treatment distance is defined the separation gap between the light source, and human skin. The treatment distance impact the power density on skin, which relationship is governed by the inverse square law. Inverse square law is defined as the power density of a point-like source is proportion to the inverse square of the law, as shown in **Figure 2-20**[127]. As the distance between light source, and target increases from r to 2r, the light intensity decreases from I to ¼ of its original value (I). Therefore, the treatment distance between the human skin, and light source need to be considered in order to confirm that the power density to be too low

due to the larger treatment distance of photobiomodulation.

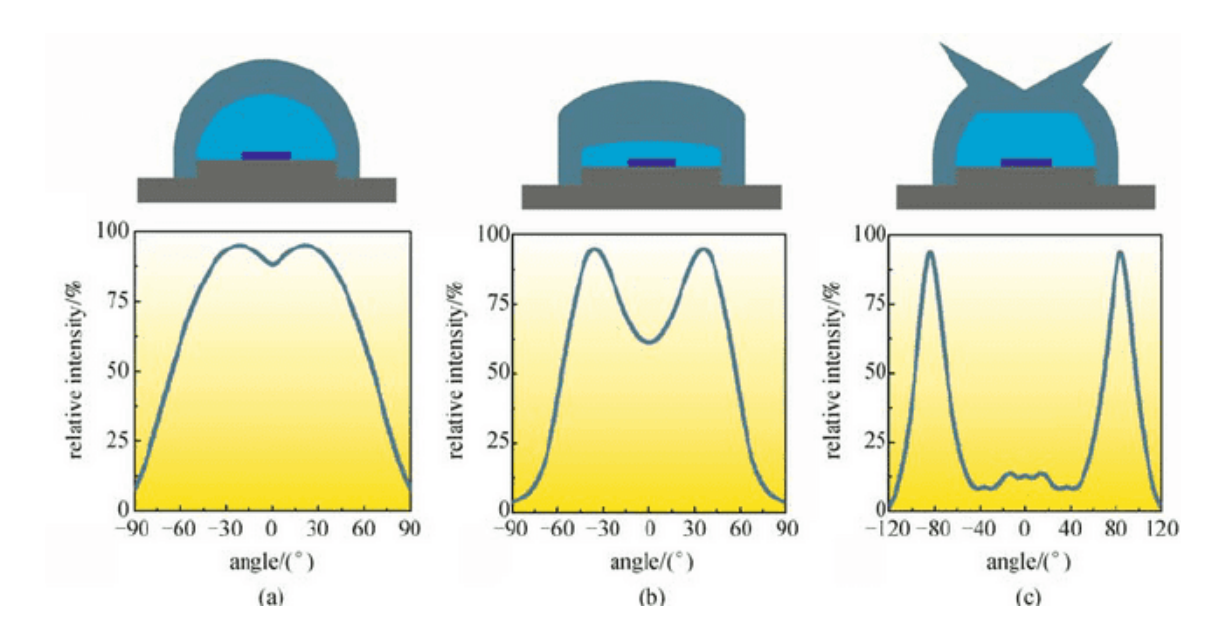


Figure 2-21. Three types of LEDs light distribution.(a) Lambertian lens. (b) Batwing lens. (c) side emitting lens.

Large area photobiomodulation is normally conducted by an array of point-light source, like numbers of laser diodes, and LEDs. For LEDs, its light is directional, which is normally characterized with viewing angle. Viewing angle is defined as the angel at which the brightness decreases to 50% of its maximum value. In addition, there are different types of light distribution among LEDS, including Lambertian, Batwing, and side emitting, as shown in **Figure 2-21**[128]. These characteristics may influence the power density of the array, in which the array light intensity is inhomogeneous with both higher intensity, and lower intensity. Based on previous light parameters studies, it is suggested that the variation of light intensity among panels need to be controlled for efficient treatment. Based on this, it is critical to design the distribution, and spacing between the LEDs to design the spot design for efficient photobiomodulation.

In summary, photobiomodulation can be optimized through changing the design or

selection of light source, and the mechanical design of the panel. The treatment efficiency of the photobiomodulation is highly associated with light parameters, including wavelength, and power density of light. Additionally, the mechanical design of the panel, such as shape, spacing between LEDs, and the distance from the target tissue may influence the power density of the light. Therefore, a comprehensive approach that takes in account both the light source, and the mechanical design of the panel is essential for achieving efficient photobiomodulation.

2.4.4. Development of flexible photobiomodulation device

Table 2-1. Table about the recent flexible photobiomodulation device.

No.	Peak	Type of light	Size	Thickness	Power	Light	Ref.
	Wavelength	source	(Area)			power	
			2			density	
Unit	nm	/	mm ²	μm	/	mW cm ⁻²	/
1	633	OLED	9-69	676	< 10 V	18.31	[129]
2	669	OLED	10*10	6	40 mA cm ⁻²	~8	[130]
3	630	μLED	3 *4	737	~1.2 V	22	[131]
4	630	μLED	20* 20	2000	3V (100 mA)	~0.3	[132]
5	630	LED	-	-	153.6 mA	11600	[133]
6	630	LED	50* 50	-	~1.5 V	~15.05	[134]

Considering the treatment time, and the diversity of the treatment area, flexible photobiomodulation panel can conform to the human body seamless are preferred. This flexible device can conduct photobiomodulation with high power efficiency, comfortability, and convenience are preferred. Based on this, researchers have developed different kinds of flexible photobiomodulation devices with different techniques. Details of the recent flexible photobiomodulation panel or accessories was listed out in Table 2-1. In the following section, we are going to search these flexible photobiomodulation systems, and studies their advantages,

and limitations.

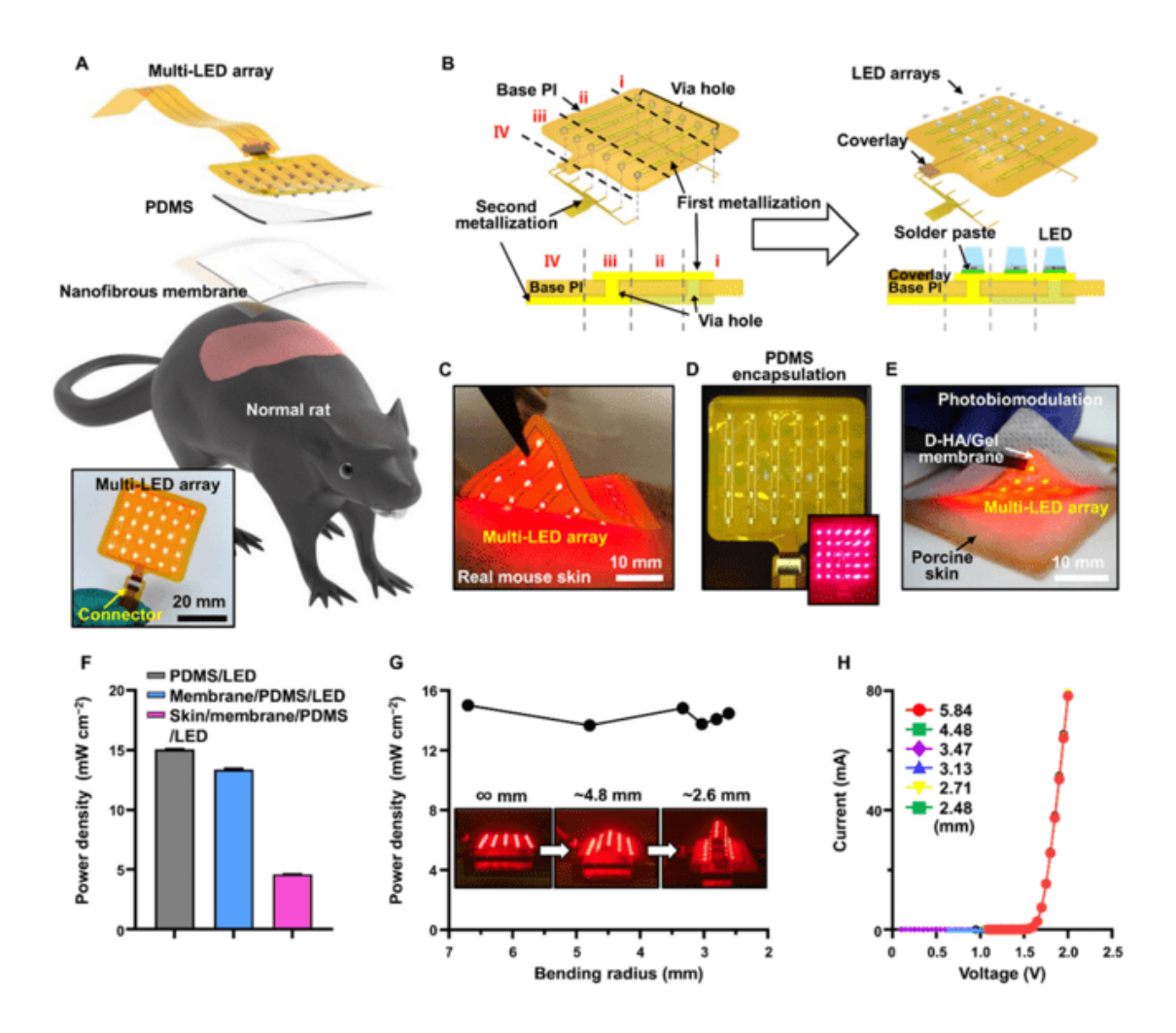


Figure 2-22. Attachable µLEDs photobiomodulation panel. (a) Design concept of the PBM panel. (b) A schematic illustration of the fabrication process of the PBM panel. (c-e) Digital image of the panel. (f-g) Measured power density of the panel with or without loading. (h) Electrical properties of the panel.

A rising trend is using μLEDs as the light source for flexible device. Micro-LEDs is defined as the size of LEDs smaller than 100 μm[135]. μLEDs can provide light with higher brightness, higher contrast ratio, better resolution, faster response, longer lifetime, better environment stability, and wider viewing angel than OLED[136]. One example of flexible photobiomodulation panel is based on multi-LED array with a adhesive hyaluronic acid-based gelatine nanofibrous membrane, as depicted in **Figure 2-22**[134]. The power density of the

panel was 13.37 mW cm⁻². Another μLED based panel with a surface area of 2×2 cm-2 was developed with 900 μLEDs. A light diffusion layer composed of silica dispersed among PDMS was assembled onto it to improve the light scattering. Current μLED based photobiomodulation panel is very small, normal in the range of several centimetres because of the difficult in mass transfer, energy efficiency, structure design, and defects management[137]. This may limit the photobiomodulation applications, especially for skin decease requiring large are treatment.

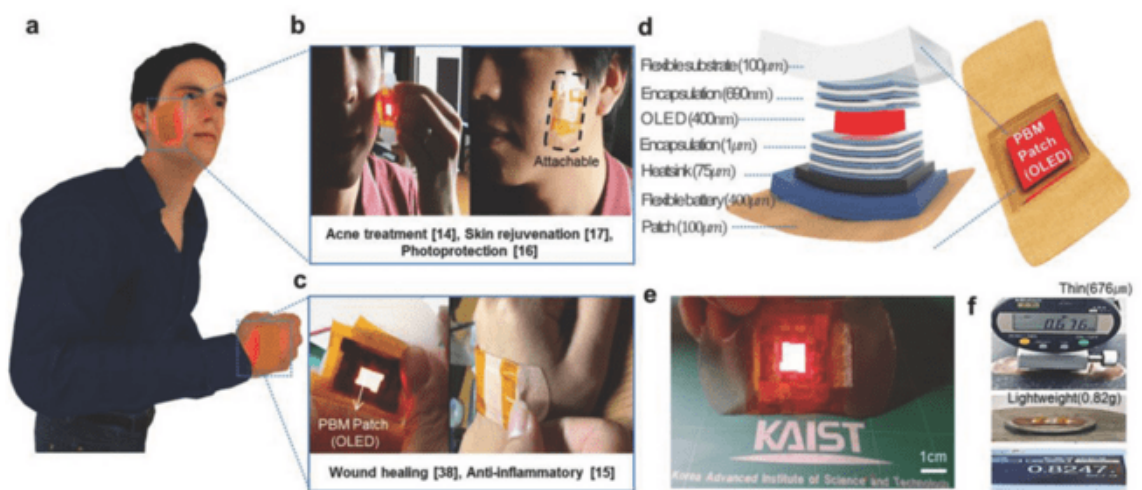


Figure 2-23. OLED photobiomodulation patch. (a) Design concept of the OLED panel. (b-c, e-f) Digital images of the OLED panel. (d) A schematic illustration of the structure of the panel.

Another trend is using organic light emitting diode (OLED) as light source. OLED is composed of film organic compound to emit light. One example of OLED photobiomodulation patch was developed, as shown in **Figure 2-23**[138]. The weight of the panel is only 0.82 g, the thickness is 676 µm[129]. The operation life is over 300 hr. This panel can effectively stimulate fibroblast proliferation, and enhance fibroblast migration. Another attachable phototherapy patch was developed with only 6 um thickness. However, this patch combined with a dressing film only can operate for more than 100 h, during which time the light intensity continuous to decrease[130]. A recent research developed a relatively large textile-based OLED with the peak wavelength of 470 nm to treat neonatal jaundice[139]. The size of the

OLED is 189 mm in length, 39 mm in width, and 0.91 mm in thickness. Even through OLED panel has been enlarged, they still fall short of commercial photobiomodulation panels, and the stability of illumination or operation life remains a challenge.

From above studies, it can find out that current potential techniques for the development of flexible photobiomodulation panel facing the size problems, lower power density, and stability problems. These techniques are more applicable to develop panel to conduct point-to-point photobiomodulation with limited treatment area. For the disease affecting larger areas, such as radioactive dermatitis, and ulcer, there is a demand to develop new large flexible photobiomodulation panel.

2.4.5. Photobiomodulation for radioactive dermatitis

Since our understanding of radioactive dermatitis, and the mechanism of photobiomodulation is limited, it is imperative to conduct comprehensive studies involving various clinical trials to confirm the optical properties of the light used in the treatment. In recent years, several clinical studies were conducted to use photobiomodulation as treatment of radioactive dermatitis. This can lower the grades of the radioactive dermatitis, and pain scores of patients[140]. A clinical study was conducted for neck, and head cancer radioactive dermatitis. It conducted 2 session photobiomodulation in each week, total 14 sessions. The energy dose rate is 4 J/cm². The photobiomodulation use IR laser diodes, which is handpiece. The wavelength of the light was 808 nm or 905 nm, and the irradiance was 0.168 W/cm². The results that photobiomodulation can decrease the severity of radioactive dermatitis, in which numbers of people getting grade 2, and/or grade 3 is less[141]. Another clinical studies was conducted to prevent acute radiodermatitis by photobiomodulation[142]. It includes 120 breast cancer patients with a radiation treatment does rate of 40 Gy. The severity of the skin among

control group, and the laser group is different, in which the percentages of patients with photobiomodulation experiencing RTOG grade 2 is lower. (30% vs 6.7% for the placebo, and laser group). The used photobiomodulation device is laser based, in which the beam size is only 19.625 cm². The irradiance value of the treatment was 0.168 W/cm², with treatment durations ranging from 300 to 600 seconds. Compared to previous wearable devices, this irradiance level is very high, and cannot be easily achieved. Based on this, it is reasonable to study current commercial PBM devices to more clearly identify this value.

From the clinical studies, it can find that most used photobiomodulation device are hand-held, with limited treatment area. In addition, the total treatment period of the photobiomodulation last for one or two months, in which the patient needs to come to clinics for 2 or 3 times. This brings many inconveniences to the treatment. The development of the wearable photobiomodulation device can address these issues to allow patients to receive treatment at home. The patients do not need to go to clinics regularly. In addition, previous literature review found out that our human body shape, and size can be influenced by the respiration, and body movement. This may cause variation to the treatment dose rate. The treatment efficiency may in doubts. The fitting between photobiomodulation panel, and human contour are essential. Wearable electronics conforming to the human contour can minimize these variations, in which the light from the device can be more homogenous, and hence enhancing treatment efficiency.

From above literature reviews, we can preliminary summarize several requirements on different fields for efficient photobiomodulation, as follows:

Flexibility: This wearable photobiomodulation panel need to conform the shape, and contour of the breast to minimize the variation of the treatment light. The ability of the device

to mold to individual anatomical differences is fundamental in achieving consistent therapeutic outcomes.

Power density of the light: Considering the first law, and second law of photobiology, the energy density of the light needs to over certain threshold. This lowest threshold needs to be confirmed in the later section.

Uniformity of the irradiance: In addition to the treatment effect, there is an upper limit to the power density due to the dose rate, and the heating problems, and a lower limit due to the second law of photobiology. The irradiance variation among the panel cannot be too large. The highest irradiance of the panel cannot cause cell damage, while the lowest irradiance of the panel needs to over certain threshold to realize treatment.

In summary, the development of efficient wearable photobiomodulation devices for breast cancer therapy or other applications requires careful consideration of the device's flexibility, power density, and irradiance uniformity. These parameters are integral to the design, and functionality of PBM devices, ensuring that they deliver safe, effective, and consistent therapeutic benefits.

2.5. Summary and Perspectives

In this chapter, a comprehensive review about the flexible pressure sensation device, and photobiomodulation was conducted. Conventional pressure sensation device/interface face limitations in wearable application due to its material properties, and conformability. A recent approach is using different types of flexible sensors for pressure sensation as the input channel, while its signal is highly influenced by the environment, like temperature, relative humidity, and electric field. The sensitivity of the sensor cannot compare to conventional switch-based

input device because of its mechanism. Otherwise, there are various types of body signals, in which the signal amplitude varies by orders of magnitudes. It is challenging to develop an pressure input device or pressure sensitive devices with a fixed initiation threshold for different wearable applications. Based on this, it is demand to develop new flexible input device applicable to wearable applications, with good flexibility, signal stability, and reliability.

Cancer is a common cause of death around the world, for which radiation treatment is a general treatment. Along with treatment, radiation can harm health, and normal cells, causing serious side effect to the human, especially radiation dermatitis. Radiation dermatitis seriously influences the cancers' patient life psychologically, and physiologically. Its pathology manifests with inflammation, pain, moist desquamation, and ulcer in serious case. There is no widely accepted treatment to relieve radiation dermatitis. Most of the treatment requires further studies to be proven. Even among cancer patients, breast cancer patients face more serious challenges in managing, and treatment of radioactive dermatitis because the contour, and shape of the breast variation in the radiation treatment is large, leading to a more inhomogeneous radiation dose distribution, results in higher risk of skin toxicity. It is valuable to develop, and integrate a novel wearable electronic supportive care system into breast cancer patient daily life to relieve the symptoms of radiation dermatitis.

Photobiomodulation is an ancient method to treat different disease, like wound healing, inflammation, and depression. Although many studies were conducted to prove the effectiveness of the photobiomodulation, three are still many unknown areas about its mechanism, particular the correlation between the disease pathology, and the cellular response of photobiomodulation. This challenges the treatment effectiveness of the photobiomodulation. Treatment effectiveness of photobiomodulation are determined by the treatment parameter, including light wavelength, treatment time, power density, and device configuration. In details,

the dose rate of photobiomodulation need to account for the biphasic dose response, while the light power density disobeys the Bunsen-roscoe law or reciprocity law. To facilitate the prevalence of photobiomodulation, different flexible photobiomodulation with different techniques are developed to allow the conduction of remote, and customization photobiomodulation. However, these sizes, and power density of these flexible devices are limited. These are not applicable to the clinics, only for the lab. It is advocated to develop a new flexible photobiomodulation conforming to contour of the human body, with relatively large area, and higher power density.

2.6. References

- [1] R. Yin, D. Wang, S. Zhao, Z. Lou, G. Shen, 'Wearable Sensors-Enabled Human–Machine Interaction Systems: From Design to Application', *Adv. Funct. Mater.*, vol. 31, no. 11, pp. 1–24, 2020, doi: 10.1002/adfm.202008936.
- [2] W. Heng, S. Solomon, and W. Gao, 'Flexible Electronics and Devices as Human–Machine Interfaces for Medical Robotics', *Adv. Mater.*, vol. 34, no. 16, p. 2107902, 2022, doi: 10.1002/adma.202107902.
- [3] Reliability and Failure of Electronic Materials and Devices. Accessed: May 15, 2024. [Online]. Available: https://learning.oreilly.com/library/view/reliability-and-failure/9780120885749/XHTML/B978012088574900001X/B978012088574900001X.xh tml
- [4] D. R. Kiran, 'Reliability Engineering', United States: Elsevier Science & Technology, 2016. doi: 10.1016/B978-0-12-811035-5.00027-1.
- [5] K. G. Krishna, S. Parne, N. Pothukanuri, V. Kathirvelu, S. Gandi, and D. Joshi, 'Nanostructured metal oxide semiconductor-based gas sensors: A comprehensive review', *Sens. Actuators Phys.*, vol. 341, p. 113578, Jul. 2022, doi: 10.1016/j.sna.2022.113578.
- [6] M. Tonezzer and L. Van Duy, 'Gas Sensors', in *Encyclopedia of Sensors and Biosensors (First Edition)*, R. Narayan, Ed., Oxford: Elsevier, 2023, pp. 185–208. doi: 10.1016/B978-0-12-822548-6.00113-8.
- [7] 'Physiological basis for human autonomic rhythms: Annals of Medicine: Vol 32, No 5'. Accessed: Aug. 08, 2024. [Online]. Available: https://www-tandfonline-com.ezproxy.lb.polyu.edu.hk/doi/abs/10.3109/07853890008995937

- [8] J. Hu, 'Fabric permeability testing', in *Fabric Testing*, United Kingdom: Elsevier Science & Technology, 2008. doi: 10.1533/9781845695064.189.
- [9] J. Y. Hu, Y. I. Li, and K. W. Yeung, '15 Air permeability', in *Clothing Biosensory Engineering*, Y. Li and A. S. W. Wong, Eds., in Woodhead Publishing Series in Textiles., Woodhead Publishing, 2006, pp. 252–260. doi: 10.1533/9781845691462.252.
- [10] Y. Huang, X. Fan, S.-C. Chen, and N. Zhao, 'Emerging technologies of flexible pressure sensors: materials, modeling, devices, and manufacturing', *Adv. Funct. Mater.*, vol. 29, no. 12, p. 1808509, 2019.
- [11] J. Hu, G. Dun, X. Geng, J. Chen, X. Wu, and T.-L. Ren, 'Recent progress in flexible micro-pressure sensors for wearable health monitoring', *Nanoscale Adv.*, vol. 5, no. 12, pp. 3131–3145, Jun. 2023, doi: 10.1039/D2NA00866A.
- [12] A. Fiorillo, C. Critello, and S. Pullano, 'Theory, technology and applications of piezoresistive sensors: A review', *Sens. Actuators Phys.*, vol. 281, pp. 156–175, 2018.
- [13] J. Li, T. Wu, H. Jiang, Y. Chen, and Q. Yang, 'Ultrasensitive Hierarchical Piezoresistive Pressure Sensor for Wide-Range Pressure Detection', *Adv. Intell. Syst.*, vol. 3, no. 11, p. 2100070, 2021, doi: 10.1002/aisy.202100070.
- [14] L. Wen *et al.*, 'A General Strategy for Rapidly Optimizing Wearable Resistive Pressure Sensors', *Adv. Electron. Mater.*, vol. 9, no. 8, p. 2300201, 2023, doi: 10.1002/aelm.202300201.
- [15] C.-L. Choong *et al.*, 'Highly Stretchable Resistive Pressure Sensors Using a Conductive Elastomeric Composite on a Micropyramid Array', *Adv. Mater. Deerfield Beach Fla*, vol. 26, Jun. 2014, doi: 10.1002/adma.201305182.
- [16] S. Chen, Y. Song, and F. Xu, 'Flexible and Highly Sensitive Resistive Pressure Sensor Based on Carbonized Crepe Paper with Corrugated Structure', *ACS Appl. Mater. Interfaces*, vol. 10, no. 40, pp. 34646–34654, Oct. 2018, doi: 10.1021/acsami.8b13535.
- [17] R. B. Mishra, N. El-Atab, A. M. Hussain, and M. M. Hussain, 'Recent progress on flexible capacitive pressure sensors: From design and materials to applications', *Adv. Mater. Technol.*, vol. 6, no. 4, p. 2001023, 2021.
- [18] K.-H. Ha, H. Huh, Z. Li, and N. Lu, 'Soft capacitive pressure sensors: trends, challenges, and perspectives', *ACS Nano*, vol. 16, no. 3, pp. 3442–3448, 2022.
- [19] Z. Ahmad, 'Polymer Dielectric Materials', in *Dielectric Material*, IntechOpen, 2012. doi: 10.5772/50638.
- [20] Z. Ahmad, 'Polymer dielectric materials', in *Dielectric material*, IntechOpen, 2012.

- [21] R. B. Mishra *et al.*, 'Recent Progress on Flexible Capacitive Pressure Sensors: From Design and Materials to Applications', *Adv. Mater. Technol.*, vol. 6, no. 4, pp. 1–34, Apr. 2021, doi: 10.1002/admt.202001023.
- [22] T. Li *et al.*, 'Flexible Capacitive Tactile Sensor Based on Micropatterned Dielectric Layer', *Small*, vol. 12, no. 36, pp. 5042–5048, Sep. 2016, doi: 10.1002/smll.201600760.
- [23] J.-O. Kim *et al.*, 'Highly Ordered 3D Microstructure-Based Electronic Skin Capable of Differentiating Pressure, Temperature, and Proximity', 2018, doi: 10.1021/acsami.8b19214.
- [24] V. Fernicola, M. Banfo, L. Rosso, and D. Smorgon, 'Investigation of capacitive-based relative humidity sensors and their stability at high temperature', *Int. J. Thermophys.*, vol. 29, pp. 1668–1677, 2008.
- [25] B. Aksoy, Y. Hao, G. Grasso, K. M. Digumarti, V. Cacucciolo, and H. Shea, 'Shielded soft force sensors', *Nat. Commun.*, vol. 13, no. 1, p. 4649, Aug. 2022, doi: 10.1038/s41467-022-32391-0.
- [26] G. Gautschi and G. Gautschi, *Piezoelectric sensors*. Springer, 2002.
- [27] M. C. Sekhar, E. Veena, N. S. Kumar, K. C. B. Naidu, A. Mallikarjuna, and D. B. Basha, 'A Review on Piezoelectric Materials and Their Applications', *Cryst. Res. Technol.*, vol. 58, no. 2, p. 2200130, 2023, doi: 10.1002/crat.202200130.
- [28] Y. Wu, Y. Ma, H. Zheng, and S. Ramakrishna, 'Piezoelectric materials for flexible and wearable electronics: A review', *Mater. Des.*, vol. 211, p. 110164, 2021.
- [29] S. Sapkal, B. Kandasubramanian, and H. S. Panda, 'A review of piezoelectric materials for nanogenerator applications', *J. Mater. Sci. Mater. Electron.*, vol. 33, no. 36, pp. 26633–26677, 2022.
- [30] C. Zhi, S. Shi, Y. Si, B. Fei, H. Huang, and J. Hu, 'Recent Progress of Wearable Piezoelectric Pressure Sensors Based on Nanofibers, Yarns, and Their Fabrics via Electrospinning', *Adv. Mater. Technol.*, vol. 8, no. 5, p. 2201161, 2023, doi: 10.1002/admt.202201161.
- [31] X. Lu, H. qu, and M. Skorobogatiy, 'Piezoelectric Micro- and Nanostructured Fibers Fabricated from Thermoplastic Nanocomposites Using a Fiber Drawing Technique: Comparative Study and Potential Applications', *ACS Nano*, vol. 11, Feb. 2017, doi: 10.1021/acsnano.6b08290.
- [32] J. Chun, K. Y. Lee, C.-Y. Kang, M. W. Kim, S.-W. Kim, and J. M. Baik, 'Embossed Hollow Hemisphere-Based Piezoelectric Nanogenerator and Highly Responsive Pressure Sensor', *Adv. Funct. Mater.*, vol. 24, no. 14, pp. 2038–2043, 2014, doi: 10.1002/adfm.201302962.

- [33] W. Navaraj and R. Dahiya, 'Fingerprint-enhanced capacitive-piezoelectric flexible sensing skin to discriminate static and dynamic tactile stimuli', *Adv. Intell. Syst.*, vol. 1, no. 7, p. 1900051, 2019.
- [34] S. Wang, L. Lin, and Z. L. Wang, 'Triboelectric nanogenerators as self-powered active sensors', *Nano Energy*, vol. 11, pp. 436–462, 2015.
- [35] Q. Zhou, J. Pan, S. Deng, F. Xia, and T. Kim, 'Triboelectric nanogenerator-based sensor systems for chemical or biological detection', *Adv. Mater.*, vol. 33, no. 35, p. 2008276, 2021.
- [36] P. Yang *et al.*, 'Monitoring the Degree of Comfort of Shoes In-Motion Using Triboelectric Pressure Sensors with an Ultrawide Detection Range', *ACS Nano*, vol. 16, no. 3, pp. 4654–4665, Mar. 2022, doi: 10.1021/acsnano.1c11321.
- [37] Z. Lin *et al.*, 'Large-Scale and Washable Smart Textiles Based on Triboelectric Nanogenerator Arrays for Self-Powered Sleeping Monitoring', *Adv. Funct. Mater.*, vol. 28, no. 1, p. 1704112, Jan. 2018, doi: 10.1002/adfm.201704112.
- [38] Y. Wang, L. Zhu, and C. Du, 'Flexible Difunctional (Pressure and Light) Sensors Based on ZnO Nanowires/Graphene Heterostructures', *Adv. Mater. Interfaces*, vol. 7, p. 1901932, Jan. 2020, doi: 10.1002/admi.201901932.
- [39] Y. Luo *et al.*, 'Technology Roadmap for Flexible Sensors', *ACS Nano*, Mar. 2023, doi: 10.1021/acsnano.2c12606.
- [40] D.-J. Shin, 'Performance and usability of flexible membrane keyboards', PhD Thesis, Virginia Tech, 2005.
- [41] J. Romero, M. H. Azarian, C. Morillo, and M. Pecht, 'Effects of Moisture and Temperature on Membrane Switches in Laptop Keyboards', *IEEE Trans. Device Mater. Reliab.*, vol. 18, no. 4, pp. 535–545, Dec. 2018, doi: 10.1109/TDMR.2018.2866776.
- [42] Y. Zhang, J. Zou, H. Wang, C. Zhou, and X. Chen, 'A single-layer less-wires stretchable wearable keyboard based on pressure switch conductive textile', *Smart Mater. Struct.*, vol. 31, no. 10, p. 105008, Oct. 2022, doi: 10.1088/1361-665X/ac8adb.
- [43] B. Ju *et al.*, 'Inkjet Printed Textile Force Sensitive Resistors for Wearable and Healthcare Devices', *Adv. Healthc. Mater.*, vol. 10, no. 20, p. 2100893, 2021, doi: 10.1002/adhm.202100893.
- [44] S. Liu, K. Ma, B. Yang, H. Li, and X. Tao, 'Textile Electronics for VR/AR Applications', *Adv. Funct. Mater.*, vol. 31, no. 39, p. 2007254, 2021, doi: 10.1002/adfm.202007254.
- [45] S. Coren, L. M. Ward, and J. T. Enns, Sensation and perception. John Wiley & Sons

- Hoboken, NJ, 2004.
- [46] M. Wang et al., 'Artificial Skin Perception', Adv. Mater., vol. 2003014, pp. 1–20, 2020, doi: 10.1002/adma.202003014.
- [47] X. Wang *et al.*, 'Bio-inspired artificial synaptic transistors: evolution from innovative basic units to system integration', *Mater. Horiz.*, vol. 10, no. 9, pp. 3269–3292, 2023, doi: 10.1039/D3MH00216K.
- [48] L. A. Jones, *Haptics*. in The MIT Press essential knowledge series. Cambridge, Massachusetts: The MIT Press, 2018.
- [49] K. Parida, H. Bark, and P. S. Lee, 'Emerging Thermal Technology Enabled Augmented Reality', *Adv. Funct. Mater.*, vol. 2007952, no. June, 2021, doi: 10.1002/adfm.202007952.
- [50] 'Frontiers | Nanowire FET Based Neural Element for Robotic Tactile Sensing Skin'. Accessed: May 16, 2024. [Online]. Available: https://www.frontiersin.org/journals/neuroscience/articles/10.3389/fnins.2017.00501/full
- [51] K. O. Johnson, 'The roles and functions of cutaneous mechanoreceptors', *Curr. Opin. Neurobiol.*, vol. 11, no. 4, pp. 455–461, 2001.
- [52] A. Handler and D. D. Ginty, 'The Mechanosensory Neurons of Touch and their Mechanisms of Activation', *Nat. Rev. Neurosci.*, vol. 22, no. 9, pp. 521–537, Sep. 2021, doi: 10.1038/s41583-021-00489-x.
- [53] V. G. Macefield, 'Physiological characteristics of low-threshold mechanoreceptors in joints, muscle and skin in human subjects', *Clin. Exp. Pharmacol. Physiol.*, vol. 32, no. 1–2, pp. 135–144, 2005, doi: 10.1111/j.1440-1681.2005.04143.x.
- [54] A. Zimmerman, L. Bai, and D. D. Ginty, 'The gentle touch receptors of mammalian skin', *Science*, vol. 346, no. 6212, pp. 950–954, Nov. 2014, doi: 10.1126/science.1254229.
- [55] V. E. Abraira and D. D. Ginty, 'The Sensory Neurons of Touch', *Neuron*, vol. 79, no. 4, pp. 618–639, Aug. 2013, doi: 10.1016/j.neuron.2013.07.051.
- [56] A. E. Saddik, M. Orozco, M. Eid, and J. Cha, 'Human Haptic Perception', in *Haptics Technologies*, in Springer Series on Touch and Haptic Systems., Berlin, Heidelberg: Springer Berlin Heidelberg, 2011, pp. 45–66. doi: 10.1007/978-3-642-22658-8_3.
- [57] G. E. A. Abreu and M. E. H. Aguilar, *Neurons: Dendrites and Axons*. BoD Books on Demand, 2019.
- [58] 'Neurons and Sensory Receptors', in *Comparative Vertebrate Neuroanatomy*, John Wiley & Sons, Ltd, 2005, pp. 19–48. doi: 10.1002/0471733849.ch2.

- [59] F. Rice and P. Albrecht, '6.01. Cutaneous Mechanisms of Tactile Perception: Morphological and Chemical Organization of the Innervation to the Skin', *Senses Compr. Ref.*, vol. 6, Dec. 2008, doi: 10.1016/b978-012370880-9.00340-6.
- [60] M. Barnett and P. Larkman, 'The action potential', *Pract. Neurol.*, vol. 7, pp. 192–7, Jul. 2007.
- [61] J. M. Sullivan and F. E. Schweizer, 'Neurotransmitter release from presynaptic terminals', *eLS*, pp. 1–7, 2001.
- [62] M. Edmonds, C. Manu, and P. Vas, 'The current burden of diabetic foot disease', *J. Clin. Orthop. Trauma*, vol. 17, pp. 88–93, 2021.
- [63] P. Laing, 'The development and complications of diabetic foot ulcers', Am. J. Surg., vol. 176, no. 2, pp. 11S-19S, 1998.
- [64] D. Armstrong, T.-W. Tan, A. Boulton, and S. Bus, 'Diabetic Foot Ulcers: A Review', *JAMA*, vol. 330, pp. 62–75, Jul. 2023, doi: 10.1001/jama.2023.10578.
- [65] A. M. Ibrahim, 'Diabetic foot ulcer: synopsis of the epidemiology and pathophysiology', *Int J Diabetes Endocrinol*, vol. 3, no. 2, p. 23, 2018.
- [66] M. E. Edmonds and A. V. Foster, *Managing the diabetic foot*. John Wiley & Sons, 2014.
- [67] K. Mai, 'Monitoring and assessment of diabetic patients by Intelligent Footwear System', 2014, Accessed: May 30, 2024. [Online]. Available: https://theses.lib.polyu.edu.hk/handle/200/7522
- [68] R. L. Actis *et al.*, 'Multi-plug insole design to reduce peak plantar pressure on the diabetic foot during walking', *Med. Biol. Eng. Comput.*, vol. 46, no. 4, pp. 363–371, Apr. 2008, doi: 10.1007/s11517-008-0311-5.
- [69] K. Moulaei, M. Malek, and A. Sheikhtaheri, 'A smart wearable device for monitoring and self-management of diabetic foot: A proof of concept study', *Int. J. Med. Inf.*, vol. 146, p. 104343, Feb. 2021, doi: 10.1016/j.ijmedinf.2020.104343.
- [70] W. R. Ledoux, J. B. Shofer, M. S. Cowley, J. H. Ahroni, V. Cohen, and E. J. Boyko, 'Diabetic foot ulcer incidence in relation to plantar pressure magnitude and measurement location', *J. Diabetes Complications*, vol. 27, no. 6, pp. 621–626, 2013, doi: 10.1016/j.jdiacomp.2013.07.004.
- [71] B. Iraj, F. Khorvash, A. Ebneshahidi, and G. Askari, 'Prevention of Diabetic Foot Ulcer', *Int. J. Prev. Med.*, vol. 4, no. 3, pp. 373–376, Mar. 2013.
- [72] M. W. Whittle, *Gait analysis: an introduction*. Butterworth-Heinemann, 2014.

- [73] W. Tao, T. Liu, R. Zheng, and H. Feng, 'Gait Analysis Using Wearable Sensors', *Sensors*, vol. 12, no. 2, Art. no. 2, Feb. 2012, doi: 10.3390/s120202255.
- [74] M. J. Armstrong and M. S. Okun, 'Diagnosis and Treatment of Parkinson Disease: A Review', *JAMA*, vol. 323, no. 6, p. 548, Feb. 2020, doi: 10.1001/jama.2019.22360.
- [75] W. C. Roller, S. Glatt, B. Vetere-Overfield, and R. Hassanein, 'Falls and Parkinson's disease', *Clin. Neuropharmacol.*, vol. 12, no. 2, pp. 98–105, 1989.
- [76] A. H. Snijders *et al.*, 'Physiology of freezing of gait', *Ann. Neurol.*, vol. 80, no. 5, pp. 644–659, 2016.
- [77] B. Yang *et al.*, 'Intelligent wearable system with accurate detection of abnormal gait and timely cueing for mobility enhancement of people with Parkinson's disease', *Wearable Technol.*, vol. 3, p. e12, 2022, doi: 10.1017/wtc.2022.9.
- [78] M. Mancini *et al.*, 'Measuring freezing of gait during daily-life: an open-source, wearable sensors approach', *J. Neuroengineering Rehabil.*, vol. 18, pp. 1–13, 2021.
- [79] O. Agu, G. Hamilton, and D. Baker, 'Graduated compression stockings in the prevention of venous thromboembolism', *Br. J. Surg.*, vol. 86, no. 8, pp. 992–1004, 1999.
- [80] J. M. Macdonald, N. Sims, and H. N. Mayrovitz, 'Lymphedema, lipedema, and the open wound: the role of compression therapy', *Surg. Clin.*, vol. 83, no. 3, pp. 639–658, 2003.
- [81] M. J. Denton, 'Fit, stretch, and comfort', *Textiles*, 1972.
- [82] M. Piñeros, L. Mery, I. Soerjomataram, F. Bray, and E. Steliarova-Foucher, 'Scaling Up the Surveillance of Childhood Cancer: A Global Roadmap', *JNCI J. Natl. Cancer Inst.*, vol. 113, no. 1, pp. 9–15, Jan. 2021, doi: 10.1093/jnci/djaa069.
- [83] L. A. C. Vieira *et al.*, 'Incidence of radiodermatitis in breast cancer patients during hypofractionated radiotherapy', *Rev. Esc. Enferm. USP*, vol. 56, p. e20220173, 2022.
- [84] M. F. Häfner, L. Fetzner, J. C. Hassel, J. Debus, and K. Potthoff, 'Prophylaxis of acute radiation dermatitis with an innovative FDA-approved two-step skin care system in a patient with head and neck cancer undergoing a platin-based radiochemotherapy: a case report and review of the literature', *Dermatology*, vol. 227, no. 2, pp. 171–174, 2013.
- [85] L. C. Gutiérrez, P. Khosravi-Shahi, and Y. E. Álvarez, 'Management of dermatitis in patients with locally advanced squamous cell carcinoma of the head and neck receiving cetuximab and radiotherapy', *Oral Oncol.*, vol. 48, no. 4, pp. 293–297, 2012.
- [86] J. L. Soriano, B. Clares, A. C. Calpena, and E. B. Souto, 'Therapy for prevention and treatment of skin ionizing radiation damage: a review', *Int. J. Radiat. Biol.*, vol. 95, no. 5,

- pp. 537–553, May 2019, doi: 10.1080/09553002.2019.1562254.
- [87] J. L. Ryan *et al.*, 'Curcumin for Radiation Dermatitis: A Randomized, Double-Blind, Placebo-Controlled Clinical Trial of Thirty Breast Cancer Patients', *Radiat. Res.*, vol. 180, no. 1, pp. 34–43, 2013.
- [88] K. Müller and V. Meineke, 'Radiation-induced alterations in cytokine production by skin cells', *Exp. Hematol.*, vol. 35, no. 4, Supplement, pp. 96–104, Apr. 2007, doi: 10.1016/j.exphem.2007.01.017.
- [89] M. Spalek, 'Chronic radiation-induced dermatitis: Challenges and solutions', *Clin. Cosmet. Investig. Dermatol.*, vol. 9, pp. 473–482, 2016, doi: 10.2147/CCID.S94320.
- [90] J. Wei *et al.*, 'Radiation-induced skin reactions: mechanism and treatment', *Cancer Manag. Res.*, pp. 167–177, 2018.
- [91] Y.-M. Lim *et al.*, 'Preparation of hydrogels for atopic dermatitis containing natural herbal extracts by gamma-ray irradiation', *Radiat. Phys. Chem.*, vol. 78, no. 7–8, pp. 441–444, 2009.
- [92] K. Zasadziński, M. J. Spałek, and P. Rutkowski, 'Modern dressings in prevention and therapy of acute and chronic radiation dermatitis—a literature review', *Pharmaceutics*, vol. 14, no. 6, p. 1204, 2022.
- [93] C. Shang, D. Xu, and W. Oncologie Journal, 'Epidemiology of Breast Cancer', vol. vol.24, May 2023.
- [94] M. K. Thompson *et al.*, 'Practice-changing radiation therapy trials for the treatment of cancer: where are we 150 years after the birth of Marie Curie?', *Br. J. Cancer*, vol. 119, no. 4, pp. 389–407, Aug. 2018, doi: 10.1038/s41416-018-0201-z.
- [95] S. Harris, '6. Radiotherapy for Early and Advanced Breast Cancer', *Int. J. Clin. Pract.*, vol. 55, no. 9, pp. 609–612, 2001, doi: 10.1111/j.1742-1241.2001.tb11140.x.
- [96] 'Radiation therapy for breast cancer: Literature review Medical Dosimetry'. Accessed: May 29, 2024. [Online]. Available: https://www.meddos.org/article/S0958-3947(16)30045-0/abstract
- [97] I. J. Das, C.-W. Cheng, D. A. Fein, and B. Fowble, 'Patterns of dose variability in radiation prescription of breast cancer', *Radiother. Oncol.*, vol. 44, no. 1, pp. 83–89, Jul. 1997, doi: 10.1016/S0167-8140(97)00054-6.
- [98] A. J. Kole, L. Kole, and M. Moran, 'Acute radiation dermatitis in breast cancer patients: challenges and solutions', *Breast Cancer Targets Ther.*, vol. Volume 9, pp. 313–323, May 2017, doi: 10.2147/BCTT.S109763.

- [99] M. R. Hamblin, 'Mechanisms and applications of the anti-inflammatory effects of photobiomodulation HHS Public Access', *Biophys*, vol. 4, no. 3, pp. 337–361, 2017, doi: 10.3934/biophy.2017.3.337.
- [100] M. T. T. Wong-Riley *et al.*, 'Photobiomodulation Directly Benefits Primary Neurons Functionally Inactivated by Toxins: ROLE OF CYTOCHROME c OXIDASE *', *J. Biol. Chem.*, vol. 280, no. 6, pp. 4761–4771, Feb. 2005, doi: 10.1074/jbc.M409650200.
- [101] J. Dunn and M. H. Grider, 'Physiology, adenosine triphosphate', 2020.
- [102] S. Di Meo, T. T. Reed, P. Venditti, and V. M. Victor, 'Harmful and beneficial role of ROS', *Oxid. Med. Cell. Longev.*, vol. 2016, 2016.
- [103] X. Yu, H. Liu, J. Klejnot, and C. Lin, 'The cryptochrome blue light receptors', *Arab. BookAmerican Soc. Plant Biol.*, vol. 8, 2010.
- [104] O. N. Krokhin, 'Laser: a source of coherent light', *Phys.-Uspekhi*, vol. 54, no. 1, p. 3, 2011.
- [105] R. J. Keyes and T. M. Quist, 'LIGHT-EMITTING DIODES', LED Light., p. 198, 2024.
- [106] V. Heiskanen and M. R. Hamblin, 'Photobiomodulation: Lasers vs Light Emitting Diodes?', *Photochem. Photobiol. Sci. Off. J. Eur. Photochem. Assoc. Eur. Soc. Photobiol.*, vol. 17, no. 8, pp. 1003–1017, Aug. 2018, doi: 10.1039/c8pp00176f.
- [107] B. H. Mahmoud, C. L. Hexsel, I. H. Hamzavi, and H. W. Lim, 'Effects of visible light on the skin', *Photochem. Photobiol.*, vol. 84, no. 2, pp. 450–462, 2008.
- [108] H. J. Vreman, R. J. Wong, and D. K. Stevenson, 'Phototherapy: current methods and future directions', in *Seminars in perinatology*, Elsevier, 2004, pp. 326–333.
- [109] M. Mogensen, H. A. Morsy, L. Thrane, and G. B. Jemec, 'Morphology and epidermal thickness of normal skin imaged by optical coherence tomography', *Dermatology*, vol. 217, no. 1, pp. 14–20, 2008.
- [110] A. Krishnaswamy and G. V. Baranoski, 'A biophysically-based spectral model of light interaction with human skin', in *Computer graphics forum*, Wiley Online Library, 2004, pp. 331–340.
- [111] V. V. Tuchin, 'Light-tissue interactions', Biomed. Photonics Handb., pp. 3–1, 2003.
- [112] M. F. Yang, V. V. Tuchin, and A. N. Yaroslavsky, 'Principles of light-skin interactions', *Light-Based Ther. Skin Color*, pp. 1–44, 2009.
- [113] A. Krishnaswamy and G. V. G. Baranoski, 'A Biophysically-Based Spectral Model of Light Interaction with Human Skin', vol. 23, no. 3, 2004.

- [114] T. Herzinger et al., 'S1-Guidelines on UV phototherapy and photochemotherapy', JDDG J. Dtsch. Dermatol. Ges., vol. 14, no. 8, pp. 853–876, 2016, doi: 10.1111/ddg.12912.
- [115] P. H. Hart, S. Gorman, and J. J. Finlay-Jones, 'Modulation of the immune system by UV radiation: more than just the effects of vitamin D?', *Nat. Rev. Immunol.*, vol. 11, no. 9, pp. 584–596, 2011.
- [116] D. L. Narayanan, R. N. Saladi, and J. L. Fox, 'Ultraviolet radiation and skin cancer', *Int. J. Dermatol.*, vol. 49, no. 9, pp. 978–986, 2010.
- [117] P. V. Algvere, J. Marshall, and S. Seregard, 'Age-related maculopathy and the impact of blue light hazard', *Acta Ophthalmol. Scand.*, vol. 84, no. 1, pp. 4–15, 2006.
- [118] P. Avci et al., 'Low-level laser (light) therapy (LLLT) in skin: stimulating, healing, restoring', in *Seminars in cutaneous medicine and surgery*, NIH Public Access, 2013, p. 41.
- [119] 'Blue light disrupts the circadian rhythm and create damage in skin cells Dong 2019 International Journal of Cosmetic Science Wiley Online Library'. Accessed: May 30, 2024. [Online]. Available: https://onlinelibrary.wiley.com/doi/abs/10.1111/ics.12572
- [120] H. Serrage *et al.*, 'Under the spotlight: mechanisms of photobiomodulation concentrating on blue and green light', *Photochem. Photobiol. Sci.*, vol. 18, no. 8, pp. 1877–1909, 2019.
- [121] Y.-Y. Huang, S. Sharma, J. Carroll, and M. Hamblin, 'Biphasic Dose Response in Low Level Light Therapy An Update', *Dose-Response Publ. Int. Hormesis Soc.*, vol. 9, pp. 602–18, Sep. 2011, doi: 10.2203/dose-response.11-009.Hamblin.
- [122] Y.-Y. Huang, S. K. Sharma, J. Carroll, and M. R. Hamblin, 'Biphasic dose response in low level light therapy—an update', *Dose-Response*, vol. 9, no. 4, p. dose-response, 2011.
- [123] G. L. Flores Luna *et al.*, 'Biphasic Dose/Response of Photobiomodulation Therapy on Culture of Human Fibroblasts', *Photobiomodulation Photomed. Laser Surg.*, vol. 38, no. 7, pp. 413–418, Jul. 2020, doi: 10.1089/photob.2019.4729.
- [124] V. M. Gómez-López and J. R. Bolton, 'An approach to standardize methods for fluence determination in bench-scale pulsed light experiments', *Food Bioprocess Technol.*, vol. 9, pp. 1040–1048, 2016.
- [125] R. Zein, W. Selting, and M. R. Hamblin, 'Review of light parameters and photobiomodulation efficacy: dive into complexity', *J. Biomed. Opt.*, vol. 23, no. 12, p. 1, Dec. 2018, doi: 10.1117/1.JBO.23.12.120901.
- [126] J. Shen, X. Tao, D. Ying, and C. Hui, 'Side-emitting Properties of POFs with Surface Patterns in Bent Woven Fabrics', *Open. Address PolyU Pres.*, p. 235, 2011.

- [127] N. Voudoukis and S. Oikonomidis, 'Inverse Square Law for Light and Radiation: A Unifying Educational Approach', *Eur. J. Eng. Technol. Res.*, vol. 2, no. 11, Art. no. 11, Nov. 2017, doi: 10.24018/ejeng.2017.2.11.517.
- [128] Z. Liu, S. Liu, K. Wang, and X. Luo, 'Status and prospects for phosphor-based white LED packaging', *Front. Optoelectron. China*, vol. 2, pp. 119–140, 2009.
- [129] Y. Jeon *et al.*, 'A Wearable Photobiomodulation Patch Using a Flexible Red-Wavelength OLED and Its In Vitro Differential Cell Proliferation Effects', *Adv. Mater. Technol.*, vol. 3, no. 5, p. 1700391, 2018, doi: 10.1002/admt.201700391.
- [130] Y. Jeon, H. R. Choi, K. C. Park, and K. C. Choi, 'Flexible organic light-emitting-diode-based photonic skin for attachable phototherapeutics', *J. Soc. Inf. Disp.*, vol. 28, no. 4, pp. 324–332, 2020, doi: 10.1002/jsid.882.
- [131] H. Kim, M. J. Kim, Y. W. Kwon, S. Jeon, and S. Lee, 'Benefits of a Skull-Interfaced Flexible and Implantable Multilight Emitting Diode Array for Photobiomodulation in Ischemic Stroke', vol. 2104629, pp. 1–16, 2022, doi: 10.1002/advs.202104629.
- [132] J. H. Lee *et al.*, 'Wearable Surface-Lighting Micro-Light-Emitting Diode Patch for Melanogenesis Inhibition', *Adv. Healthc. Mater.*, vol. 12, no. 1, p. 2201796, 2023, doi: 10.1002/adhm.202201796.
- [133] K. Liu, H. Chen, Y. Wang, M. Wang, and J. Tang, 'Wearable Flexible Phototherapy Device for Knee Osteoarthritis', 2021.
- [134] S. Y. Lee *et al.*, 'Combinatorial wound healing therapy using adhesive nanofibrous membrane equipped with wearable LED patches for photobiomodulation', *Sci. Adv.*, vol. 8, no. 15, p. eabn1646, Apr. 2022, doi: 10.1126/sciadv.abn1646.
- [135] T.-Y. Lee *et al.*, 'Technology and applications of micro-LEDs: their characteristics, fabrication, advancement, and challenges', *Acs Photonics*, vol. 9, no. 9, pp. 2905–2930, 2022.
- [136] Y. Huang, E.-L. Hsiang, M.-Y. Deng, and S.-T. Wu, 'Mini-LED, Micro-LED and OLED displays: present status and future perspectives', *Light Sci. Appl.*, vol. 9, no. 1, p. 105, 2020.
- [137] Z. Chen, S. Yan, and C. Danesh, 'MicroLED technologies and applications: characteristics, fabrication, progress, and challenges', *J. Phys. Appl. Phys.*, vol. 54, no. 12, p. 123001, 2021.
- [138] 'A Wearable Photobiomodulation Patch Using a Flexible Red-Wavelength OLED and Its In Vitro Differential Cell Proliferation Effects Jeon 2018 Advanced Materials Technologies Wiley Online Library'. Accessed: Dec. 23, 2022. [Online]. Available: https://onlinelibrary.wiley.com/doi/pdf/10.1002/admt.201700391

- [139] S. Choi, Y. Jeon, J. H. Kwon, C. Ihm, S. Y. Kim, and K. C. Choi, 'Wearable Photomedicine for Neonatal Jaundice Treatment Using Blue Organic Light-Emitting Diodes (OLEDs): Toward Textile-Based Wearable Phototherapeutics', *Adv. Sci.*, vol. 9, no. 35, p. 2204622, 2022, doi: 10.1002/advs.202204622.
- [140] B. R. L. de Aguiar, E. N. S. Guerra, A. G. C. Normando, C. C. Martins, P. E. D. dos Reis, and E. B. Ferreira, 'Effectiveness of photobiomodulation therapy in radiation dermatitis: A systematic review and meta-analysis', *Crit. Rev. Oncol. Hematol.*, vol. 162, p. 103349, Jun. 2021, doi: 10.1016/j.critrevonc.2021.103349.
- [141] J. Robijns *et al.*, 'Photobiomodulation therapy for the prevention of acute radiation dermatitis in head and neck cancer patients (DERMISHEAD trial)', *Radiother. Oncol.*, vol. 158, pp. 268–275, May 2021, doi: 10.1016/j.radonc.2021.03.002.
- [142] J. Robijns *et al.*, 'Prevention of acute radiodermatitis by photobiomodulation: A randomized, placebo-controlled trial in breast cancer patients (TRANSDERMIS trial)', *Lasers Surg. Med.*, vol. 50, no. 7, pp. 763–771, 2018, doi: 10.1002/lsm.22804.

Chapter 3. Bioinspired mechanoreceptors with turnable pressure threshold

3.1. Introduction

The previous chapter examined different types of the input device for pressure sensation, and their limitations on wearable applications. Thereby, a stable, and flexible input device with diverse pressure thresholds is in demand to the development of the novel pressure sensation, and HMI. This can provide a more direct, convenient, and stable interaction, and sensation between electronic systems, and users for wearable applications. In this chapter, we have developed a fabric-based mechanoreceptor with a novel structure to bionic the working mechanism of human skin mechanoreceptors. This structure can control the mechanoreceptor with different pressure thresholds to fit different applications, ensuring a good on-off ratio (1*10*8), and reliable performance under repeated compressions (>40000 cycles). We have also investigated its mechanism, and the interrelationship between the pressure threshold of the mechanoreceptors, and the structural parameters of the insulation layer, such as the material filling rate, height of the structure, and material modulus. This relationship offers a valuable insight for the design, and fabrication of the mechanoreceptors to achieve the desired specific pressure threshold. In addition, this fabric-based mechanoreceptor was also evaluated from different aspects to hold significant potential for use in wearable healthcare devices.

3.2. Experimental Design

This chapter is dedicated to the development of a single mechanoreceptor with a turnable pressure threshold suitable for various wearable applications. To achieve this, a novel structure of the mechanoreceptor was designed, fabricated, and characterized. Furthermore, this study investigates the interrelationship between the design parameters of the

mechanoreceptors, and their corresponding pressure thresholds to facilitate tunability, a feature critical for practical applications. This investigation reveals that the pressure threshold of the mechanoreceptor can be adjusted through a range of parameters, rather than being constrained to a single factor. Given the multiplicity of controllable dimensions, the processing requirement associated with any specific dimension can be reduced by exploiting the synergistic effects of multiple dimensions, including area material filling rate, PDMS height, PDMS modulus, TPU adhesion size, and compression area. Overall, the experimental work described in this chapter is segmented into several phases: design, fabrication, characterization, and analysis of the factors influencing the pressure threshold of the mechanoreceptors. The framework for the experimental work is illustrated in **Figure 3-1**.

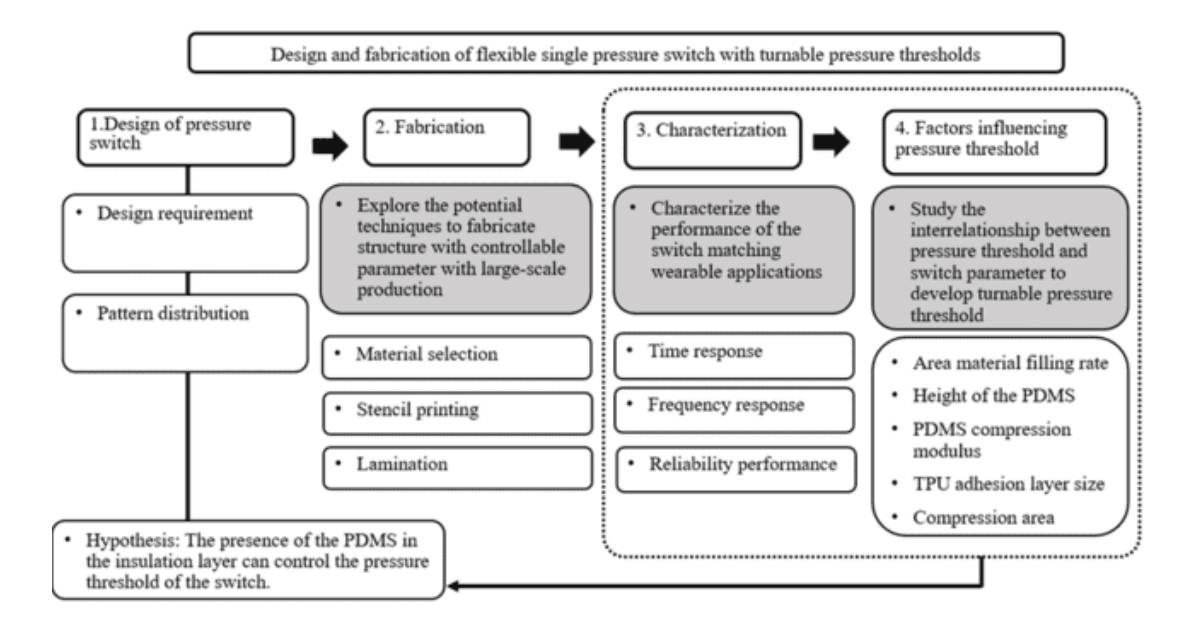


Figure 3-1. Research framework.

3.3. Preliminary study

Prior to conduct systematic experiments, and analysis, we undertook preliminary research to inform the design of the mechanoreceptor for turnable pressure threshold. These involved the initial material selection for fabrication, assessment of the fabrication technique,

and exploration about the impact of various structural parameters on the pressure threshold of the mechanoreceptor.

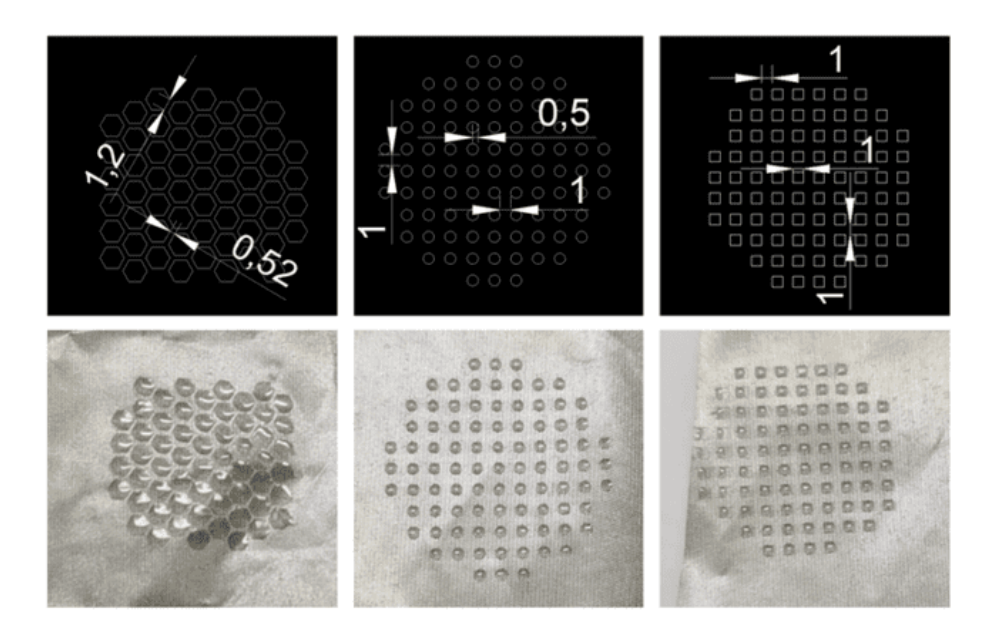


Figure 3-2. Image of the printed PDMS pattern.

First, we hypothesized that the structure fabrication within the insulation layer of the mechanoreceptor have an impact on its pressure threshold. For the structure within the insulation layer, PDMS were firstly selected as the material for its elastic deformation, and formability. The formability of the PDMS was firstly evaluated. A stencil with various patterns was fabricated via laser cutting. PDMS was then stencil printed onto the conductive fabric. The image in **Figure 3-2** proved PDMS printing applicability. In the process, it was observed that the viscosity of the PDMS influencing the printing quality. PDMS with limited pot life was good to printing, which viscosity is more controllable with time. In addition to printability, the formation of the insulation layer between the conductive fabric was assessed. The presence of the PDMS structure between the conductive fabric formed a gap between the electrodes, fabricating a pressure sensitive mechanoreceptor. As shown in **Figure 3-3**, the mechanoreceptor resistance can be decreased under compression. One challenge is that the mechanoreceptor is easy to be short circuit due to the softness of the conductive fabric. To

avoid this, additional shell material should be required.

In addition, we also explored the encapsulation materials, including PDMS, and TPU membrane. For PDMS, it is challenge to control the flowability in the solidification process, and it can easily to cause a short circuit. TPU adhesion layer flowability, and melting can be controlled via the lamination temperature, pressure, and time. We also investigated the effects of TPU films with various thickness, and the melting temperature to the fabrication process of mechanoreceptor. TPU membrane with low melting temperature in the lamination process tends to flow, and deform quickly, which brings a challenge to the formation of the insulation layer. There is also a higher risk of short circuit because the deformed TPU may adhere upper, and lower electrode together. Under the consideration of the usage scenario, and fabrication process, we decided to use TPU with relative high lamination temperature as the adhesion layer in the latter studies.



Figure 3-3. Image of the fabric-based mechanoreceptor on-off resistance.

On the other hand, a preliminary test was conducted to evaluate the impacts of PDMS patterns in insulation layer on the pressure threshold of the mechanoreceptor. A stencil was fabricated with different circle patterns. The impact of the pattern on pressure threshold was evaluated, as shown in **Figure 3-4**. The result proved that the pressure threshold can be

controlled through patterning in the insulation layer. However, circular pattern deformation was more, and the area filling rate was worse than that of square pattern. In further studies, square pattern would be used.

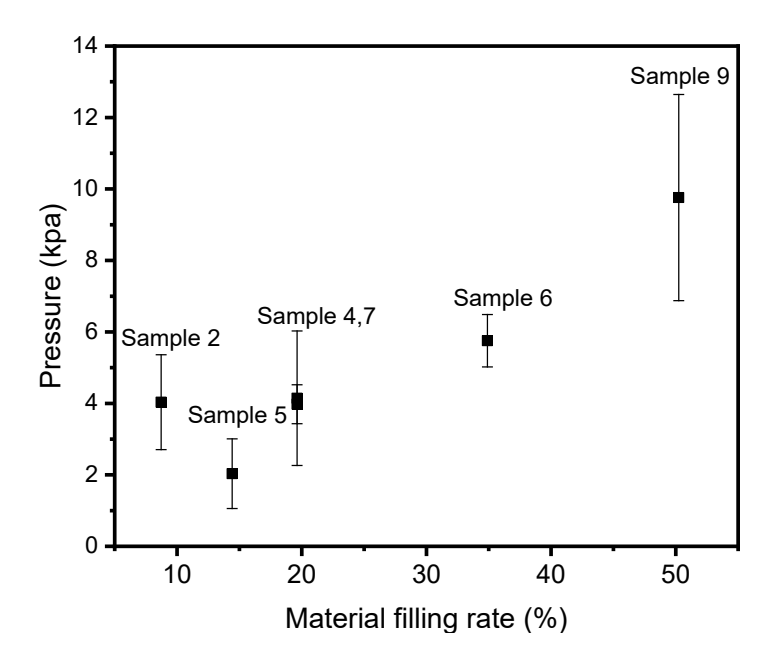


Figure 3-4. Interrelationship between PDMS material filling rate, and measured pressure threshold.

Above preliminary study mainly focuses on the feasibility of the fabricating pattern in the insulation layer to control the mechanoreceptor pressure threshold, and explore the material compatibility in the fabrication process. Further studies will be conducted to improve the design of the flexible mechanoreceptor, and fully evaluate its performance on different aspects.

3.3.1. Design of the mechanoreceptor

Throughout the preliminary studies, the controllability of PDMS pattern in the insulation layer was put in practice to discuss its pressure threshold turnability. Based on the result of the preliminary studies, we have improved that the pressure threshold of the flexible mechanoreceptor can be controlled via designing its structure. **Figure 3-5** demonstrates the

exploded structure of the flexible mechanoreceptor. It comprises of total six layers in the following order: composite fabric, electrode, TPU spacer, PDMS structure, electrode, and composite fabric. In the context of the mechanoreceptor's structure, the insulation layer is the critical layer to its functionality. The insulation layer in this structure is positioned between the electrodes, includes TPU spacer, and PDMS structure. Conventional mechanoreceptor insulation layer only consists of a film spacer with hole, and lack of any supporting unit[1], [2]. The pressure threshold of the mechanoreceptor is only relied on the material rigidity of the electrode, and input setting, like size of compression, and key design[2]. Therefore, the pressure threshold of the mechanoreceptor is limited, covering only the range of 1 to 3 N (GB/T 30091-2013). In this novel flexible mechanoreceptor, the inclusion of the elastic supporting elements in the insulation layer can control its pressure threshold in a wide range, not only relying on the rigidity of the electrode. The wide range of controllable pressure threshold explores its potential application on wearable applications.

The pressure threshold of the mechanoreceptor is in relation to the elastic microstructure between the electrodes. Therefore, it is essential to research the techniques producing controllable, and reproducible microstructure at low cost. PDMS were selected as the material for microstructure because of its advanced stability, easy processing, and shaping properties. There are many researches focusing on fabricating different microstructure in the field of sensors, like moulding, electrospinning, and substrate stretching[3]. Moulding is the common technique, wherein the mold can directly use commercial or biological materials, like sandpaper[4], lotus leaf[5], salt, and sugar[6], or fabricating with lithography techniques[7]. However, using these materials as mold faces the challenge of unreproducible microstructure, and the microstructure cannot be controlled in different sizes. The mold fabricated from lithography is expensive, and requires specialized equipment. Therefore, other techniques fabricating reproducible, and controllable structure need to be explored.

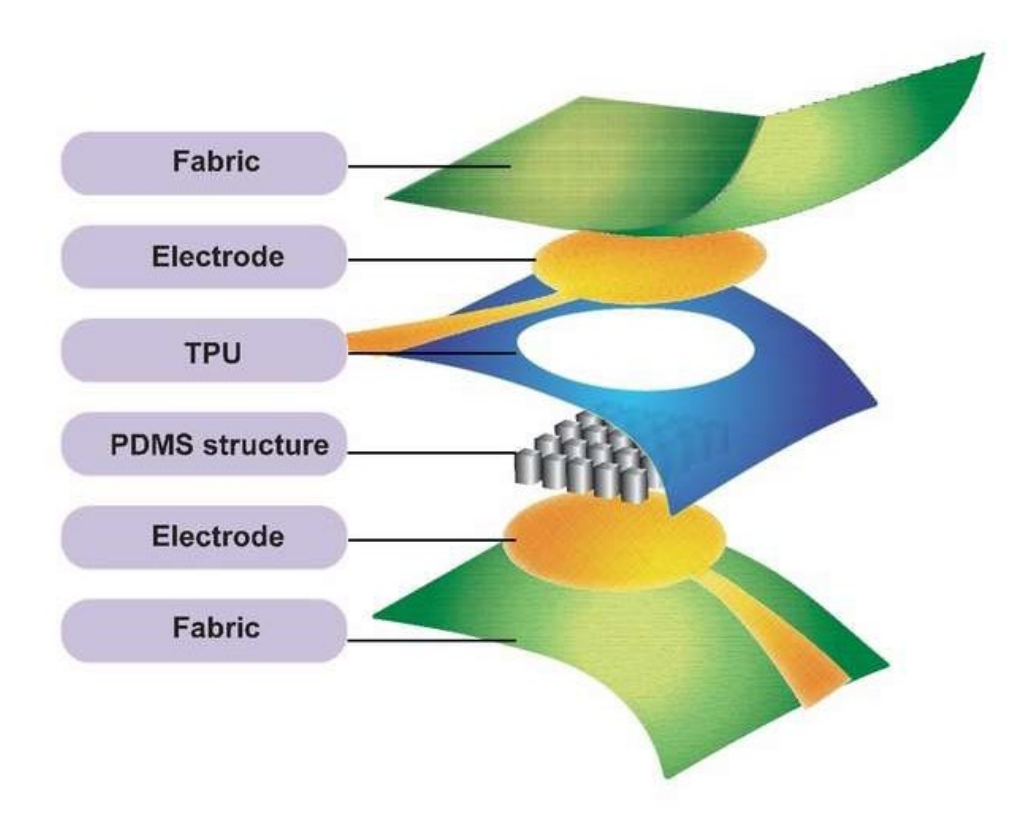


Figure 3-5. A schematic illustration of the structure of textile-based mechanoreceptor.

Stencil printing is a standard cost-effective approach to deposit solder paste in the surface mounting of electronics. In the process, a blade was used to press viscous materials through pre-defined aperture in a solid foil on a substrate. Stencil printing does not require massive equipment or high qualified techniques. The stencil can be fabricated by UV laser cutting with high precision. Considering these, adopting stencil printing to fabricate microstructure onto the electrode is a potential way. In the preliminary study, we only proved that the applicability of the stencil printing for PDMS structure. However, further research is required to control, and analyse the quality of the printing patterns.

3.4. Experiment

The preceding section outlines an overview of preliminary study on fabric-based mechanoreceptors. This session introduces the parameters of the selected materials, fabrication

process, characterization techniques, and the details of the structural parameters' studies related to PDMS, with the aim of comprehensively study the fabric-based mechanoreceptor.

3.4.1. Materials and Tools

Table 3-1. Materials and tools.

Material/Tool	Source				
Conductive fabric	Zhiyuan Xiangyu Functional Fabrics Co., Ltd.				
PDMS: Dragon 20	Smooth-On Inc.				
PDMS: Ecoflex 00-30	Smooth-On Inc.				
PDMS: Smooth-Sil 940	Smooth-On Inc.				
PDMS: Smooth-Sil 960	Smooth-On Inc.				
TPU membrane	Jinda Plastic Insulation Co.,Ltd				
Fabric	Jiaxing Yingcheng Textile Co., Ltd.				
Stencil	Botong SMT laser steel Co.,Ltd				

The mechanoreceptor is composed of composite fabric as shell, electrode, and insulation layer, which insulation layer includes PDMS structures, and TPU spacer.

The electrode of the mechanoreceptor used conductive fabric from Zhiyuan Xiangyu Functional Fabrics Co., Ltd. It is polyester fabric coated with nickel, copper, and nickel in order. The thickness of the conductive fabric is 0.03 mm, and its electrical conductivity is 6.56 mΩ /cm⁻² by ST-2558C multifunction digital four-probe tester. The conductive fabric was cut out in desired shape (circle 20 mm in diameter with an output electrode) via laser cutting.

The PDMS structure was fabricated using various types of PDMS. The PDMS types include Ecoflex 00-30, Dragon skin 20, Smooth-Sil 940, and Smooth Sil 96 from Smooth-On Inc. Their harnesses are 5A, 20A, 40A, and 60A, respectively. For Dragon skin 20, and Ecolfex 00-30, the PDMS mixing proportion is 1:1, while the crosslink ratio for the other two types is 1:10.

TPU membrane was from Jinda Plastic Insulation Co., Ltd, with a thickness of only 0.1 mm. The suggested melting temperature is in the range of 90-100 °C.

3.4.2. Fabrication of the mechanoreceptor

Figure 3-6 illustrates the whole fabrication process of the textile-based mechanoreceptor. It was start on the design, and fabrication of the stencil. Different patterns were designed using Autocad, and then used to fabricate the corresponding stencil through laser cutting. Next, PDMS was prepared. Dragon skin 20 PDMS was mixed up in the ratio of 1:1, and waited to reach the desired viscosity for around 30 mins. PDMS was poured onto the stencil to imprint the corresponding pattern onto the conductive fabric, followed by solidification at room temperature. After printing, the conductive fabric with PDMS microstructure was laminated onto the composite fabric at 120°C for 3s. This process was repeated again on another electrode without PDMS structure. Then, a TPU membrane was cut with a hole (16 mm in diameter), and applied onto the laminated electrode, followed by another lamination at 85°C for 3s. Finally, the two sets of electrodes were placed face to face to laminate with the help of a stencil at 85°C for 3s. The PDMS structure was located between two layers

of conductive fabric, as insulation layer.

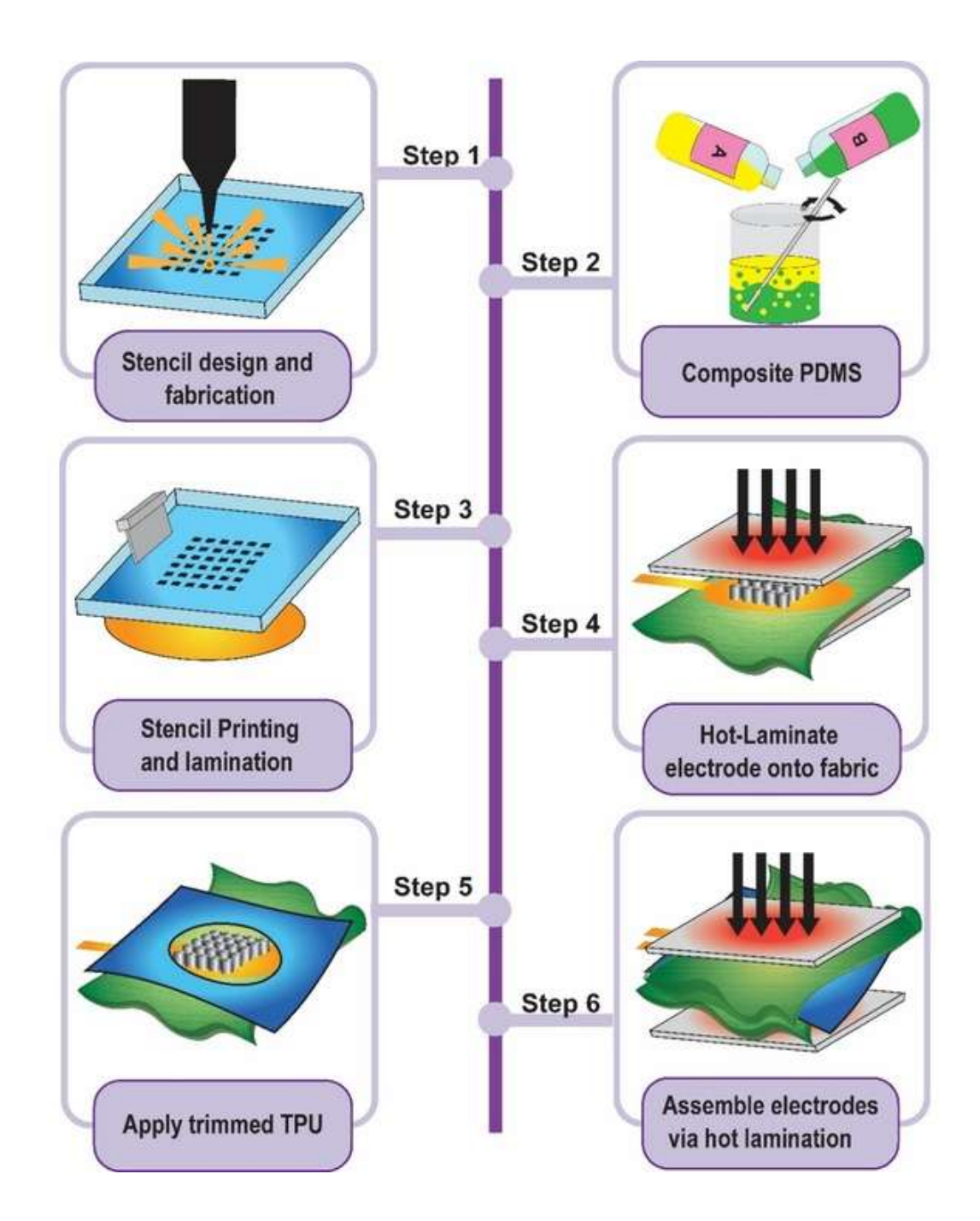


Figure 3-6. A schematic illustration of the fabrication of the textile-based mechanoreceptor.

3.4.3. Surface and structural characterization

Optical microscopy (Leica M165C, Leica Microsystems Ltd., Hong Kong) was utilized to evaluate the surface of the conductive fabric, and measure the structural dimensions of the

PDMS structure after printing. In addition, it was used to observe the cross-section of the mechanoreceptor to study its mechanism. A digital display thousandth thickness gauge (Sanliang Measuring Tools Co., Ltd., China) was used to measure the thickness of conductive fabric, composite fabric, TPU membrane, and the mechanoreceptor.

3.4.4. Evaluation of the mechanoreceptor

The electromechanical performance of the mechanoreceptor can be evaluated in different terms, includes on-off ratio, pressure threshold, time response, frequency response, and reliability of the mechanoreceptor under different conditions, such as repeated compressions, and laundry.

The on-off ratio of this textile-based mechanoreceptor was measured by a multimeter (F101, Fluke corporation), and a RK2681N insulation resistance tester from Shenzhen Meiruike Electronic Technology Co., Ltd. In details, the off-state resistance was measured by the electrical insulation tester because its lower detection limit is $10 \text{ k}\Omega$. The on-state resistance of the mechanoreceptor was measured by the multimeter because it upper limit is only $120 \text{ M}\Omega$. Through using these devices, the overall performance of the on-off ratio of the mechanoreceptor was evaluated.

The mechanoreceptor's pressure threshold, time response, frequency response, and reliability under repeated compressions were tested using a power source, an Agilent 34401a multimeter, and Instron 5566 Universal Testing Machine. The detailed set-up was illustrated in **Figure 3-7**. In these tests, the Instron 5566 was used to generate, and applied compression force to the mechanoreceptor, with a fixed compression region (10 mm in diameter). The power source provided the electrical signal to the mechanoreceptor, and then the electrical performance of the mechanoreceptor was monitored by the multimeter in connection to

computer for real-time monitoring, and analysis. For the internal connection, the positive electrode of the mechanoreceptor was connected with the positive electrode of the power source, while the negative electrode of the mechanoreceptor was connected to the positive electrode of the multimeter. Furthermore, the negative electrode of the power source connected to the negative electrode of the multimeter. In the test, it was observed when the pressure exceeded the pressure threshold of the mechanoreceptor, the voltage may rise to the settled value (0.3 or 0.2 V). By monitoring the voltage response, the mechanoreceptor electrical performance in response to the different mechanical input signals could be investigated. Specially, the compression stress provided by the Instron 5566 was settled at 10 kPa in time response, frequency response, and repeated compression test.

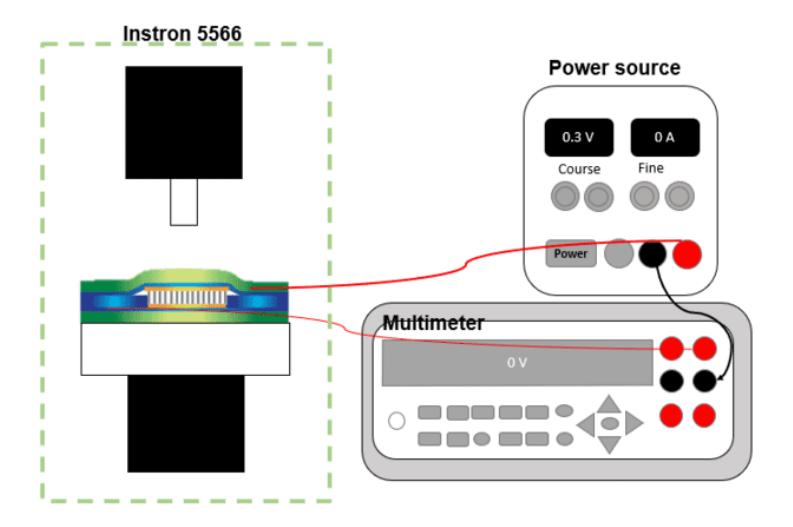


Figure 3-7. A schematic diagram of the experiment set-up of the electromechanical characterization.

3.4.5. Reliability test with laundry cycles

Besides evaluating the electrical mechanical performance of the mechanoreceptor, we also investigated the mechanoreceptor stability under repeated laundry processes. The laundry process was conducted based on the standard of AATCC LP1 Home laundry: Machine washing.

The test used 1.8 kg laundering ballast pieces, and 66 g AATCC standard laundry powder with a commercial laundry machine. The electrical performance, include off-state resistance, and the mechanical response of the mechanoreceptor throughout the 20 cycles of laundry were verified. The experiment set-up was followed the procedures outlined in the previous session 3.2.4.

3.5. Results and Discussion

In the experimental analysis, we firstly compared the dimensions of the printed PDMS to the design to discuss the potential of stencil printing in structural fabrication. Then, the mechanism, and the performance of the mechanoreceptor were studied. We also conducted a comprehensive analysis to discuss the effects of structural parameters of the insulation layer on the pressure thresholds of the mechanoreceptor.

3.5.1. PDMS structure evaluation

In the experiment, we designed, and fabricated stencils with different patterns, and used them to stencil print PDMS onto the conductive fabric to assess the possibility of using stencil printing to print reproducible PDMS pattern.

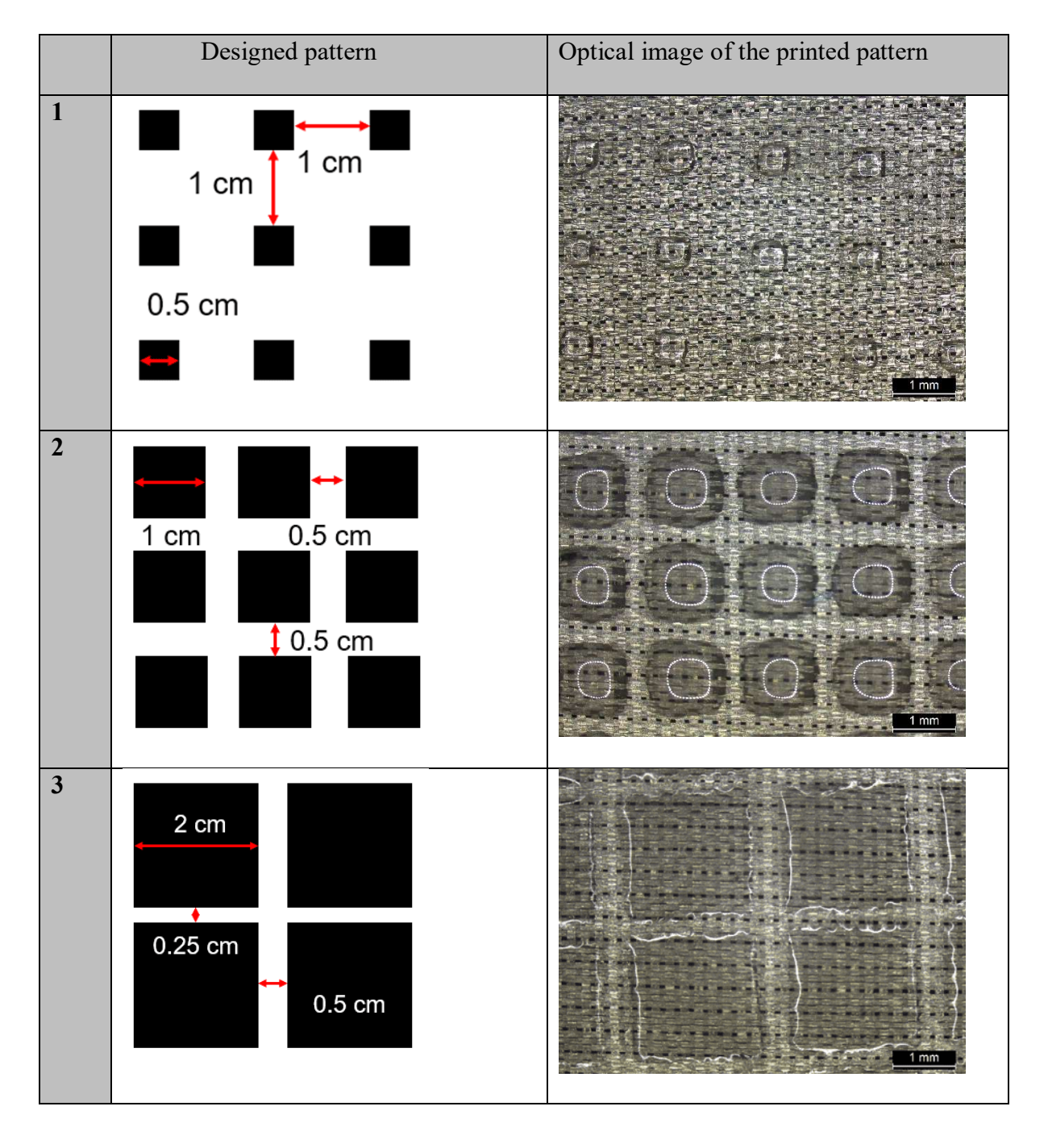


Table 3-2. Design, and optical image of the PDMS structure.

Table 3-2 illustrates the optical images of the stencil printed PDMS structures on the conductive fabric. The designed pattern 1 square dimension is 0.5 mm, while the distance between squares is 1 mm. The actual size of the PDMS structure after printing is 0.53 mm (SD: 0.03), while the horizontal distance between squares is 0.98 mm (SD: 0.021), and distance in

vertical is 0.96 mm (SD: 0.021). The designed pattern 2 square dimension is 1 mm, while the distance between squares is 0.5 mm. The actual size of the PDMS structure after printing is 1.23 mm (SD: 0.038), the horizontal distance is 0.24 mm (SD: 0.034), and the vertical distance is 0.29 mm (SD:0.021). The designed pattern 3 square dimension is 2 mm, while the horizontal distance between squares is 0.5 mm, and the vertical distance is 0.25 mm. The actual size of the PDMS structure after printing is 2.01 mm (SD: 0.011), the horizontal distance is 0.435 mm (SD: 0.05), and the vertical distance is 0.18 mm (SD: 0.028).

Through comparing the dimension of the squares to the designed pattern, it can be observed that the printed pattern may slightly (1%-23%) larger than the designed pattern. In addition, the printed pattern is not perfect square, in which the edge is blurred, and no sharp angles. This may be caused by the flowability of the PDMS. After stencil printing, PDMS retains a certain degree of fluidity. The printed PDMS pattern may expand to the non-printed area during the solidification period.



Figure 3-8. Image of the deformed mechanoreceptor.

In addition, the stencil printing in the laboratory is hand-held, making it difficult to control the pressure, and the printing speed, and the squeegee angle. These factors are key elements to the printing quality. Further studies can be conducted to control the printed pattern

quality. One possible improvement involves integrating a heating device at an automatic stencil printing for on-time solidification. However, even there is a variation between the printed pattern, and design, the printed pattern can be reproducible, and large-scale produced in an efficient, and low-cost way in stencil printing.

Finally, we fabricated the corresponding mechanoreceptor based on the patterned structure. The fabricated mechanoreceptor thickness is only 0.455 mm (SD: 0.014), showing good deformability. It can be bend by a squeezer, as shown in **Figure 3-8.**

3.5.2. Mechanism of the mechanoreceptor

This novel mechanoreceptor has good on-off ratio due to this unique structure. We have explored its mechanism with the evidences from optical images of the cross-section of mechanoreceptor. The mechanism of this textile mechanoreceptor is based on the piezoresistive sensor with architecture microstructure.

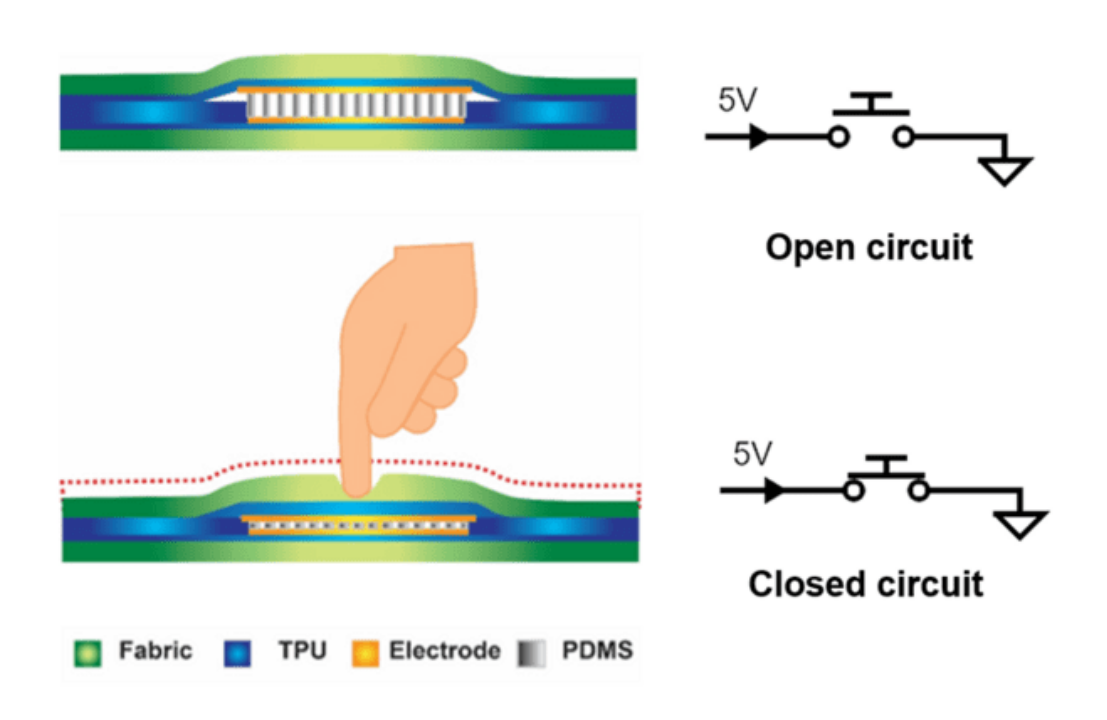
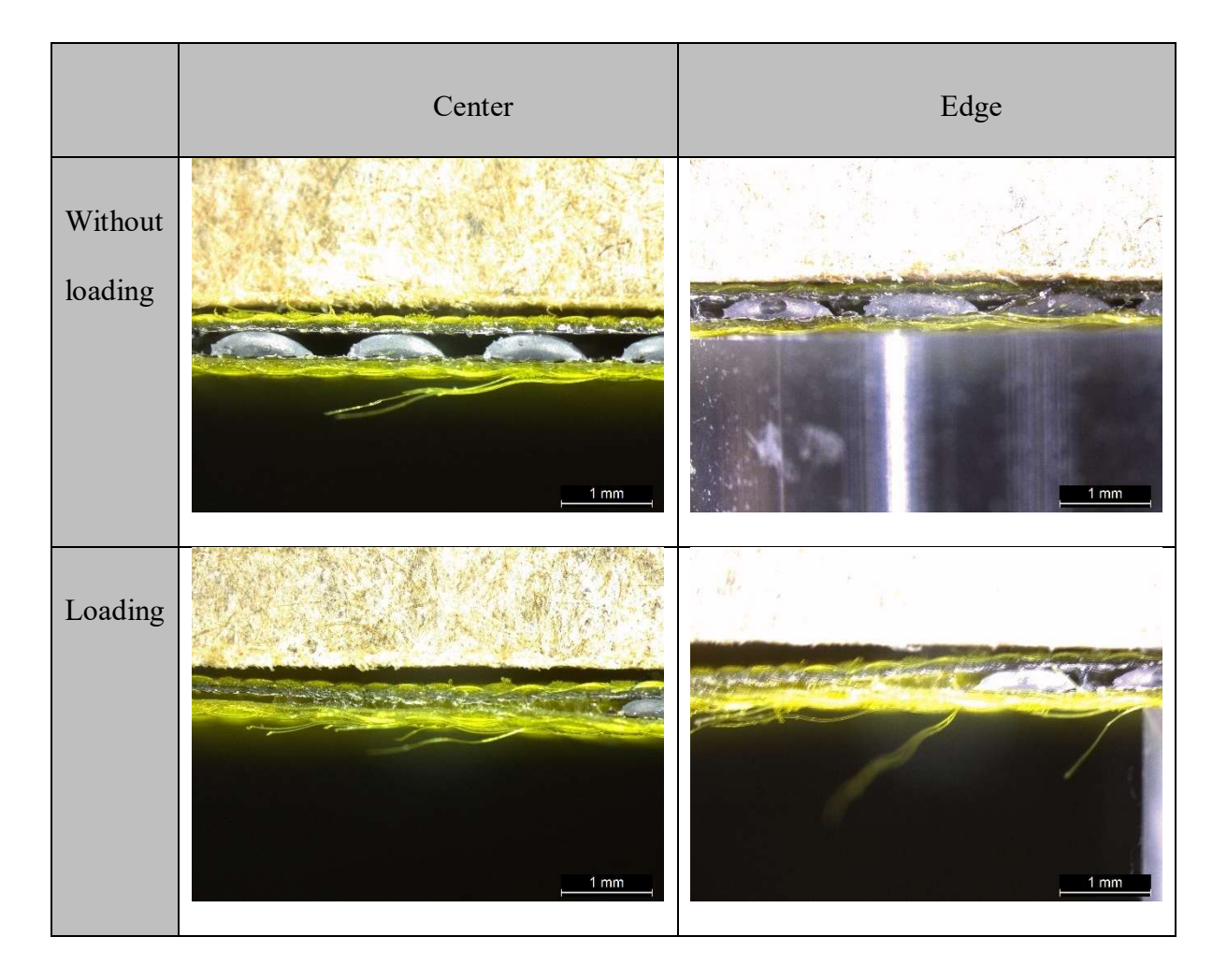


Figure 3-9. A schematic diagram about the cross-section of the mechanoreceptor, and the corresponding electric diagram.

Table 3-3. Optical image of the cross-section of mechanoreceptor with or without loading.



In **Figure 3-9**, the presence of TPU spacer, and PDMS pillars creates many small voids between the electrodes, as insulation layer. Without compression, the upper electrode may separate with the lower electrode, as open circuit, and "off-state". When compressed, the PDMS pillars firstly deform, decreasing in height, and increasing in width, while the total volume of the PDMS remains constant. It indicates PDMS fillers may take part of the void. As the PDMS deforms, the thickness of the insulation layer may decrease in consequence. As the compression force continuously increases, the upper electrode may pull downward, and in contact with the lower electrode as a closed circuit (**Figure 3-9**). A conductive path is formed, and the resistance decreases sharply, as "on-state". The pressure threshold of the

mechanoreceptor is defined as the compression pressure value at which the resistance of the mechanoreceptor decreases sharply. When the pressure is relieved, the PDMS pillars may recover to their original shape. This can support the upper electrode back to its original position, and separating with lower electrode, forming an opened circuit. The recovery of the mechanoreceptor is not only relied on material rigidity, and also related to the PDMS pillars. We comprehensively evaluated the cross-section of this textile-based mechanoreceptor with or without loading via optical microscopy.

In Table 3-3, the total thickness of mechanoreceptor from optical image is measured at 0.69 mm (SD: 0.02), the thickness under loading is 0.423 mm (SD: 0.009). The PDMS height at the center of the mechanoreceptor is 0.274 mm (SD: 0.018), while the pillars deform to 0.217 (SD:0.016) under loading. This matches to the mechanism as the PDMS pillars deform under compression. In addition, it can be observed that after PDMS deformation, the upper electrode may in contact with the bottom electrode. At the edge of mechanoreceptor, the TPU spacer thickness is 0.091 mm (SD: 0.002), while TPU spacer thickness is similar. Therefore, PDMS pillars may deform under the loading, in response to its mechanism.

3.5.3. On-off ratio

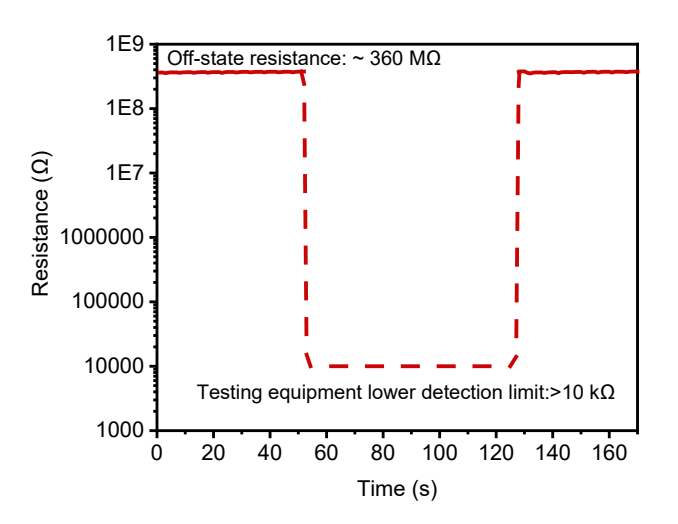




Figure 3-10. (a) On-off resistance of the mechanoreceptor (Insulation resistance tester). (b) Image of the off resistance of the mechanoreceptor under pressing.

On-off ratio is the key parameter to the functionality of the mechanoreceptor, indicating the ratio between on-state, and off-state. High on-off ratio is essential to effectively distinguish the input signal to control the overall system. In addition, it can improve the signal-to-noise ratio, sensitivity, and control efficiency. Hence, a flexible mechanoreceptor with high on-off ratio is preferred.

Under the compression of Instron 5566 machine, the off-state resistance of the single mechanoreceptor is higher to 360 M Ω (Figure 3-10 (a)). However, its on-state resistance shows zero on the screen because the lower detection limit of the machine is 10 k Ω . Based on this, we used a normal multimeter to measure the on-state resistance, as shown in Figure 3-10 (b). The on-state resistance was only 3.3 Ω under pressing. The on-off difference can be higher to eight orders of magnitudes (10⁻⁸). This level on-off ratio can be comparable to commercial products. The off-state resistance of these novel mechanoreceptor exhibits a certain degree of variations, with some samples off-state resistance is at giga ohm level. This can be attributed

to the structure, and fabrication process. In the fabrication process, the PDMS structure only fixed onto the lower electrode. Due to the lack of adhesion between the upper electrode, and PDMS structure, there exists a certain degree of freedom for the electrode to move upward. The separation distance between the lower, and upper electrode is longer, in conjunction with thick insulation layer in the structure, may contribute to a high off-state resistance. However, even there is a variation to the off-state resistance, the overall off-state resistance is in hundreds of megaohm level, comparable to commercial products.

3.5.4. Response time and Recovery time

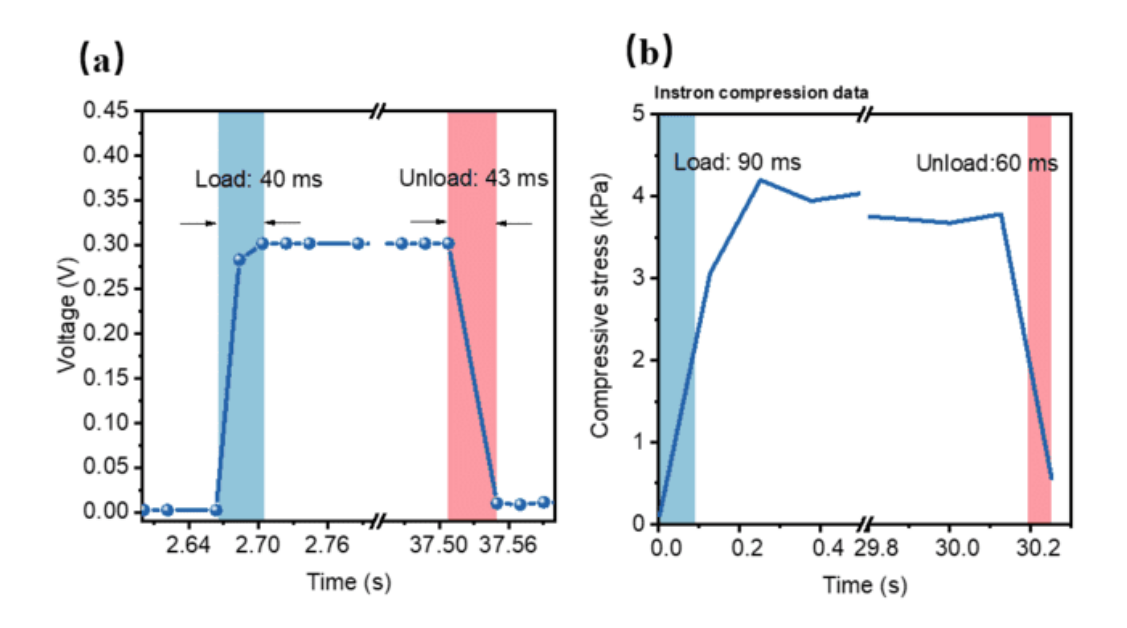


Figure 3-11. (a) Response time, and recovery time of the pressure mechanoreceptor,, and (b) corresponding Instron compression data.

Response time is defined as the time required for the mechanoreceptor react to a pressure stimulus. Faster response time is important to the operation efficiency, signal integrity, energy efficiency, safe, and reliability. For example, the mechanoreceptor with faster response time can transmit the state on time to minimize the delay. We measured the response time, and recovery time of the mechanoreceptor. **Figure 3-11 (a)** shows that the response time of the

mechanoreceptor is 40 ms, while the recovery time of the mechanoreceptor is 43 ms. The response time surpasses that of the majority of flexible mechanoreceptors, and resistive sensors commonly used as input devices. Compare to the response time, the recovery time is longer than that of around 7.5% because of the PDMS viscoelastic properties. Under recovery, the PDMS process some delayed time-dependent recovery after the relieve of compression stress. In addition, the delayed recovery may vary among the mechanoreceptors with different pressure thresholds.

3.5.5. Frequency response

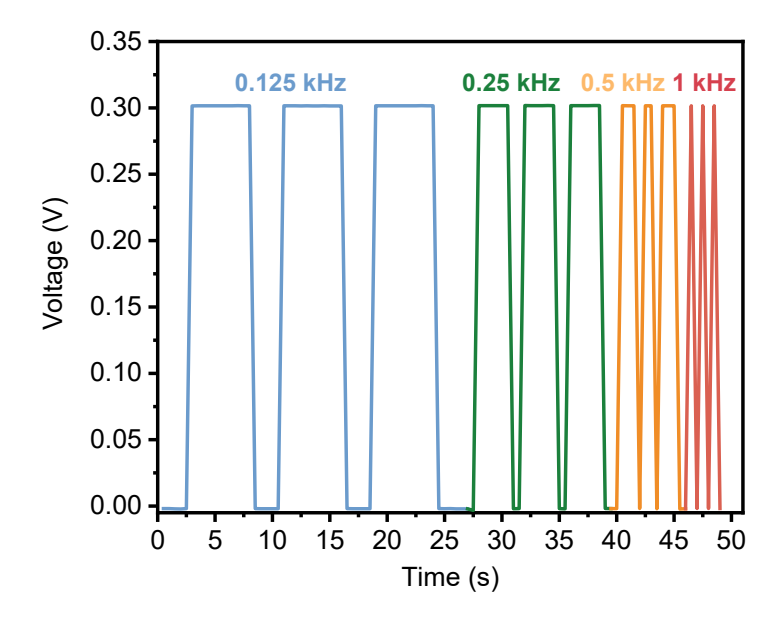


Figure 3-12. Frequency response of the mechanoreceptor.

Considering the diversity of the usage scenario, the mechanoreceptor needs to be responded on time. Frequency response provide insights into how quickly, and accurately the mechanoreceptor can detect the output signal. We have evaluated the frequency response of the mechanoreceptor under different frequency of compressions. From **Figure 3-12**, it can find out that the voltage of the mechanoreceptor can be changed under different frequency of compressions. In this experiment, the highest frequency is 1 kHz because the sampling

frequency of the multimeter is limited to 400ms. This frequency performance can be appropriate to most of gait or pressure applications, like normal walking step frequency is around 1.8 Hz. For health monitoring applications, like respiration, and heart-beat, further studies need to be conducted. However, the frequency response is partially limited by its delayed response time. Due to this, the frequency response of the mechanoreceptors may vary with its pressure threshold.

3.5.6. Reliability of mechanoreceptor

3.5.6.1. Repeated compressions

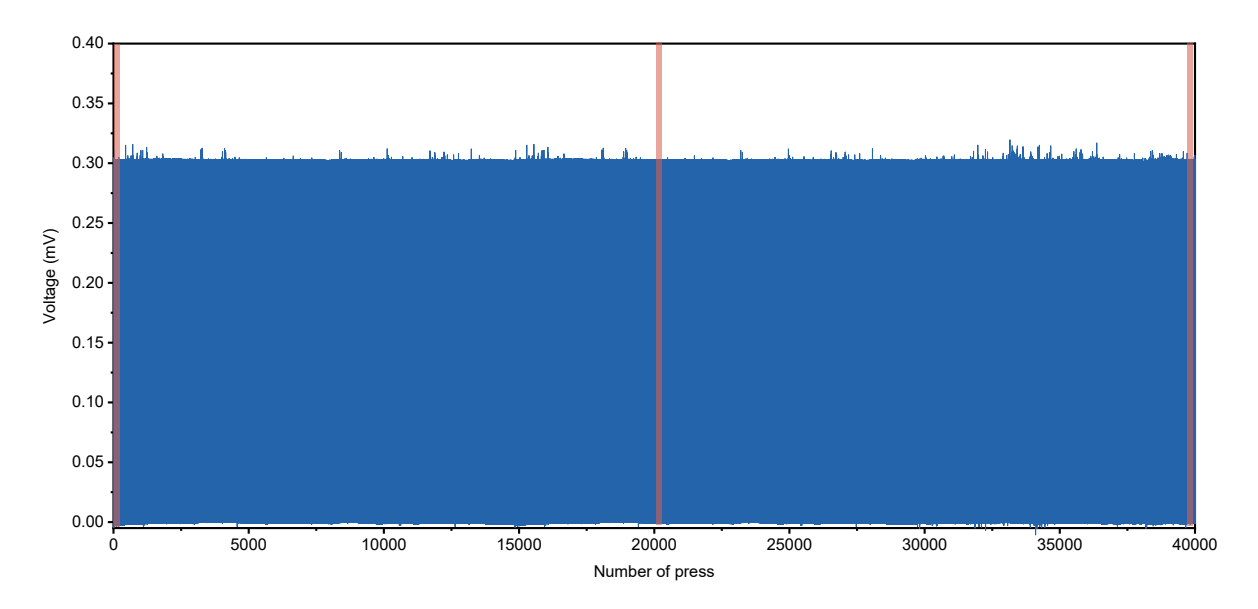
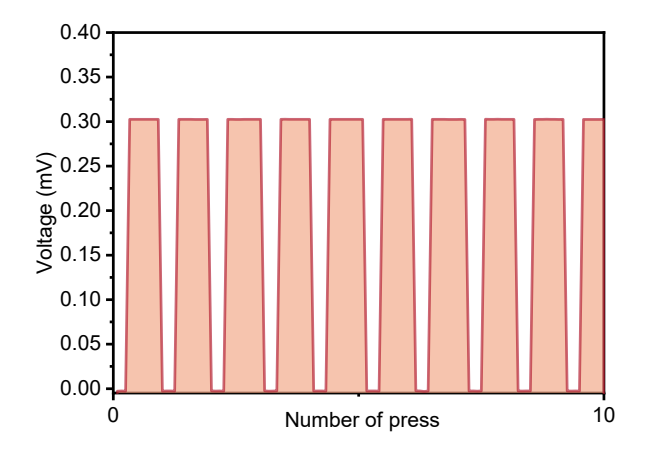


Figure 3-13. Voltage of the mechanoreceptor under 40000 compressions.

For wearable application, stability, and reliability of the mechanoreceptor are the most important parameters for its practical, and long-term application. This can ensure consistent functionality, user comfort, safe, and energy efficiency. We conducted over 400000 compression cycles, as shown in **Figure 3-13**. From the overall graph, it can find out that more noise occurred with the increase of the compression times, but the mechanoreceptor off-state, and on-state can be maintained. There was no short circuit or open circuit after 40000

compression cycles. In summary, there is a deterioration on the mechanoreceptor stability after 40000 compression cycles, but within a controllable range.

We conducted detailed analysis on the voltage response of the mechanoreceptor at 1 cycle, 20000 cycle, and 39550 cycle (**Figure 3-14-3-17**). It was obvious that number of cycles of in these figures is larger than 10 cycles because the compression cycles calculation is based on the data collection point of the first compression cycles. As the recovery time of the mechanoreceptors is longer than the response time, additional time is necessary to achieve full recovery from the PDMS deformation. The compression of the Instron machine is heavily dependent on the positional movement of the load cell. Consequently, the data collection points may be reduced at the late period, leading to an increase in the number of compression cycles.



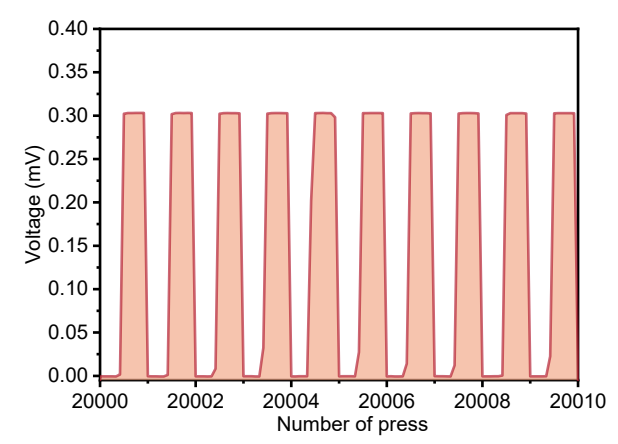
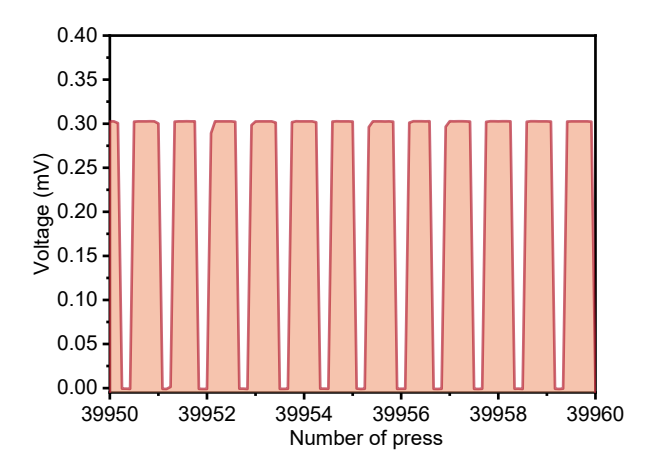


Figure 3-14. Voltage response at 1-10 cycles.

Figure 3-15. Voltage response at 20000 cycles.



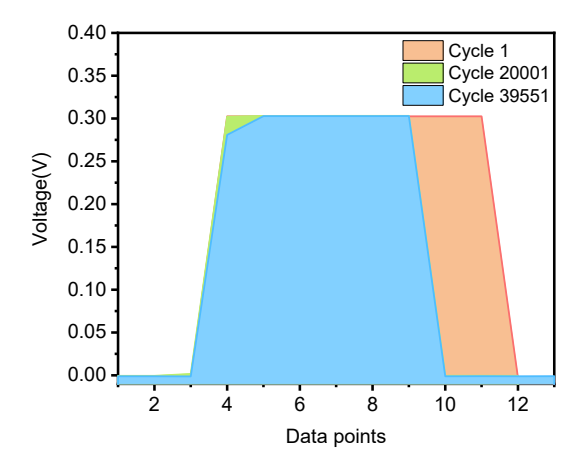


Figure 3-16. Voltage response at 39550 cycles.

Figure 3-17. Voltage response of cycle 1, cycle 20001, and cycle 39551.

In Figure **3-20**, it is evident that the on-state period of cycle 20001, and cycle 39501 is longer than the initial period. Furthermore, the response of cycle 39501 requires more time for stabilization. This can be attributed to the viscoelastic nature of PDMS, as the molecular chains gradually reorganize, and adjust after repeated compressions, leading to prolonged stabilization times, and extended on-state periods.

3.5.6.2. Laundry

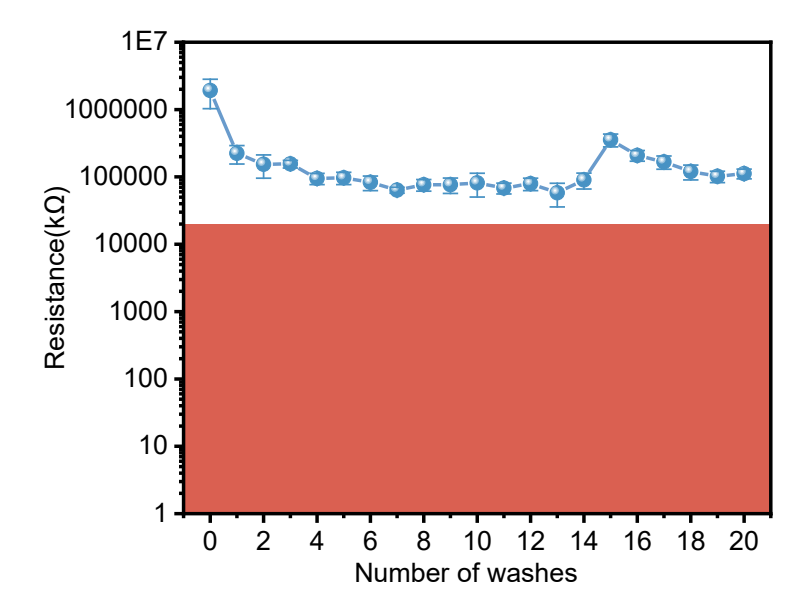


Figure 3-18. Off-state resistance of the mechanoreceptor throughout 20 washing cycles.

In the context of wearable applications, the reliability of mechanoreceptors in laundry settings is a critical consideration due to potential chemical, mechanical, and water-related damage. Based on this, we conducted total 20 cycles of laundries to examine its reliability from the aspect of off-state resistance, and electromechanical performance. In **Figure 3-18**, the off-state resistance of the mechanoreceptor throughout 20 laundry cycles can be kept at above 20 $M\Omega$ (shaded area), which meet the qualified level in the GB/T 30091-2013 standard in usages. In details, the off-state resistance of the array can be higher to Giga ohm at initial. After washing, the off-state resistance may decrease to Mega ohm level, and remain at around 100 $M\Omega$. However, a slight recovery at 15 cycles was observed, attributed to the extended recovery duration (5 days) during holidays. This indicates that eight hours of flat drying is not enough to recover the mechanoreceptors after washing. In addition, it was observed that the humidity

of the environment may influence the recovery of off-state resistance.

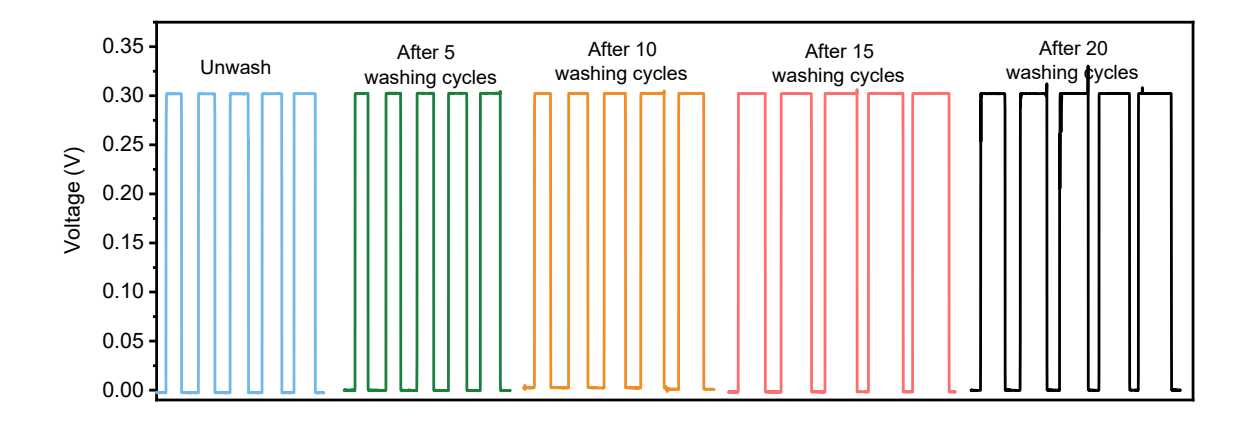


Figure 3-19. Electromechanical performance of the mechanoreceptor throughout 20 washing cycles.

Figure 3-19 illustrates the electromechanical response of the mechanoreceptor after different cycles of laundries. It is evident that the on-state period under compressions becomes longer as the laundry cycles increases. This implies that the PDMS structure may suffer certain degrees of damage, which compression threshold decreases. The on-off resistance ratio can be maintained. Otherwise, more noise has been occurred, and the off-state voltage condition is also not stable after 20 laundry cycles. This indicates that the PDMS structure were greatly damaged to reduce the stability of the mechanoreceptors. The stability of the mechanoreceptors throughout washing is mainly depended one the adhesion of the PDMS structure onto the electrode. This adhesion is influenced by types of PDMS, and material filling rate.

3.5.7. Factors influencing mechanoelectrical characterization of mechanoreceptor

From the discussion of the mechanism of the mechanoreceptor, it can find out that the PDMS structure plays a significant role in controlling the pressure threshold of the mechanoreceptor. Based on this, we conducted a series of experiments to analysis the influence of the PDMS structure on its pressure threshold, focusing on the material filling rate, height

of PDMS, and PDMS modulus.

3.5.7.1. Material filling rate

Table 3-4. Parameters of the PDMS, and corresponding material filling rate.

	Width	Horizontal Spacing	~ .	No. per	No. per	single		Material filling rate
Unit	mm	mm	mm	/	/	mm^2	/	%
S1	0.50	1.00	1.00	6.67	6.67	0.25	44.44	11.11
S2	0.75	0.75	0.75	6.67	6.67	0.56	44.44	25.00
S3	1.00	1.00	0.50	5.00	6.67	1.00	33.33	33.33
S4	1.00	0.50	0.50	6.67	6.67	1.00	44.44	44.44
S5	1.50	0.50	0.50	5.00	5.00	2.25	25.00	56.25
S6	2.00	0.50	0.50	4.00	4.00	4.00	16.00	64.00
S7	2.00	0.50	0.25	4.00	4.44	4.00	17.78	71.11
S8	3.00	0.50	0.50	3.08	3.08	9.00	9.46	85.18

According to the mechanism of the mechanoreceptor, there is a cavity filled with PDMS structure, as the insulation layer located between the electrodes. PDMS structure greatly influences the pressure threshold of the mechanoreceptor. Since the compression region/compression cavity is fixed, we used a term "material filling rate" to summarize the size, and distribution variation of the PDMS. Material filling rate refers to the ratio of the volume of PDMS filling the cavity to the total volume of the cavity. This can effectively characterize the size, and distribution of the PDMS structure. In details, the size of structure becomes larger, the distance between PDMS structures decreases, the material filling rate then increases, and vice versa. We designed eight types of patterns with different sizes of square, and distribution, and the corresponding material filling rate ware calculated. Details of the structural parameter

are shown in Table 3-4.

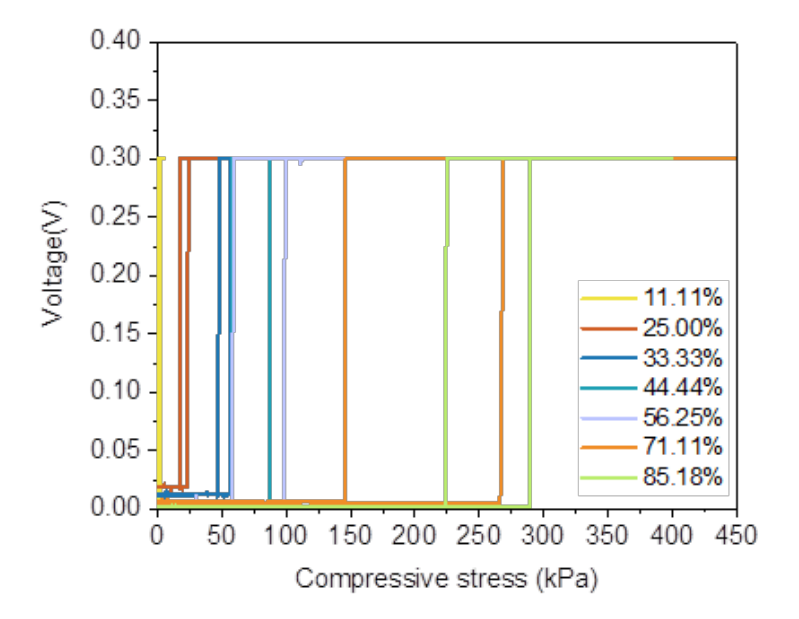


Figure 3-20. Voltage response of the mechanoreceptor versus different material filling rate (0.1 mm in Height, DS 20).

Based on the pattern, we fabricated a series of mechanoreceptors with different material filling rates. Then, the interrelationship between the material filling rate, and the pressure threshold of the mechanoreceptor was analysed. In **Figure 3-20**, as the compression stress continuous increases over a certain threshold, the mechanoreceptor may change to on-state, and the voltage increase sharply, forming a rectangular shape in the graph. In details, the lowest material filling rate of the mechanoreceptor is 11.11%, its pressure threshold can be lower to 3.12 kPa, as the material filling rate increase 44.44%, the corresponding pressure threshold also increases to 77.69 kPa; the material filling rate increases to 71.11%, the pressure threshold also increases to 276.26 kPa.

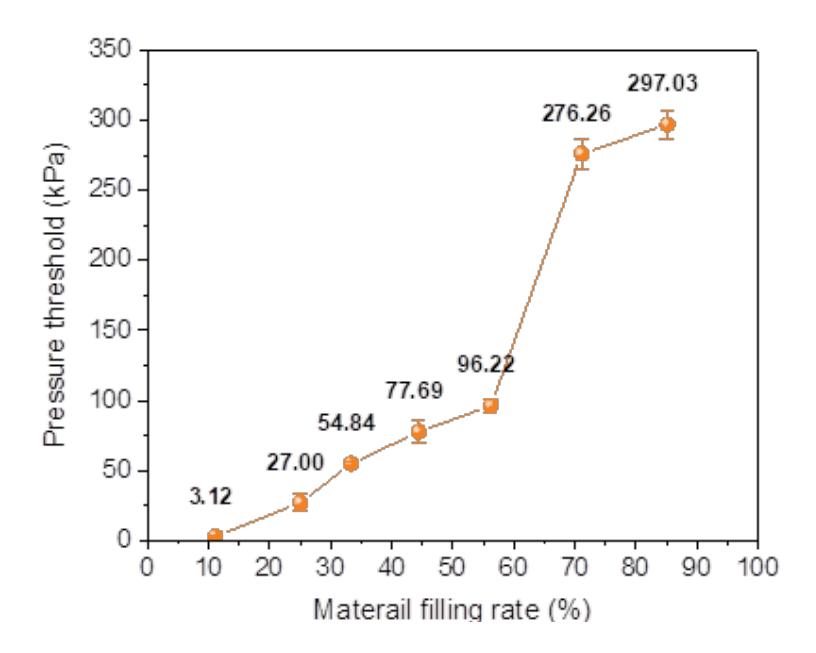


Figure 3-21. Interrelationship between material filling rate, and the pressure threshold of mechanoreceptor (0.1 mm in Height, DS 20).

Figure 3-21 summarizes the interrelationship between pressure threshold, and the material filling rate of the mechanoreceptor. As the material filling rate increases, the pressure threshold increases non-linearly. The difference of the pressure threshold between the material filling rate of 71.11, and 85.18% is only 20.77 kPa. We can magnify at a small cross-section area of the mechanoreceptor to analysis the functionality of the mechanoreceptor. These can be simplified as a three-point bending, in which the supporters are two PDMS structure, and the specimen for bending is a composite containing composite fabric, and conductive fabric. At final compression, the upper electrode may contact the lower electrode, which indicates that the deflection of the centre is fixed (The perpendicular distance of the bending is fixed). Based on the bending moment equation, the distance between PDMS supporter decreases, the bending moment may increase, and then the compression force finally increases.

3.5.7.2. Stencil thickness

Table 3-5. Thickness measurement of the PDMS.

Stencil thickness	Height	Standard variation		
mm	mm	/		
0.1	0.118	0.009		
0.15	0.156	0.004		
0.2	0.212	0.014		
0.25	0.255	0.006		
0.3	0.328	0.026		

Besides the variation of the structure varies in two dimensions, the structure dimension also can be varied in three dimensions. Stencils with different thickness (0.1 mm, 0.15 mm, 0.2 mm, 0.25 mm, and 0.3 mm) were fabricated. Corresponding mechanoreceptors with the same material filling rate were fabricated, and tested to investigate the interrelationship between the height of the structure, and the pressure threshold of the mechanoreceptor. The height of the PDMS pillars was matched to the designed stencil, while there is a variation in the height among samples. In details, the thickness of PDMS structure is 0.118 mm (SD: 0.009) with a 0.1 mm thick stencil. The thickness of the structure is 0.328 mm (SD: 0.026) with 0.3 mm thick stencil. Printing variation increases with the stencil thickness, hence the control of the PDMS structure becomes challenge with thicker stencil. These can be attributed to the printing pressure, temperature, and the viscosity of the PDMS during printing. This height variation indicates that the printed pattern (material filling rate) also has variation among samples. These variations may deteriorate the sample variation in pressure threshold. The pressure thresholds of the mechanoreceptors may have relatively large variations.

In **Figure 3-22**, the pressure threshold of the PDMS with 0.1 mm thick stencil is 54.84 kPa, while the pressure threshold increases 214.29 kPa as the stencil thickness is 0.15 mm, and then the pressure threshold increases to 428.82 kPa as the stencil thickness is 0.2 mm. The pressure threshold is 1173.23 kPa as the stencil thickness is 0.25 mm, and increase to 1466.78 kPa as the stencil thickness is 0.3 mm.

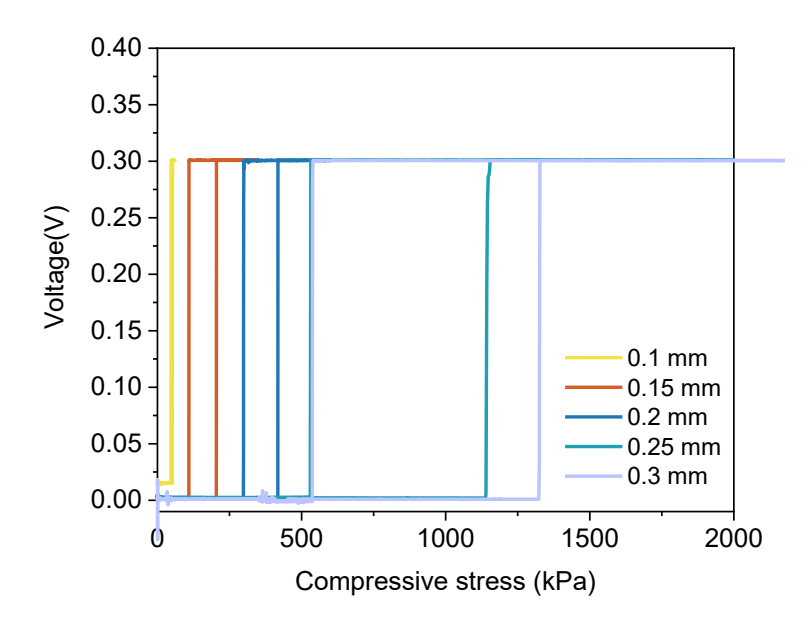


Figure 3-22. Voltage response of the mechanoreceptor versus different height of stencil (Area material filling rate: 33.33%, DS 20).

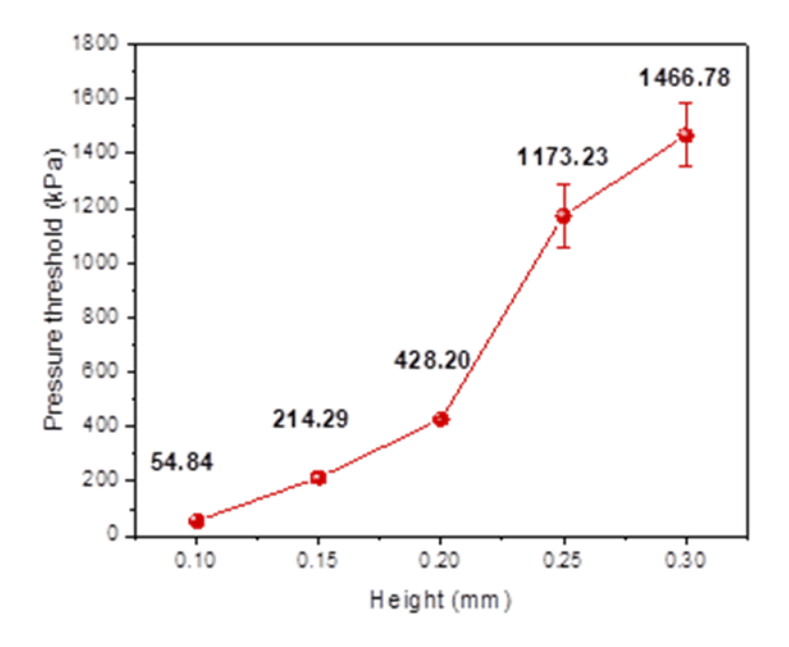


Figure 3-23. Interrelationship between stencil thickness, and the pressure threshold of mechanoreceptor (Area material filling rate: 33.33%, DS 20).

Figure 3-23 illustrates the overall relationship between the height of the PDMS structure, and the pressure threshold. As the height of the PDMS increases, the pressure threshold also increases. The increase in the pressure threshold of the mechanoreceptor is a result of multiple factors. Similar to the previous analysis, only a small part of the

mechanoreceptor was simplified as a three-point bending structure. The increase in the height of the PDMS indicates the perpendicular distance between the specimen (composite fabric, and conductive fabric), and the lower electrode. As the height of the PDMS structure increases, the bending curvature may become larger, leading to a higher bending moment, and ultimately, the compressive stress may increase. Additionally, as the height of the PDMS structure increases, the deformation of the PDMS also increases, indicating that the contact area of the PDMS to the electrode increases. This may decrease the distance between the two PDMS squares as supporters. Considering the three-point bending, the decrease in the distance between supporters also increases the bending moment, and then increases the compressive stress. Consequently, the corresponding pressure threshold of the mechanoreceptor may increase.

3.5.8. Hardness of PDMS

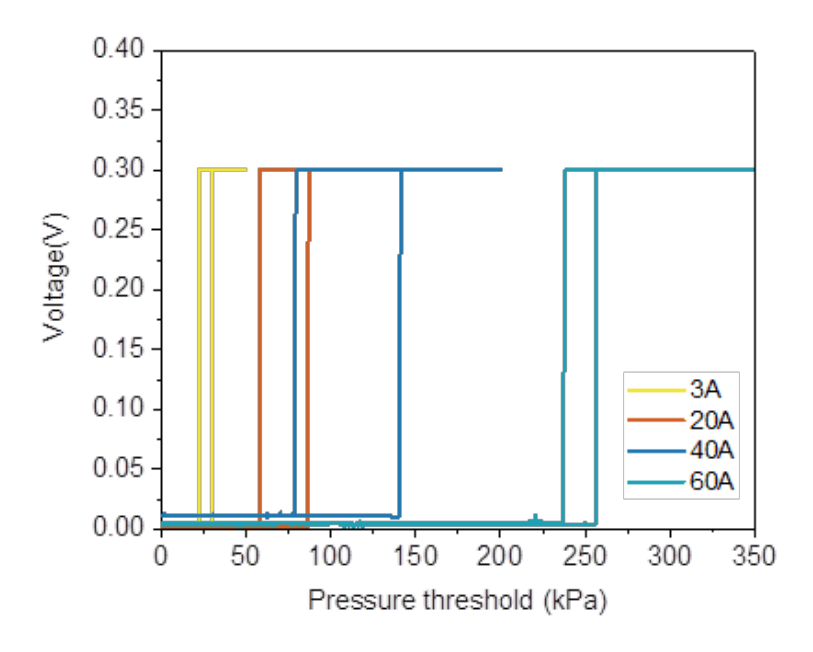


Figure 3-24. Voltage response of the mechanoreceptor versus different modulus PDMS.

Besides changing the dimension of the PDMS, we also can used different types of PDMS to adopt the pressure threshold of the mechanoreceptor. PDMS with different young's modulus or shore hardness were used to study the effect of material modules on the pressure

threshold of the mechanoreceptor. In **Figure 3-24**, the mechanoreceptor using PDMS with 3A shore hardness characterize with 34.48 kpa pressure threshold, the pressure threshold using 10A increase to 77.69 kPa, the pressure threshold then increased to 248.24 kPa using the 60A shore hardness PDMS.

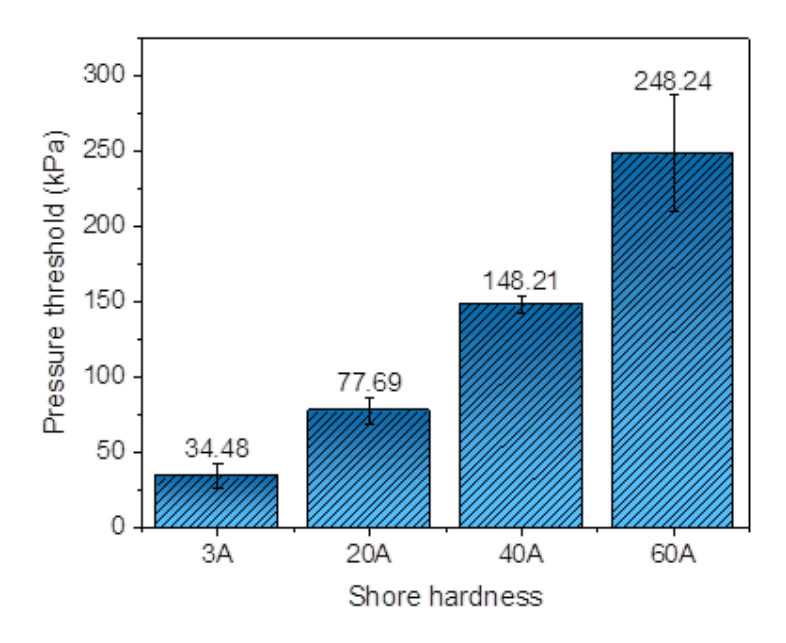


Figure 3-25. Interrelationship between the pressure threshold, and PDMS modulus (0.1mm in height, Area material filling rate: 44.44%).

Figure 3-25 summarizes the interrelationship between the material modulus, and the pressure threshold of the mechanoreceptor. As the shore hardness of the PDMS increases, the pressure threshold of the corresponding mechanoreceptor also increases. The relationship is linear. For example, the different between 20A, and 40A share hardness PDMS is 2 times, while the pressure threshold of the mechanoreceptor is 1.91 times.

The increase of the pressure threshold is mainly depended on the deformation requirement of the PDMS. The pattern, and height of the PDMS inside the mechanoreceptor being the same, the on-state condition of these textile mechanoreceptors is also the same. The composite fabric, and electrode need to pull to the same position for conduction. This implies

that the PDMS structure with various heights needs to deform to a certain level at which the upper electrode, and lower electrode may contact each other. If the compression modulus of PDMS is higher, more load is required to deform the PDMS to the "on-state", and vice versa. In addition, the poison ratio of the PDMS also can affect the pressure threshold. Hard PDMS may deform less, thereby the distance between PDMS structures reduce less, and the compressive stress can be reduced. Since the change of the distance between PDMS is limited by the poison rate, the effect of the distance between structures on pressure threshold is limited. Previous test also proved that the increase of the material filling rate (smaller distance between structure) only increases the pressure threshold of the mechanoreceptor in tens of kpa. In summary, the modulus of the PDMS is significant in controlling the pressure threshold to different pressure threshold, while material filling rate is more appropriate for precise control.

3.6. Conclusion

In summary, a novel textile-based mechanoreceptor was fabricated, in which insulation layer embedding PDMS structure to support the upper electrode to control its pressure threshold for various applications. This novel structure demonstrates a good on-off ratio, exceeding eight orders of magnitudes. In addition, the interrelationship between the pressure thresholds, and the structural parameter of PDMS, including material filling rate, height of the PDMS structure, and the material modulus, have been explored. In details, increasing material filling, or height of structure, or material modulus, can increase the pressure threshold across different levels, from several kilopascals to hundreds of kilopascals, and even reaching megapascals. This can help to design, and fabricate the mechanoreceptor with various pressure threshold from controlling different parameters, not only limited to the material rigidity.

In addition, the performance of the mechanoreceptors also has been tested

comprehensively. The response time, and recovery time of the mechanoreceptor is 40 ms, and 43 ms. The mechanoreceptor also can respond under 1 kHz compression. The PDMS structure can help the mechanoreceptors to recover under repeated compressions (>40000 cycles). Otherwise, these mechanoreceptors can sustain a number of laundry cycles, with stable offstate resistance and mechanical performance.

While this switch-type mechanoreceptor excels in discrete threshold detection—offering significant advantages in stability, tunability, and durability for applications like activity onset/cessation detection or safety triggers—its operational principle imposes a fundamental limitation: it functions as a binary (on/off) sensor. Consequently, it cannot provide continuous pressure monitoring or quantify gradient pressure information.

This limitation renders it unsuitable for health-monitoring scenarios requiring continuous magnitude measurement, such as gait analysis, tissue interface pressure mapping, or vital sign monitoring (e.g., pulse waveform acquisition). Therefore, future work should explore integrating this robust threshold-sensing mechanism with complementary analog-sensing elements to create hybrid systems capable of both discrete triggering and continuous pressure quantification.

3.7. References

- [1] P. H. Dietz, B. Eidelson, J. Westhues, and S. Bathiche, 'A practical pressure sensitive computer keyboard', in *Proceedings of the 22nd annual ACM symposium on User interface software and technology*, 2009, pp. 55–58.
- [2] B. Ju *et al.*, 'Inkjet Printed Textile Force Sensitive Resistors for Wearable and Healthcare Devices', *Adv. Healthc. Mater.*, vol. 10, no. 20, p. 2100893, Oct. 2021, doi: 10.1002/adhm.202100893.
- [3] A. J. Cheng *et al.*, 'Recent Advances of Capacitive Sensors: Materials, Microstructure Designs, Applications, and Opportunities', *Adv. Mater. Technol.*, vol. n/a, no. n/a, p.

- 2201959, doi: 10.1002/admt.202201959.
- [4] W. Jia et al., 'Flexible and Highly Sensitive Piezoresistive Pressure Sensor with Sandpaper as a Mold', *Nano*, vol. 14, no. 07, p. 1950081, Jul. 2019, doi: 10.1142/S1793292019500814.
- [5] Y. Wan *et al.*, 'A Highly Sensitive Flexible Capacitive Tactile Sensor with Sparse and High-Aspect-Ratio Microstructures', *Adv. Electron. Mater.*, vol. 4, no. 4, pp. 1–8, 2018, doi: 10.1002/aelm.201700586.
- [6] O. Atalay *et al.*, 'A highly sensitive capacitve-based soft pressure sensor based on a conductive fabric and a microporous dielectric layer', *Adv Mater Technol*, vol. 3, p. 1700237, 2018, doi: 10.1002/admt.201700237.
- [7] S. R. A. Ruth, V. R. Feig, H. Tran, and Z. Bao, 'Microengineering Pressure Sensor Active Layers for Improved Performance', *Adv. Funct. Mater.*, vol. 30, no. 39, Sep. 2020, doi: 10.1002/adfm.202003491.

Chapter 4. Textile-based mechanoreceptor-synaptic array

4.1. Introduction

The proceeding chapter focuses on the design, fabrication, and characterization of a single textile-based mechanoreceptor. It also investigated the interrelationship between pressure thresholds, and the PDMS structural parameters to explore the potential of fabricating mechanoreceptors with various pressure thresholds for wearable applications. However, single mechanoreceptor is limited in their functionality to facilitate pressure sensation, and humanmachine interaction. There is a need to assemble the mechanoreceptors together to realize different functionality. This chapter introduces a textile-based spiral sensor-synaptic array containing a total of 16 keys, with only two output electrodes. In the design, each key is series connected with a resistor. The resistance of each key is different, ranging from 1Ω to $50 \text{ k}\Omega$, with a difference of more than 3 k Ω . The average resistance difference between keys is 3.226 $k\Omega$. The key identification primarily relies on the on-state resistance variation, rather than point scanning. Combining the function of the resistors, and the pressure threshold of the mechanoreceptors, this array can equip with sensation and synaptic function to filter out the noise for efficient information transmission. This approach can avoid the complex connection between the system, and the input device, and does not require complicated algorithms for point identification, resulting in power, and time savings. In addition, this array demonstrates good flexibility, water-repellent properties, and good stability in various environments, including cyclic temperature, high temperature, low temperature, and maximum mechanical load. These performances are comparable to commercial products. Furthermore, the pressure threshold of this textile array is lower than that of the commercial keypad.

4.2. Experimental Design

This chapter is dedicated to develop a textile-based pressure sensor-synaptic array to control the system for various functionality. In the preliminary study, we propose to design the array, select, and fabricate flexible resistors, and search method for a reliable, and stable connections. For array design, we initially studied two commercial keypads- membrane keypad, and rubber keypad.

4.2.1. Study of commercial flexible keypad

In the market, there are generally two types of flexible keypads, namely membrane keypads, and rubber keypads, as depicted in **Figure 4-1**, and **Figure 4-2**. Upon disassembling these two keypads, we conducted a comprehensive study on their material, mechanism, electrode design, and others. **Figure 4-1** illustrates the composition of the rubber keypad. It is obvious that the rubber keypad is composed of a rubber shell and a printed circuit board. Since the core of this keypad is rigid, we focus on another type of keypad in further studies.



Figure 4-1. Photo of the rubber keypad.

The second membrane keypad composition is illustrated in Figure 4-2. It is composed

of a shell layer for aesthetics, and two printed circuit boards. In detail, the printed circuit board is a silver printed circuit on PET film. The pressing area of the film was moulded into a dome shape to achieve displacement in the compression for a good user experience. When the finger presses the key, the upper silver circuit board may deform, from dome shape to flat, in contact with the lower electrode to form a conductive path. In addition, the compression area electrode is in the network to increase the electrical contact area under pressing. There are a total of eight electrodes, of which four are vertical as the upper electrodes, and another four for horizontal as the lower electrode. The total eight electrodes are then in connection with the pin socket connector for data processing, and power supply. In addition, an addition algorithm is required to determine the position of the compressed key.

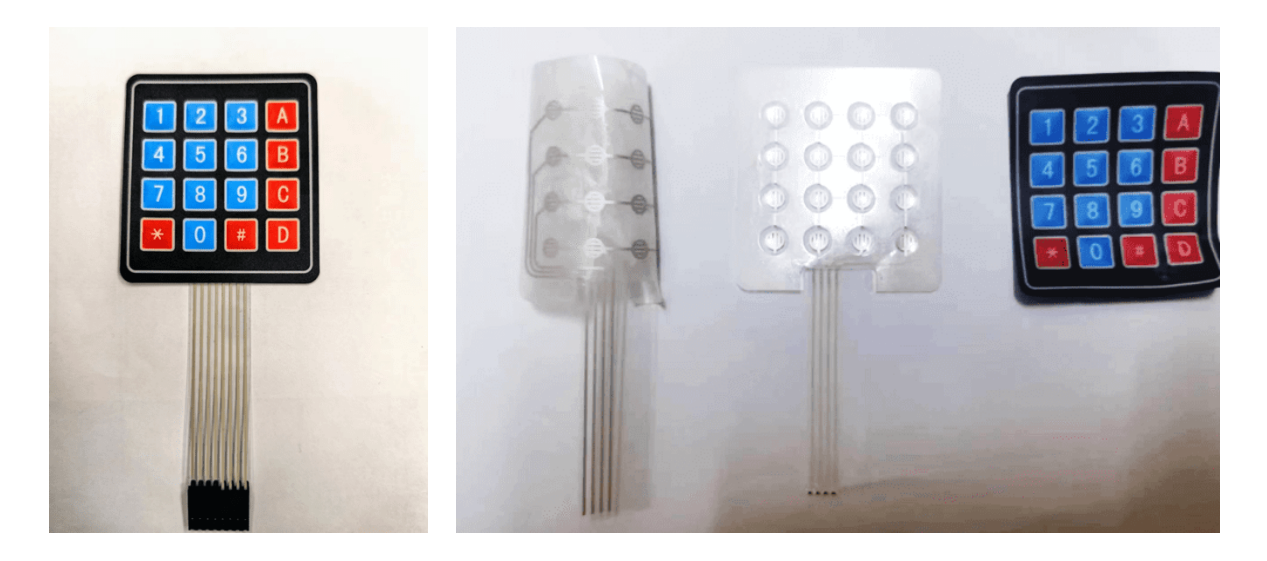


Figure 4-2. Photo of the membrane keypad.

'The thickness of the keypad is 0.871 mm (SD: 0.048), measured by the Sanliang thickness gauge. The weight of the keypad is 0.08 g/cm². However, this keypad flexibility is poor because the molded film needs to possess a certain degree of rigidity to ensure the recovery of the deformation after pressing. It is difficult to deform the keypad, as shown in **Figure 4-3**. Besides, the pressure threshold of this keyboard was tested, which requires around 28.02 kPa (SD: 3.24) for initiation, as shown in **Figure 4-4**. Based on this, it is demanded to

develop a mechanoreceptor-synaptic array with a lower pressure threshold for a good humanmachine interface.



Figure 4-3. Deformation of the membrane keypad.

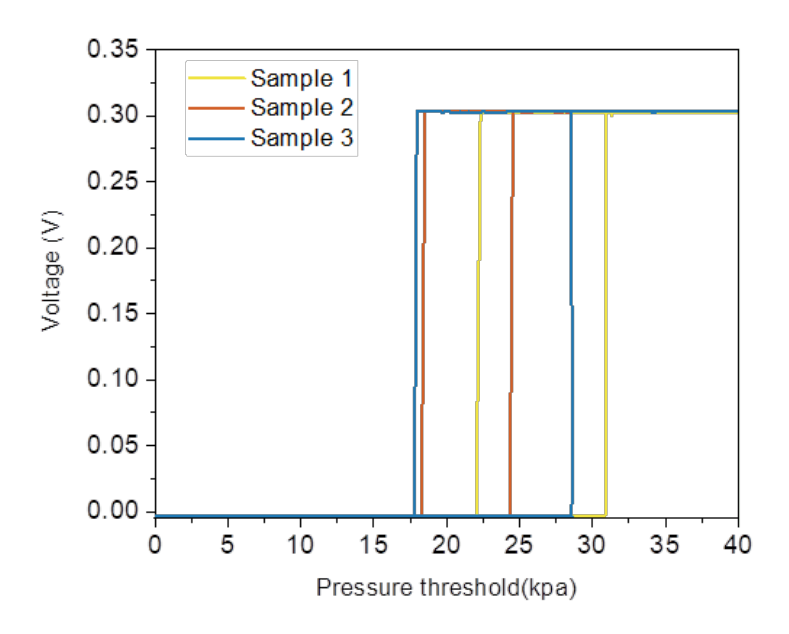


Figure 4-4. Pressure threshold of the membrane keypad.

4.2.2. Textile-based sensor-synaptic array design

To realize effective HMI, a number of pressure mechanoreceptors need to be integrated together to collectively control the electronic system. The current commercial keypad is limited

at the connection, flexibility, and pressure threshold. In addition, a complicated algorithm is in demand for signal processing, which poses challenges in the aspects of energy consumption, and time delay. It is not applicable to wearable applications.

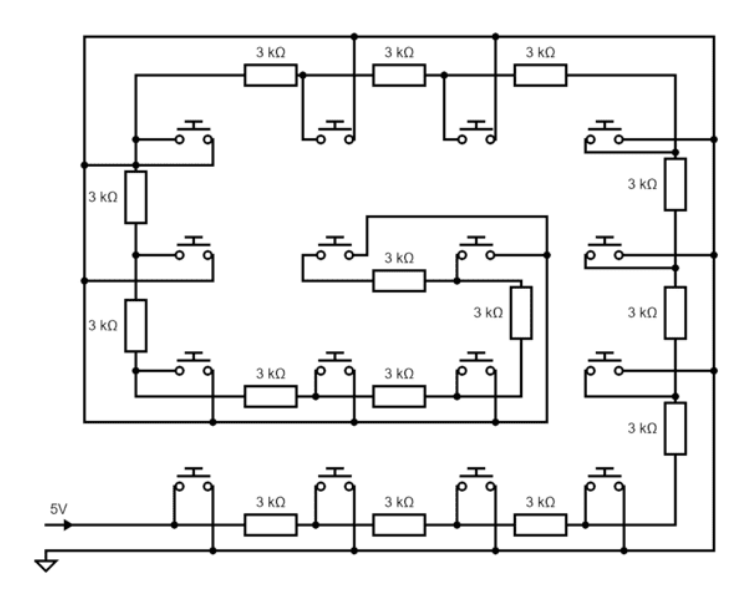


Figure 4-5. Electric diagram of the textile sensor-synaptic array.

Based on this, we designed a spiral shape array consisting of 16 mechanoreceptors, in which every mechanoreceptor is series connected to a flexible resistor. This array only has two output electrodes for charging and data processing. This simplifies the connection between the array, and the system avoiding the breakage of the connection. **Figure 4-5** outlines the electric diagram of the array, in which every mechanoreceptor positive electrode is series connected to a 3 k Ω resistor. As the number of keys increases, 3 k Ω resistance is added to each key resistance. The on-state resistance of each key is different, which ranges from 1 Ω to 45 k Ω . When we press the key, the resistance output of each key is unique, no additional algorithms are needed to determine the pressed key position. The resistance variation of the keys can form different electrical spikes for preliminary data processing. Time and energy can be saved.

Figure 4-6 illustrates the exploded structure of the textile pressure sensor-synaptic

array, which is similar to previous single textile-based pressure mechanoreceptors. It consists of composite fabric for protection, conductive fabric as the electrode, TPU membrane as the adhesion layer, PDMS structure, another set of conductive fabric, flexible resistors, and fabric in order. The component of this mechanoreceptor-synaptic array is made of flexible materials, leading to exceptional flexibility.

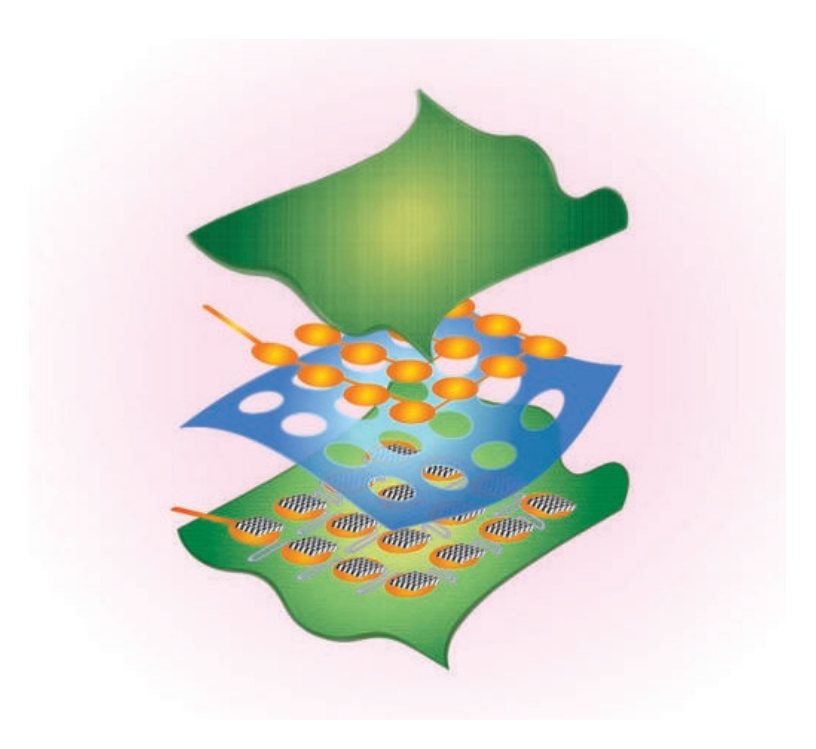


Figure 4-6. Exploded structure of the textile-based sensor-synaptic array.

4.2.3. Preliminary study

Based on the design, this mechanoreceptor-synoptics array is composed of two main components- the textile-based pressure mechanoreceptors, and the flexible resistors. We have comprehensively studied the textile-based pressure mechanoreceptors, while the flexible resistors are in the embryotic stage. Based on this, we conducted a preliminary study about the materials, dimensions, and stability of the flexible resistors.

First, we conducted experiments to select appropriate materials for flexible resistors.

Different flexible conductive films characterized by different resistances, thicknesses, and materials were considered. Upon the practical application, the stability of the film was the first priority, in which the resistance can remain stable under different mechanical force. Upon to this, we laminated different conductive films onto the composite fabric with a TPU adhesion layer, and measured its resistance variation under different mechanical forces, including bending, compression, and stretching. Considering the stability, thickness, and electrical resistance, we selected the PU conductive film filled with carbon black, and graphene for the fabrication of flexible resistors. One limitation of this film is its limited thermal stability, which specified the processing temperature of the array.

Then, we conducted experiments to determine the dimensions, and shape of the flexible resistors for array assembly. Since the resistance of the resistors is highly influenced by its dimension, the dimension, and shape of the resistors need to be examined carefully. Considering the smaller size of the keypad, the resistor was designed in a serpentine shape to reduce the occupied area. Then, different lengths, and widths of flexible resistors were designed via Autocad and fabricated via laser cutting. The resistance of the serpentine resistors was measured with a multimeter. Considering the mechanism, and properties of laser cutting, the size of the resistors may differ from the design. We have used an optical microscope to measure the actual width, and length of the resistors.

Besides the study of resistors, the connection between the resistors, and the electrode is critical to the performance of the textile-based mechanoreceptor-synaptic array. Since the materials, and the structure of the electrodes, and resistors are different, it is challenging to develop a stable reliable connection. In initial, we tried to use lamination to fix the resistors, and the electrode onto the composite fabric in contact with each other. However, the electrical connection between the two components is poor. We then tried to print silver conductive ink

onto the electrode and then applied the resistor onto it with drying. It was obvious that the printed ink was cracked after lamination. Finally, we applied a double-side conductive adhesive tape ($3M^{TM}$ XYZ-Axis Electrically Conductive Tape 9713) filled with conductive filler between the resistor, and the electrode. Since the resistance of the adhesive tape is around 20 Ω (Overlap area: 6 mm * 3 mm), there is a slight increase in the resistance to the key resistance.

In summary, we selected materials for the resistor's fabrication, designed it into the appropriate shape, and studied the interconnection between the resistors, and the electrode. In the following section, we are going to study the fabrication, and characterization of the textile keyboard.

4.3. Experiment

This session introduces the materials used for the textile-based sensor-synaptic array fabrications, fabrication techniques, processing temperature, and the different characterization techniques for the performance of the sensor-synaptic array.

4.3.1. Materials

The materials used for the fabrication of textile-based pressure mechanoreceptors are consistent with those outlined in Chapter 3. Additional materials are required to assemble the mechanoreceptors together as an array to realize control and monitor the system in HMI. The total materials for the experiments are listed in **Table 4-1**. Details are as below:

To realize key identification of the array, a conductive PU film was used to fabricate the flexible resistor. The conductivity of the PU film was $150\Omega/\text{sq}$, its thickness was only around 0.05 mm. The conductive PU film is made up of carbon black, graphene, and

polyurethane.

A conductive double-side tape (3MTM XYZ-Axis Electrically Conductive Tape 9712) from 3M Electronic speciality was used for the connection of resistor, and mechanoreceptors. It is an acrylic adhesive filled with conductive fibers. Its contact resistance is in the range of $10\text{-}20~\Omega$, which is varied depending on the substrate. In addition, the long-term operation temperature can be above 70° C, the short-term operation temperature can be above 120° C.

Table 4-1. Materials and Tools.

Material/Tool	Source
Conductive fabric	Zhiyuan Xiangyu Functional Fabrics Co., Ltd.
PDMS: Dragon 20	Smooth-On Inc.
PDMS: Ecoflex 00-30	Smooth-On Inc.
PDMS: Smooth-Sil 940	Smooth-On Inc.
PDMS: Smooth-Sil 960	Smooth-On Inc.
TPU membrane	Jinda Plastic Insulation Co.,Ltd
Fabric	Jiaxing Yingcheng Textile Co., Ltd.
Stencil	Botong SMT laser steel Co.,Ltd
Conductive PU film	Saihong digital co., ltd.
Conductive double-side tape	3M Electronic speciality

4.3.2. Textile-based sensor-synaptic array fabrication

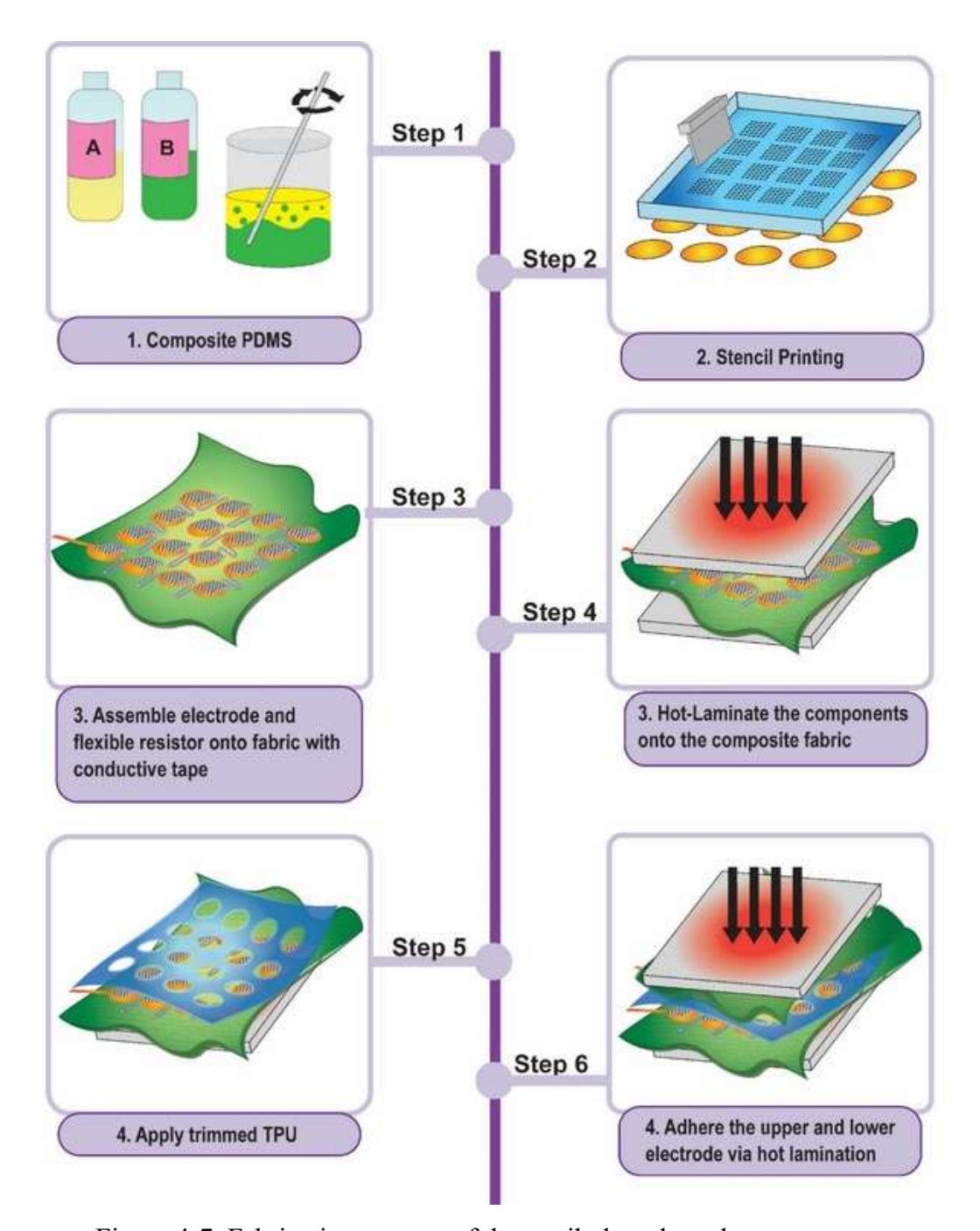


Figure 4-7. Fabrication process of the textile-based mechanoreceptors array.

Figure 4-7 illustrates the fabrication process of the textile sensor-synaptic array. Prior to fabrication, we designed and fabricated a series of flexible resistors in serpentine shape on conductive polyurethane film via laser cutting. These resistors were measured and selected. First, PDMS was prepared in the proportion of 1:1 and waited for around 30 mins for viscosity.

Then, the PDMS was poured onto the stencil to print the pattern onto the conductive fabric, followed by the solidification at room temperature for around 60 mins. Considering the thermal stability of the conductive PU film, which may undergo dimension change with temperature leading to resistance variation, the solution was applying some extra TPU onto the composite fabric to lower the lamination temperature from 120°C to 85°C. Then, the electrode with PDMS structure, and resistors were fixed temporarily onto the composite fabric, based on the design. An extra conductive acrylic tape was applied between the mechanoreceptor's electrode, and the flexible resistor to ensure a reliable and stable electrical connection. Next, a hot lamination was conducted to fixed those onto the composite fabric at 85°C for 3s. Then, a TPU membrane was cut out with 16 holes (16 mm in diameter) and applied onto the electrode with another hot lamination at 85 °C for 3s. After the fabrication of the lower set electrode, another set of conductive fabrics was fixed onto another composite fabric following the design, with a lamination at 120°C for 3s. After this, the laminated upper electrode was aligned in position with the lower set electrode. A final lamination was conducted with the help of a stencil to avoid short circuits at 85 °C for 3s.

4.3.3. Characterization

The textile sensor-synaptic array was evaluated from different aspects to confirm its practicality. These experiments include basic electrical performance, waterproof performance, stability (temperature stability, mechanical stability, and longevity), and user experience.

4.3.3.1. Electrical characterization

For the electrical performance of the sensor-synaptic array, we employed the terms "on-state", and "off-state" resistance to assess its functionality and stability. The on-state resistance

was measured using a multimeter (F101, Fluke Corporation) to measure the resistance of the textile array, and the flexible resistor. For off-state resistance, an RK2681N insulation resistance tester from Shenzhen Meiruike Electronic Technology Co., Ltd. was used in the following test to measure the off-state resistance of the array. Considering the design of the array, each key resistance is also measured.

4.3.3.2. Bending performance of the array

Considering the wearable application, the bending performance of the array is a valuable parameter contributing to the user experience from the aspects of comfortability, and practicability. In this study, the bending performance of the array can be evaluated from two aspects: the bending rigidity of the array, and the functionality under different bending radii. We utilized a KES bending meter (KES-FB2-S, KATO TECH CO., LTD.) to test the bedning rigidity of the array. Considering the limitation of the machine, the whole set of the textile mechanoreceptors array was cut into ten pieces, in which each piece's width was around 1 cm. In the test, a piece of array has been inserted into the holder of the machine to test the required bending force. After the test, the bending loads of all pieces were added up to evaluate the whole array's bendability.

For the functionality of the array under bending, we fabricated a series of acrylic tubes with different radii (4 cm, 5 cm, 6 cm, 7 cm, 8 cm, and 9 cm). The array was adhered to the acrylic tube. A multimeter (F101, Fluke Corporation) was used to test the array for short circuits. In addition, the array performance under bending was also tested in various directions.

4.3.3.3. Water immersion test



Figure 4-8. Experimental set up of water immersion test.

The unique structure of the pressure mechanoreceptors endow its good waterproof performance, and the outside composite fabric may act as a shell to protect the inner circuit, and functional element. Based on this, we conducted a water immersion test (IEC 60529). Level 7 as the highest testing level was selected. According to the standrad, an acrylic tube with 120 cm height was produced. The samples were immersed in the water at the 1 m below the water for 30 mins (Figure 4-8). We evaluate the array performance from the on-state resistance variation and the water permeation of the array. The resistance of the sample was measured by the multimeter (F101, Fluke Corporation). For water permeation of the array, we used a red dye paper to assess whether the water entering the insulation layer. The dyed paper has two sides, in which one side is painted with red dye, and another side is white. The red dye is water-soluble. When the red dye expose to water, it may permeate to the white side. We can evaluate the completiveness of the white to evaluate the water permeation of the TPU encapsulation. Based on this, we stuck the red dye paper at the edge of the array, and wrapped it around TPU encapsulation.

4.3.3.4. Temperature test

The temperature stability of the mechanoreceptors ensures consistent, and reliable performance across a wide range of conditions. Good environmental stability can help to prevent the resistance variation, and malfunctions in many applications. To comprehensively study the thermal stability of the array, we conducted three types of temperature tests, including cyclic temperature test, high-temerpature test, and low-temperature test. These tests were conducted according to the standard GB/T 30091-2013. For the array performance evaluation, the off-state resistance, and on-state resistance were measured before, and after the test by a multimeter, and insulation resistance tester.

For the cyclic temperature test, samples need to stay at two different temperatures -- 40°C for 30 mins, and then 50°C for 30 mins, as one cycle. The transition time for the temperature change needs to keep below 3 mins. A total of five cycles were conducted. After five cycles of temperature exposure, the arrays were recovered at room temperature for 2 hours. After this, the evaluation of the on-state, and off-state resistance were conducted.

Besides the cyclic temperature test, we conducted low-temperature, and high-temperature tests based on the GB/T 30091-2013. In the high temperature test, three samples were in the oven settlled the temperature at 50°C for 72 hours. In the low-temperature test, three samples were in the climatic chamber settled the temperature at -40°C for 72 hours. In both tests, the samples were recovered at room temperature for 2 hours before the testing, in which the on-off resistance was measured with a multimeter, and the insulation resistance tester.

4.3.3.5. Mechanical stability of the textile array

The maximum mechanical load refers to the maximum amount of force that the

keyboard can withstand without experiencing damage or deformation. It is a critical parameter to evaluate the longevity, and stability of the array. According to GB/T 30091, a 100 N load was applied to the array for 60 +5 s. The off-state resistance was measured. In this experiment, Instron 5566 was used to generate the force, while the RK2681N insulation resistance tester was used to evaluate the recovery of the off-state resistance. This can confirm that the keyboard weather was damaged by mechanical load,

4.3.3.6. Usabiliy

In practical applications, it is essential to minimize the signal variation from the textile array to avoid malfunctions. To assess the resistance stability under different types of pressing, we invited three partcipants to press the textile arrays and recorded the corresponding resistance of each key. This evaluates the resistance stability under different types of pressing. This helps to identify the potential issues, and make necessary adjustments to ensure consistent, and stable signal transmission.

4.4. Result and discussion

In the experimental analysis, we first evaluated the key resistance of the array, and the array performances, including water-repellent properties, bending properties, and stability at various conditions.

4.4.1. Textile-based array resistance

The control of key resistance among samples presents a critical challenge to the textile array fabrication and practical application. To realize different key position identifications, we integrated a flexible resistor made up of conductive PU film into the array. The key

identification mainly relies on the key resistance instead of point scanning. For correct, and precise key detection, there are two types of variation that need to be minimized. First, the resistance variation among samples needs to be minimized to allow mass production and practical application. Second, the resistance difference between keys needs to be controlled in range, to avoid the false detection of the key position. In previous studies, we found that it is difficult to realize a stable, reliable, and reproducible connection between resistors, and mechanoreceptors due to their surface morphology, structure, and material compositions. An additional conductive double-sided tape is required. Another serious problem is the shape deformation of the flexible resistors in the lamination process. Due to this, the lamination time, and temperature were adjusted.

Besides the connection problem, another challenge is the potential of short circuits. In the design, the upper electrode, and lower electrode may stack, and adhere together. Besides the compression area, the insulation between the electrodes is realized by the TPU membrane. Since the thickness of the TPU membrane is only 0.1 mm, it may partially melt in the lamination process. Then, there is a high potential for circuit exposure after the lamination, especially the interface between the flexible resistors, and conductive fabric. There is a a higher risk of short circuit after the final hot lamination. In the fabrication process, we have made several adaptations. We first reduce the lamination temperature, and the lamination time to control the melting of the TPU to avoid the exposure of the circuit. Additionally, we have modified the design of the lamination stencil by enlarging the size of the compression area to limit the diffusion of TPU. After that improvement, we have successfully fabricated the spiral shape sensor-synaptic array as shown in **Figure 4-9**.



Figure 4-9. Photo of the textile mechanoreceptors array..

To evaluate the possibility of large-scale production, and the practicability, the resistance variation among samples, and keys need to be controlled. The 16 keys of three sets of textile arrays were fabricated, and their resistance was measured. **Figure 4-10** illustrates the actual resistance value of each key. It is observed that there is a steady increase of the resistance, in line with the design. In detail, the resistance of key 1 is $0.01 \text{ k}\Omega$, key 2 resistance is $3.34 \text{ k}\Omega$; key 3 resistance is $6.38 \text{ k}\Omega$, and so on. The average resistance standard deviation among keys was 0.182. The resistance variation among samples is limited, making it suitable for mass production.

To realize effective key position identification, the resistance difference between keys is the critical boundary to identify different levels/positions of the key. Based on this, we calculated the resistance difference between keys, which includes the resistance of flexible resistors, and connection, by deleting previous key resistance. **Figure 4-11** demonstrates the resistance difference between each key. The average resistance difference between keys was $3.226 \text{ k}\Omega$, and the average standard deviation was 0.11. It can be observed that the resistance difference between keys can be kept in the range of $2.5 \text{ to } 4.5 \text{ k}\Omega$, indicating a clear gap

between key resistance for identification.

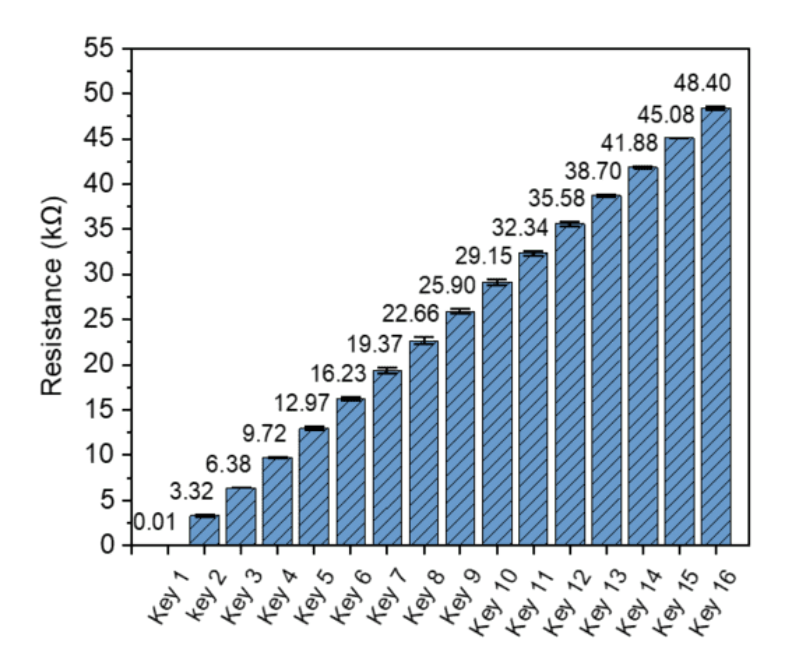


Figure 4-10. Textile-based sensor-synaptic array resistance.

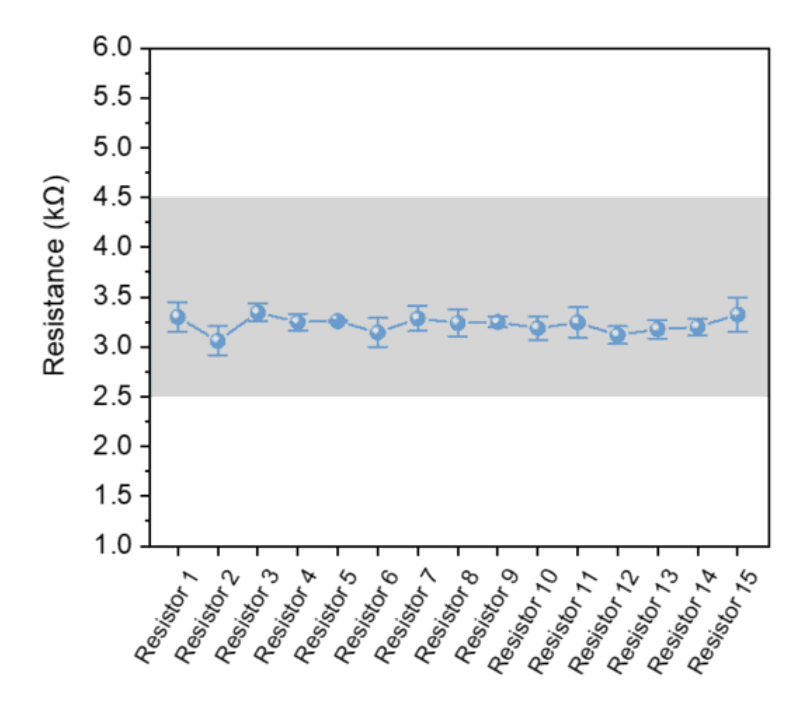


Figure 4-11. Resistance different between keys.

These results preliminarily proved the functionality of these textile keyboards, and then more experiments will be conducted for practical applications, and better user experiences.

4.4.2. Bending performance of the textile-based sensor-synaptic array

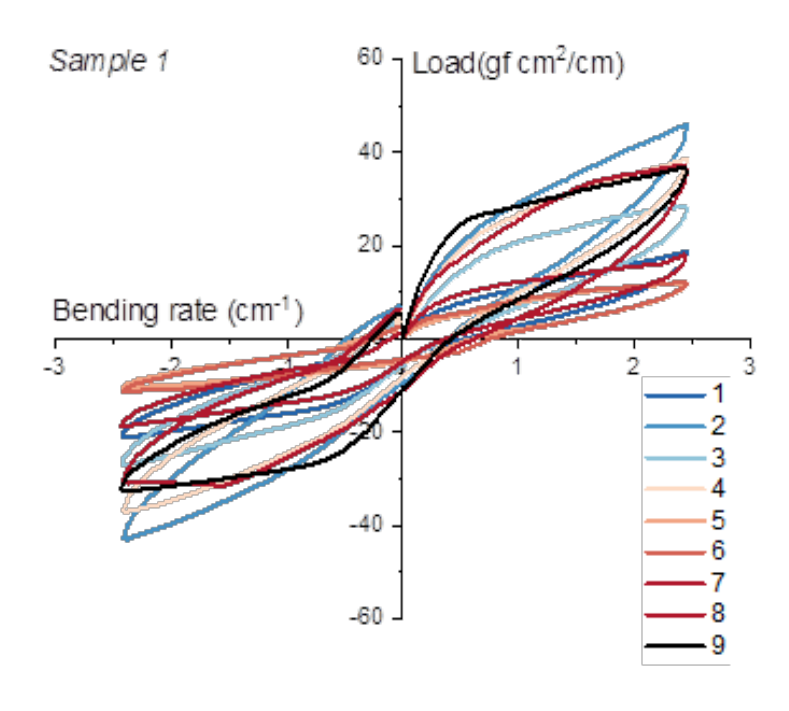


Figure 4-12. Bending curve of the textile sensor-synaptic array.

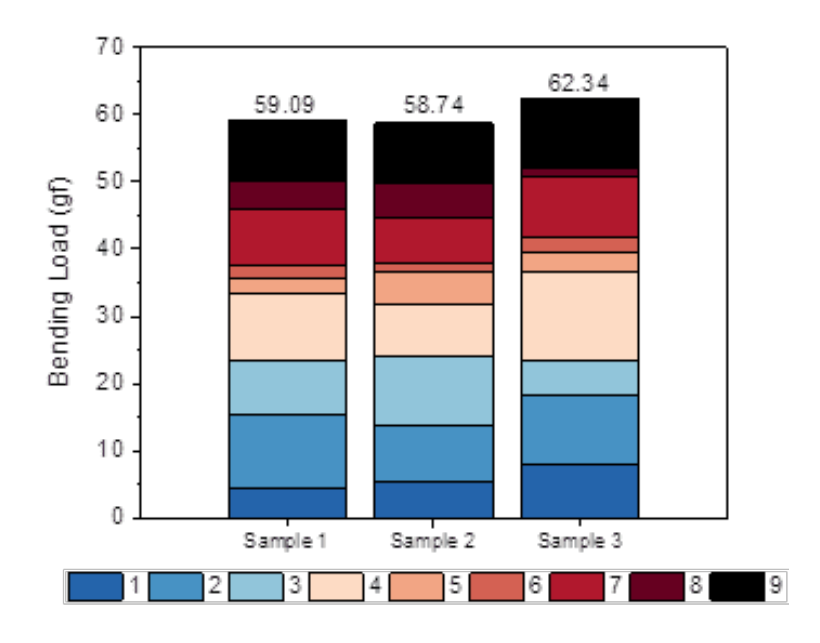
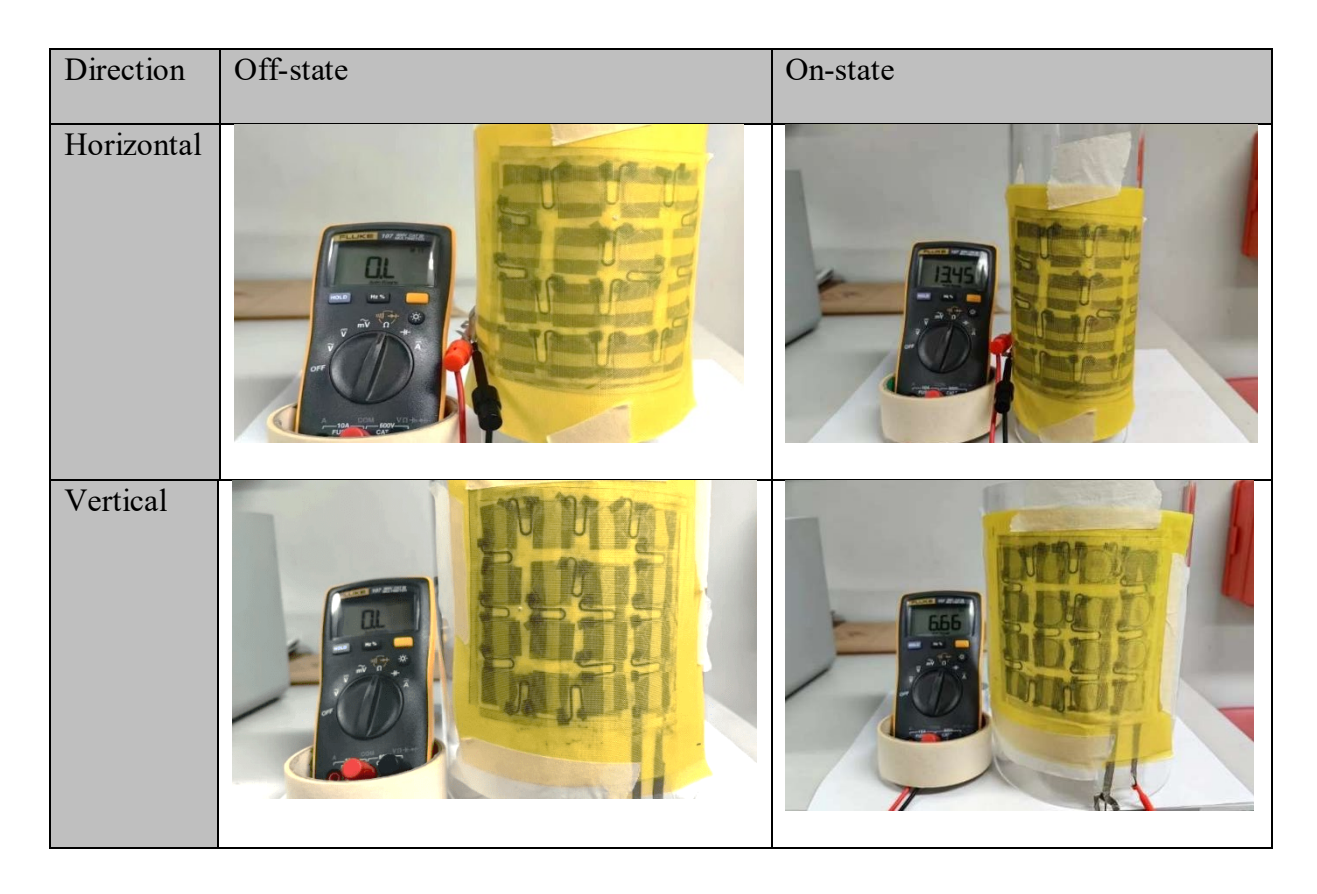


Figure 4-13. Bending force of three textile-based sensor-synaptic array samples.

Wearable applications require various degrees of bending, which improve the user comfort, and endow the array ability to withstand mechanical stress, and deformation. This

also explores the potential applications. **Figure 4-12** outlines one of the bending curves of the array in the test, and **Figure 4-13** summarizes the total load required to bend the whole textile array. The average bending load among the three samples is 60.22 gF, equal to 0.588N. However, commercial membrane keypad is very rigid because the recovery of the keypad is only relies on the membrane keyboard. This keyboard bending rigidity is over the upper limitation of the KES machine. In addition, this textile keyboard shows a better deformation than the commercial one.

Table 4-2. Functionality of the sensor-synaptic array under bending.



Considering the wearable application, the usage scenario may involve bending. The array functionality under different bending radii were evaluated. As shown in **Table 4-2**, bending along its output electrode direction, the array can remain off-state under the bending radius of 5 cm, while the array was short-circuited when the bending radius is 4 cm. When bending perpendicular to its output electrode, the array can remain in the off-state under an 8 cm bending, while the array was short-circuited under a 7 cm bending. The bending

performance of the array along its output electrode is better than that of the perpendicular direction. A possible explanation is the wiring direction of the textile array. When the wire is perpendicular to the bending, more stress may be generated to the mechanoreceptor's electrode, causing deformation, and contact with the upper electrode, forming a short circuit. Considering the bending radius, these arrays can be applied to the trunk (like the abdomen, and back), and thighs of human, or home textiles, like a cushion, and pillows. It was noticeable that the functionality of the array under bending may be varied with its output electrode direction. The directionality of the array needs to be considered in the applications. However, this test only considers the function of the array under bending and does not evaluate the effect of bending on mechanoreceptor pressure thresholds.

4.4.3. Water immersion test

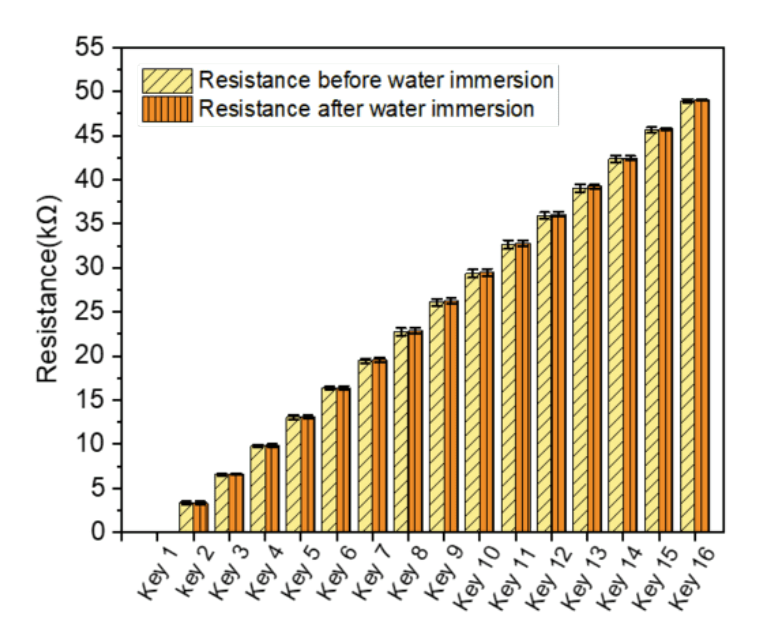


Figure 4-14. Sensor-synaptic array key resistance variation before, and after the water immersion test.

Considering the wearable application, it is important to evaluate the water encapsulation properties. In this experiment, we evaluated the performance of the textile

mechanoreceptors array from two aspects: (1) Water permeability of the structure and (2) Resistance variation of the array before, and after the test.

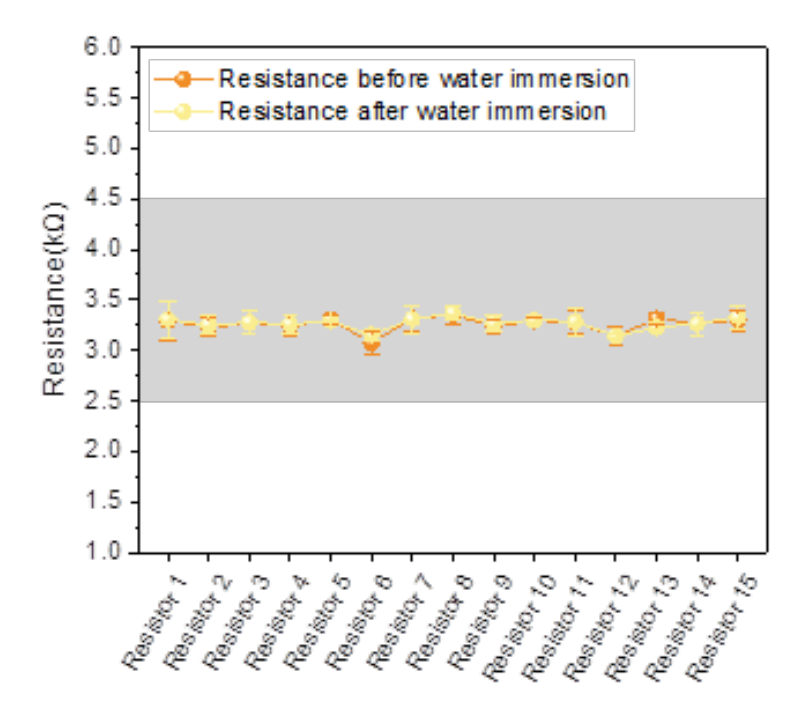
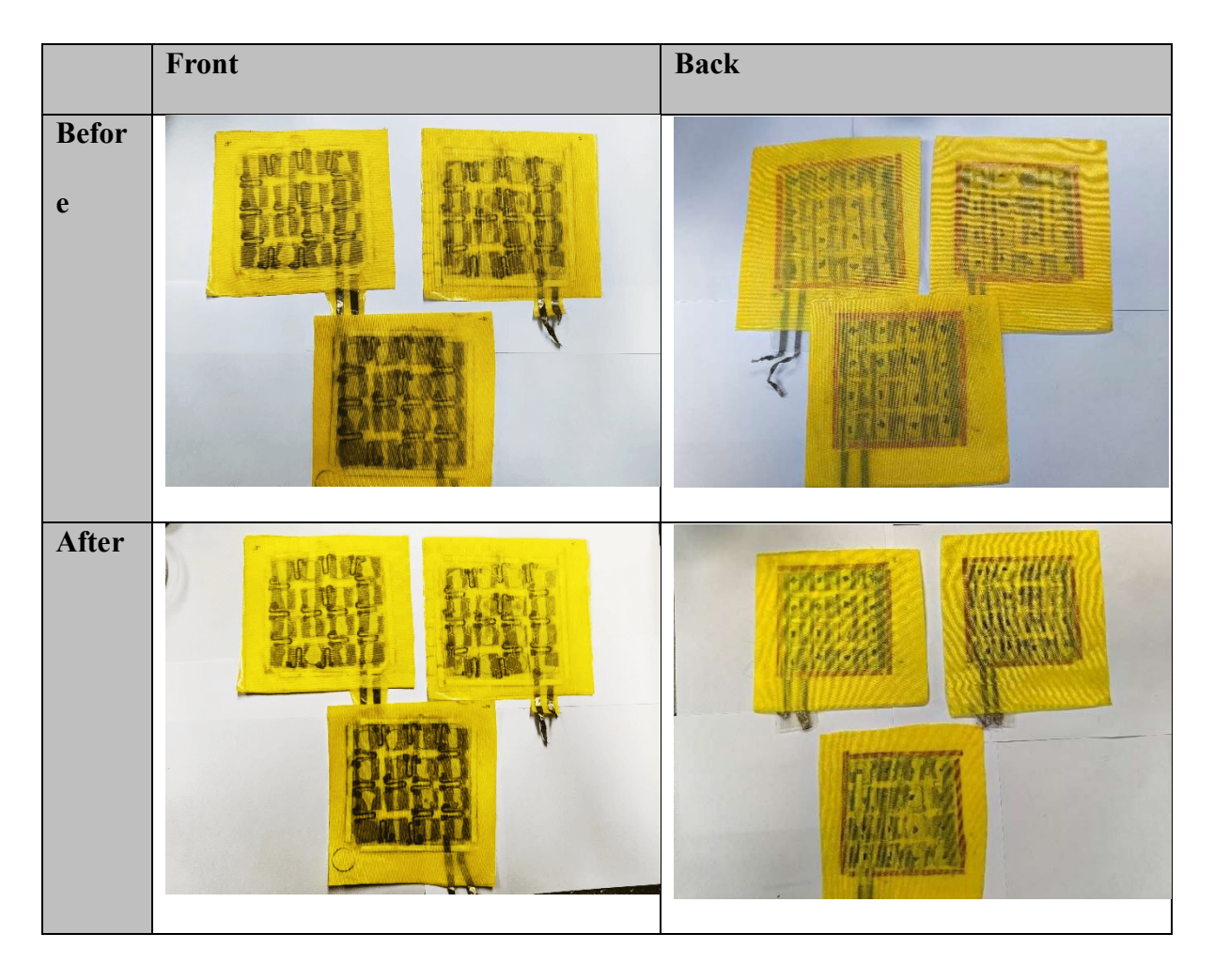


Figure 4-15. Resistance difference between keys before, and after the water immersion test.

For the electrical performance, the on-state resistance of the array was measured. Figure 4-14 compares the actual resistance of the textile array if each key before and after 30 min water immersion. It is obvious that there is no difference in the actual resistance of the keys. Figure 4-15 plots the resistance difference between each key. The average resistance difference between keys before the test is $3.26 \text{ k}\Omega$, while after the test is $3.27 \text{ k}\Omega$. There is no significant difference in key resistance before and after the water immersion test in the pair-T test. This proved that the water immersion does not influence the conductive material performance of the array, and the interconnection between mechanoreceptors, and electrode.

Table 4-3. Optical image of the sensor-synaptic array.



This textile array uses TPU membrane as encapsulation material. As mentioned in the methodology, the waterproof property was evaluated by comparing the colour difference of the front page of the array. In **Table 4-3**, it was evident that the front page of the ink paper was still white. After 30 mins of water immersion, there is no colour change on the front side and back side of the paper. The TPU encapsulation can successfully protect the array from water permeation.

4.4.4. Environmental stability test

To evaluate the environmental stability, we conducted three different types of temperature tests, in which the results were discussed in the below session.

4.1.1.1. Cyclic temperature test

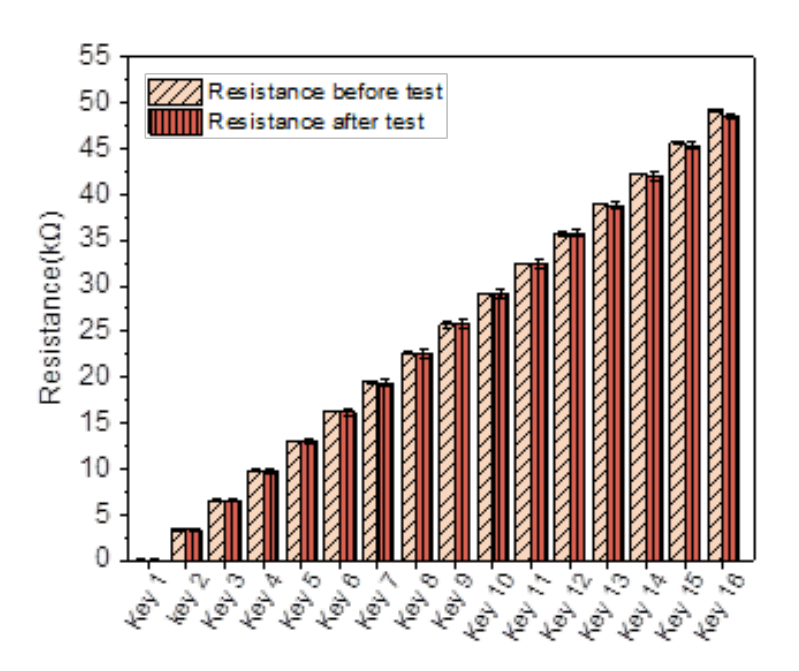


Figure 4-16. Sensor-synaptic array key resistance before, and after the cyclic temperature test.

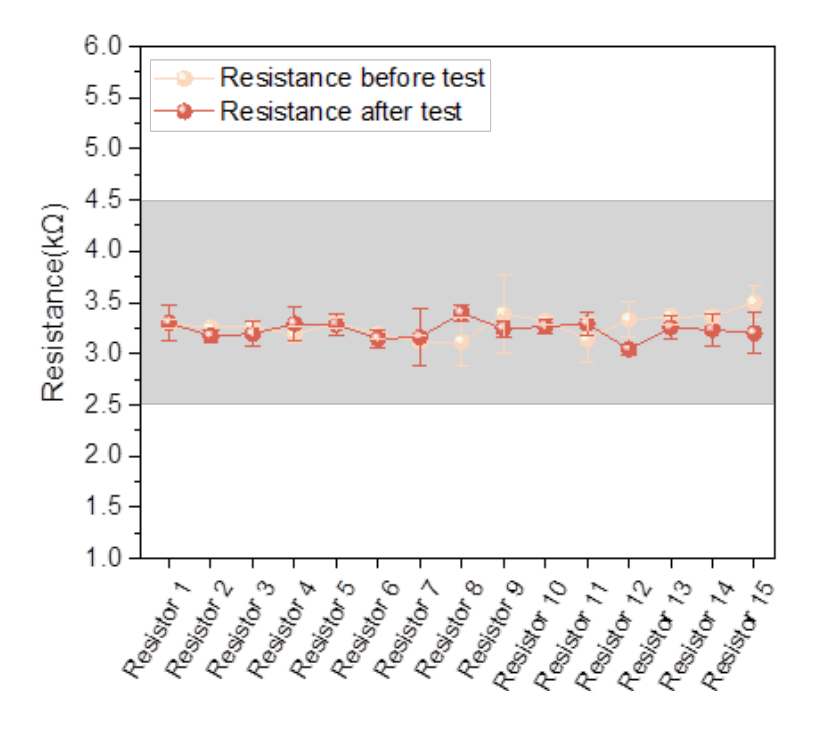


Figure 4-17. Resistance difference between keys before, and after the cyclic temperature test.

The cyclic temperature test is designed to ensure that the mechanoreceptors can maintain their performance, and reliability under the expected temperature variations. **Figure**

4-16 compares the resistance difference before, and after the cyclic temperature test. There is no significance in the actual resistance of the keys. **Figure 4-17** compares the resistance difference between keys before and after the cyclic temperature test. The average resistance difference before the test was 3.27 k Ω (SD:0.10), while the average resistance difference after the test was 3.23 K Ω (SD: 0.08). This proved that the double-side conductive acrylic tape and the flexible resistor performance is stable in the temperature variation.

Besides on-state resistance, the off-state resistance of the whole textiles array was weighted, as shown in Table **4-4**. We also conducted a pair T-test to analyze the difference in the result. It is evident that there is no degradation in the off-state resistance of the array.

Both the on, and off resistance of the keyboard after the test proved that these keyboards can be applied in the scenario with temperature variations, without damage. Additionally, the off-state resistance of the keyboard fulfills the requirement in the standard (20 M Ω).

Table 4-4. Off-state resistance of the keyboard before, and after cyclic temperature test.

Parameter	State	Sample 1	Sample 2	Sample 3
Resistance	Before	$405.7~\mathrm{M}\Omega$	204.7 MΩ	220.0 ΜΩ
	After	393.3 ΜΩ	435.6 ΜΩ	367.5 ΜΩ
Current	Before	0.24 μΑ	0.48 μΑ	0.45 μΑ
	After	0.25 μΑ	0.22 μΑ	0.27 μΑ

4.1.1.2. Low temperature test

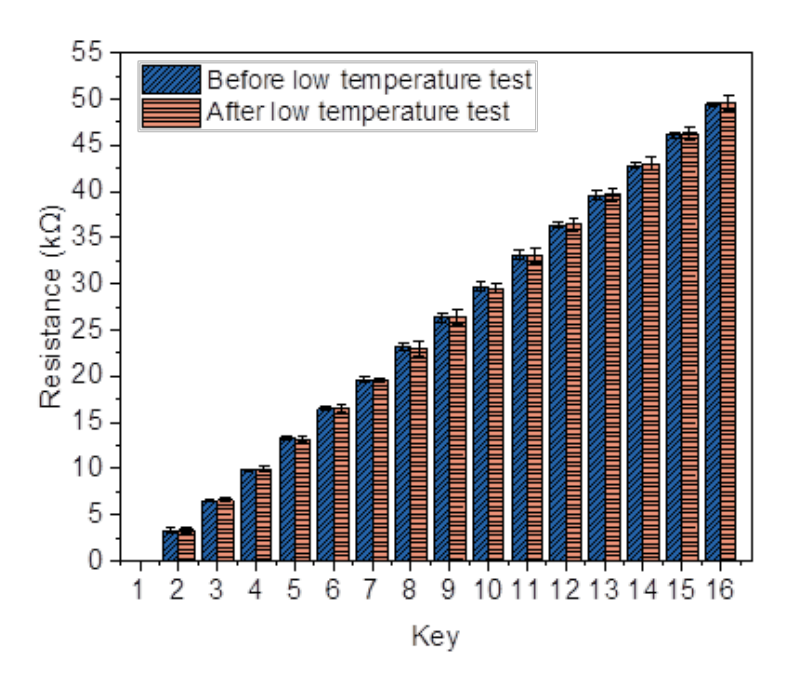


Figure 4-18. Sensor-synaptic array key resistance before, and after low temperature test.

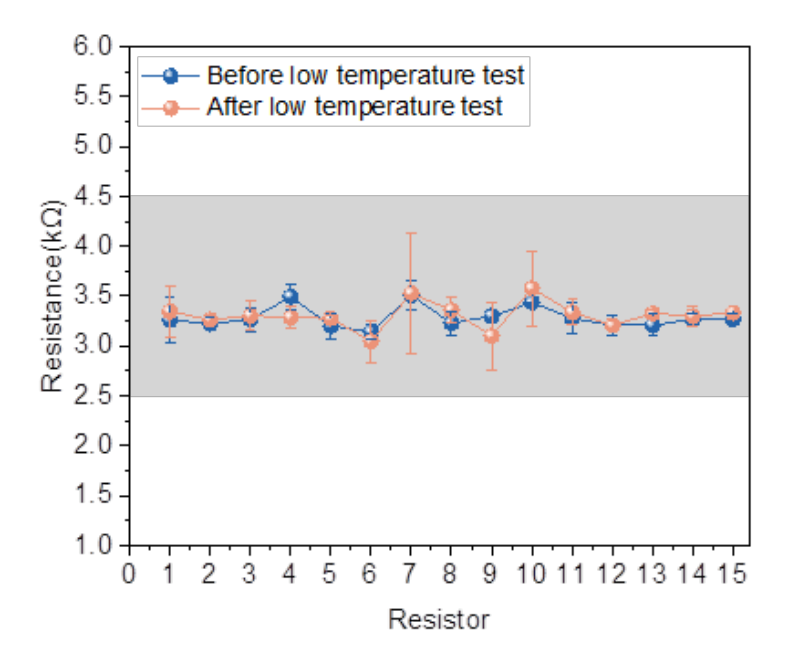


Figure 4-19. Resistance difference between keys before, and after the low temperature test.

The low-temperature testing lies in its ability to validate the performance, reliability, and safety of materials, and products in cold environments. **Figure 4-18** compares the key resistance of the array before, and after the cold temperature test. There is no significant

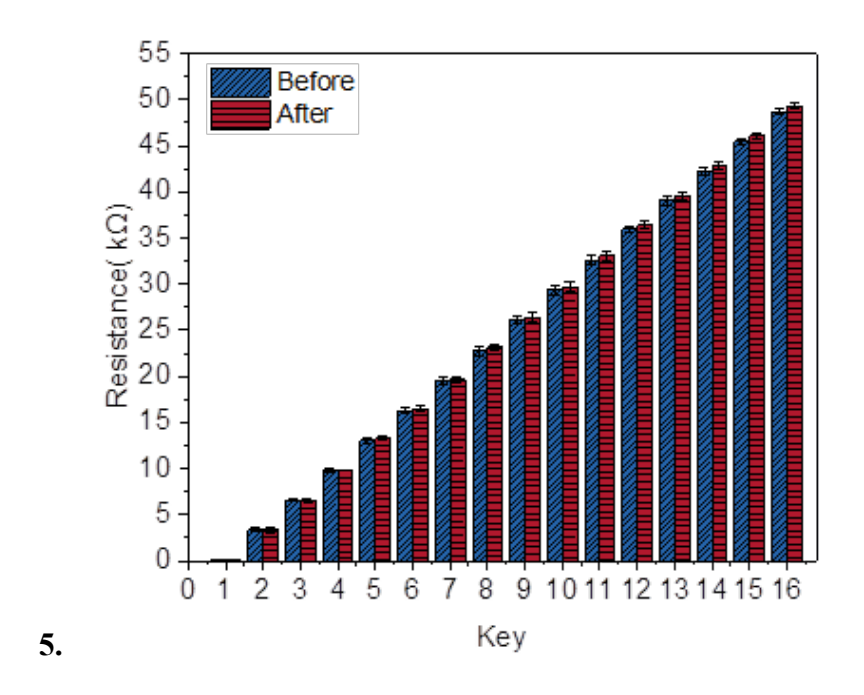
difference in the resistance before and after the test. **Figure 4-19** depicts the resistance difference before and after the low temperature test. There is no significant difference before, and after the test in the pair T-test. Additionally, the resistance variation for certain keys has been increased after the test, while the whole set is still kept in the range.

Table 4-5. Off-state resistance of the keyboard before, and after low temperature test.

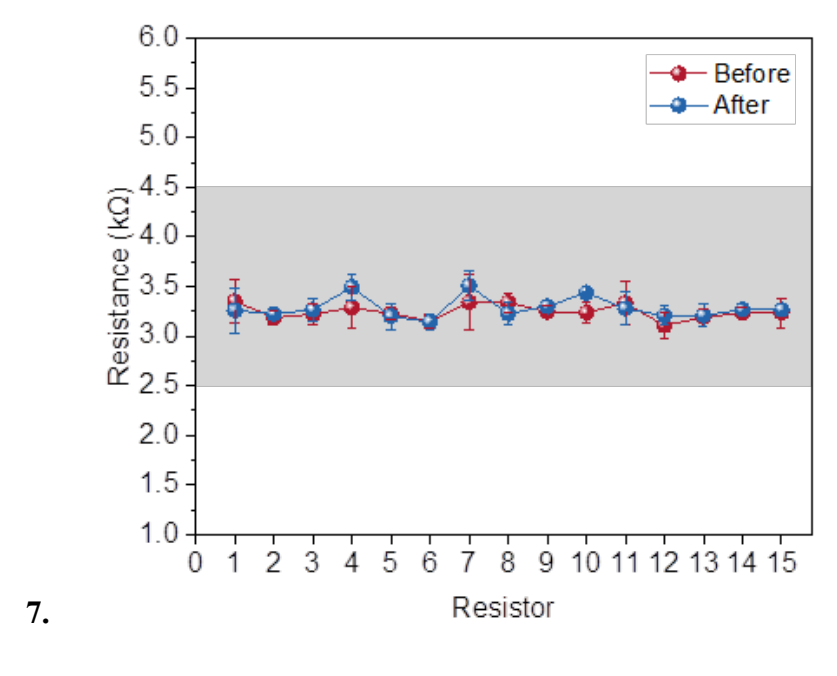
Parameter	State	Sample 1	Sample 2	Sample 3
Resistance	Before	606.8 MΩ	372.8 MΩ	371.8 MΩ
	A 6:	1747.160	04.07.140	106 4340
	After	174.7 MΩ	94.97 MΩ	106.4 MΩ
Current	Before	164.8 nA	0.26 μΑ	0.26 μΑ
	After	0.57 μΑ	1.05 μΑ	0.93 μΑ

Table 4-5 demonstrates the off-state resistance of the array before and after the test. The average off-sate resistance of the array before the test was 450.4 MΩ, while it decreased to 125.25 MΩ. There is a significant difference in the off-state resistance in the pair T-test. The off-state resistance decreased around 73.23%. This indicates that the textile keyboard's off-state resistance may deteriorate at a very low temperature. The decrease in the off-state resistance of the textile keyboard indicates that the gap distance between the upper, and lower electrodes is narrow, indicating that the contact between the upper electrode, and the PDMS structure is stronger. One possible explanation is the cold-welding phenomenon. Another is related to the moisture within the structure. Low temperature may condense the moisture to connect the PDMS, and the electrode closely. The insulation gap may become smaller, so the off-state resistance decreases.

4.1.1.3. High temperature test



6. Figure 4-20. Sensor-synaptic array key resistance before, and after the high temperature test.



8. Figure 4-21. Resistance difference between keys before, and after the high temperature test.

High-temperature test aims to evaluate the reliability, and endurance of the materials,

and the textile keyboard at a high temperature. Figure 4-20 illustrates the actual resistance of each key of the textile sensor-synaptic array. There is no notable difference between the resistance before and after the test. **Figure 4-21** outlines the resistance difference between keys before, and after the test. The average resistance difference before the experiment was 3.24 k Ω (SD:0.07), while the average resistance after the test was 3.28 k Ω (SD:0.108). We also conducted pair T-test about the resistance difference. This is no significant difference before and after the test. The interconnection and conductive materials of the textile sensor-synaptic array can sustain after the high-temperature test.

Table 4-6. Off-state resistance of the keyboard before and after high temperature test.

Parameter	State	Sample 1	Sample 2	Sample 3
Resistance	Before	293.3 ΜΩ	435.6 ΜΩ	367.5 ΜΩ
	After	248.0 ΜΩ	255.8 ΜΩ	294.8 ΜΩ
Current	Before	0.25 μΑ	0.22 μΑ	0.27 μΑ
	After	0.39 μΑ	0.4 μΑ	0.33 μΑ

The off-state resistance of the array was also evaluated. The average off-state resistance before the experiment was 365.4 M Ω , while the off-state resistance after the test was 266.2 M Ω in **Table 4-6**. We also conducted pair T-test to analyse the difference of the result. It is evident that there is no degradation in the off-state resistance of the array. In addition, the off-state resistance is higher than that of the requirement in standard (20 M Ω).

4.4.5. Longevity of the resistive keyboard

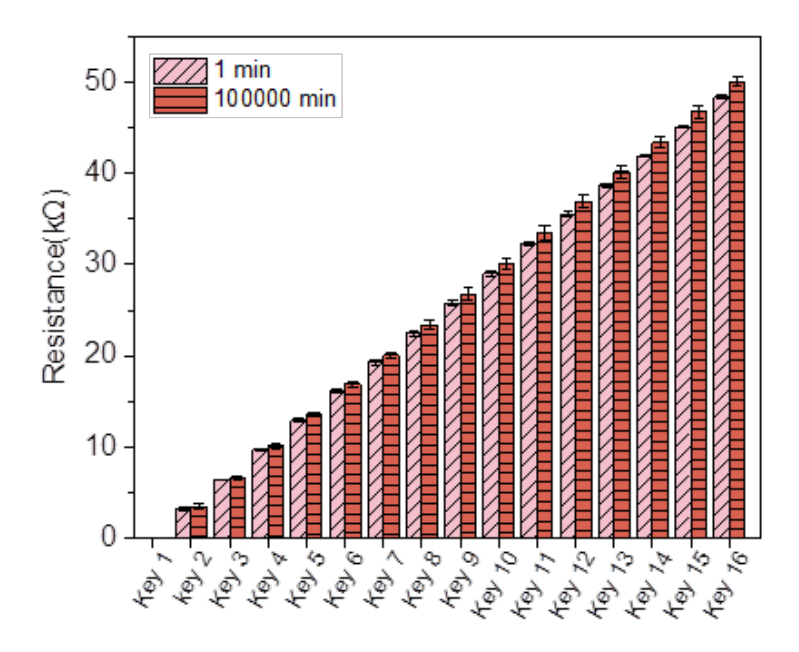


Figure 4-22. Key resistance of sensor-synaptic array at 1 min and 100000 min.

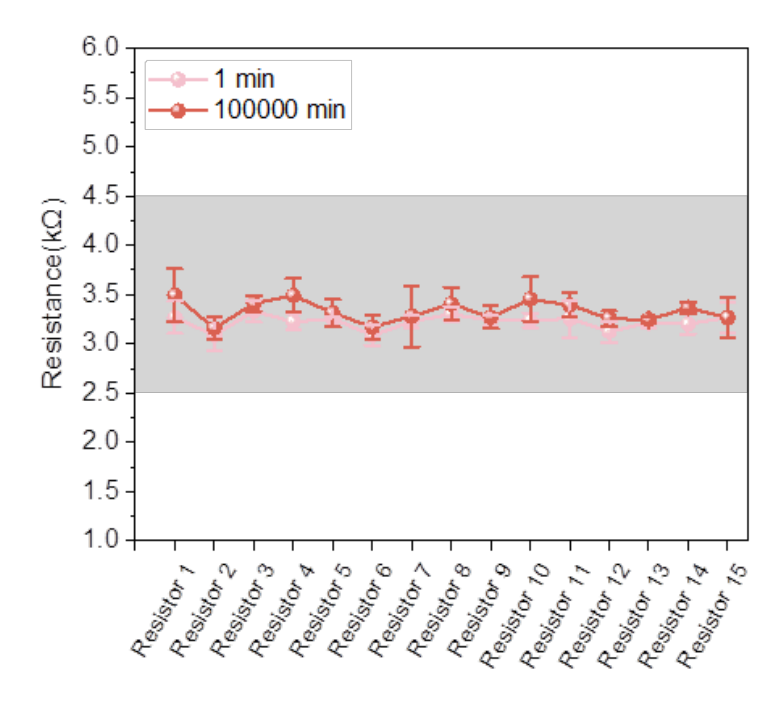


Figure 4-23. Resistance difference between keys at 1 min and 100000 min.

Long-term stability of the sensor-synaptic array is critical to the usage. The resistance of three arrays has been monitored over 3 months. **Figure 4-22** illustrates each key resistance

variation over three months. Since the last key resistance is the sum of the previous key resistance, the variation of the previous key may stack to the final one. It was clear that the actual resistance of the mechanoreceptors at the back was slightly higher than its initial period, while the actual resistance variation of the front mechanoreceptors is not obvious. For Key 2, the resistance at 1 min is $3.278~\text{k}\Omega$ (SD: 0.150), and at 100000~mins is $3.521~\text{k}\Omega$ (SD: 0.234). It increases around 7.41%. For Key 16, the resistance at 1 min is $48.33~\text{k}\Omega$ (SD: 0.152), and at 100000~mins is $50~\text{k}\Omega$ (SD: 0.529). It increases by around 3.4%. The actual resistance variation is quite large, out of the detection boundary. **Figure 4-23** demonstrates the change of resistance difference between each key. The average resistance difference of the array at 1 min was $3.22~\text{k}\Omega$, while the average resistance difference between keys at 100000~min was $3.33~\text{k}\Omega$. The average resistance increases around 3.4% with time.

Since the above two figures cannot illustrate the resistance variation along times, we selected four keys as examples to analyze their actual resistance variation along time in **Figure 4-17**. First, all four keys (key 4, key 8, key 12, and key 16) resistance before 1000 mins is relatively stable, without a sharp increase. From 1000 mins to 10000 mins, the variation of the resistance become larger, but the key resistance can be kept in the detection range. However, the resistance of the keys continuously increases in the later period. At 100000 mins, three out of four keys resistance is out of the detection range. It can find that there is a very high requirements on resistance variation among keys due to the serpentine design, so the connection between the flexible resistors, the mechanoreceptors, and even the flexible resistor material needs to be further improved.

One possible explanation is the adhesion of the double-side conductive adhesive tape may deteriorate along time, the electrical connection between resistors, and mechanoreceptors decreases. Then, the resistance difference between keys after 100000 mins becomes larger. In

addition, this tape performance also can be influenced by the temperature, relative humidity, and pressure. Based on this, it is in demand to develop a more reliable connection between resistors, and mechanoreceptors.

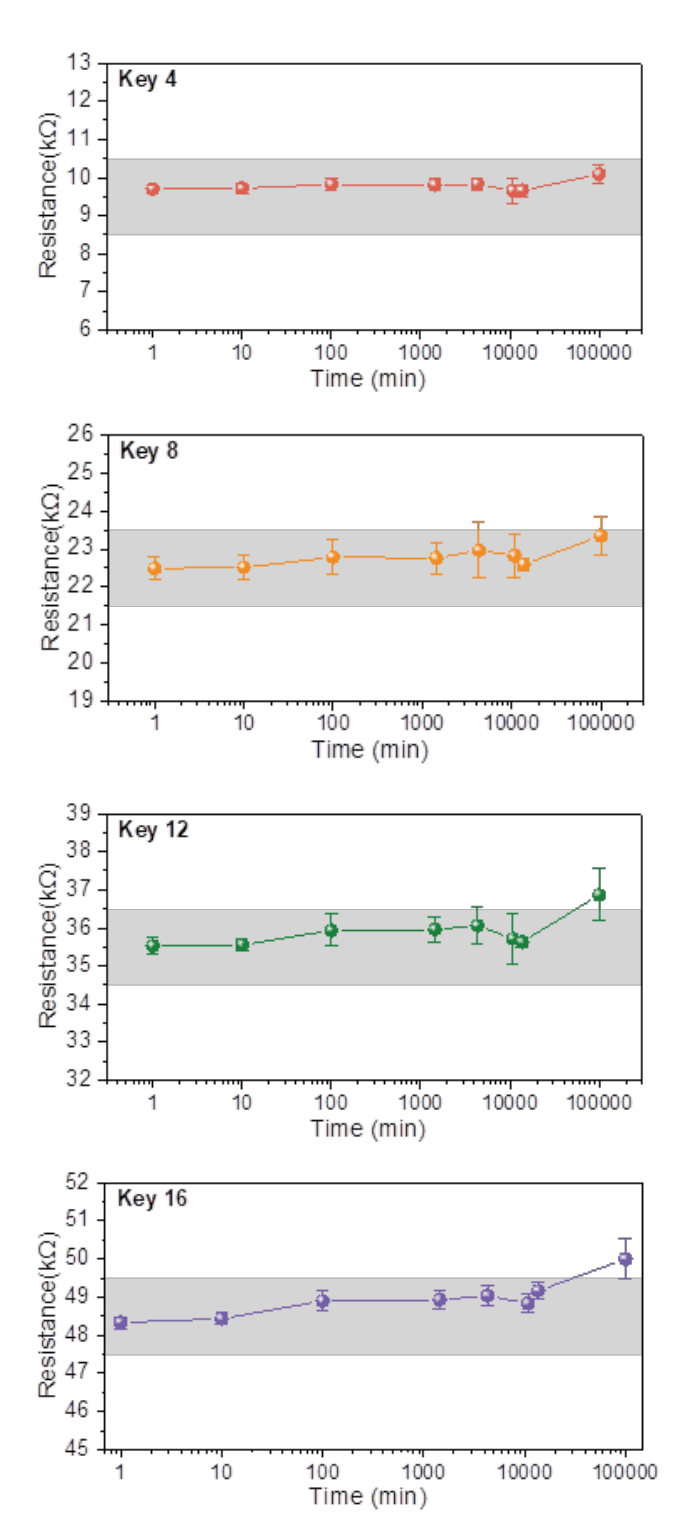


Figure 4-24. Key 4, 8, 12, and 16 resistance variation along time.

4.4.6. Mechanical stability of the sensor-synaptic array

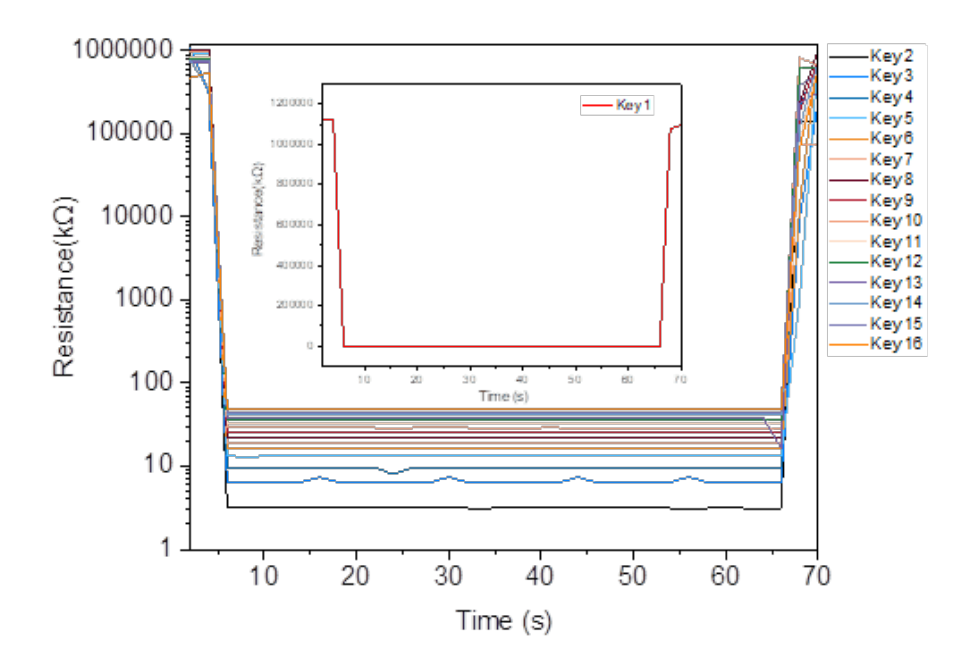


Figure 4-25. Resistance measurement of mechanoreceptors array under maximum mechanical force.

Figure 4-18 illustrates the variation of the off-state resistance of the array under maximum mechanical load compression. The off-state resistance can recover to its initial after 60 s 100 N compression. The off-state resistance after the test can be over 20 M Ω , over the qualified level in the standard. This proved that the maximum mechanical load does not damage the textile sensor-synaptic array.

4.4.7. Pressing by different people

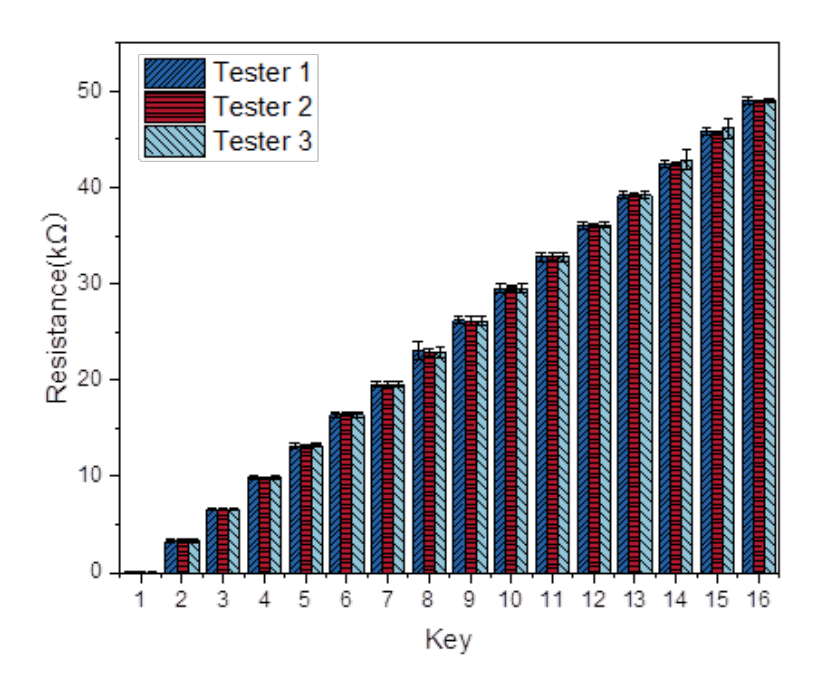


Figure 4-26. Actual resistance of the textile array under different tester pressing.

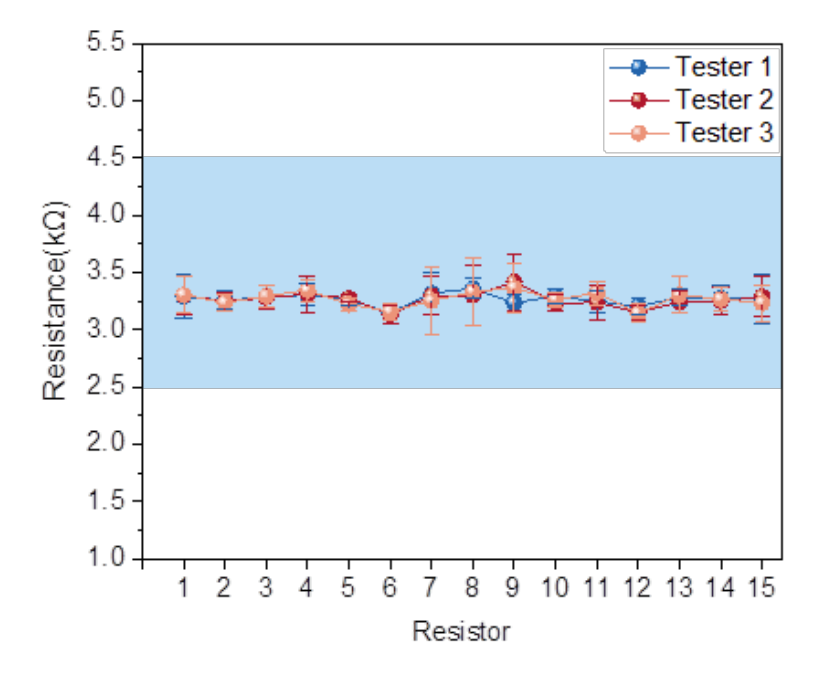


Figure 4-27. Resistance difference between keys under different tester pressing.

The resistance of each key of the array under pressed was measured by different testers.

Figure 4-19 illustrates the actual key resistance of three samples pressed by three users. It was

obvious that there was no significance in the actual resistance of the key pressed by different people. **Figure 4-20** demonstrates the resistance difference between keys under different testers pressing. The resistance variation under different people pressing is consistent, and is located within the detection range. This proved that the resistance variation of the keys under different pressing is limited, and is advanced in practical applications. However, the user provided feedback that the position of the compression cannot be confirmed during usage. Therefore, labels or other aesthetic designs will be added for improvement.

4.5. Conclusion

In this chapter, the textile sensor-synaptic arrays were assembled in a spiral shape. In the array, mechanoreceptors were series connected with a flexible resistor to control each key resistance. The final key resistance is in the range of 1Ω to $52.5 \text{ k}\Omega$. The array key resistance and the resistance difference can be well controlled to realize practical, and large-scale production. The resistance difference among the single mechanoreceptors mimics the neural synapse to filter out part of the information for efficient information processing. In addition, the array can function under a certain degree of bending, and show good bending rigidity. The textile array shows good waterproof properties, and stability under different environments, including cyclic temperature changes, cold temperatures, and hot temperatures.

However, the long-term stability of the textile keyboard needs further studies because of the connection material limitation. For the current textile array, another limitation is that the key identification only can identify one pressing point, not multiple points.

4.6. References

[1] A. Rühl, 'Fundamentals', in On the Time Temperature Dependent Behaviour of Laminated

- Amorphous Polymers Subjected to Low-Velocity Impact, A. Rühl, Ed., Berlin, Heidelberg: Springer, 2017, pp. 9–43. doi: 10.1007/978-3-662-54641-3_2.
- [2] J. Arrese, G. Vescio, E. Xuriguera, B. Medina-Rodriguez, A. Cornet, and A. Cirera, 'Flexible hybrid circuit fully inkjet-printed: Surface mount devices assembled by silver nanoparticles-based inkjet ink', *J. Appl. Phys.*, vol. 121, no. 10, 2017.
- [3] A. Apicella, L. Nicolais, G. Astarita, and E. Drioli, 'Effect of thermal history on water sorption, elastic properties and the glass transition of epoxy resins', *Polymer*, vol. 20, no. 9, pp. 1143–1148, 1979.
- [4] C. Kerr, N. C. MacDonald, and S. Orman, 'Effect of certain hostile environments on adhesive joints', *J. Appl. Chem.*, vol. 17, no. 3, pp. 62–65, 1967.

Chapter 5 Integration of mechanoreceptors for wearable application

5.1. Introduction

In the previous chapter, we mainly focused on the design, and fabrication of the pressure-sensitive mechanoreceptors for human-machine interaction. A corresponding array was fabricated with additional functions to enhance the efficiency of the interactions. The previous two chapters realize the basic functionality of the mechanoreceptors, while it still needs more exploration before it can be applied in practice. Building upon this foundation, the current chapter focuses on the exploration of the applications of these mechanoreceptors by integrating them into different wearable products, like garments, and accessories. Throughout the integration process, we have conducted additional studies to improve the mechanoreceptors by reducing the size, and thickness of the mechanoreceptors in order to enhance the user experience of the developed products. Moreover, we also studied the effects of other factors (size of the mechanoreceptor and compression area) on the pressure threshold of the mechanoreceptors, in addition to the PDMS structural factors. It can explore the design freedom of the mechanoreceptor's pressure thresholds. Finally, we have developed three distinct prototypes, fitting to the users to improve their life quality.

The first prototype focuses on the diabetic foot. Patients with diabetics face reduced sensation, making them prone to ulcers due to the large pressure of wearing shoes. The integration of mechanoreceptors into the sock can develop a pressure monitoring system to monitor the pressure whether over the damaged threshold. This system can help users to select appropriate footwear to avoid ulcers. The second prototype is for Parkinson's patients. Due to this disease, patients may suffer impaired balance coordination, and may be prone to fall. An alarm system, in which the mechanoreceptors can be integrated into the stocking to conduct

simple gait analysis. If the gait pattern differs to normal, a signal can be generated to remind the caregivers to provide immediate support to the patients to avoid further damage due to falling. The final prototype is an initial pressure sensation platform to measure the pressure. For baby and children, it is difficult for them to express their discomfort. Based on this, the pressure platform can assist parents and caregivers in monitoring the appropriateness of the garment, like diapers, and pajamas. Furthermore, this pressure sensation platform holds the potential way to simulate the pressure sensation of human skin, where various mechanoreceptors are responsible for detecting different ranges of pressure for different purposes.

The above three prototypes leverage the unique capabilities of the mechanoreceptors, and its array for different applications, demonstrating the potential of this technology. In addition, further research, and studies are required to change the users experiences, and these products fit the demands of users.

5.2. Design of the wearable products

To explore the potential of the mechanoreceptors for different wearable applications, three different wearable products were designed based on the user demand. We conducted a thorough investigation into the users' need across the three applications to design the corresponding wearable products. The research includes determining the number of mechanoreceptors, their position, the corresponding pressure threshold, mechanism, and outputs.

Sock for diabetic foot ulcer: Diabetic foot ulcer is the common non-traumatic lower limb amputation, which risk factors include diabetic periphneuropahty, foot deformity, and trauma, with diabetic peripheral neuropathy[1]. Patients with diabetic peripheral neuropathy

face a loss of protective sensation, resulting in abnormally high, repetitive, and undetected pressures applied to the weight-bearing plantar surface of the foot[2]. Semmes-Weinstein monofilaments are a common test to evaluate sensory loss. The plantar threshold for diminished protection threshold is 244 kPa from the Touch-TestTM evaluator chart. Most previous plantar pressure monitoring systems are insole, while many studies pointed out that the ulcer is also caused by the shear force[3,4]. Monitoring shear force is challenging with insole monitoring systems because the shear force position is out of the boundary of the insole. Based on this, a sock pressure monitoring system is preferred because it can monitor the 3D pressure of the foot.

Table 5-1. Position of the mechanoreceptors for diabetic foot.

Mechanoreceptor Number	Position
Mechanoreceptor 1	Metatarsal head 1
Mechanoreceptor 2	Metatarsal head 2
Mechanoreceptor 3	Hallux
Mechanoreceptor 4	Side of the hallux
Mechanoreceptor 5	Side of the little toe

Considering the loss of pressure sensation, the pressure threshold of the diabetic foot ulcer was settled as 250 kPa. Besides pressure, the location of the pressure sensation are key factor in the prevention of the diabetic foot ulcers. Referring to previous studies, we have designed to integrate five mechanoreceptors to different positions as shown in **Table 5-1**. An electronic yarn and the battery were used to provide a visual signal as a warning to the users. The corresponding circuit was shown in **Figure 5-1**, in which the mechanoreceptors are series connected. When the plantar pressure is over 250 kPa, the circuit will be closed as a short circuit to turn on the LEDs. **Figure 5-2** demonstrates the overall design of the sock and the

mechanism.

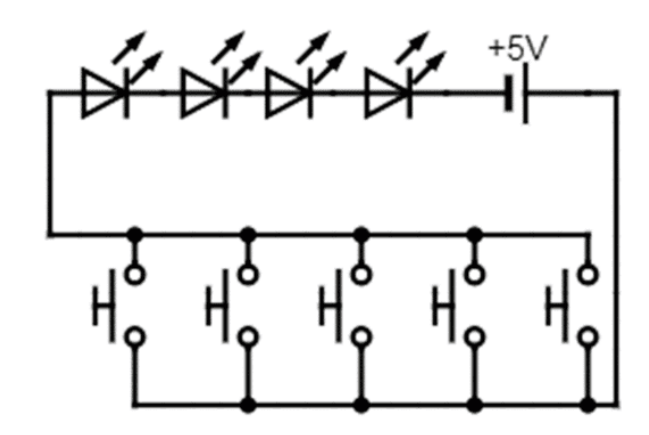


Figure 5-1. Electric diagram of the diabetic foot sock.



Figure 5-2. Overall design of the sock pressure monitoring system.

Sock for Parkinson's patient: Parkinson's patients are easy to fall due to the freezing of gait, where the patient temporarily inability to move the feet forward[5,6]. To effectively detect falling, it needs to determine the state of each foot. In detail, if one of the feet is on the ground, the patient is in the normal state of walking. However, when the two of the feet are not on the ground, it can be concluded that the patient is falling. Based on this, the mechanoreceptors need

to be integrated into a pair of socks. Differ from the diabetic foot sock, the pressure threshold of the mechanoreceptors needs to be lower to determine whether the foot is on the ground. Considering other insole gait analysis systems, these mechanoreceptors's pressure threshold depended on the body weight, and the size of the footwear. The pressure threshold was settled at 30 kPa. The system for the Parkinson's patient is shown in **Figure 5-3**, in which the two socks integrating with mechanoreceptors are connected with an Arduino board. In usage, the Arduino needs to determine the state of each sock's mechanoreceptors and record the on-off time. After this, it then calculates the time difference between the on-state of one sock, and the off-state of another sock. If the time difference is over 10 s, an alarm will be generated to warn caregivers.

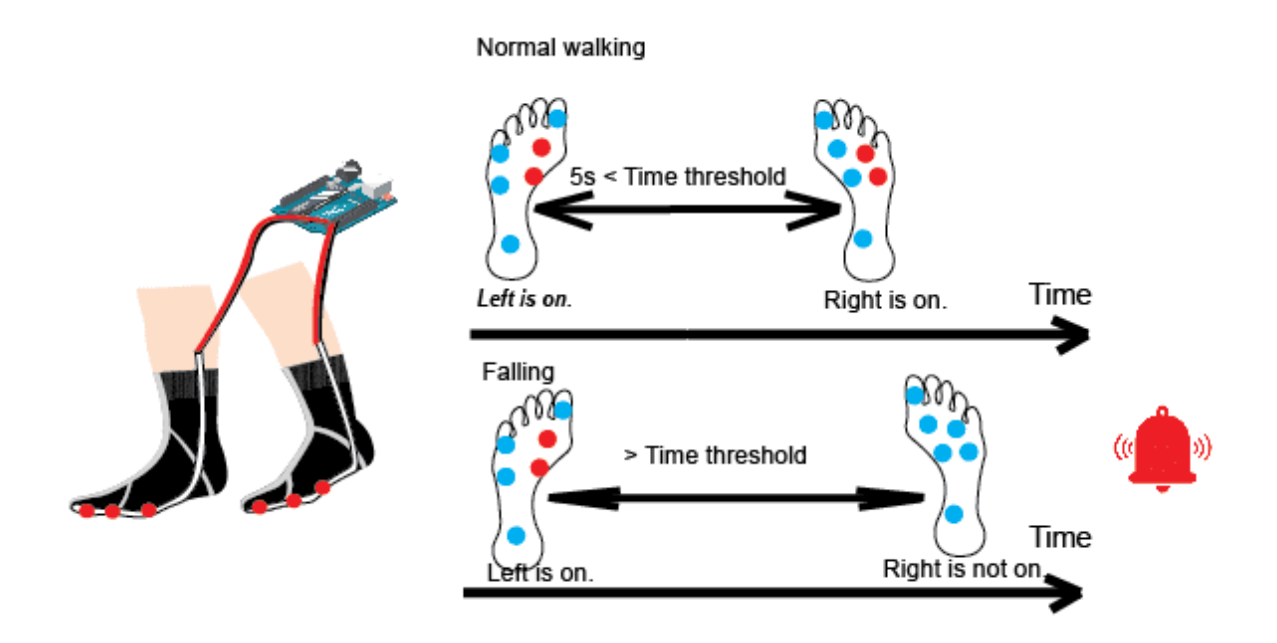


Figure 5-3. Mechanism, and design of the sock for Parkinson patient.

Pressure sensation platform: Since the mechanoreceptor pressure threshold can be designed and controlled, we tried to integrate the mechanoreceptors from two dimensions into three dimensions, to fabricate a pressure sensation platform. In addition, we fabricated an array for position detection with the integration of flexible resistors. **Figure 5-4** illustrates the cross-

section of the pressure sensation platform. It is evident that three different mechanoreceptors are overlapped, and series-connected with flexible resistors made up of conductive polyurethane film filled with carbon black, and graphene.

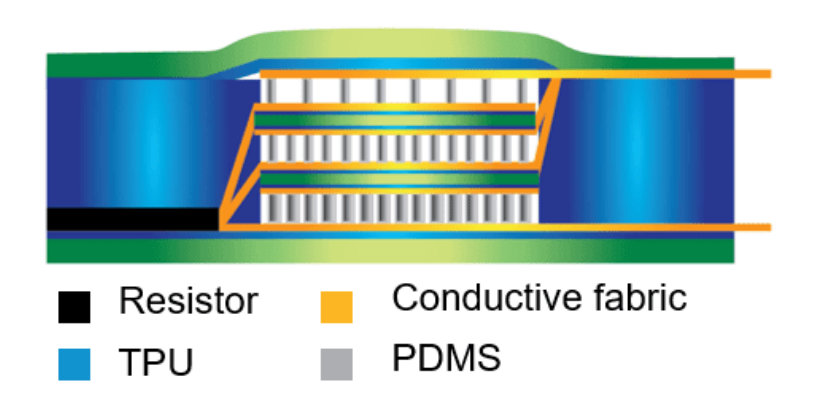


Figure 5-4. Cross-section of the pressure sensation platform.

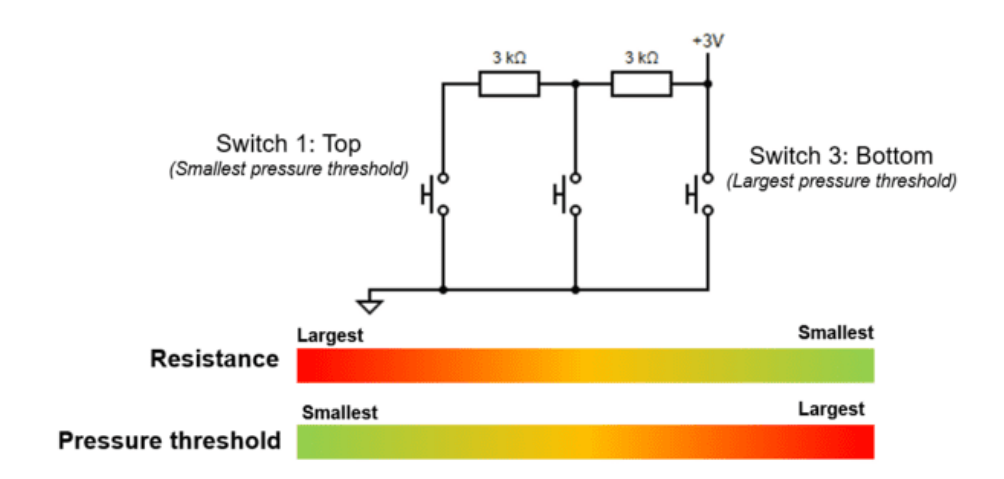


Figure 5-5. Electric diagram of the pressure sensation platform.

In detail, the mechanoreceptors with the largest pressure threshold (denser PDMS structures) are located at the bottom, and the mechanoreceptors with the smallest pressure threshold (sparse PDMS structures) are located at the top. For electrical connection, the mechanoreceptors with the smallest thresholds, and the middle one were series connected with flexible resistors. The corresponding electric diagram is shown in **Figure 5-5**. The resistance of mechanoreceptors with the largest pressure was lowest, while the resistance of

mechanoreceptors with the smallest pressure threshold was highest.

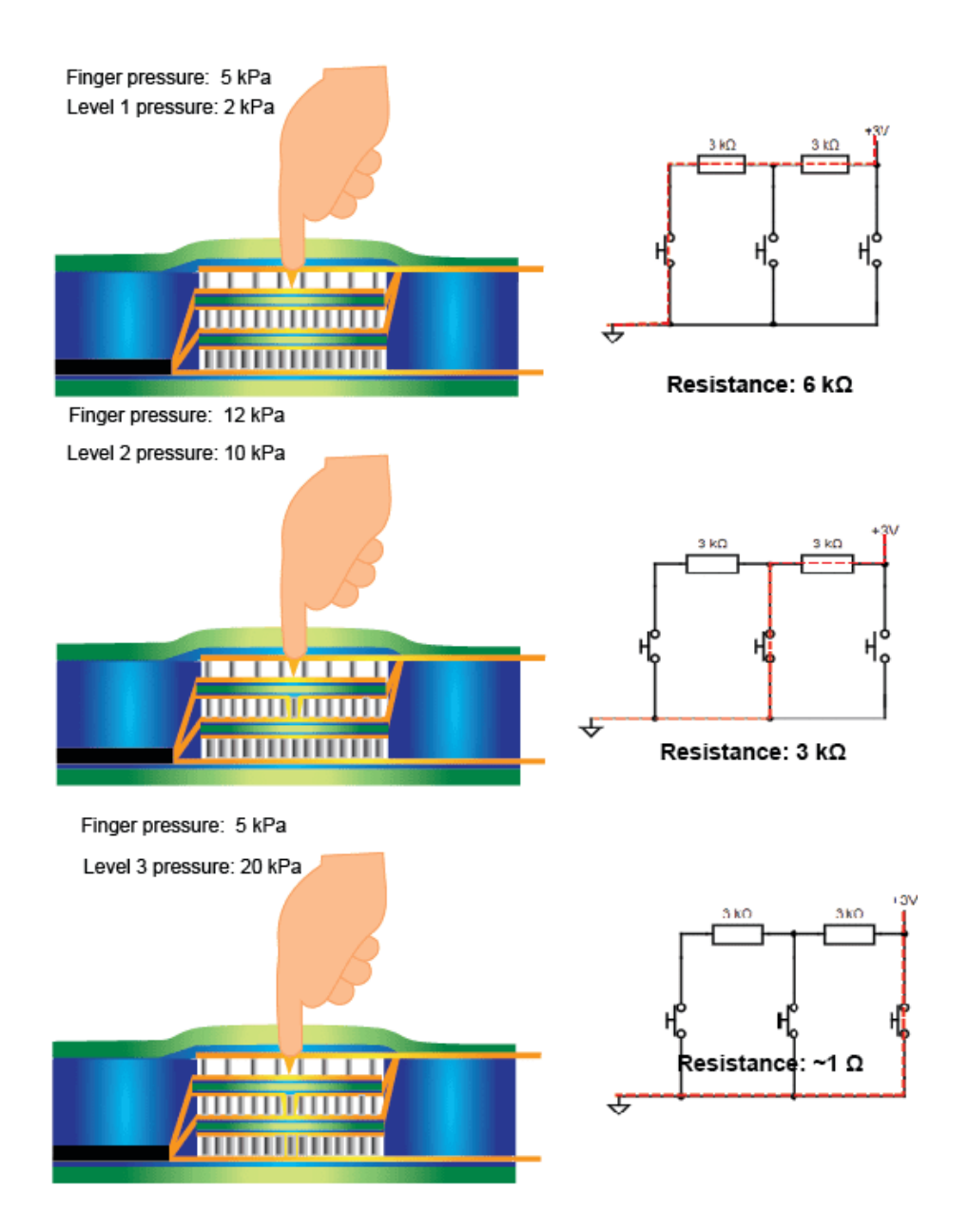


Figure 5-6. Mechanism of the pressure sensation platform.

Figure 5-6 demonstrates the mechanism of the sensation platform. When the pressure exceeds 2 kPa, the resistance output is 6 k Ω . As the pressure continuously increases to 10 kPa, the resistance output changes to 3 k Ω . When the pressure surpasses 20 kPa, the resistance drops to 1 Ω .

5.3. Preliminary experiment

In the preliminary experiments, we proposed to investigate the material applicability of the mechanoreceptors, and their array to wearable applications, and make necessary adaptations accordingly. Given the format of the wearable product, the sock is subjected to varying degrees of stretch in wear. The whole mechanoreceptors systems need to withstand stretch without damage.

There are two main primary considerations for this problem. The first one is related to the fixation or integration method of mechanoreceptors. The integration may not deteriorate the properties of the textile products. In addition, the connection or fixation method needs to be reliable to confirm that the mechanoreceptors cannot detach away from the textile product in wear, and usage. Another consideration is the design, and integration/development of flexible circuits, and other electronic components on wearable products. To realize the functionality, the mechanoreceptors require the cooperation of other electric elements, like batteries, and circuits. Previous circuits using conductive fabric, and polyurethane film are applicable to wearable products not require stretching. Considering the stretchability of the sock, the circuit also needs more development to be stretchable with an affordable electrical variation. In addition, the connection between the mechanoreceptors, and other electronic components also requires further study to ensure it can be sustained under stretching.

For the fixation problem of mechanoreceptors, we have tried several methods and evaluated their reliability in usage. We first tried to use lamination method to fix the mechanoreceptors onto the sock. After wearing the sock, the stretching in wear can easily detach the mechanoreceptors away from the sock because the applicability of the outside composite fabric with the TPU is not good. Another serious problem is the addition of TPU

may deteriorate the tensile properties of the sock, in which part of the fabric cannot be stretched. We then considered conventional sewing to fix the mechanoreceptors onto the sock. Directly sewing mechanoreceptors onto the sock may destroy the encapsulation, and/or the structure of the mechanoreceptors. We preferred to fix the mechanoreceptors onto a medium, which is also in charge of the electrical connection, and data transmission. An elastic bandage was selected. The solution for the second problem is using conductive yarn to replace the conductive polyurethane film. Even if the conductive yarn is flexible, the stretchability of the yarn is limited. Based on this, we need to design a serpentine circuit to withstand the stretching. For the serpentine circuit, the distance between the electrodes of the mechanoreceptors is small. Appropriate design needs to be selected to avoid short circuits.

The preliminary experiment only initially explores the integration method of the mechanoreceptors, and the array to the wearable product. There are still many problems, including the design of the mechanoreceptors, involving the compression area, and the size, calibration, and testing of the wearable products.

5.4. Experiment

The experiment of this chapter can be divided into three parts. The first part is related to the material testing. The material selected for the prototype was tested to evaluate its tensile, and the properties variation whether fitting to the usage of the product, not influencing the functionality of the mechanoreceptors. The second part is related to the design, fabrication, and calibration of the mechanoreceptors. Considering the applications, the parameters of the mechanoreceptors need further studies to be adopted. The final part is the testing of the wearable product, in which the mechanoreceptors can function normally under usage.

5.4.1. Materials

The materials used for the fabrication of mechanoreceptors, and their array are similar to Chapter 2, and Chapter 3. However, considering the application scenarios, and accessories, some additional materials will be used to develop the wearable systems.

Sports socks are used. Considering the skin condition, and application scenario, socks with more cushion from the brand SHUPA (Z081-Z082) were used. The sock composition was 69.5% polyester and 28.1 % polyamide.

An elastic bandage from Taobao is used to fit the mechanoreceptors onto the elastic accessories. As mentioned above, it also serves as a buffer layer to sustain the stretch during wearing, instead of mechanoreceptor to stretch in usage. The thickness of the bandage was 0.8 mm measured by a digital display thousandth thickness gauge (Sanliang Measuring Tools Co., Ltd., China).

To fabricate a stretchable circuit, conductive yarn was selected and used to replace the conductive fabric because its freedom of design is wider. The conductive yarn from Qingdao Zhiyuan Functional Fabrics Co., Ltd. was used. The conductivity of the yarn was. The yarn is a 2-ply yarn, in which the ply count is 70D.

5.4.2. Fabrication process of the prototype

The fabrication process of the mechanoreceptors is similar to the procedure in Chapter 3. Furthermore, the mechanoreceptors fabrication process was improved, taking into account the carrier textile properties, and the application requirements.



Figure 5-7. A schematic illustration of the serpentine circuit design.

Sock for diabetic foot ulcer: First, a serpentine circuit was designed, as shown in **Figure 5-7.** In details of the circuit design, two electrodes were fabricated with alternating interconnected triangles, and lines. The arrangement of triangles is opposite each other and staggered. This design was chosen to accommodate the stretchability of the sock without compromising the structural integrity. The integration, and the connection between the mechanoreceptors, and the circuit are simpler, so there is without short-circuit issue. Consequently, the circuit pattern was sewn onto the bandage using silver conductive yarn, and a sewing machine. **Figure 5-8** illustrates the photo of the stitched flexible circuit on the bandage.

Then, the mechanoreceptors with corresponding pressure thresholds were fabricated, and tested on the Instron 5566 machine, and an Agilent 34001a multimeter. The fabrication process of the mechanoreceptor was similar to the previous chapter. The mechanoreceptors were fixed and connected to the flexible circuit with stitching. An TPU layer was applied to both sides of the bandage to protect the circuit and mechanoreceptors. The entire bandage was then fixed to the sock with normal yarn. Additionally, a polyimide circuit with LEDs was wrapped with yarn, serving as electronic yarn, as demonstrated in **Figure 5-9.** The electronic yarn was connected to a lithium battery, and the pressure sensation system was based on the design.



Figure 5-8. Photo of the flexible stretchable circuit.



Figure 5-9. Photo of the electronic yarn.

Sock for Parkinson's patient: The fabrication process of this sock is similar to that of the sock for diabetic patients. The flexible circuit was produced with the silver conductive yarn, and bandage through machine sewing, and then the mechanoreceptors were fabricated, and connected to the circuit. The entire set-up was fixed to the sock via hand-sewing. Unlike the sock for diabetic foot, a pair of socks is needed for gait analysis, in which the pressure threshold and positions of the mechanoreceptors are different. Each sock contains six mechanoreceptors. One is located at the heel, and the other five are located at the forefoot. The pressure threshold of the mechanoreceptor was settled at 30 kPa, depending on the human body weight, and feet size. Two socks were finally connected to an Arduino board. In addition to the hardware set-up, a programme was created to determine whether the patient is falling or not.

Pressure sensation platform: The pressure sensation platform structure is very complex, and its assembly step is different from that of the mechanoreceptors described in

previous chapters. In detail, the PDMS structure was firstly stencil printed on the electrode, followed by solidification. Three different types of PDMS structures, each indicating three different pressure thresholds, were printed.

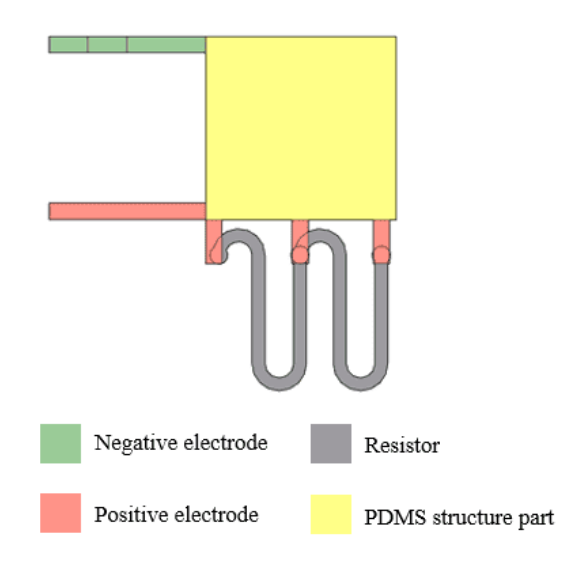


Figure 5-10. A schematic diagram of the connection of the pressure sensation platform.

Referring to **Figure 5-4**, there are a total of four composite fabric layers, of which two are located in the middle of the platform, and two are located as shells. An additional TPU layer was laminated on both sides of the middle two composite fabrics. In the case of these two composite fabrics, one side laminated the electrodes with PDMS structure, and another side laminated with the pure electrode. In the cases of the shell composite fabrics, one outer shell composite fabric was only laminated with PDMS structure, and another one was only laminated with electrode.

After these, three additional TPU layers were cut with a 16 mm diameter hole, and laminated to the PDMS structure at 80°C for 3s. Consequently, the four layers of composite fabrics were stacked, and connected with resistors, and conductive tape. The three positive electrodes were series connected with resistors, and all three negative electrodes also were overlapped to form the output electrode, as demonstrated in **Figure 5-10**. Finally, a hot

lamination was conducted to assemble all layers together at 80°C for 3s.

5.4.3. Testing

The testing process can be divided into material testing, mechanoreceptor testing, and wearable product testing. Material testing is primarily concerned with evaluating the tensile strength, and longevity of the material to confirm its suitability for the applications. Mechanoreceptor testing is focused on ensuring that the pressure threshold of the mechanoreceptors aligns with the specific requirements of the applications. Meanwhile, wearable product testing is centered on assessing the functionality of the mechanoreceptor in the wearable format, ensuring that it matches the performance in laboratory testing. In addition, we conducted an improvement on the user experience of the mechanoreceptor. Details of the experiments will be provided in the subsequent section.

5.4.3.1. Material Testing

As previously mentioned, bandage acts as an important carrier for the fixation of the mechanoreceptor, and the circuit function. Selecting an appropriate bandage is essential. The tensile strength of the bandage was measured with Instron 5544 in extension mode to ensure that the elasticity of the bandage can sustain the stretching of the sock during wear. There are two types of samples for evaluation: one is the pure bandage, and another is the bandage encapsulated with a TPU layer for protection. In details of the sample fabrication, the bandage was laminated with two layers of TPU 0.1 mm in thickness at 80 °C for 3 s. The tensile strength fabric sample was 15 cm in length. The testing speed was 300 mm/min.

In addition to the bandage tensile strength, cyclic tensile tests were also conducted to evaluate the longevity of the bandage, and the laminated bandage. The stretch rate was set at

30%. The stretching cycles were settled at 100 cycles, aligning with the replacement frequency of the sock.

In addition to the above bandage mechanical properties, the electrical properties of the serpentine circuit were tested. The resistance variation of the serpentine circuit under stretching was evaluated with Instron 5566, and an Agilent multimeter 34001a. The sample size of the circuit was 15 mm in diameter. The stretch rate was set at 30%. Instron 5566 provides stretching, while the multimeter records the resistance variation.

5.4.3.2. Mechanoreceptors testing

Mechanoreceptor parameter study: Chapter 2 explores the potential of controlling the parameters of the PDMS structure to control the pressure thresholds of the mechanoreceptors. Apart from these factors, there are other parameters influencing the pressure threshold of the mechanoreceptors. The most important two factors are the size of mechanoreceptors and the compression area. Both factors play a crucial role in the integration of mechanoreceptors in wearable applications. It is valuable to investigate the impact of these factors on the mechanoreceptors.

One premise for the functionality of this mechanoreceptor is that the mechanoreceptors size needs to be larger than the compression area. If the compression area is larger than the size of the mechanoreceptors, the generated pressure will be applied to the non-compression area, resulting in the non-contact of the electrodes under compression. In the design of this experiment, the compression area, and the size of the mechanoreceptor may interact with each other to influence the pressure threshold. The size of the mechanoreceptor was determined by the TPU hole size, which was settled as 6 mm, 8 mm, 10 mm, 12 mm, 14 mm, 16 mm, 18 mm, and 20 mm in diameter. The compression area was settled as 4 mm, 6 mm, 8 mm, 10 mm, 12

mm, 14 mm, 16 mm, and 18 mm in diameter. The experiment design is listed in **Table 5-2**, in which the blue shade area indicates the parameters of the conducted experiments.

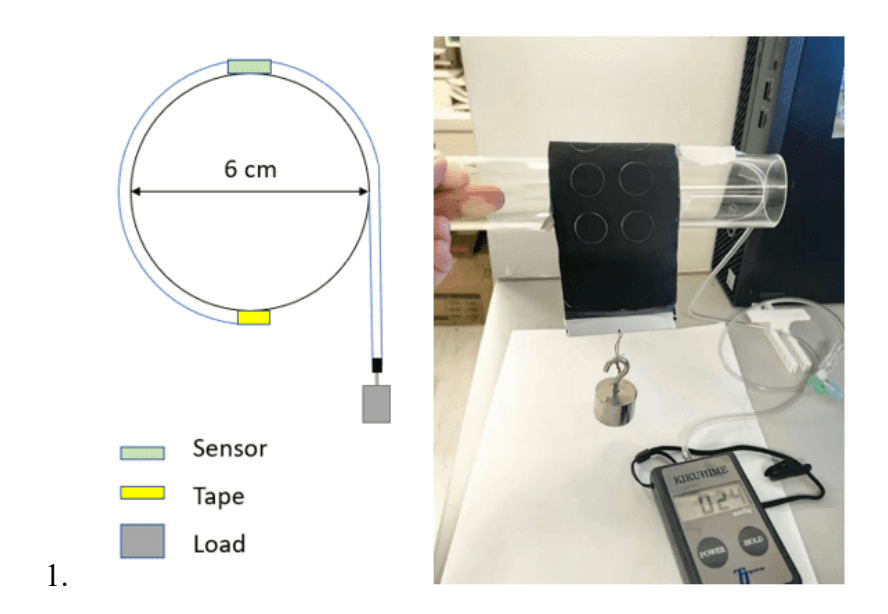
Table 5-2. Experiment design about the compression area, and size

	Compression area (mm)									
		4	6	8	10	12	14	16	18	
Size of mechanoreceptor (mm)	6									
	8									
	10									
	12									
	14									
	16									
	18									
	20									

In the details of the experiment, different acrylic cylinders were fabricated with different diameters corresponding to the compression area parameter. The fabrication process of the mechanoreceptor was the same as that of the Chapter 3, except that the TPU hole was cut in different sizes. Then, Instron 5566, an Agilent multimeter, and a power source were used to evaluate the interrelationship between the pressure thresholds, the compression area, and the size of the mechanoreceptor.

Wearable applications: In the context of wearable applications, mechanoreceptors with corresponding pressure thresholds were fabricated. The pressure threshold of the fabricated mechanoreceptors was then measured to assess whether it matched the required specifications. To examine the electromechanical properties of the mechanoreceptor, an Agilent 34401a multimeter, Instron 5566, and a power source were utilized. In addition, considering the usage scenario can involve bending, different radii acrylic hemispheres were fabricated to facilitate pressure mechanoreceptor testing.

5.4.3.3. User experience improvement



2. Figure 5-11. Experiment set-up of the pressure measurement.

To improve the comfort of the mechanoreceptor system, we attempted to use thinner fabric to replace the composite fabric to reduce the thickness of the array. The thickness of the mechanoreceptors was measured by the thickness gauge (Sanliang Measuring Tools Co., Ltd., China).

In addition, the pressure after wearing the mechanoreceptors was measured. Two acrylic tubes with a diameter of 6 cm, and 4 cm were used. A pressure sensor (Kikuhimie pressure measuring device) was used to measure the pressure in mmHg, while the precision of the measurement is +/- 8 mmHg. The dimension of the mechanoreceptor array was 6.5 cm in width and 19.5 cm in length. One side of the array was fixed onto the tube with tape. Another side of the array was fixed with a plastic stick. Then, a 95.84 g weight was added to the plastic stick. The plastic stick can ensure that the pressure is uniformly applied to the array. **Figure 5-11** illustrates the pressure measurement of the thinner mechanoreceptors array.

To further evaluate the improvement of the mechanoreceptors with thinner fabric, we measured the bending rigidity of the mechanoreceptors with the pure bending tester KAWABATA system. The sample size used for the measurement was 7 cm in width.

5.5. Results and discussion

The following section will discuss the result from the material, mechanoreceptors, and then to the wearable applications.

5.5.1. Material tensile properties

Figure 5-13 shows the tensile properties of the bandage, and Figure 5-14 shows the tensile properties of the laminated bandage. The maximum tensile strength of pure bandage was around 230.67 N (SD: 56.07), while the maximum tensile strength was around 285.17 N (SD: 10.02). TPU layer may act as adhesive to limit the deformation of the yarn and fabric under stretching. The tensile strength of the laminated bandage is higher than that of pure by about 23.62%. In addition, there is a greater variation in the tensile strength of the pure bandage than that of the bandage with TPU because the initiation of the bandage damage is the breakdown of fiber, while the laminated bandage broke down completely.

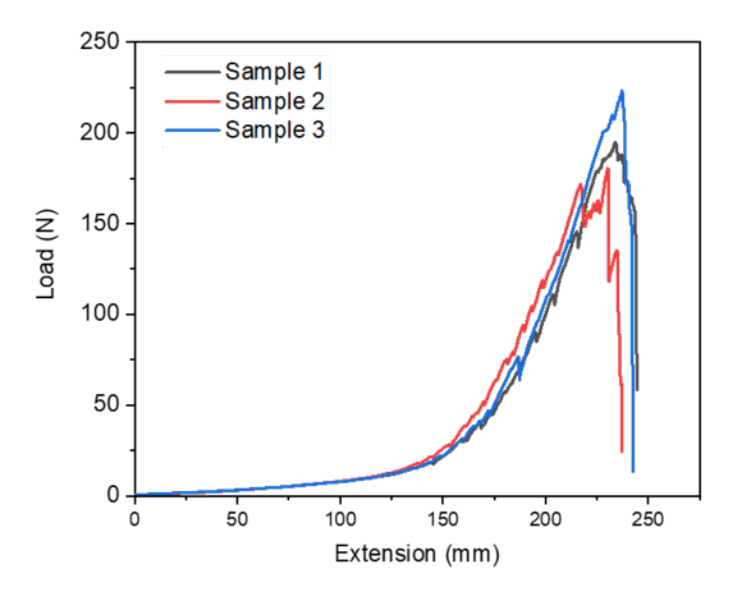


Figure 5-12. Tensile properties of the bandage.

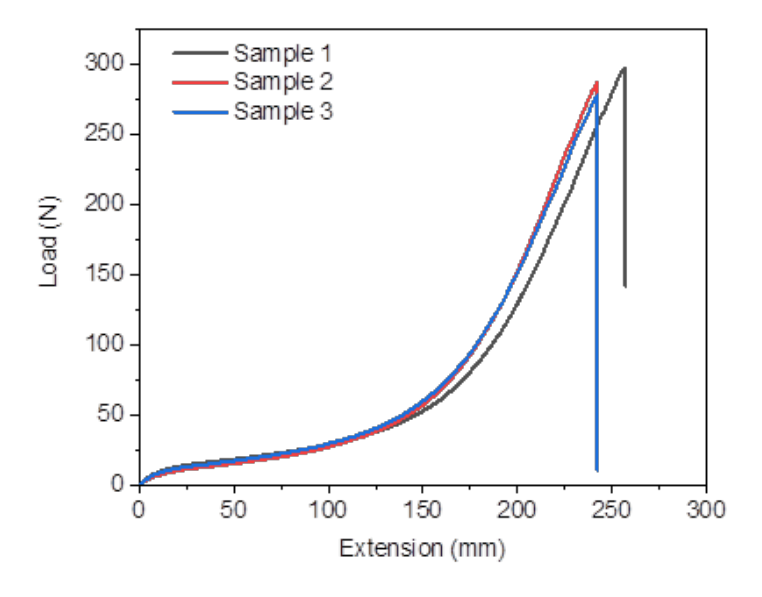


Figure 5-13. Tensile properties of the encapsulated bandage.

We also conduct one hundred stretching cycles at 30% stretching. **Figure 5-15** illustrates the cyclic tensile properties of the pure bandage, and **Figure 5-16** demonstrates the cyclic tensile properties of the laminated bandage. Compared to these two figures, it was obvious that the laminated bandage required a larger force for stretching to 30%. The difference in stretching force was over 8 times. This result brings challenge to the comfort, and usage of the sock. Another notable difference is that the tensile strength of the laminated bandage

decreases as the stretching cycles increase. Additionally, the laminated bandage appearance after 100 cycles of stretching is not the same as the initial state. The color may change to white, indicating the delamination of TPU after usage. This suggests that adding the TPU layer as an encapsulation layer may not be appropriate for long-term usage. It is suggested to use other materials, and fabrication techniques to develop water-proof layers for the stretchable circuit.

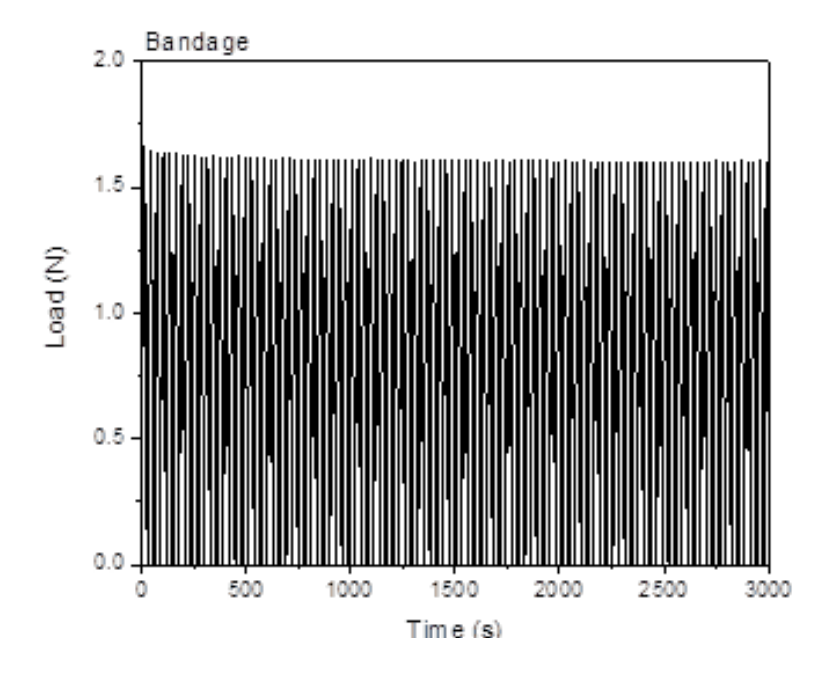


Figure 5-14. Cyclic tensile properties of the bandage

The resistance variation of the serpentine circuit in the bandage was evaluated with 100 stretching cycles with a strain rate of 30%. **Figure 5-17** illustrates the results. At the initial, the resistance of the circuit was only 116.57 Ω . At the strain rate of 30%, the resistance increased to 146.64 Ω . It increased around 25.79 %. When wearing the sock, the circuit resistance will increase. Additionally, the resistance of the circuit cannot return to its initial after the relieving of the stretch. After 100 cycles of stretching, the resistance of the circuit was 136.31 Ω . It increased around 16.9%. At the 100 cycles of stretching, the resistance of the circuit at 30% stretching was 193.13 Ω . The difference between the resistance value at cycle 1, and cycle 100 was 31.70 Ω . Even though there is a great change in the resistance value of the serpentine

circuit, the high on-off ratio of the mechanoreceptors over eight orders of magnitude can confirm the functionality or decision-making of the wearable products is not influenced by the resistance changing in wearing the products. The resistance variation in stretching can be attributed to the structural deformation of the yarn with longer conductive paths, and the change of contact points between the conductive fiber within the yarn.

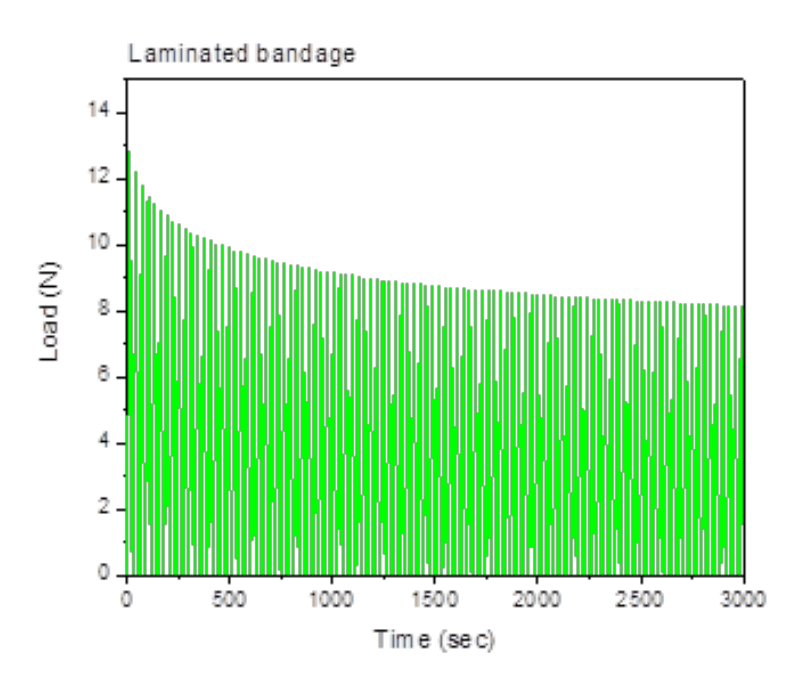


Figure 5-15. Cyclic tensile properties of the laminated bandage

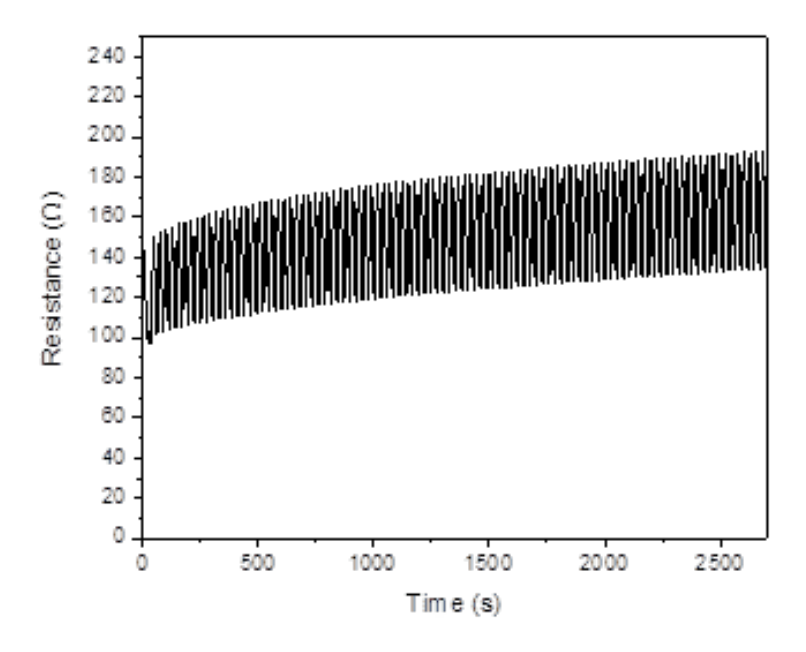


Figure 5-16. Resistance change of the serpentine circuit(strain rate: 30%).

5.5.2. Interrelationship between pressure thresholds, and other factors

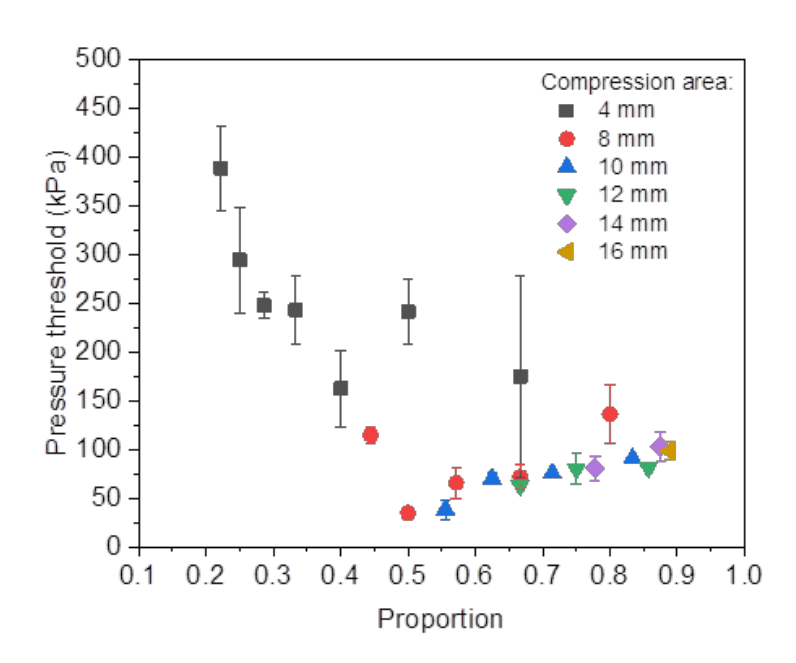


Figure 5-17. Pressure threshold of the mechanoreceptors with different sizes.

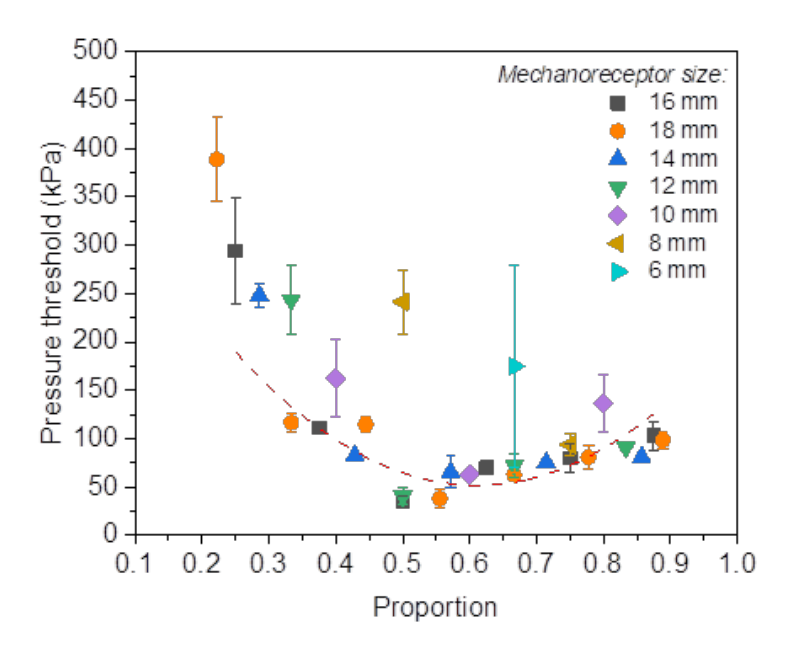


Figure 5-18. Pressure thresholds of the mechanoreceptors with different compression area.

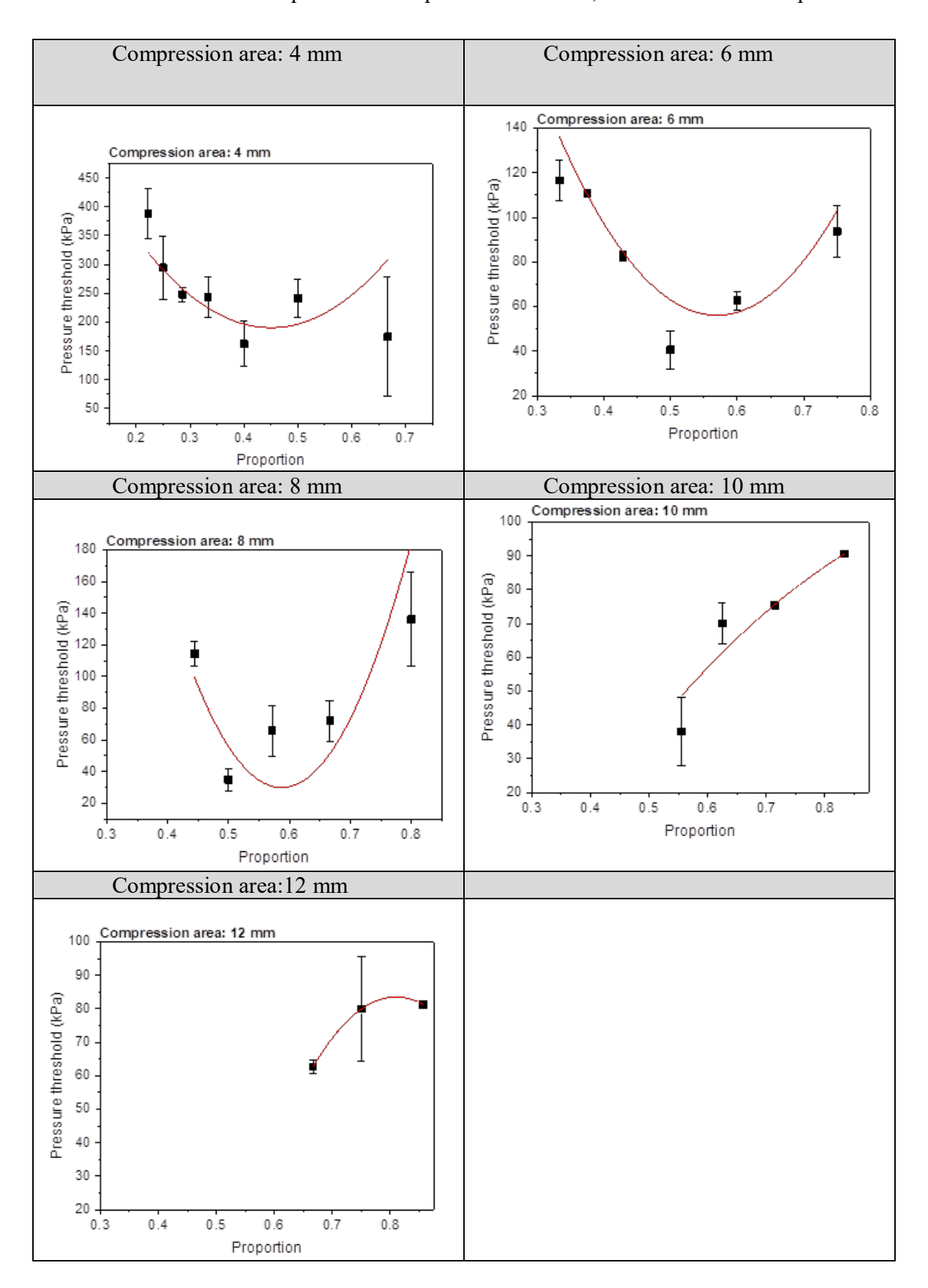
Reducing the size of the mechanoreceptors is a crucial step in adopting the mechanoreceptors for different wearable applications. However, it is important to consider that the size of the mechanoreceptors may influence the compression pressure threshold of the mechanoreceptors. Despite the PDMS structural parameters, there are two other factors relating to the size of mechanoreceptors influencing the pressure threshold-compression area, and the size of the mechanoreceptors. The previous two chapters only studied the pressure threshold based on the same compression area (10 mm in diameter), and the size of the mechanoreceptors (TPU hole: 16 mm in diameter). We found out that the compression area should be smaller than the size of the mechanoreceptors. If the compression area is larger than the size of the mechanoreceptors, the force will be applied to the TPU instead of the PDMS structure. Then, the PDMS structure cannot be deformed, the conductive electrode cannot be in contact with each other.

Based on this, we conducted a systematic study on the impact of the compression area, and the mechanoreceptor size. Since these factors interact with each other, we calculated the proportion between them to analyze their effects. **Figure 5-18** illustrates the effect of the size of the mechanoreceptors when the compression area is fixed. **Figure 5-19** depicts the effect of the compression area on its pressure threshold when the size of the mechanoreceptor is fixed. These two figures show that the relationship between the proportion to the compression area/size of the mechanoreceptors is a quadratic relationship.

For a detailed analysis, we plotted the interrelationship between the proportion to the compression area or the size of the mechanoreceptors for each group, as shown in **Table 5-3**, and **Table 5-4**. Clear parabola trends are evident in these graphs. This suggests that when the proportion is lower, the pressure threshold may be larger. When the proportion is larger, the pressure threshold also will be larger. An optimal proportion exists if the pressure threshold of

the mechanoreceptors is preferred to be lower[7]. This differed from the results of a pressure-sensitive resistor, in which the pressure threshold decreases as the size of the hole increases. It can be attributed to the presence of the PDMS structure in the insulation layer. With a smaller compression area, the compression moment can be equal to a three-point bending. The moment of the upper electrode is smaller. However, since the area is small, the force will be larger. Conversely, when the compression area is over a certain ratio, its compression cannot be equivalent to a three-point bending. The deformation of the upper electrode needs to be more. The distance between the electrode and the TPU spacer is shorter. As a result, more force is required to deform the upper electrode in contact with the lower electrode.

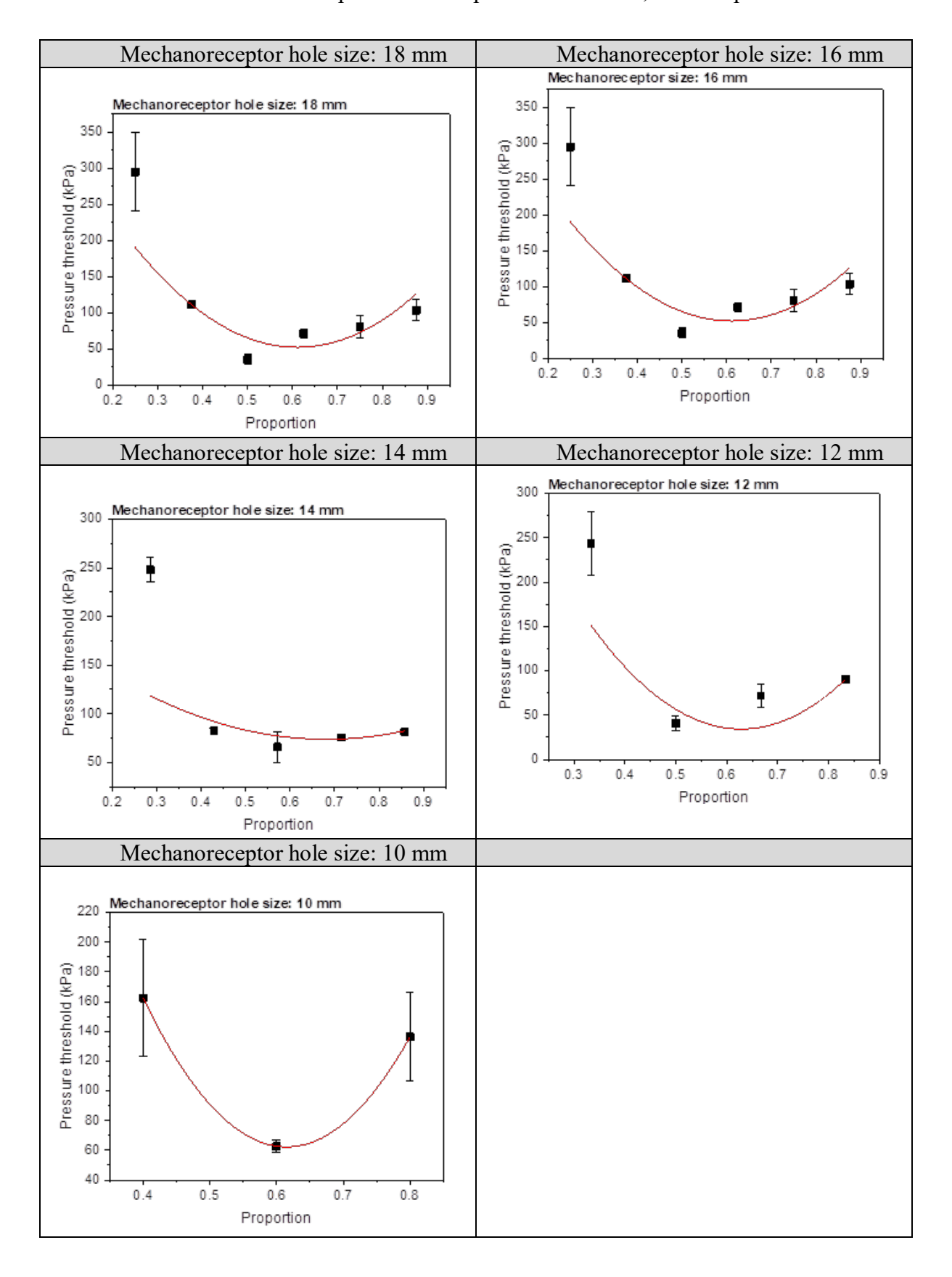
Table 5-3. Interrelationship between the pressure threshold, and the mechanoreceptor size



In addition to the optimal ratio between the size of the mechanoreceptor, and compression area, it was obvious that as the proportion became smaller, there was a larger variation among sample pressure thresholds. This may be attributed to several reasons, as follows: When the compression area is reduced to 4 mm, there is a great variation in the arrangement of PDMS structures in the compressed area. In particular, the smallest unit of the structure with an 11.11% material filling rate may contain four PDMS pillars, and its area is around 2.5 *2.5 mm. Under the compression area of 4 mm, it only can cover 1.6 units. The effects of the structural variation impacting the pressure threshold will be enlarged. The variations encompass the deformation of the structure during printing, the arrangement of the structure in the compression area, like number of pillars in the compression area, and the location of the compression. For current control of the fabrication, and PDMS structure, it is more appropriate to use a larger compression area instead of a smaller one.

On the other hand, it is necessary to reduce the above variation for practical applications. One solution is adding a fixed compression area to the outside shell of the mechanoreceptor to reduce the compression position variation. Given that the human body contour normally follows a curved line rather than a straight line, this approach could enhance the performance of the mechanoreceptors.

Table 5-4. Interrelationship between the pressure threshold, and compression area



5.5.3. Testing of diabetic foot pressure monitoring system

Considering the shape and pressure distribution of the foot, bending needs to be considered in designing the pressure threshold of the mechanoreceptors. The position of the mechanoreceptors in the sock suffers different degrees of bending. Considering the design of the sock for diabetic patients, we measure the radius of the bending at different foot positions of a silicone foot model. The shape of the silicone foot model is established through the utilization of 3D scanning data, ensuring a precise 1:1 representation of real human feet. At the side of the hallux, the diameter radius of the curvature was measured at around 2.5 cm, while the diameter radius of the curvature at the side of the toe was measured as 1.5 cm.

Considering the unpredictable effects of compression areas in wearable applications, we took the approach of fixing a PDMS pad on the mechanoreceptor to fix the compression area. The diameter of the pad was 6 mm. In details of the mechanoreceptors' pressure threshold, it was observed that bending increases the requirement of the pressure threshold. Through experiments, it found out that the mechanoreceptor at higher bending degrees, like 30 degrees, the pressure threshold may only remain in the range of 10 to 30% at the plain. Based on this, the designed pressure threshold of the mechanoreceptor at the bending radius of 1.5 cm, and 2.5 cm was estimated to be approximately 2 MPa.

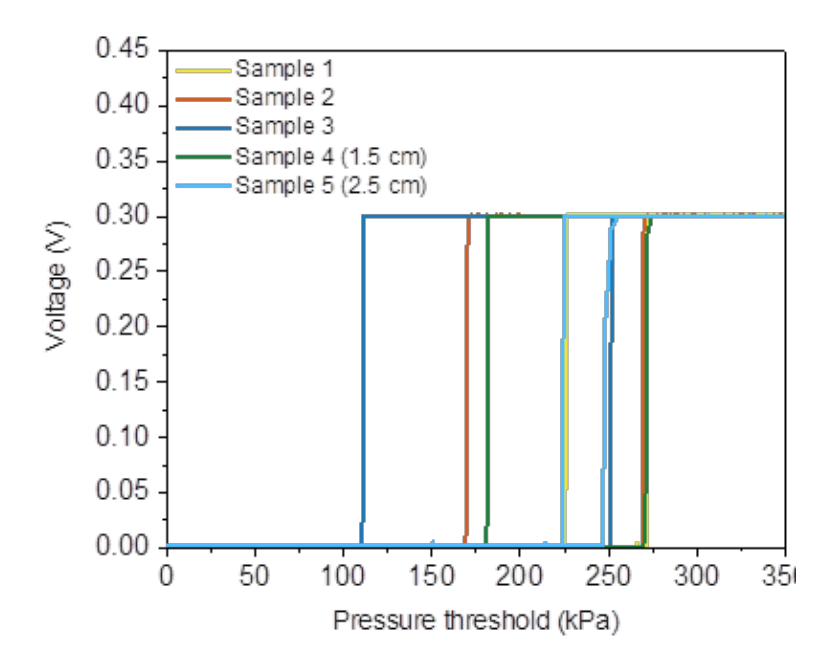


Figure 5-19. Voltage response of the mechanoreceptors under compression.

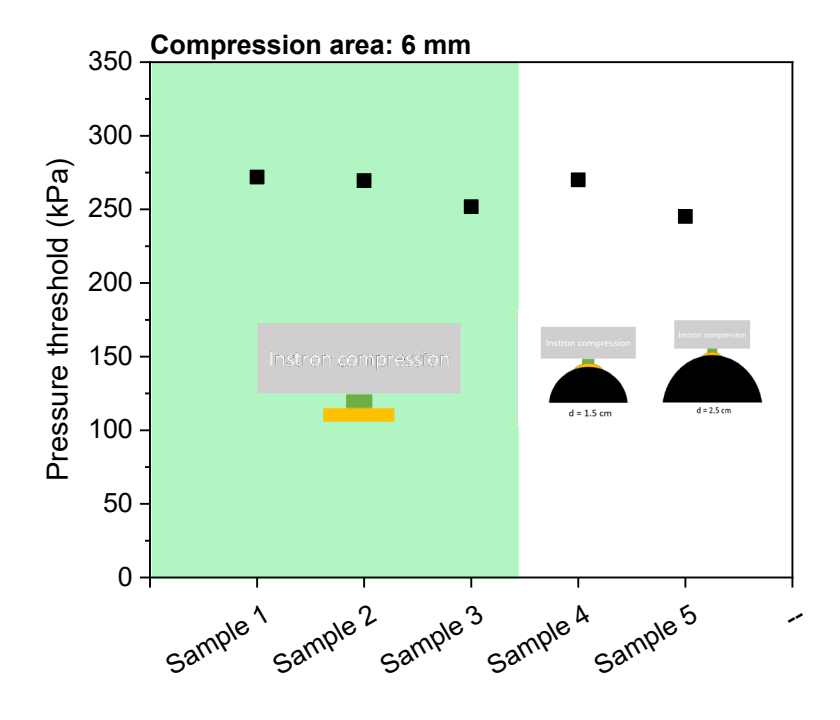


Figure 5-20. Pressure threshold of the mechanoreceptors.

Then, five mechanoreceptors were fabricated, in which pressure threshold was controlled via material and PDMS structure design. Three mechanoreceptors were measured under compression without bending. Another two mechanoreceptors were fixed on an acrylic

hemisphere with a diameter of 1.5 cm, and 2.5 cm respectively to simulate the shape of the foot. **Figure 5-20** depicts the voltage response of the mechanoreceptors under compression, while **Figure 5-21** summarizes the pressure threshold of the five mechanoreceptors.

It was found that all five mechanoreceptors' pressure threshold was over 250 kPa. The average pressure threshold of the mechanoreceptors was 261.71 N. The standard deviation was around 12.34. The control of the pressure threshold of the mechanoreceptors is not very accurate, and precise, but it can serve as a benchmark to remind the sensation loss of diabetic patients.



Figure 5-21. Mannequin wearing the sock for diabetic patients. Left: LED is in off-state.

Right: LED is in on-state.

Then, we integrated the five mechanoreceptors into a sock as shown in **Figure 5-22**. The left photo demonstrates the outlook of the sock, while the right photo demonstrates the onstate of the mechanoreceptors. Throughout testing, it was discovered that the connection between the battery, and the bandage is not very reliable. It is easy to be broken due to the rigid nature of the connection. Since the sock is stretchable, the stretchability is not only in the x-direction, but also in the y-direction. Therefore, it is suggested to develop a stretchable

connection between the rigid electrical components, and the flexible components.

5.5.4. Testing of Parkinson gait analysis system

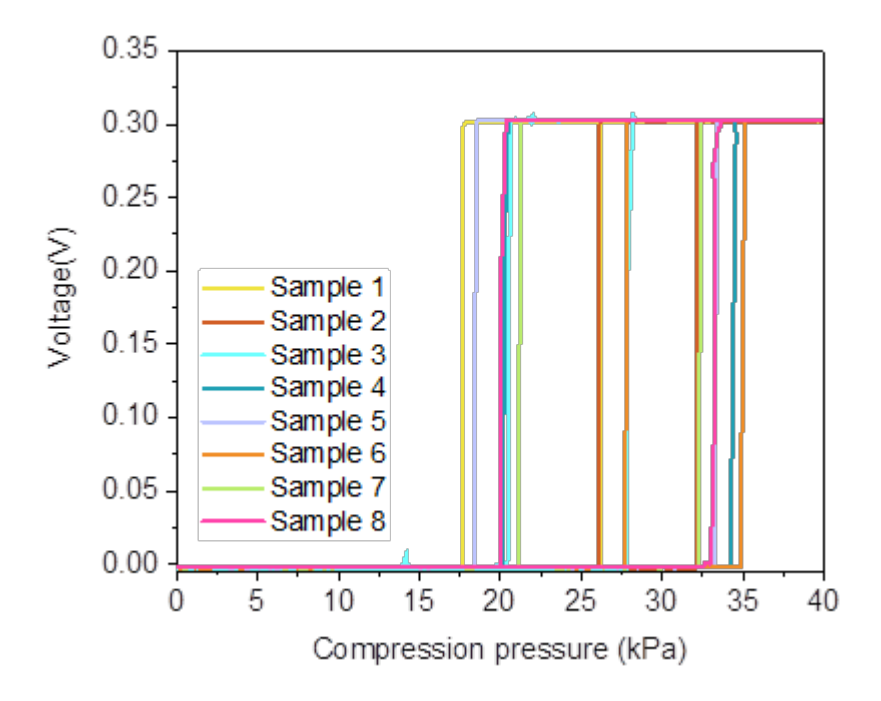


Figure 5-22. Voltage response of the mechanoreceptor for Parkinson patient.

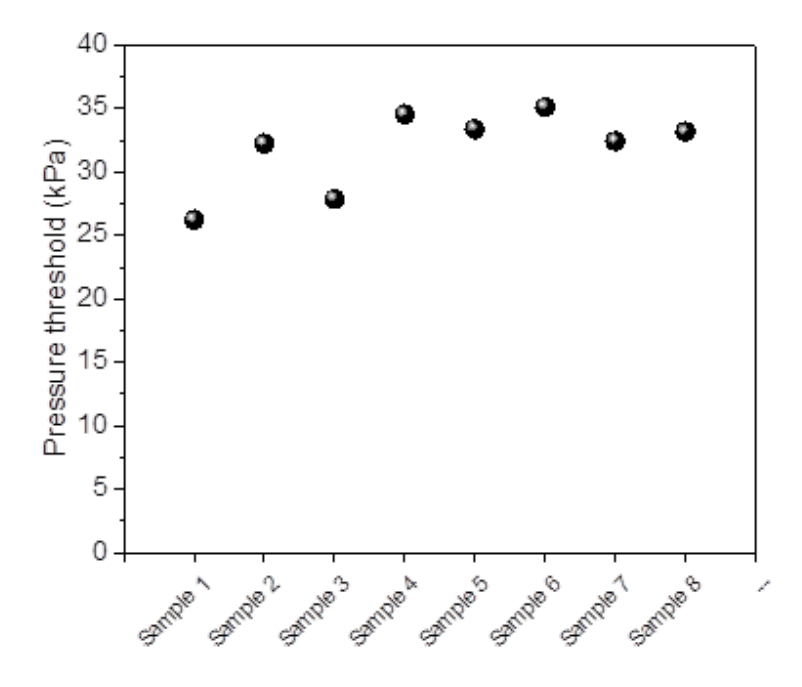


Figure 5-23. Pressure threshold of the mechanoreceptor for Parkinson patient.

Differing to the mechanoreceptors in the sock for diabetic patients, the mechanoreceptors in the sock for Parkinson's patient are located at plantar of the foot. There is no obvious bending condition involved. The mechanoreceptor was tested under the plantar compression. Figure 5-22 illustrates the voltage response of the mechanoreceptors, and Figure 5-23 illustrates the pressure threshold of the mechanoreceptors. The average pressure threshold of the mechanoreceptor was 31.87 N, and the standard deviation was 3.166. The mechanoreceptors were then integrated into the flexible circuit, and then into the sock. Figure 5-24 demonstrates the sock for Parkinson's patients.



Figure 5-24. Photo of the sock for gait analysis.

We measured the resistance of the socks while the user was sitting, as illustrated in Figure 5-25. Despite the user being seated, the socks remained in the on-state, indicating that the mechanoreceptors are highly sensitive to the foot's condition. This sensitivity shows great potential for gait analysis. The on-state resistance for the left sock was 250.6 Ω , whereas for the right sock, it was 0.9 Ω . Due to time constraints, the corresponding software will be

developed at a later stage.



Figure 5-25. Photo of the measurement of the sock when the users in sitting.

5.5.5. Pressure sensation platform

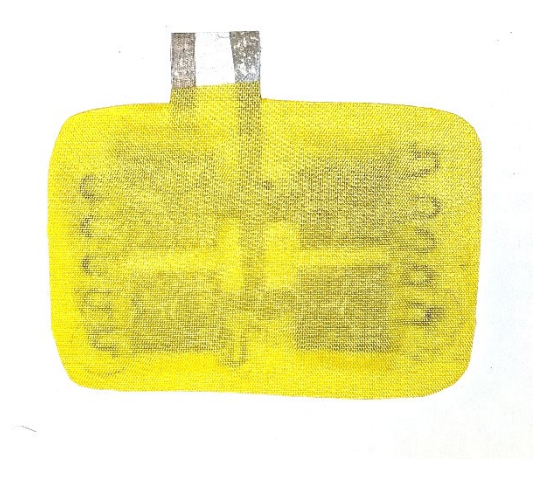


Figure 5-26. Photo of the pressure sensation platform.

For the pressure sensation platform, we fabricated an array of pressure sensation units consisting of four positions, as shown in **Figure 5-26.** Each unit can detect three levels of pressure, resulting in three different resistance value. In addition, the position of the compression also can be detected based on the unique resistance values. This was similar to the mechanoreceptor array in Chapter 4. The pressure sensation platform is designed to

enhance the reliability of pressure detection, enabling applications in various fields such as robotics, and prosthetics. **Figure 5-27** demonstrates the resistance value of the platform under different levels of compression. The tested compression area is around 4 mm. It was observed that the first level of the pressure platform is in the range of 200 to 300 kPa, the second level is in the range of 3000 to 7000 kPa, and the third threshold is in the range of 7000 to 90000 kPa. The pressure threshold is significantly large. However, even if three mechanoreceptors overlap, the mechanoreceptor shows a good on-off ratio. The off-state resistance is over 120 $M\Omega$, which cannot be detected by the multimeter. Besides the large pressure threshold, another serious problem is that there is a variation between the pressure thresholds at different positions. This was attributed to the fabrication variations among mechanoreceptors.

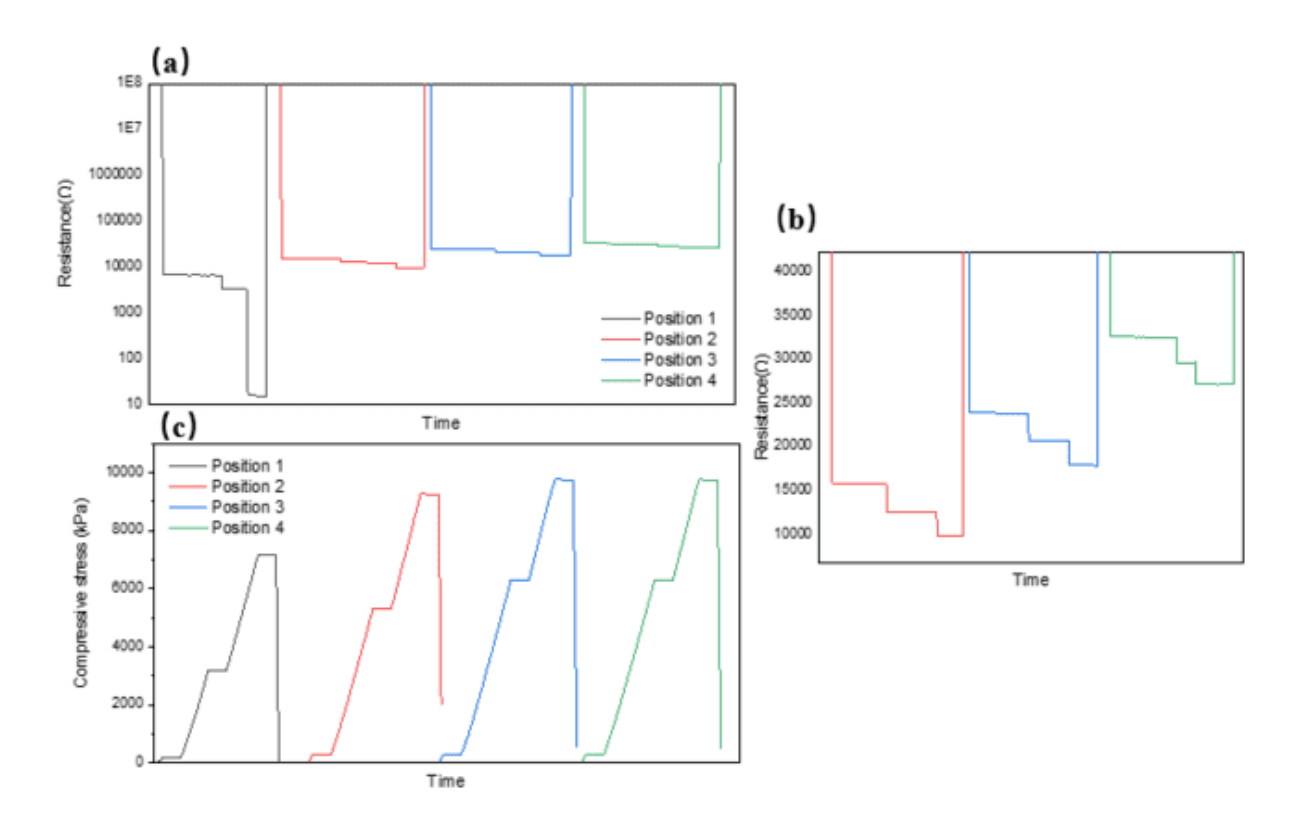


Figure 5-27. Response of the pressure sensation platform. (a) Resistance of the mechanoreceptor. (b) Enlarged of the resistance of the mechanoreceptor at position 2, 3, and 4. (c) Instron compression data.

However, the pressure threshold of this current sensation platform is significantly

higher, rendering it unsuitable for the pressure sensation for garments, and clothing. One reason for this is the poor controllability of the PDMS structure. The design of the pressure threshold of the mechanoreceptor is also typically in the range of several kPa to MPa. Additionally, previous experiments have demonstrated variations in the pressure thresholds of the mechanoreceptors. To realize multiple levels of pressure sensation below 10 kPa, there is a stringent requirement in the PDMS fabrication structure, involving the use of softer materials, and precise control of the PDMS structure deformation during printing. It is preferred to have control of the pressure threshold at the Pa level. Another factor is that the overlapping of the mechanoreceptors may impact the pressure transduction to the mechanoreceptors. The utilization of the multiple mechanoreceptors results in differences in the compression moment under the same compression force. This may impact the pressure sensation bottom mechanoreceptor. These factors will be studied in the future

5.5.6. Improvement on user experience

Table 5-5. Design of the mechanoreceptor array.

	Yellow	Black Version 1	Black Version 2
Composite fabric 1	0.15	0.09	0.09
TPU	0.1	0.1	0.05
Electrode 1	0.03	0.03	0.03
PDMS	0.1	0.1	0.1
Electrode 2	0.03	0.03	0.03
TPU	0.1	0.1	0.05
Composite fabric 2	0.15	0.09	0.09
Total thickness:	0.66	0.54	0.44

To enhance a good user experience, pressure comfort is an important parameter for wearable applications. Wearable product's comfort is highly influenced by the material stiffness and the thickness of the device. We conducted a study to reduce the thickness of the device for better pressure comfort. The mechanoreceptors array was composed of seven layers, in which the composite fabric and TPU layer thickness is over half of the device. We tried to find thinner composite fabric, and a TPU layer to replace the original one. **Table 5-5** shows the design of the array with different thicknesses of materials. **Table 5-6** displays the thickness of the mechanoreceptor array measured by the thickness gauge. Considering the structure of the mechanoreceptors, the thickness of the array was measured at different positions, including compression area, and non-compression area.

Table 5-6. Thickness measurement of the mechanoreceptor array.

Plan	Position	Thickness	Standard variation
Yellow	Compression area	0.754	0.031
	Non-compression area	0.573	0.061
Black 1	Compression area	0.570	0.052
	Non-compression area	0.469	0.011
Black 2	Compression area	0.534	0.019
	Non-compression area	0.412	0.037

From **Table 5-6**, it was found that the thickness of the mechanoreceptor array compression area can be reduced from 0.754 mm to 0.574 mm, around 24. 40 %, through changing the outside composite fabric to a thinner one. In addition, the thickness can be continually reduced to 0.534 mm. The reduction was around 6.34 %. Compared to the compression, and non-compression area, it is clear that the non-compression area thickness was relatively lower than that of compression area due to the missing of the PDMS structure.

Table 5-7, and Table 5-8 show the pressure after wearing the mechanoreceptor array on the acrylic tube with the diameter of 4 cm, and 6 cm. In the case of the sample width, we only measured the pressure at two positions. For a 6 mm acrylic tube, the average pressure of the yellow array was 22 mmHg, while the black one was 18 mmHg. The pressure decreases around 18.18% after changing the composite fabric, and TPU. For a 4 mm acrylic tube, the pressure of the yellow array was 28.5 mmHg, while the pressure of the black array was 24.5 mmHg. The pressure decreases around 14.03%. These proved that reducing the thickness of the mechanoreceptor array can reduce the pressure generated by the human body. This can improve the comfort and the user experience of the products.

Table 5-7. Pressure measurement of mechanoreceptors (6 cm).

Acrylic tube: 6 cm	Position 1 pressure	Position 2 pressure
Unit	(mmHg)	(mmHg)
Yellow array	21	23
Black array	17	19

Table 5-8. Pressure measurement of mechanoreceptors (4 cm).

Acrylic tube: 4 cm	Position 1 pressure	Position 2 pressure
	(mmHg)	(mmHg)
Yellow array	30	27
Black array	24	25

In addition to the thickness, and the pressure measurement, the bending rigidity of the

keyboard was improved significantly by using thinner fabric to replace the composite fabric. In **Figure 5-28**, it can be observed that the 8 gF was required to bend the fabric at the bending rate of 1.5 cm. This sample only contained two rows of mechanoreceptors, and the total width was only around 7 cm. For the whole array, the bending force was calculated to be 16 gF. In Chapter 2, the bending force of the yellow keyboard was around 60 gF. The bending force decreases around four times. This is a great improvement in the conformability of the black keyboard, which can broaden the potential applications.

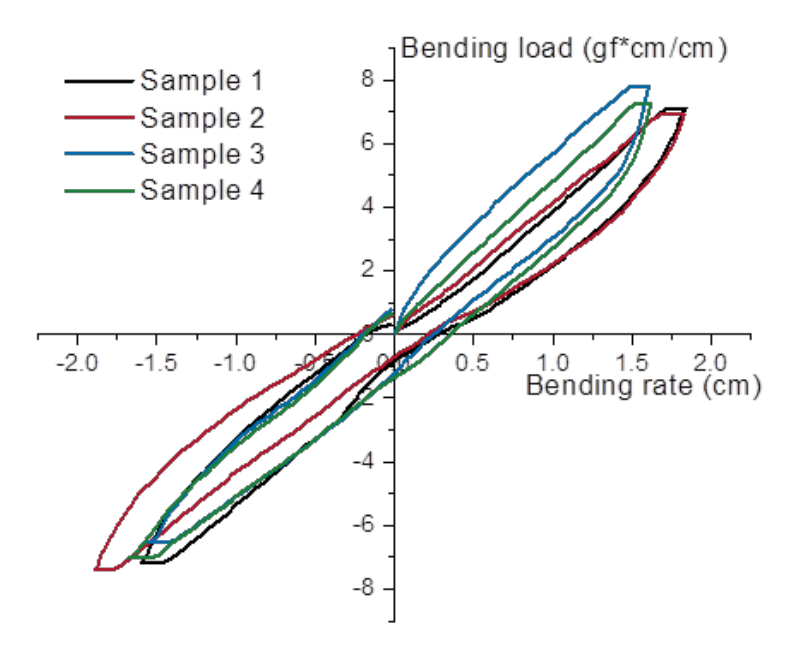


Figure 5-28. Bending rigidity of the mechanoreceptor array.

In summary, the user experience of the mechanoreceptor, and its array can be improved by using a thinner composite fabric, and TPU layer, as evidenced by measurements of thickness, pressure, and bending rigidity. However, further investigation is required to understand the impact of using thinner fabric on the mechanoreceptor's pressure threshold in later stages.

5.6. Conclusions

In this chapter, we explored the integration of mechanoreceptors, and their array into

different wearable products. One prototype is a plantar pressure alarming system for diabetic patients to select appropriate footwear to avoid overpressure. Another prototype is a simple gait analysis system to detect the falling of Parkinson's patients. The final prototype is related to a pressure sensation platform. It expands the potential of the functionality of the mechanoreceptors, not limiting to single pressure detection, and also can detect the position, and pressure.

However, there are still many problems, and challenges for the practice application of the mechanoreceptors. One is the adaptability of the materials to the applications. The above two mentioned products are stretchable accessories. This requires the circuit, connection, and all the electronic components, like resistors, need to be stretchable to withstand the force during usage. This poses challenges to the stability, reliability, and longevity of wearable products. Another challenge is the unexpected compression condition in wearable applications. All previous experience was conducted in the laboratory with fixed, and clear testing parameters. However, in wearable applications, it is difficult to fix the above testing parameters, like compression area. This may challenge the fidelity of the sensation in wearable applications. In addition to the usage scenario requirement, current controllability on the pressure thresholds of the mechanoreceptors also limits its application. Further studies will be conducted to solve the above problems.

5.7. References

- [1] X. Wang, C.-X. Yuan, B. Xu, and Z. Yu, "Diabetic foot ulcers: Classification, risk factors, and management," World journal of diabetes, vol. 13, no. 12, p. 1049, 2022.
- [2] J. V. Jorgetto, D. S. Oggiam, M. A. Gamba, and D. M. Kusahara, "Factors associated with changes in plantar pressure of people with peripheral diabetic neuropathy," Journal of Diabetes & Metabolic Disorders, vol. 21, no. 2, pp. 1577-1589, 2022.
- [3] L. Wang et al., "A review of wearable sensor systems to monitor plantar loading in the

- assessment of diabetic foot ulcers," IEEE Transactions on Biomedical Engineering, vol. 67, no. 7, pp. 1989-2004, 2019.
- [4] J. Patry, R. Belley, M. Côté, and M.-L. Chateau-Degat, "Plantar pressures, plantar forces, and their influence on the pathogenesis of diabetic foot ulcers: a review," Journal of the American Podiatric Medical Association, vol. 103, no. 4, pp. 322-332, 2013.
- [5] B. R. Bloem, J. M. Hausdorff, J. E. Visser, and N. Giladi, "Falls, and freezing of gait in Parkinson's disease: a review of two interconnected, episodic phenomena," Movement disorders: official journal of the Movement Disorder Society, vol. 19, no. 8, pp. 871-884, 2004.
- [6] A. Nieuwboer, and N. Giladi, "Characterizing freezing of gait in Parkinson's disease: models of an episodic phenomenon," Movement Disorders, vol. 28, no. 11, pp. 1509-1519, 2013.
- [7] B. Ju *et al.*, 'Inkjet Printed Textile Force Sensitive Resistors for Wearable, and Healthcare Devices', *Adv. Healthc. Mater.*, vol. 10, no. 20, p. 2100893, 2021, doi: 10.1002/adhm.202100893.

Chapter 6. Evaluation system for wearable PBM device

6.1. Introduction

The previous three chapters conducted a comprehensive study on a flexible mechanoreceptor with a novel structure, in which the pressure threshold can be controlled through various parameters, including PDMS material filling rate, height, material modulus, size, and compression areas. Considering the complication of the usage scenario, multiple parameters controllability endows a wide range of flexibility in the applications of the mechanoreceptors. Even if the application scenario limits the adoption of certain parameters, such as size, the pressure threshold can be adopted to fit the application requirement. In addition, the further derivative array of mechanoreceptors has expanded their functionality in wearable technologies, enabling precise position mapping, and pressure mapping. This underscores its potential in the monitoring of users' health conditions from different aspects, like gait, and pressure. In summary, these mechanoreceptors act as a vital interface for human-machine interaction and facilitate the development of personalized health monitoring, and interactive systems.

In the following section, we are going to study photobiomodulation (PBM) and develop a novel customized conformable PBM device for breast cancer patients to relieve the side effects of radiotherapy. Previous literature summarized several key points of the PBM: First, the dose rate exhibits a biphasic dose response, necessitating that the dose needs to keep below a certain threshold; Second, the dose rate needs to be settled over a certain threshold to confirm treatment efficiency[1,2]. However, the performance of the current commercial PBM device needs to be studied to understand their capabilities, and limitations in the market. This also helps to build up benchmarks for the development of novel PBM systems. Based on this, a comprehensive evaluation system is in demand to evaluate the PBM device from different aspects. This chapter aims to study and measure two commercial PBM devices to establish a comprehensive evaluation system for further assessment of the wearable PBM device. This system will be instrumental in providing a framework for the further assessment of wearable PBM devices, ensuring that they meet the necessary standards, and requirements for effective treatment.

6.2. Experimental design

The development of a wearable PBM device requires expertise in various disciplines including textile engineering, electrical engineering, and light technology, as depicted in **Figure 6-1**. Textile engineering is essential for producing, and/or developing materials with advanced textile properties, like flexibility, and air permeability, that can be integrated into clothing or accessories for functionality. Electrical engineering is necessary for designing the electronic components, circuits, and power sources to achieve the control, and function of the device. Light technology is crucial for developing the appropriate light sources with appropriate optical properties, like irradiance, and wavelength, to be effective for PBM therapy. In addition, the electrical properties of the PBM device may influence the optical properties of

the devices. For example, the peak wavelength of the light source may shift with the increase of current, and the irradiance level of the device is controlled through voltage, and current. This knowledge is important to build up a wearable novel PBM system. Additionally, the treatment effect of the developed PBM device requires the knowledge of biological science, such as the interaction between human skin, and light. Overall, the evaluation of a wearable PBM device necessitates a multidisciplinary approach to ensure its effectiveness, and safety for users.

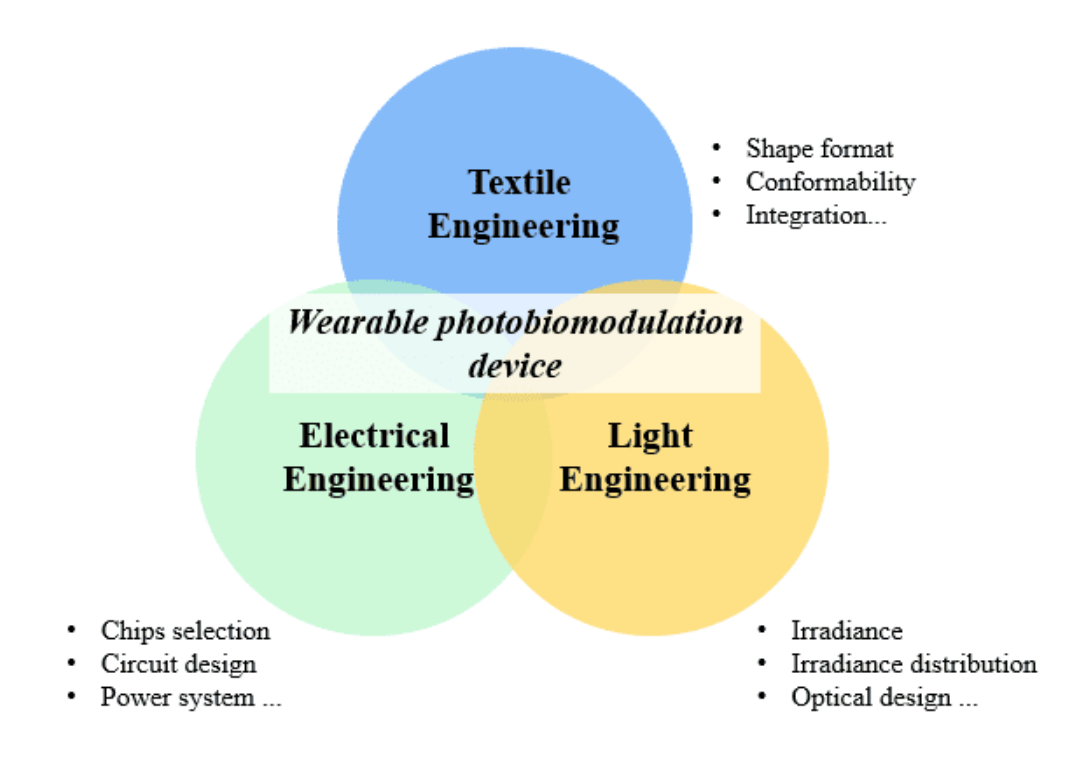


Figure 6-1. A multidisciplinary framework for wearable PBM device.

Based on this, it is essential to first establish an evaluation system for the wearable PBM device as the foundation for its development. Each property of the device has specific detailed requirements. We have referred to relevant standards and summarized the unique properties, and testing methods for the wearable PBM system. The evaluation can be broadly

classified into three aspects: electrical properties, light properties, and textile properties, as shown in Figure 6-2. Details of the testing will be discussed in the later section.

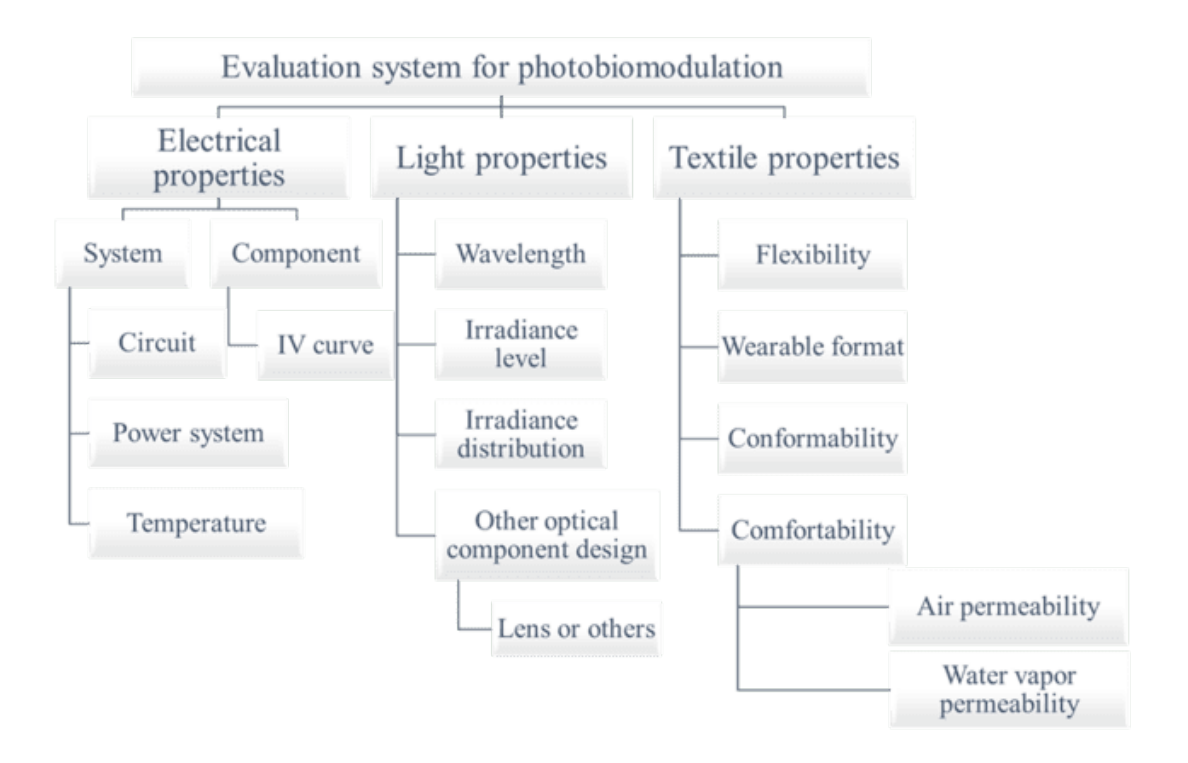


Figure 6-2. Overview of evaluation system for the wearable PBM system.

6.3. Characterization

Researching the market of the PBM device reveals three main types classified on their treatment format: wearable, hand-held or panel. Wearable and panel format PBM devices are common in the market due to their lower price, larger treatment area, and greater convenience[3]. However, the PBM panel has a larger form factor, and heavier weight, and hence requires more space to conduct treatment. In clinics, it is common to use the hand-held devices because those can target the affected position accurately. The treatment area of hand-held device is small, and only can cover several centimeters. We have selected, and tested two

different types of PBM systems- wearable, and panel-based PBM. Through testing, and analyzing the two PBM systems, a comprehensive evaluation system can be built up to understand current product performance, capabilities, and limitations in the market. The results also can help us to identify the metrics, and challenges of different PBM systems, which can be used as benchmarks for the new PBM panel. Various experiments for characterization and evaluation from different aspects are described below:

6.3.1. Electrical characterization

The electrical design of the PBM system is crucial to its performance. This includes circuit design, and the electrical components selection, determining the overall system control, and power. It is critical to user safety. The following experiments will evaluate the electrical properties of PBM devices from various aspects:

System voltage, and current: A multimeter (F101, Fluke Corporation) was used to measure the voltage, and current of the systems to study their power stability and requirement. We will compare the difference between the two systems to identify the PBM power requirement in relation to the optical properties and wearable safety requirements.

Circuit: Circuit design influences the control of the LED, power system reliability, and heat dissipation within the device. The circuit of these two PBM systems was studied and drafted to study the connection between LEDs, and the system power. This analysis provides insight into the control of the LEDs, and explores the balance between the voltage, and current

for wearable PBM products.

LED voltage, and current: The electrical properties of LEDs not only influence the overall system power, but it also significantly determines the PBM optical properties, including wavelength, and irradiance. To investigate these effects, six or five LEDs were randomly selected from the array for measurement. Initially, LED power in the system was measured by a multimeter (F101, Fluke Corporation). Then, a power source from Daxin (DX6005DS) was used to characterize the LED current and voltage in the system. These characterizations provide an insight into the specific PBM requirement on LED.

6.3.2. Optical Characterization

The optical properties of PBM devices are key factors in the treatment effects of PBM. The critical properties include the peak wavelength, wavelength shifting at different currents, irradiance of the panel, irradiance distribution along the panel, and the irradiance stability of the device. Understanding these properties is essential for the fabrication of wearable PBM, as they directly determine the effectiveness and safety of the treatment.

6.3.3. Wavelength and irradiance measurement

Wavelength, irradiance, and the irradiance distribution affect the skin penetration depth of the light. These parameters can be measured by the same device. CAS 140D array spectrometer from Instrument Systems GmbH was used to measure the wavelength irradiance

of LED, and irradiance uniformity of the array. In addition, a manual z-axis displacement table (HTZ210) from HUIKE was used for positioning in the irradiance and the wavelength measurement.

In the experiment, the PBM panel was fixed at the displacement table with/without a gap to the detector depending on the usage condition of the device. In detail, the gap between the PBM panel, and the detector was 30 cm because the panel needed to be held at a 30 cm distance from the human body. For the wearable PBM panel, there is no gap because the LED surface is directly in contact with the human kin. The irradiance value was measured and calculated from the software in the unit of W/m².

6.3.4. Irradiance distribution measurement



Figure 6-3. Experiment set-up for irradiance measurement.

Similar to irradiance measurement, the CAS 140D spectrometer from Instrument Systems GmbH was used to measure the irradiance distribution along the panel. The optical

detector was covered with black paper containing a 2 mm diameter hole. The black paper can prevent the transmission of light to the detector, except the hole area. An extra manual x-y displacement table (HTXY210) from NISHIDUN was used for movement, in which the displacement can be smaller than 0.075 mm. **Figure 6-3** shows the testing equipment and the corresponding experiment set-up.

During the experiment, the largest irradiance point of the LEDs was initially determined as the benchmark and then moved along the horizontal or vertical direction to record the irradiance at the various positions. This experiment was conducted to map the irradiance distribution across the panel.

Furthermore, if there is a secondary lens system in the PBM system, the irradiance distribution with and without the lens was evaluated. A comparison was conducted to analyze the lens functionality and its effectiveness in modifying the irradiance distribution.

6.3.5. LED viewing angle measurement

Similar to the irradiance distribution experiment, the detector will be covered with a black paper featuring a 2 mm diameter hole. The PBM panel was fixed at the displacement table. In addition, the distance between the LED, and the detector was fixed. In the experiment, the irradiance distribution of the LED was measured with the movement of the displacement table. The viewing angle of the LED was then calculated based on the measured data, and the square inverse law.

6.3.6. Temperature measurement

The generation of light from PBM devices may also generate significant heat, which is influenced by the LED power, and quality. The conversion between heat and electrical power can be over 70%[4]. Considering the interaction between PBM and the human skin, the temperature variation throughout the treatment period needs to be evaluated to avoid burning. An infrared camera from Fluke was used to monitor the temperature change of the PBM system throughout the treatment period.

6.3.7. Textile properties measurement



Figure 6-4. Photo of the KES-F8 air permeability tester.

Since one of the PBM systems is a panel, it is not a wearable product. The material and design are rigid. The textile experiment is not appropriate for the PBM panel. For the wearable PBM device, the flexibility of the circuit was measured by the pure bending tester from the KAWABATA system. Considering the rigidity of the circuit, the circuit was cut into the

samples with a width of 0.5 cm. In addition, the air permeability of the panel was measured by a KES-F8 automatic air permeability tester, as shown in **Figure 6-4.**

6.4. Result and discussion

In this section, we will first analyze the PBM panel, and then analyze the wearable PBM panel. Finally, we will compare the two systems to highlight their respective strengths and weaknesses. Furthermore, we will discuss the potential solutions for it.

6.4.1. PBM panel

6.4.1.1. Structure and component of the PBM panel

PBM panel is a common PBM product in the market, in which the panel is held up at a distance from human body for treatment. PBM panels are commonly larger to treat a wider treatment area. This device was registered in FDA (890.5500). The dimension of the system is 17.32 * 11.02* 5.12 inches, and it weighs 11.13 pounds. The suggested treatment distance was in the range of 15 cm to 30 cm.

The components of the PBM system are illustrated in Figure 6-5. The panel is covered with a metallic shell equipped with two switches, and a charging port. Inside the shell, there is an LED panel containing 10 rows of LEDs equipped with a secondary len system. A large metallic heat sink is positioned behind the LED panels for heat dissipation. In addition, there is a fan, and two LED power supply converters are located at the bottom of the shell. The

presence of the heat sink, and fan indicates that heat dissipation is a critical problem in this PBM panel. This PBM operates on a direct power supply. The input of the converter is 100-240 V/ac 50/60Hz. The converter output is in the range of 45 to 80 V, and the current is fixed at 650 mA. The power requirement of the panel differs from the direct power supply, necessitating the use of a converter. Additionally, the integration of two types of LEDs with varying electrical properties has higher requirements on the output of the converter.

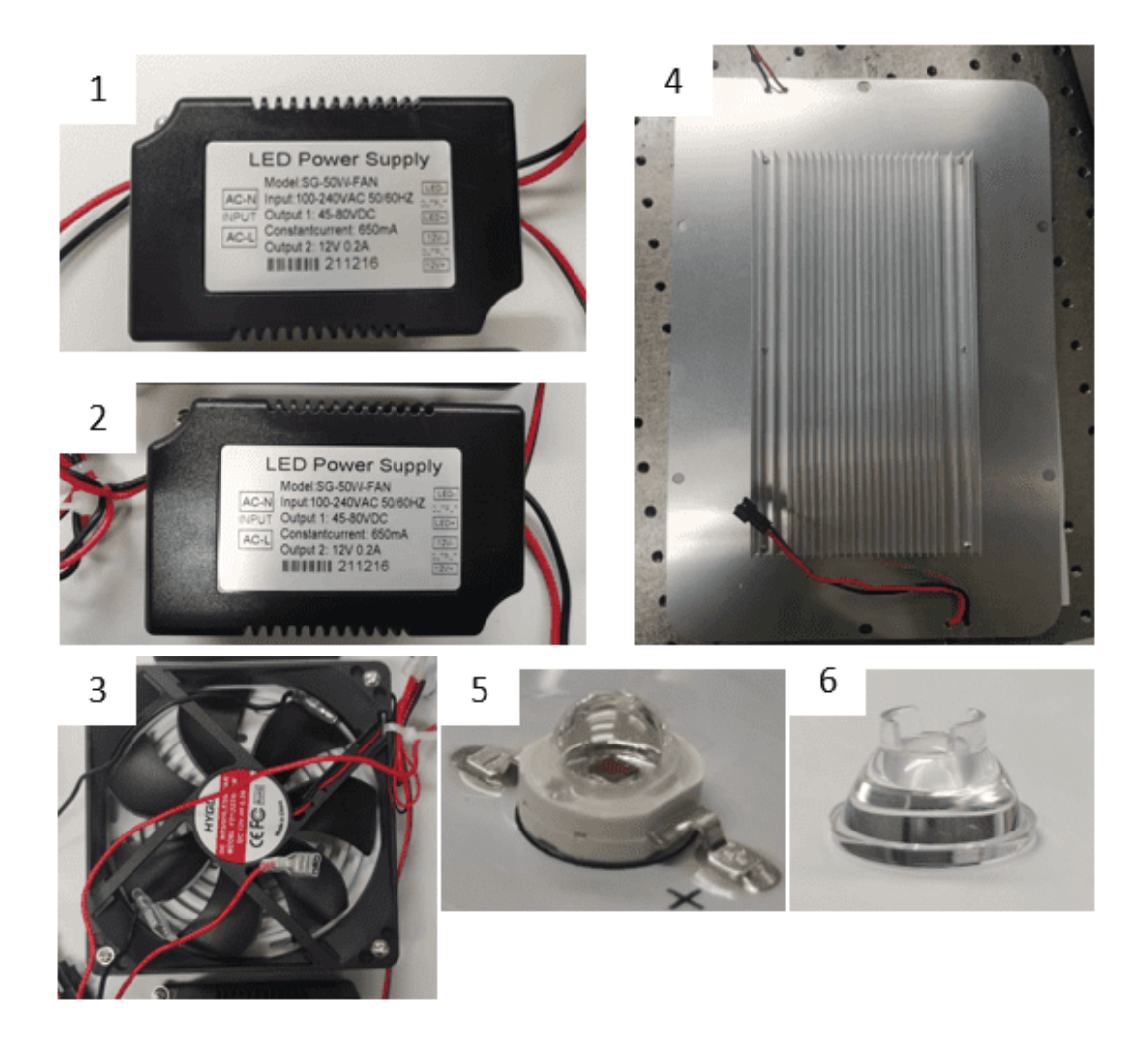


Figure 6-5. Photo of the components of the PBM panel.

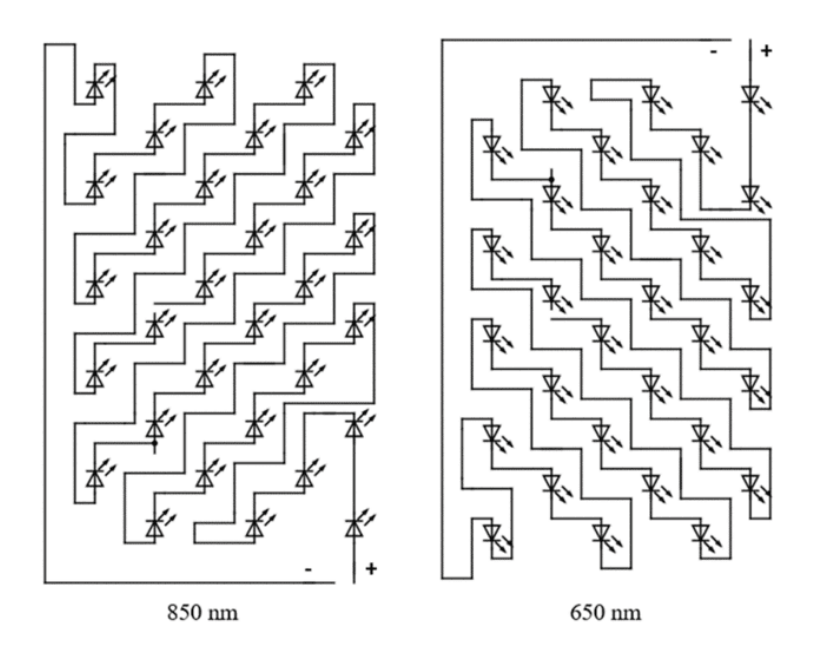


Figure 6-6. Electric circuit diagram of the PBM panel.

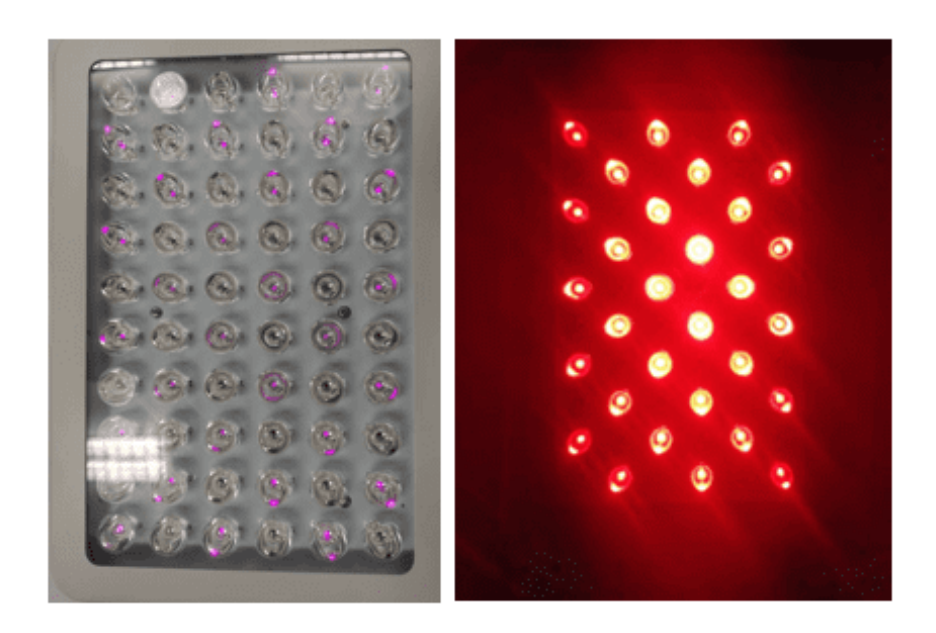


Figure 6-7. Photo of the working mode of the PBM panel. Left: 850 nm LED is on. Right: 650 nm LED is on.

In the LED panel design, there are a total of 60 LEDs, consisting of two types of LEDs with the wavelength of 650 nm, and 850 nm respectively. The inter-central distance between LEDs is maintained at 25 mm. The 850 nm LED, and 650 nm LED are arranged in an

alternating pattern within a row. The control of these two types of LED is separated in circuit, and power. The same types of LEDs are connected in series within the panel. In the event that one LED is broken, it results in the failure of the entire system. **Figure 6-6** illustrates the electric diagram of the circuit. These two types of LEDs were controlled by different switches, allowing for a total of three modes of treatment -only 650 nm LED in on-state, only 850 nm LED in on-state, or both 650 nm, and 850 nm LEDs in on-state (**Figure 6-7**). The analysis of the panel will be divided into two parts, depending on the light source.

6.4.1.2. Near-infrared LED (850 nm)

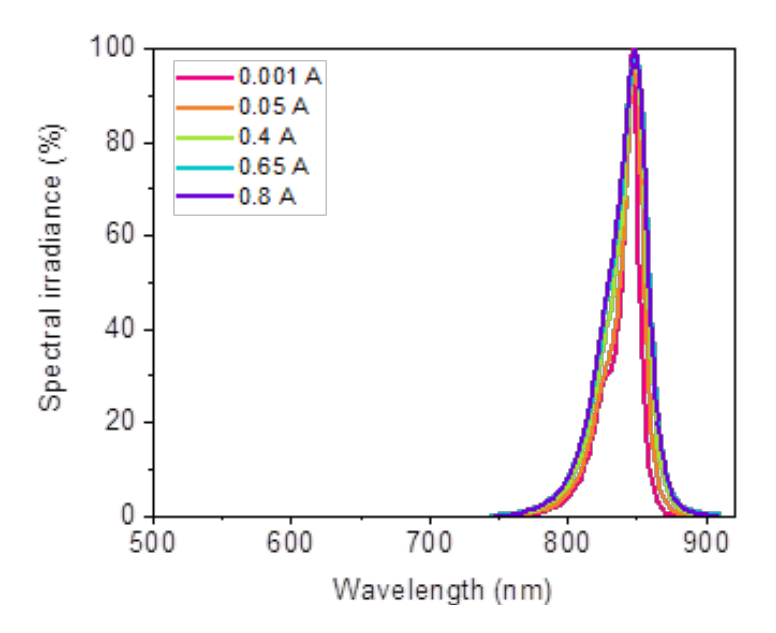


Figure 6-8. Wavelength shift of 850 nm LED at different current.

Wavelength: The wavelength of the LEDs was measured by the CAS 140D spectrometer. At a very low current (0.001 A), the peak wavelength was 846. 86 nm. The width50 was 13.5 nm. At 650 mA (working current), the peak wavelength of the near-infrared LED was 848.45 nm. The width50 was only 24. 09 nm. As the current increases to 0.8A, the

peak wavelength was 849.34 nm. The width 50 was 28.62 nm. It found out that this LED peak wavelength shifts slightly with the increase of current. However, the width50 of the wavelength increases sharply with the increase of current. The peak becomes broader, as shown in **Figure**6-8. The change of the wavelength peak can account for the increase of junction temperature, carrier density effects, auger recombination, and others. The increase of current may increase the junction temperature due to the reduction of band gap[5].

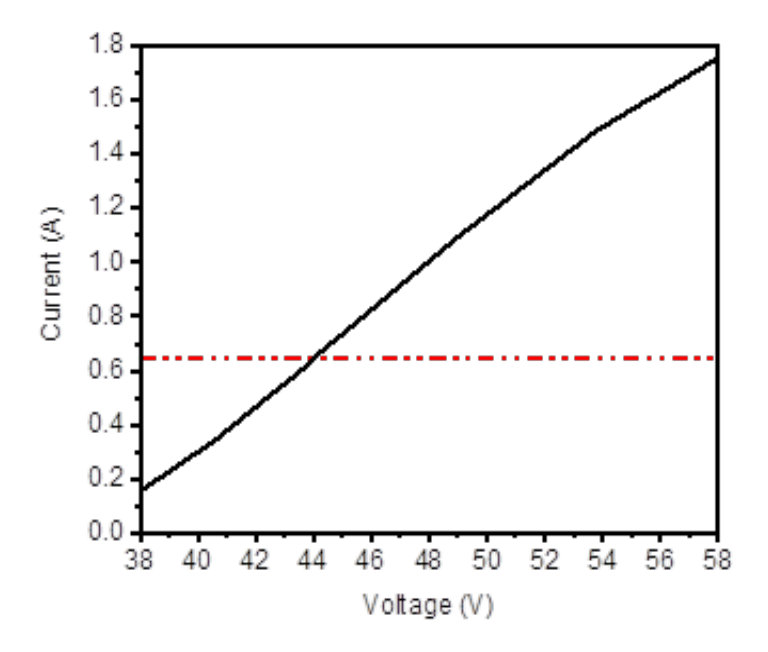


Figure 6-9. 850 nm LEDs systematic IV curve.

Systematic electrical properties: The whole system, and individual LEDs voltage, and current were measured. **Figure 6-9** illustrates the IV curve of the system. It was noticeable that the LED power requirement is quite large. The voltage of the system was 44.06 V at the fixed constant current of 650 mA.

LED electrical properties: Figure 6-10 demonstrates the IV curve of individual LEDs

on the panel. It can be that there is a slight variation in the IV curve between LEDs. **Figure 6-11** presents the average voltage and current with standard deviation. It found that as the current increases, the variation among LEDs becomes larger. At 650 mA, the average voltage of the LEDs is 1.61 V (SD: 0.01). As the current increase to 1.48A, the average voltage of LEDs is 1.95 V (SD: 0.02). Considering this, the current of the LEDs needs to be settled at the appropriate level to limit the variation between LEDs. From the above measurement results, it can be concluded that this PBM panel uses high-power LEDs, capable of operating at 1.8 A. The usage of high-power LEDs can be attributed to the need for longer treatment distance, resulting in reduced irradiance in accordance with the square inverse law.

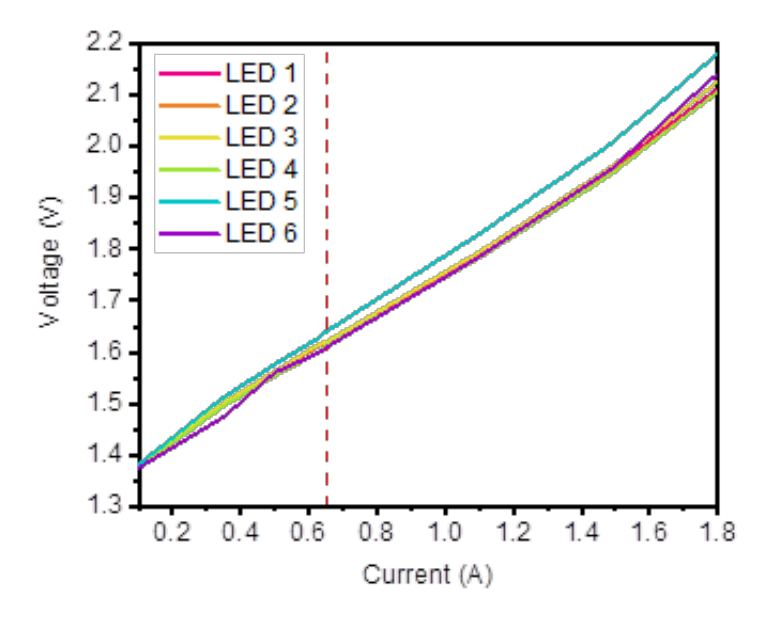


Figure 6-10. Individual 850 nm LED IV curve.

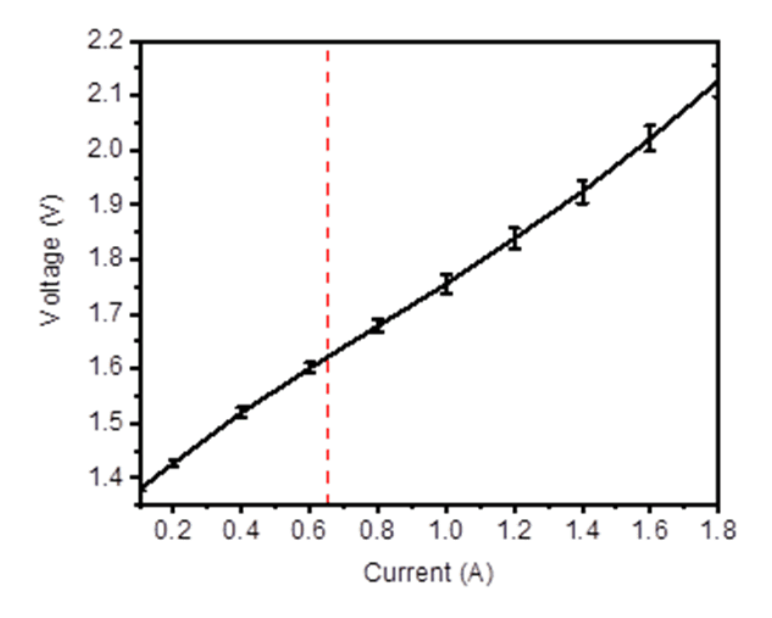


Figure 6-11. 850 nm LED IV curve.

LED optical properties: Besides voltage, and current, the irradiance level of the LEDs was also measured, and related to voltage, and current. Below six figures in **Table 6-1** illustrate the IV curve of the LEDs and corresponding irradiance.

LED 1 LED 2 1.9 80 1.9 1.8 1.8 1.7 .00 .00 .00 .00 .00 .00 .00 .00 .00 .00 1.7 7.6 (A) Aoltage (A) 1.5 (A) 1.4 7.6 (v) 1.6 (v) 1.5 (v) 1.4 1.4 1.3 10 10 0.1 0.2 0.3 0.4 0.5 0.6 0.8 0.0 0.7 0.4 0.5 0.6 0.7 0.8 0.2 0.3 Current (A) Current (A) LED 3 LED 4 80 80 1.9 1.8 1.8 70 1.7 1.7 7.6 (V) Noltage (V) 1.6 (V) 1.4 7.6 (V) Noltage (V) 1.4 (V) 1.6 1.3 1.3 10 10 1.2 0.1 0.2 0.3 0.4 0.5 0.6 0.7 0.0 0.2 0.4 0.5 0.6 0.7 0.8 0.1 0.3 0.0 Current (A) Current (A) LED 6 LED 5 80 80 1.9 1.8 1.8 .50 (_c-50 %) .40 .30 ltradiance (mM/cm²) 1.7 1.7 7.6 (A) Nottage (A) 1.5 (A) 1.4 (A) 7.6 (A) Aoltage (A) 1.5 1.4 1.3 10 10 1.2 0.0 0.1 0.2 0.3 0.4 0.5 0.6 0.7 0.8 0.1 0.2 0.3 0.4 0.5 0.6 0.7 0.8 0.0 Current (A) Current (A)

Table 6-1. 850 nm LED IV curve in relation to irradiance.

Through reviewing the above six figures, it is evident that LED exhibits variations in

irradiance, voltage, and current. At 650 mA, the average voltage of the LEDs is 1.74 V (SD: 0.023). However, the average irradiance was 54.96 mW/cm², while the standard deviation was 6.52. It found out that even with LEDs with the same electrical properties, the irradiance properties may be varied because there is a variation in the manufacturing process or fabrication materials, resulting in the performance variation. There are four major factors affecting the quality of the LEDS, including optical, and electrical properties, temperature, and electrical impedance, temporal degradation with corresponding variability. Typical variation of the parameters within a specified group is usually relatively large: the intensity can vary up to + 30%, the forward voltage typically by +0.2 V, while the colour chromaticity is usually specified by a quadrangular region of size from 0.005 to 0.03 units[6]. There are a few systems to automatically sort LED into different groups to reduce the quality variation, while this system is still in the embryotic stage. Considering this, a 30% range of irradiance variation across the panel is minimal.

6.4.2. RED light LED (660nm)

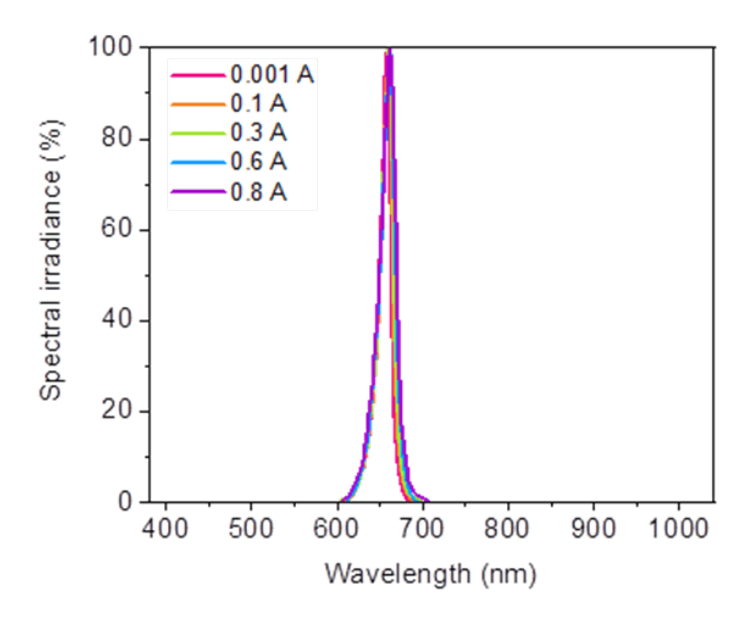


Figure 6-12. Wavelength shift of 660 nm LED.

LED wavelength: Similar to the near-infrared LED, the red-light LED wavelength was measured at different currents, depicted in **Figure 6-12**. At 0.001A, the peak wavelength was 657.51 nm, and the width50 was 14.17 nm. At 0.3A, the peak wavelength was 660.09 nm, and the width50 was 16.58 nm. As the current continuously increases to 0.8A, the peak wavelength is 661.74 nm, and the width50 is 20.43 nm. Compared to the near-infrared LED, red light LED peak wavelength, and width50 was relatively stable as the current increased.

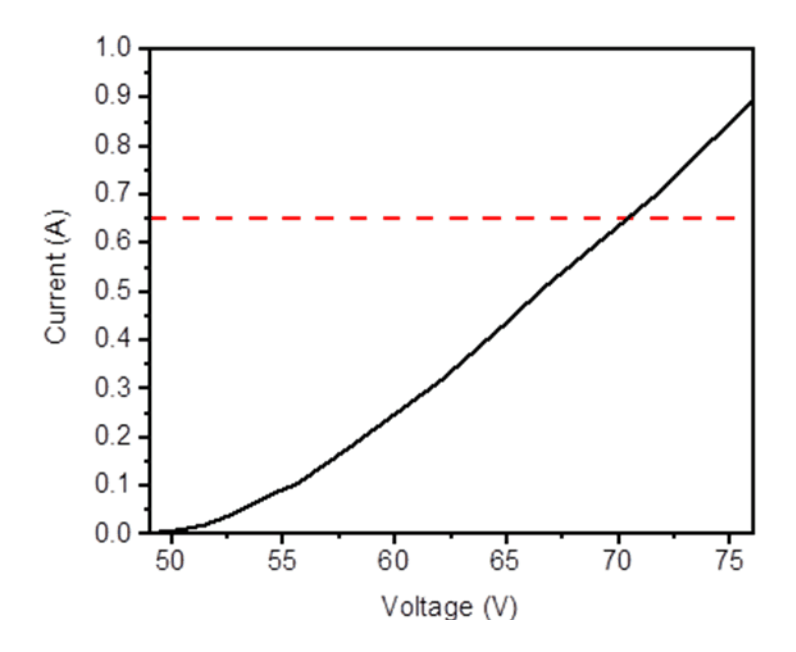


Figure 6-13. 660 nm LEDs system IV curve.

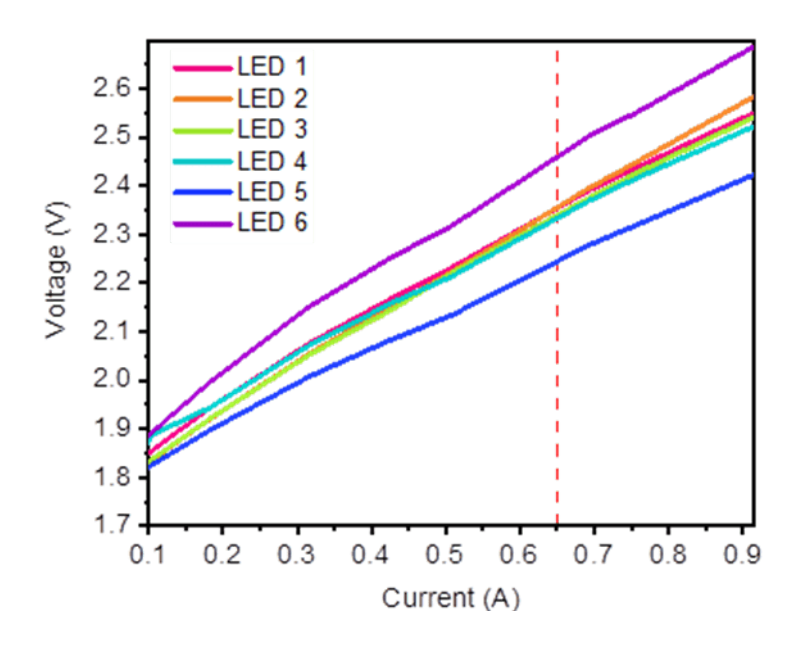


Figure 6-14. Individual 660 nm LED IV curve.

Systematic electrical properties: The red light PBM system was measured, as shown in Figure 6-13. At a constant current of 650 mA, the system voltage is 70.58 V. It was observed that the power of the red-light system was higher than that of the near-infrared LED system. This can be accounted that red light LED, and near-infrared LED electrical properties are

diverse. Consequently, there is a higher design requirement in the circuit, and power system for PBM to accommodate the discrepancy requirement of using two types of LEDs across the panel. This is crucial to ensure a reliable power supply of the device. In light of this, the power, and control system of this PBM system are separated to address their specific needs to reduce the design complexity.

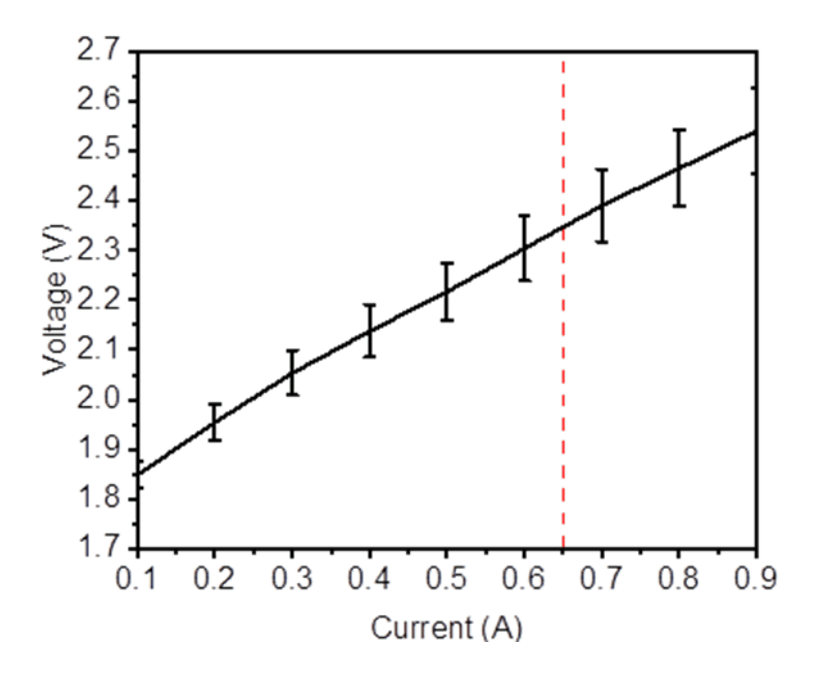


Figure 6-15. 660 nm LED average IV curve.

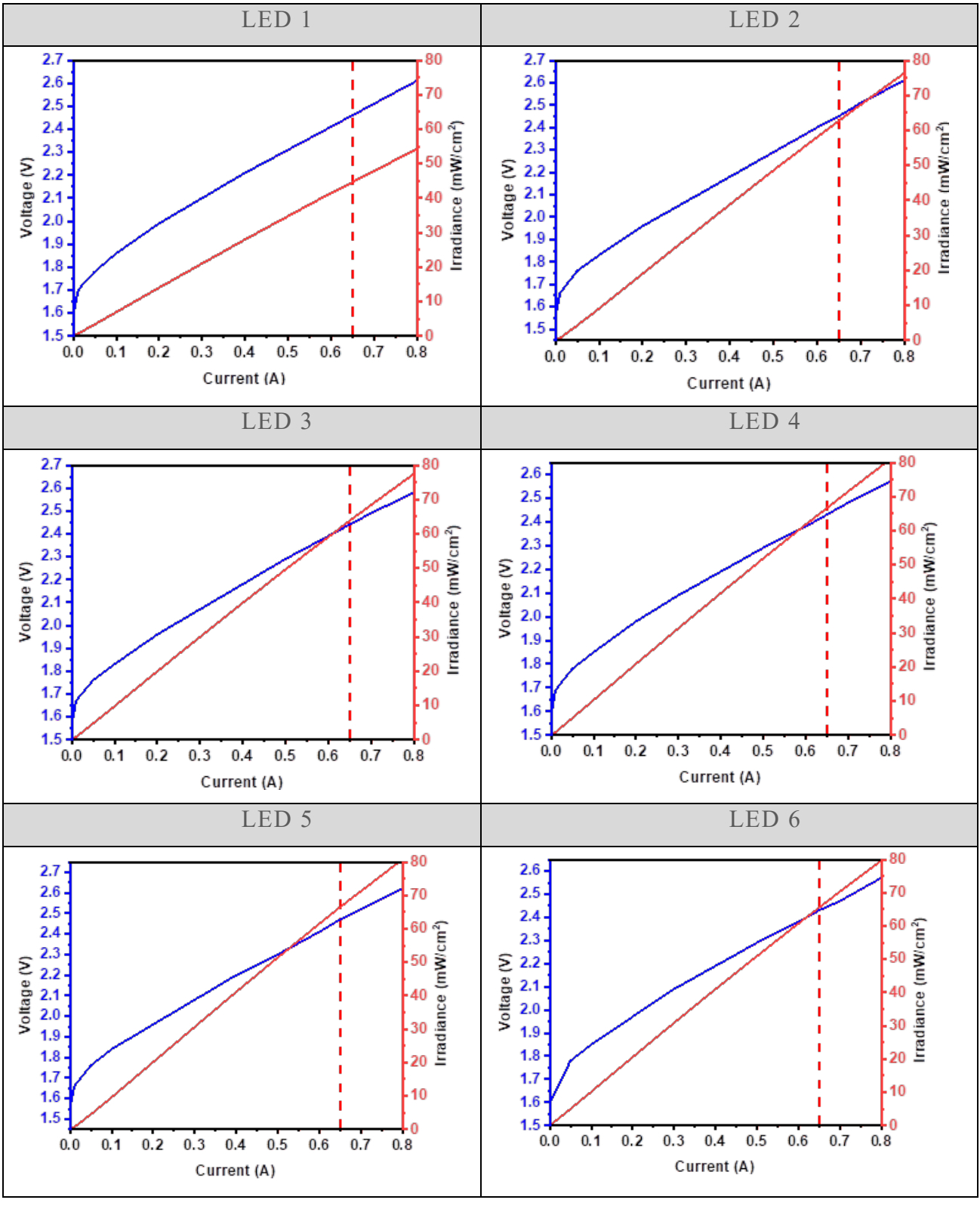
LED electrical properties: We also measured the IV curve of the red-light LEDs. Figure 6-15 presents each LEDs IV curve, and Figure 6-16 outlines the average current, and voltage with standard deviation. Similar to the near-infrared LED, the variation in voltage among the LEDs becomes larger as the current increases. At 200 mA, the average voltage was 1.95 V, and the standard deviation was 0.035. At 600 mA, the average voltage was 2.30 V, and the standard deviation was 0.065. Comparing the performance of the red-light LEDs to near-

infrared LEDs, it is evident that the variation between red-light LEDs is larger that of near-infrared LEDs. Consequently, red-light LED is more suitable to work at the lower current. This points out that the appropriate working current between types of LEDs can be different. Another important question is whether the larger variation in the electrical properties of the LEDs will result in the more varied LED optical properties.

LED optical properties: In addition to the IV properties of LED, the irradiance of each LEDs was also characterized. Below six figures in Table **6-2** depict the interrelationship between the voltage, current, and irradiance of the 660 nm LEDs.

LED 1

Table 6-2. Individual 660 nm LED IV curve, and irradiance.



Even with a constant current of 650 mA, and a voltage of approximately 2.44 V (SD:

0.014), the average irradiance was 60.77 mW/cm², and the standard deviation was 8.11. Upon reviewing the above six figures, it was observed that only sample 1 LED has a larger variation than the other five LEDs. Sample 1 LED irradiance was 44.62 mW/cm², while the other five LEDs' irradiance was at the level of over 60.00 mW/cm². Exclude the sample 1 irradiance value, the average irradiance was 64.01 mW/cm², and the standard deviation was only 2.05. Compared to the near-infrared LEDs, the red-light LEDs optical variation is relatively smaller. However, the electrical properties of 660 nm LEDs are more varied than that of the 850 nm LED. This suggests that the variation in the electrical properties of LED is not directly correlated to the LED optical performance. Consequently, it is inappropriate to evaluate the LED optical properties by measuring the IV curve of LEDs.

6.4.2.1. Secondary optical design of LED

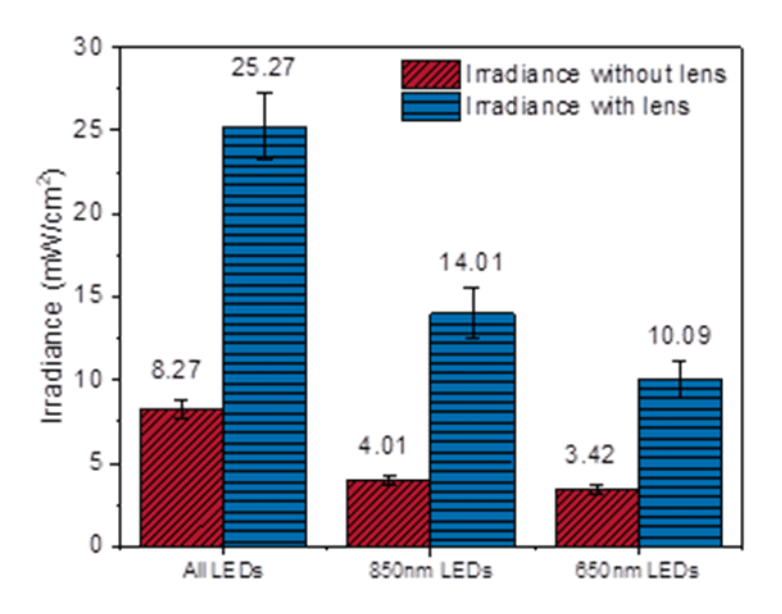


Figure 6-16. Irradiance of the panel with or without lens.

Furthermore, we also conducted an evaluation of the role and functionality of the secondary optical design in the PBM panel. We measured the irradiance difference of the commercial PBM panel with or without a lens. In **Figure 6-16**, it can be found that the irradiance with a lens in three conditions is higher than that without a lens at different modes. The irradiance of all LEDs with a lens was 25.26 mW/cm², while the irradiance decreased to 8.26 mW/cm² in the case without a lens. The irradiance of only 850 nm with a lens was 14.01 mW/cm², while the irradiance decreases to 4.01 mW/cm² in the case without a lens. The difference in the irradiance was more than three times. The difference of the irradiance may be attributed to the addition of a secondary lens to LEDs may change the LED angle to a smaller value. At the treatment distance of 30 cm, the LED coverage area is quite large, resulting in a lower irradiance per area. The presence of a secondary lens may reduce the coverage area of each LED, thereby increasing the irradiance value per unit area. Therefore, the energy for the treatment can be more effective.

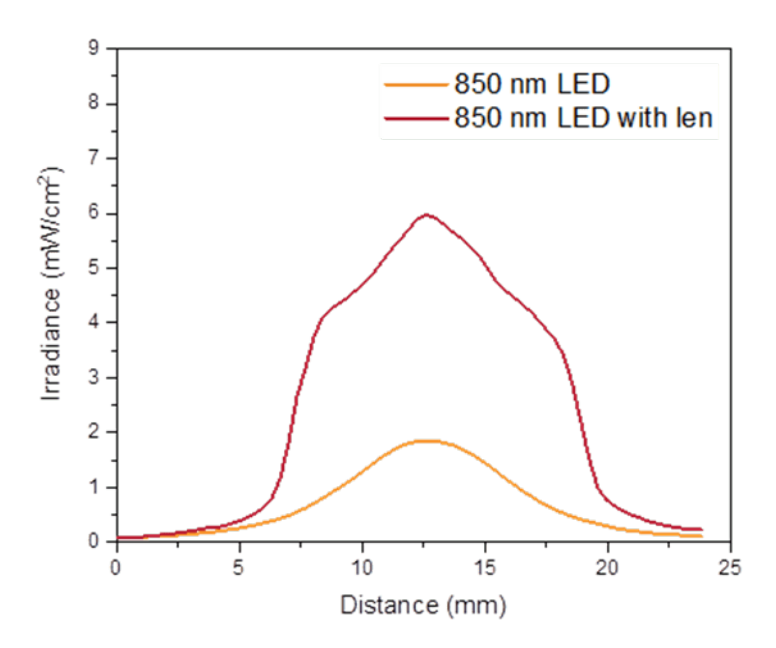


Figure 6-17. 850 nm LED irradiance distribution.

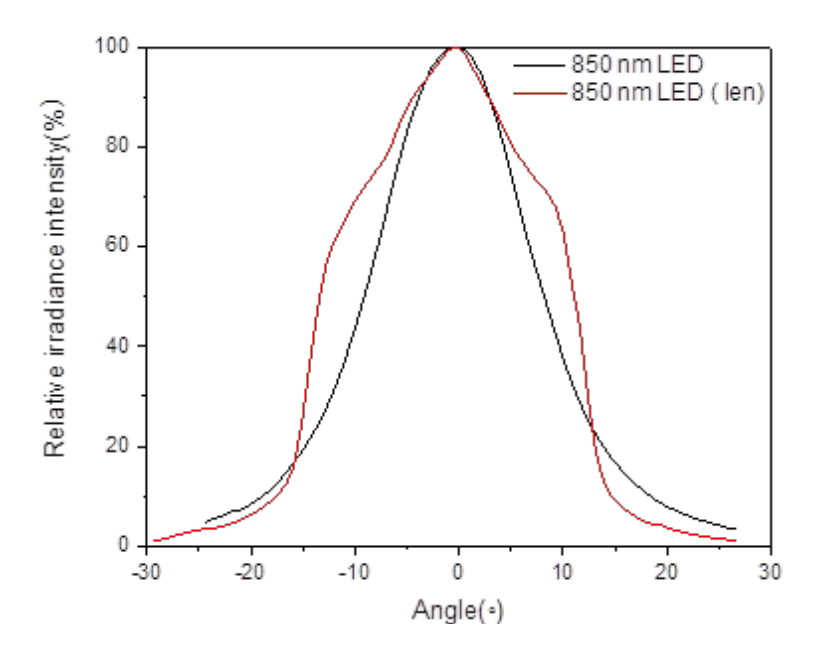


Figure 6-18. 850 nm LED viewing angle.

To further study the role of the secondary lens for the PBM panel, we measured the irradiance distribution of the single LED with or without a lens to verify the change in viewing angle. The LED was tested at a distance of 3 cm from the detector, **Figure 6-18** depicts the irradiance distribution of 850 nm LEDs. It found out that the irradiance value of the 850 nm LED with lens is larger than that of the without lens, but the difference in the distribution between two conditions is not large. Then, the angle of the LED, and its relative irradiance intensity at different angles was calculated, as demonstrated in **Figure 6-19**. It is evident that the addition of the lens focuses the light on the center of the LED. The lens may act as a reflection lens reflecting part of the light at the edge to the center to reduce the overall coverage area of LED. The irradiance per unit area will be increased to enhance the irradiance efficiency. In summary, the viewing angle of the LED becomes larger with the addition of LED.

Figure 6-19 presents the irradiance distribution of the 660 nm LED with or without

lens, and **Figure 6-20** shows the relative irradiance intensity as a function of the angle of the LEDs. These results were similar to the previous to prove that the addition of the lens may reflect part of the light at the edge to reduce the overall coverage area of the treatment. The viewing angle of the LED with a lens is larger than the LED without a lens. This indicates the coverage area with 50% irradiance is larger. Hence the energy for the treatment can be more efficient.

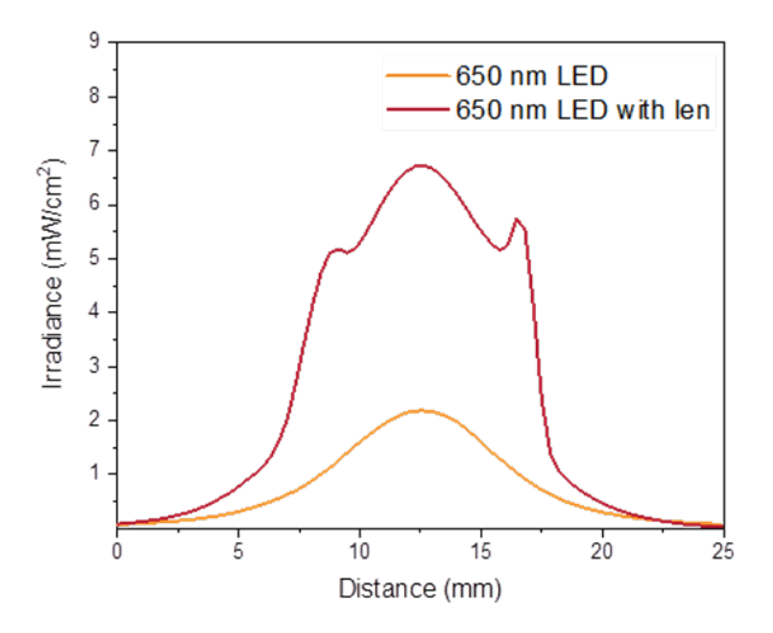


Figure 6-19. 650 nm LED irradiance distribution.

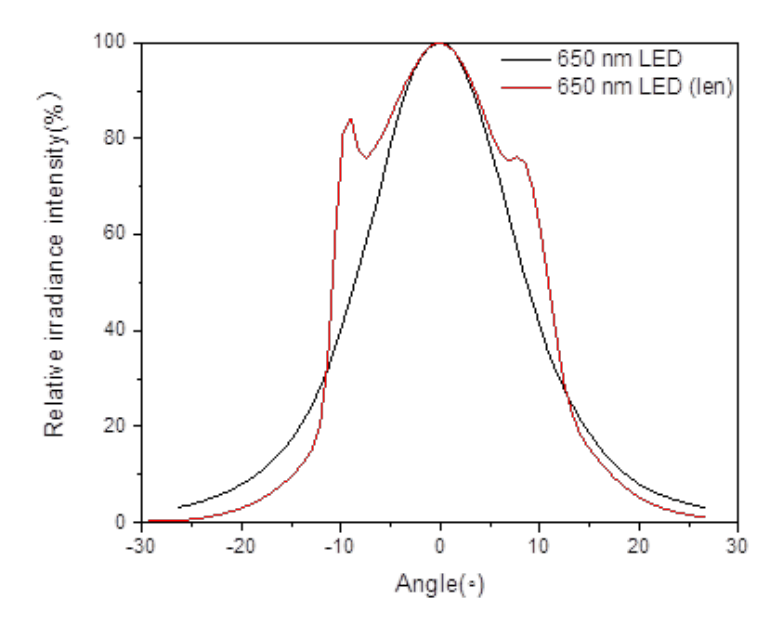


Figure 6-20. 650 nm LED viewing angle.

Based on the irradiance measurement of the LEDs, the coverage area of each LED at 30 cm treatment distance can be calculated based on the square inverse law. The coverage area of the 50% irradiance LEDs at a distance of 3 cm is around 10 cm in diameter. Through calculation, the treatment distance increases around 10 times to the measurement set-up. By applying the square inverse law, the irradiance coverage area should be 100 times the measurement. The coverage area at 30 cm was calculated to be around 100 cm. It is important to note that the treatment area irradiance is the result of the overlapping of all 60 LEDs.

6.4.2.2. PBM panel irradiance properties

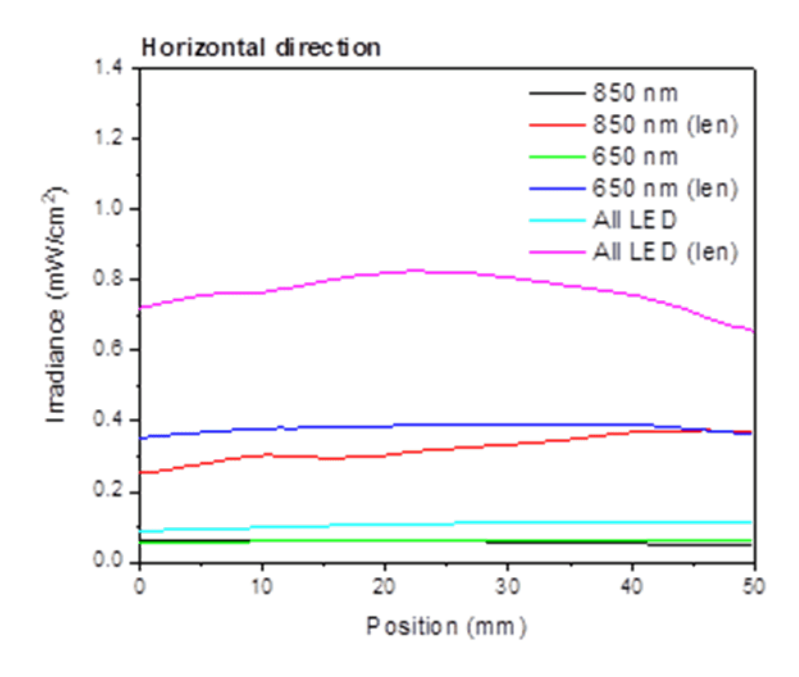


Figure 6-21. Irradiance distribution of the panel (Horizontal).

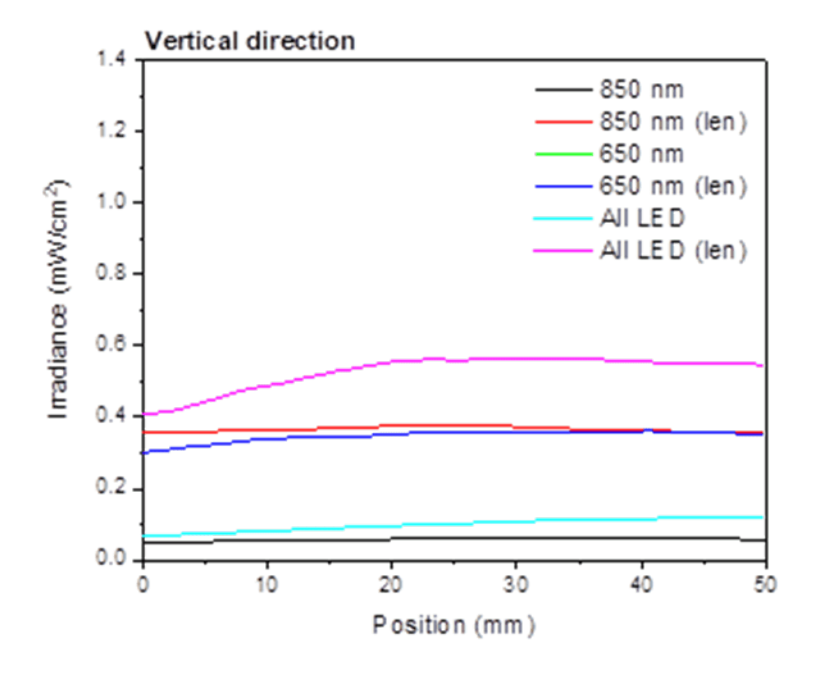


Figure 6-22. Irradiance distribution of the panel (Vertical).

The irradiance distribution across the panel was measured to evaluate the irradiance

uniformity across the panel. **Figure 6-21** illustrates the irradiance distribution of panels in different modes in the horizontal direction, while **Figure 6-22** illustrates the irradiance distribution of panels in different modes in the vertical direction. Upon reviewing the two figures, there is no obvious periodic trend in the irradiance distribution from one LED to another LED. The irradiance at the middle point between the LEDs is similar to the central irradiance of the LEDs. However, there are still some variations in the irradiance. When all LED was on, the irradiance at 0 mm was 0.4 mW/cm², and then the irradiance increased to around 0.5 mW/cm². These variations may be attributed to the variation of optical properties among LEDs.

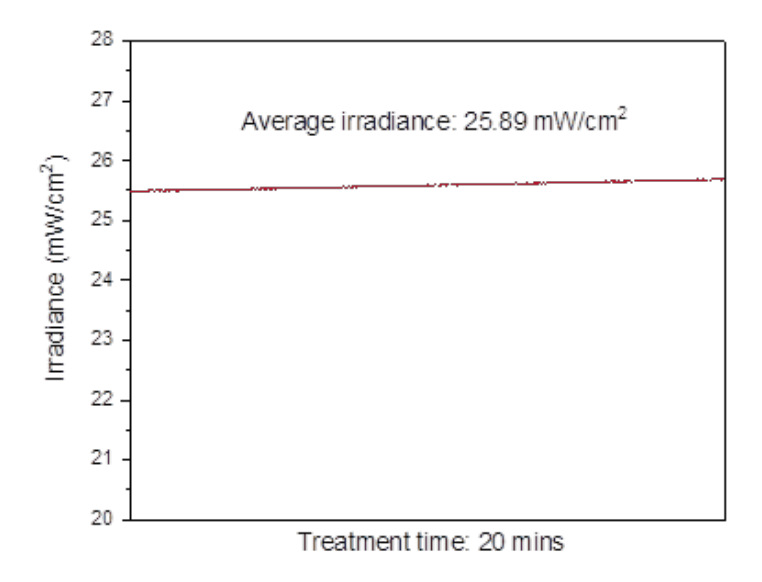


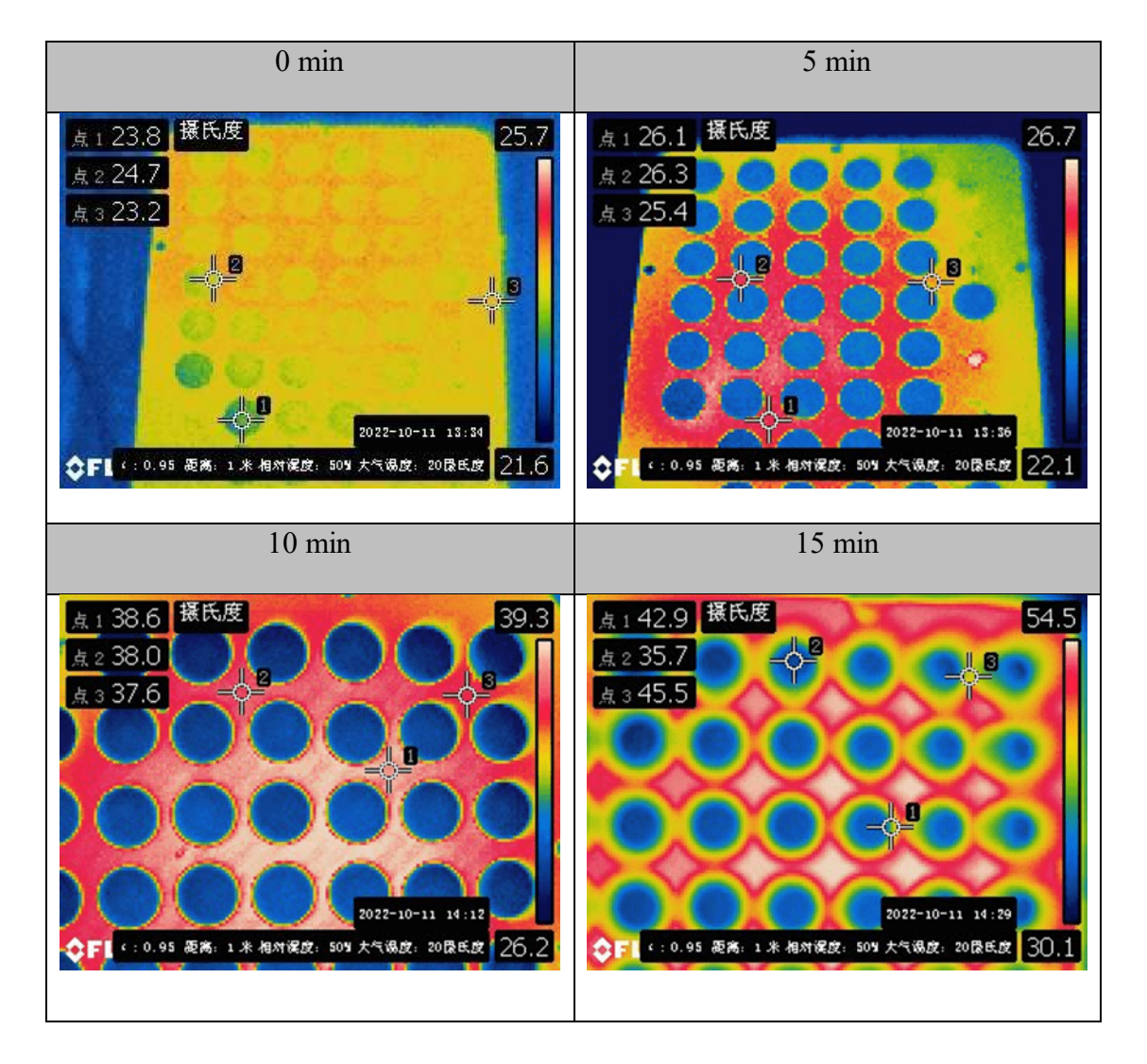
Figure 6-23. Irradiance of the panel during treatment time.

We also conducted an evaluation of the irradiance variation throughout the treatment period, as shown in **Figure 6-23**. The average irradiance was 2.3483 mW/cm² at the same position. The standard deviation of the irradiance in these 20 minutes was 0.0023. The device

may provide a stable irradiance to the user throughout the treatment.

6.4.2.3. Temperature measurement

Table 6-3. Temperature measurement of the PBM panel.



In **Table 6-3**, the PBM system with secondary lens temperature change under 20 mins treatment was evaluated by an infrared camera. At the initial, the temperature of the panel was the same as the room temperature. After 5 mins, the temperature of the panel located at the central slightly increased to 26.7 °C, and the increase of the temperature was uneven. The

position at the edge of the PBM panel was lower (around 24 °C). The temperature of the secondary lens systems was around 22.1°C. After 10 mins, the panel temperature increased to 38.0 °C. In addition, the middle position of the panel may be a little higher around 39.3°C. The temperature of the secondary lens systems also raised a little bit to 26.2°C, around 18.55%.

At the end of the treatment (20 mins), the temperature of the panel was over 50°C. For the secondary lens, the central position was around 30.1°C, and the edge was around 35.7 °C. Throughout the treatment process, this PBM panel temperature was increased from 24°C to 54°C, around 125%. In addition, the temperature is over the safety threshold, causing damage to people.

The temperature issue of this PBM panel may be attributed to the high-power LED and the electrical power of the system. As previously mentioned, the selection of high-power LEDs is necessary to ensure a certain level of irradiance over a long treatment distance. Furthermore, this PBM panel system used 650 mA constant current, and the system voltage of near-infrared LEDs, and red-light LEDs was higher at 44.06 v, and 70.58 V. The power requirement is large, and hence the generation of heat is significantly large. As mentioned in 6.4.1.1, this PBM was equipped with a heavy heat sink, and fan to relieve the generated heat. It can be found that heat dissipation problem is a critical topic to be studied when using high power LEDs.

Given the characteristics of wearable products, there is no need for long treatment distances. Therefore, it is appropriate to use a low-power LED to achieve the same irradiance level. Another consideration is the heat dissipation issues. It is difficult to equip heat sinks, and

fan to dissipate heat in wearable products, so there is a demand to explore other methods for heat dissipation.

6.4.3. Wearable PBM system

6.4.3.1. Structure and component of the wearable PBM

A wearable PBM device was selected, and tested. This device was also registered with FDA (Regulation number: 890.500). The format of this panel is a bandage, which can be wrapped around the body, and fixed with Velcro. It is non-stretchable. The dimensions of the panel were 15.7 * 8 inches, and weigh around 2.07 pounds. This panel can be connected to a direct power source or a 5V or 12 V power bank. **Figure 6-24** illustrates the front and back sides of the wearable PBM panel.

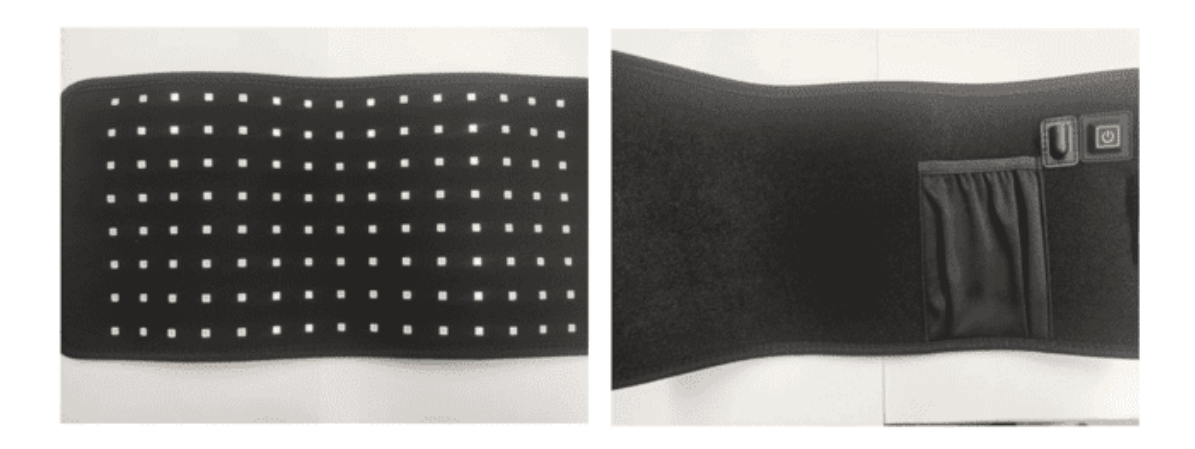


Figure 6-24. Photo of the wearable PBM panel.

This PBM panel consists of three layers. The first layer at the front is a mesh fabric with holes for light exposure and fixation of the flexible circuit. The middle layer is a flexible circuit board, and the last layer is another terry fabric equipped with rubber buttons, and a

charger port, as shown in **Figure 6-25**. The assembly of these three layers was achieved through the adhesion between the layers.

This panel is capable of emitting both 660 nm and 850 nm light. In contrast to the PBM panel, this wearable PBM only utilized a type of dual-color LED. It indicates the LED can emit both 660 nm and 850 nm LED from one single chip. The chip has six pins. In detail, there are two emitters at the left and right of the LED to emit 850 nm light, and one emitter at the center of the LED to emit 650 nm light, as shown in **Figure 6-25**. The control of the emitters is in charge of a pair of pins.

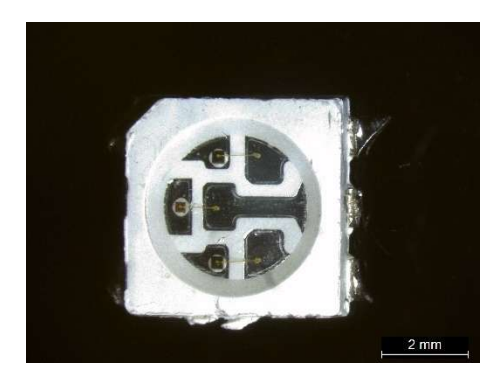


Figure 6-25. Optical image of the 5050 LED.

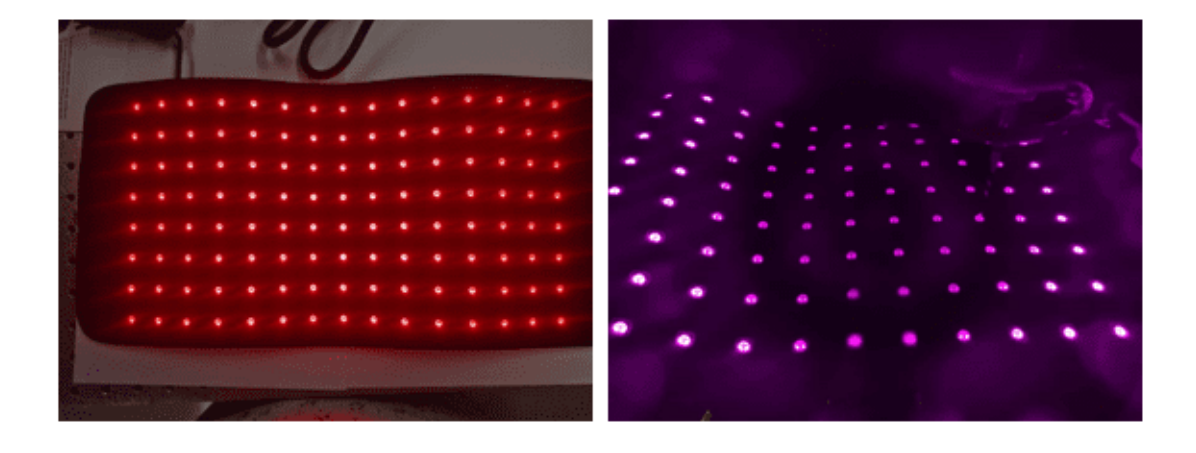


Figure 6-26. Working mode of the wearable PBM panel.

Compared to the PBM panel, there are more working modes for this wearable PBM device. The LED lighting can be in continuous mode or pulse mode. In addition, it is able to select types of emitters to work. In **Figure 6-26**, the left photo shows that only 660 nm LED was on, and the right photo shows that only 850 nm was on. Therefore, there are a total of six working modes for the wearable PBM panel. The switching of the panel depended on the number of presses of switches. For this system, the treatment is fixed at 20 mins. After 20 mins, the wearable PBM device will be turned off automatically.

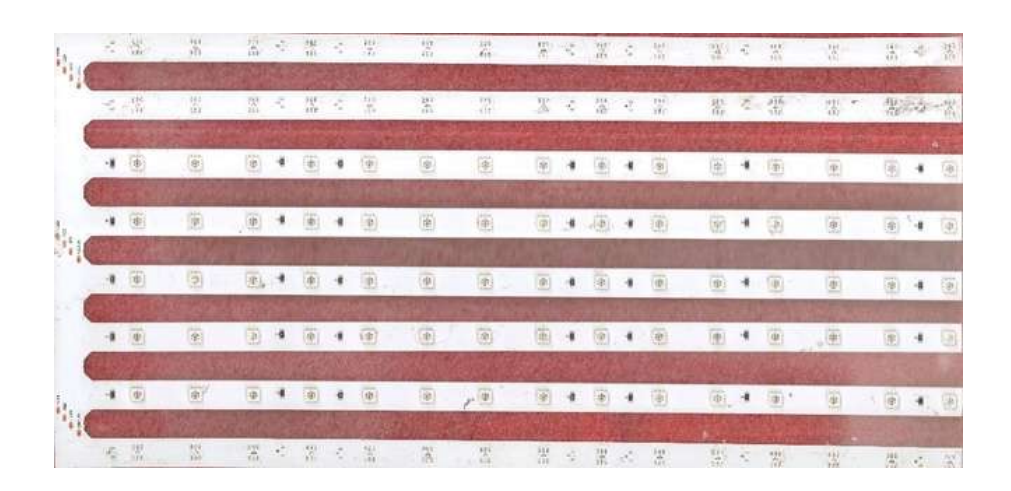


Figure 6-27. Photo of the wearable PBM circuit.

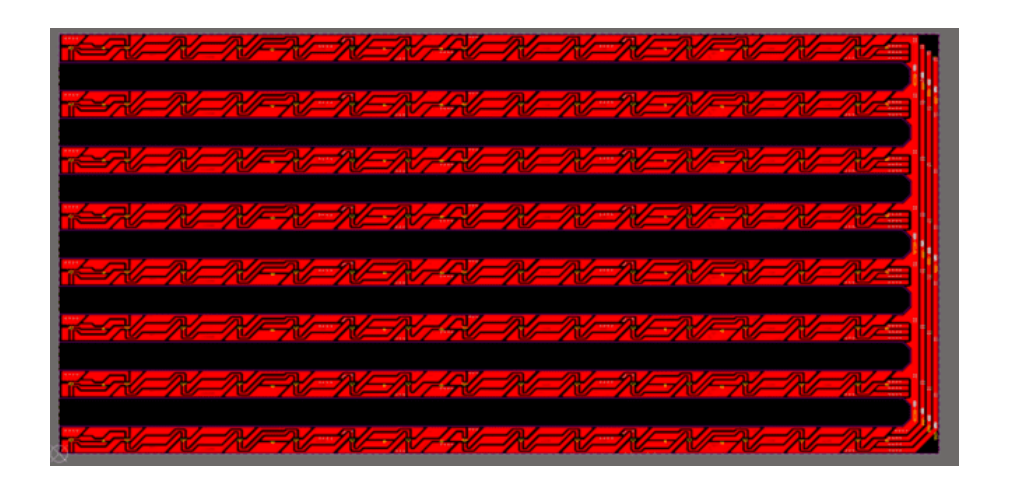


Figure 6-28. Circuit design of the wearable PBM.

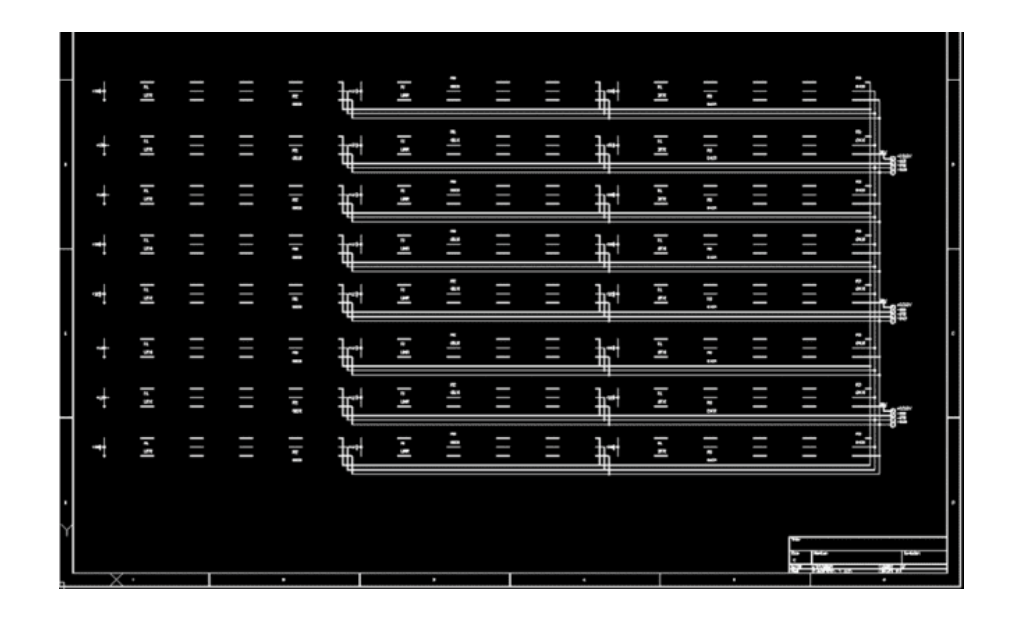


Figure 6-29. Electric diagram of the wearable PBM panel.

In detail of the circuit design, the LED panel was composed of 120 LEDs. The interdistance between LEDs was 17 mm, as shown in **Figure 6-27**. The LED chip size was 5 * 5 mm. The circuit of this PBM is a 2-layer circuit with a thickness of 0.3 mm. **Figure 6-28** illustrates the circuit design of the wearable PBM panel. It was obvious that the width of the circuit is quite wide, hence the circuit is covered with a substantial amount of copper. This can help to dissipate the generated heat in the treatment because copper processes good thermal conductivity. Additionally, the circuit is also encapsulated with an aluminum layer to help heat dissipation. This also increases the bending rigidity of the circuit for reinforcement.

As previously mentioned, each LED chip contains three emitters. Each emitter is controlled separately by different pairs of pins. **Figure 6-29** illustrates the electric diagram of the wearable PBM panel. The LEDs were divided into 8 rows, in which five LEDs are series connected in each row, and then parallel connected. There are a total of three types of resistors

in the encapsulation of 1206. The resistance of the resistor was 150Ω , 830Ω , and 240Ω . These three types of resistors are connected to different emitters to limit the current across the array. The system voltage of the panel is fixed at 12 V.

6.4.3.2. Wearable PBM panel wavelength

The wearable PBM panel wavelength was measured, as shown in **Figure 6-30**. There are two main wavelengths for this PBM panel. The peak wavelengths were 856.57 nm, and 640. 27 nm. The widt50 of the near-infrared peak was 30.29 nm, while the width50 of the red-light peak was 17.24 nm. Compared to the spectral irradiance, it can be that 850 nm light irradiance is higher than that of the 650 nm LEDs. However, the spectral irradiance may vary due to the position.

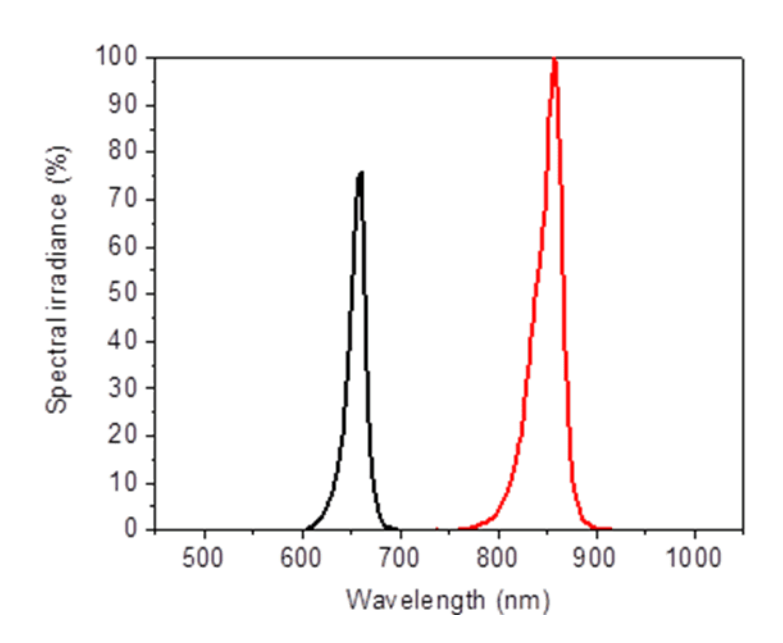


Figure 6-30. Wavelength spectrum of the wearable PBM panel.

The LED wavelength stability was evaluated with different currents, from 0.001 A to

0.3 A. **Figure 6-31** illustrates the wavelength shift of the 850 nm emitter from the LEDs. The main peak of the wavelength at 0.001 A was 853.64 nm, and the width50 was 14.98 nm. At 0.02 A, the peak wavelength was 854.44 nm, and the width50 was 28.45 nm. At 0.3 A, the peak wavelength was 883.23 nm, and the width50 increased to 65.51 nm. The peak wavelength was stable as the current increased from 0.001 A to 0.02 A, but the width50 increased by around 89.91%. The further increase of the current may shift the wavelength by around 3.3%.

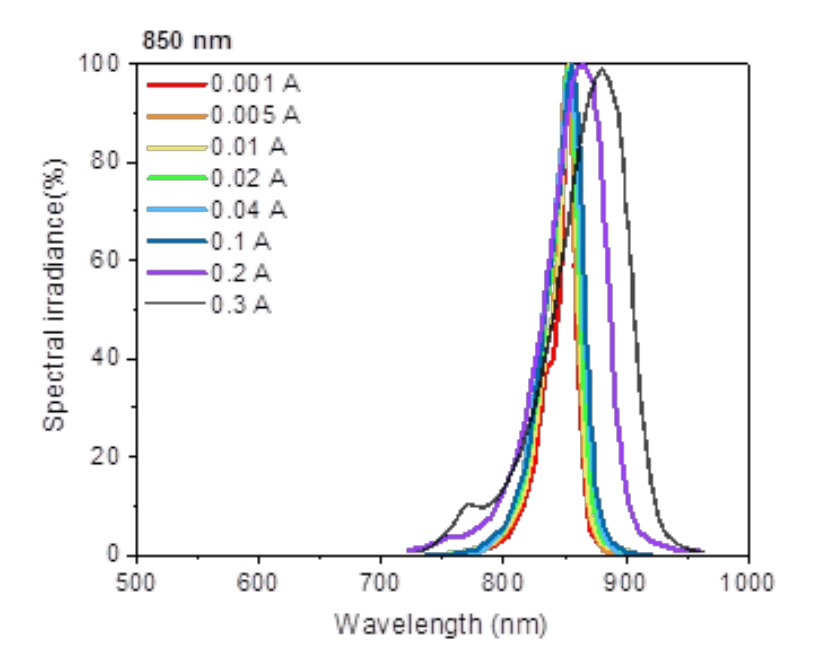


Figure 6-31. Wavelength shift of the 850 nm emitter.

Figure 6-32 illustrates the wavelength change of the 650 nm emitter from 0.001 A to 0.2 A. At 0.3 A, the emitter was completely burned. Upon reviewing the Figures, it was obvious that the peak wavelength of the LED shifts as the current increases. The main peak wavelength at 0.001A was 655.53 nm and the width50 was 12.79 nm. At 0.005 A, the main peak wavelength was 655. 96 nm and the width 50 was 15.11 nm. At 0.1 A, the peak wavelength shift to 665.12 nm and the width was 28.82 nm. The change of the peak wavelength was around

1.46%, and the width50 increased by around 125%. From the above two results, it found that the LEDs in wearable PBM is a low-power LED. It is appropriate to work at the current below 0.01A. LED optical properties deteriorate as the current increases over 0.01A.

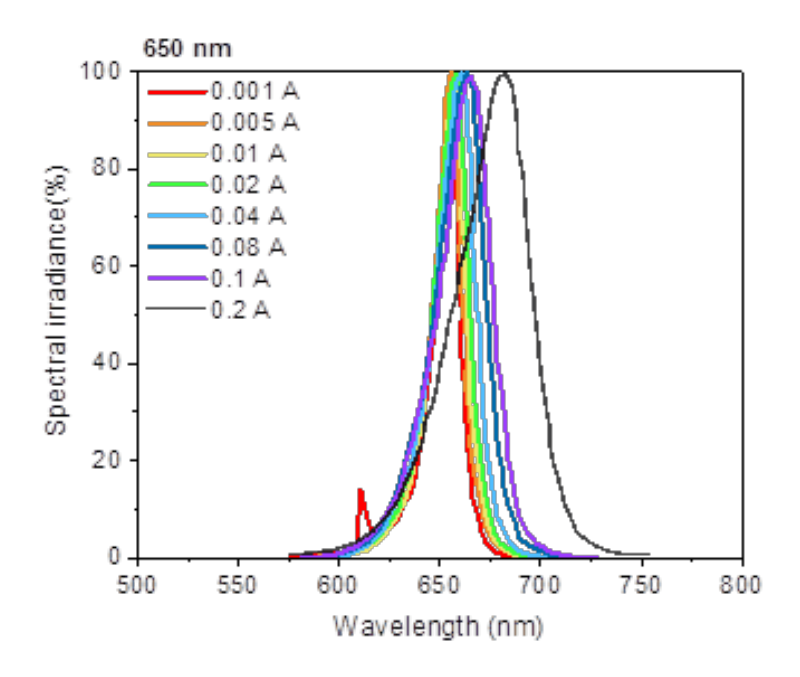


Figure 6-32. Wavelength shift of the 650 nm emitter.

6.4.3.3. Wearable PBM LED electric properties

Individual LED voltages were measured with a multimeter (**Figure 6-33**) during the working of the system. For 850 nm light, the voltage of LEDs was 1.45 V. For 660 nm light, the voltage was 1.96 V. This result was similar to the PBM panel, in which the red-light LED voltage is higher than that of near-infrared LED.

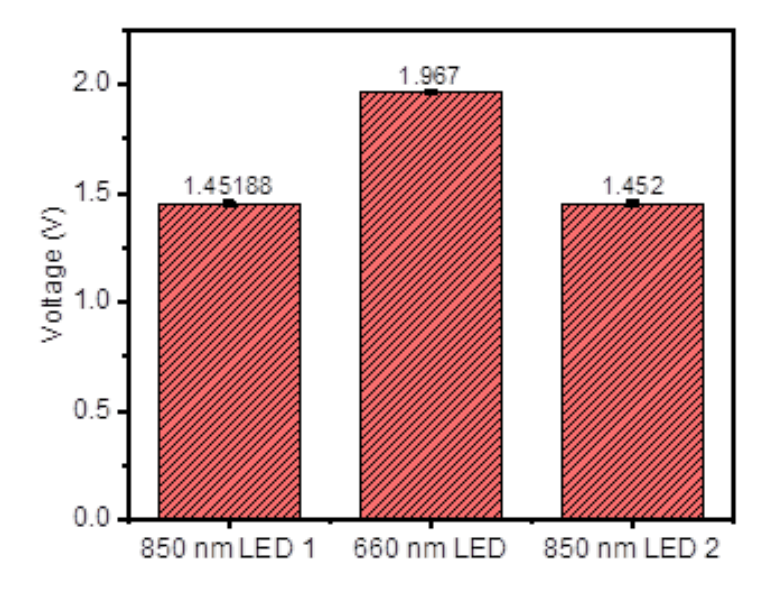


Figure 6-33. LED voltage of the wearable PBM device.

To comprehensively evaluate the electrical properties of the LEDs, we measured the IV curve of each emitter of the LED as shown in **Figure 6-31**. Refer to **Figure 6-33**, and **Figure 6-34**, it found that the current of the LED in wearable PBM was around 0.02A. The LED used in this wearable PBM was a low-power LED. The working current of the wearable PBM is smaller than the PBM panel at 325 times.

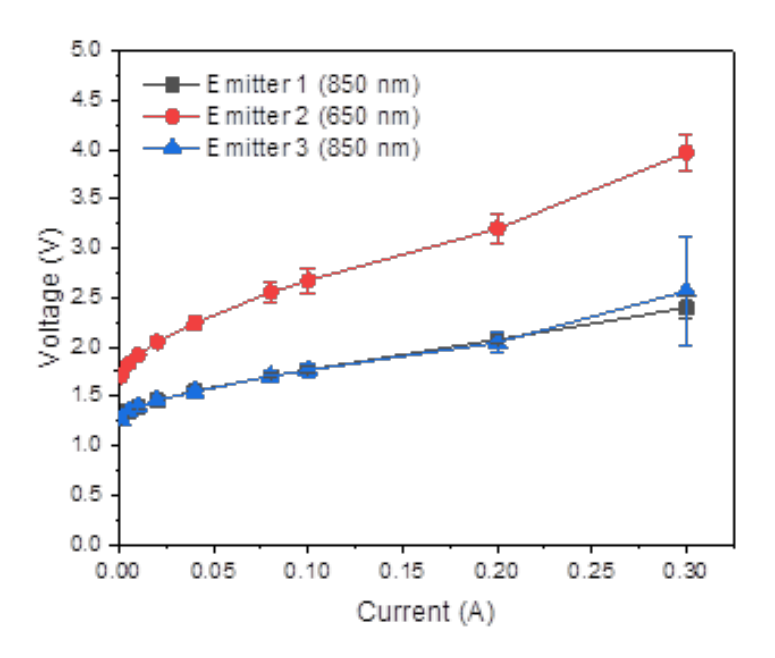
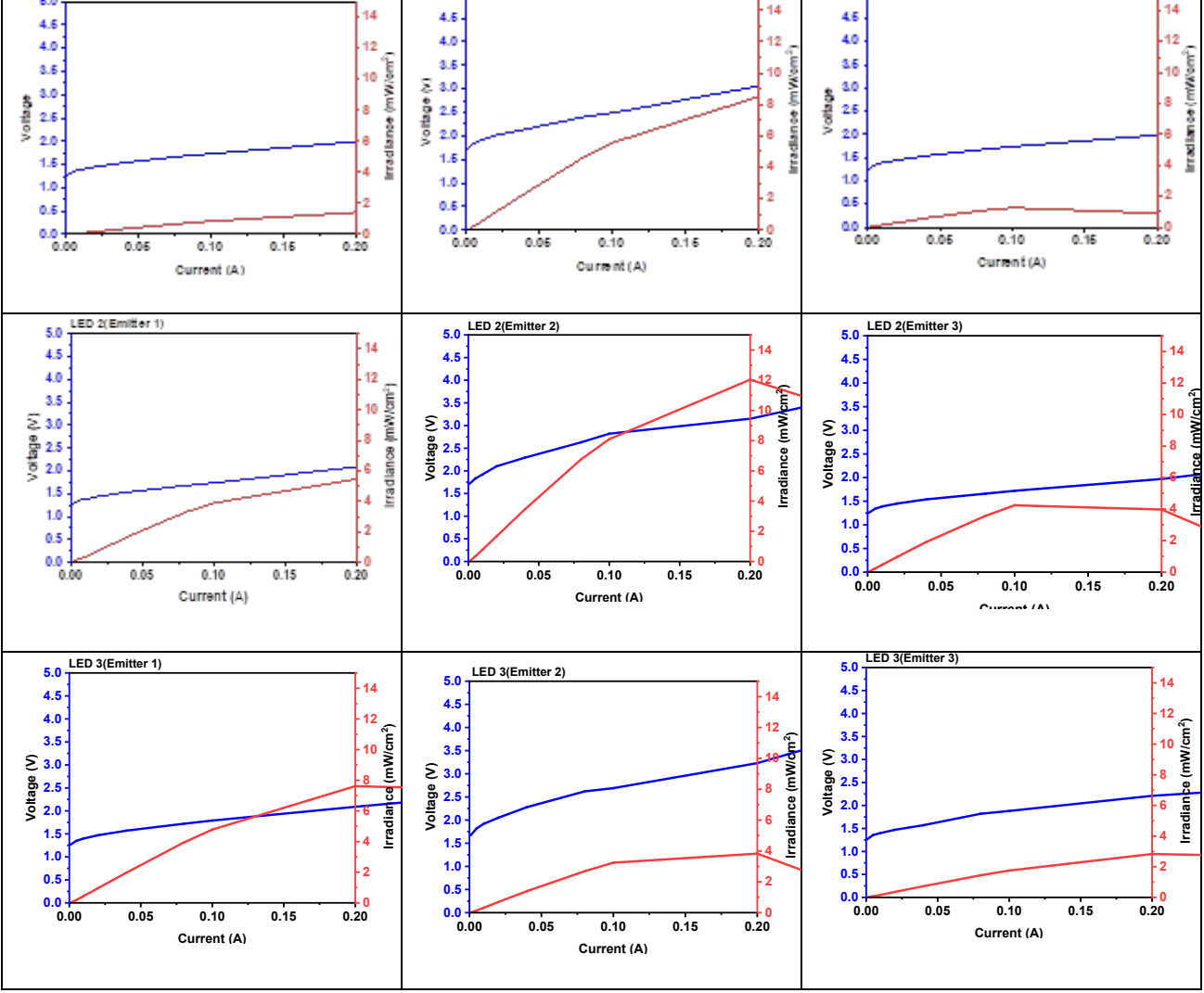


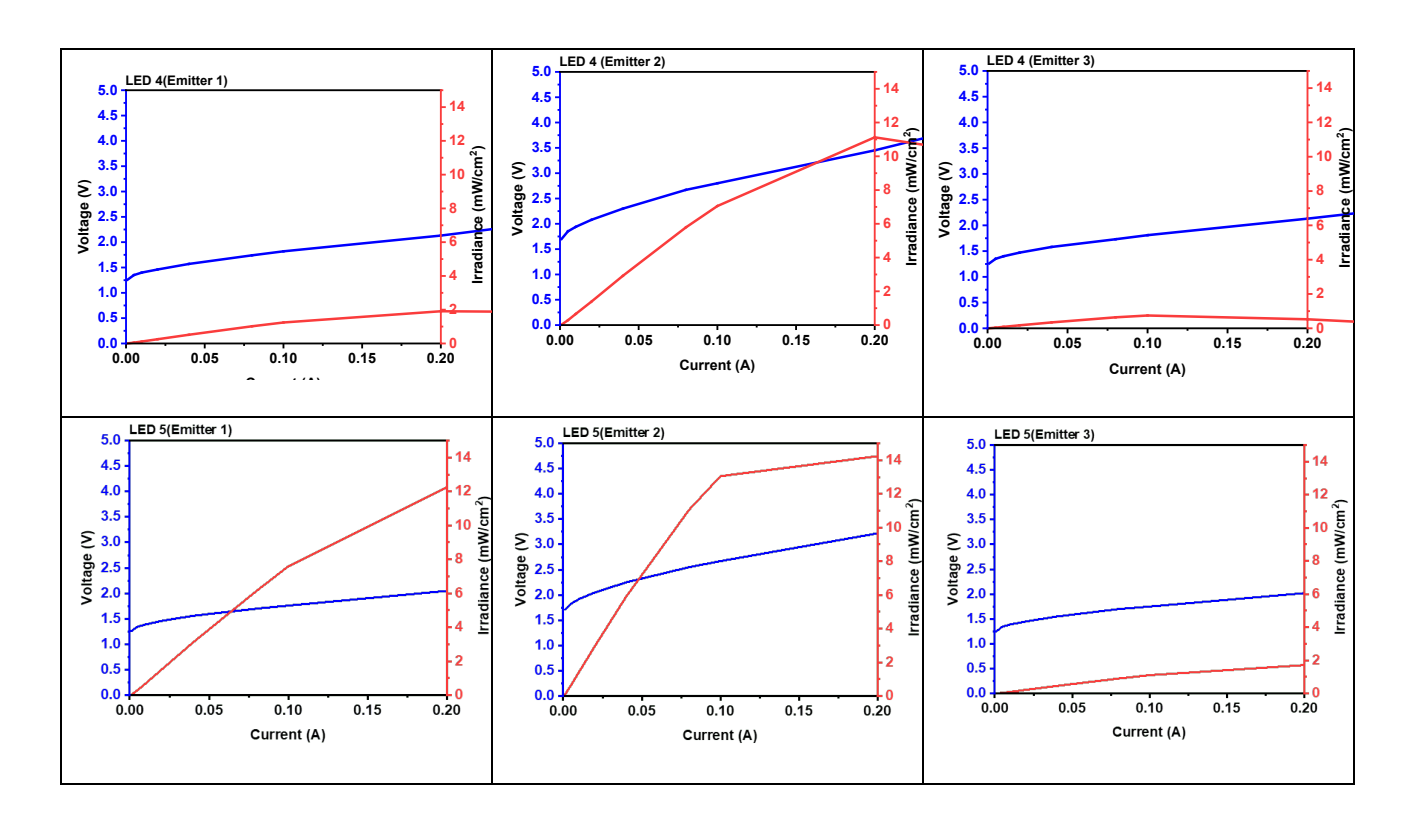
Figure 6-34. IV curve of the LED.

We also conducted an evaluation of the IV curve in response to its irradiance, as shown in Table 6-4. It found out that the irradiance variation of this LED is quite large. At the current of 0.002 A, the emitter 1 irradiance was 0.88 mW/cm² (SD: 0.655), the emitter 2 (650 nm) irradiance was 1.52 mW/cm² (SD: 0.636), and the emitter 3 irradiance was 0.786 mW/cm² (SD: 0.808).

LED 1 (Bmitter 1) 4.5 4.6 4.0 12 4.0 4.0 irradianee (mW/em²) 3.5 8.6 2.6 2.6 2.6 2.0 3.0 8.0 2.6 2.6 20 2.0 1.5 1.5 1.6 1.0

Table 6-4. IV, and irradiance of the LEDs in wearable PBM





6.4.4. Wearable PBM irradiance properties

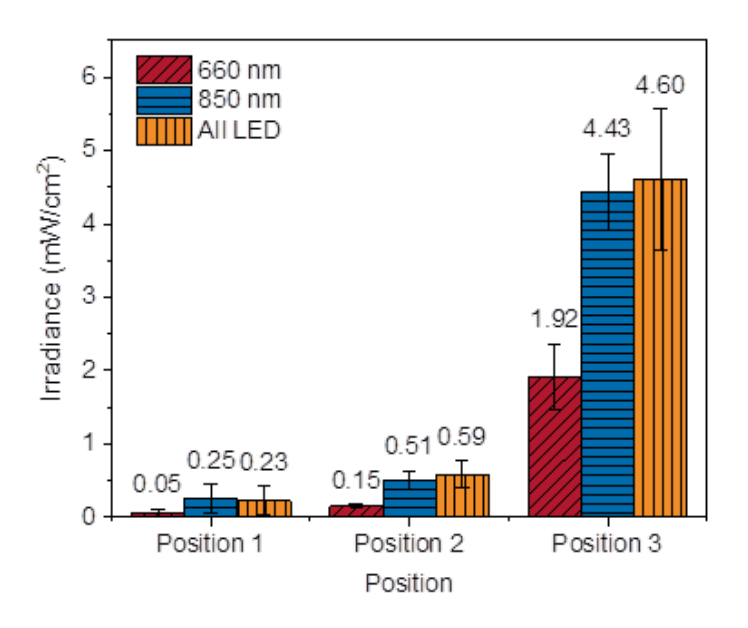


Figure 6-35. Irradiance of the wearable PBM panel.

The irradiance of the wearable PBM at different positions was measured at the continuous mode first. Position 1 indicates the center of four LEDs, position 2 indicates the

middle between 2 LEDs, and position 3 is center of the LED. According to **Figure 6-35**, the position 1 irradiance was only 0.23 mW/cm², the position 2 irradiance was 0.59 mW/cm², and the position 3 irradiance was 4.6 mW/cm². There are great differences in the irradiance amount among 660 nm emitter, and 850 nm LEDs because there are two emitters for 850 nm wavelength. In addition, the irradiance distribution is very uneven.

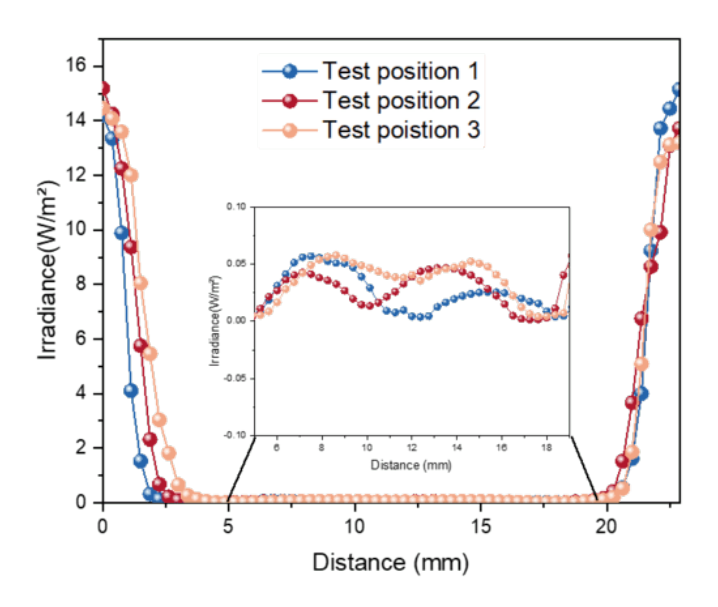


Figure 6-36. Irradiance distribution of wearable PBM (Horizontal).

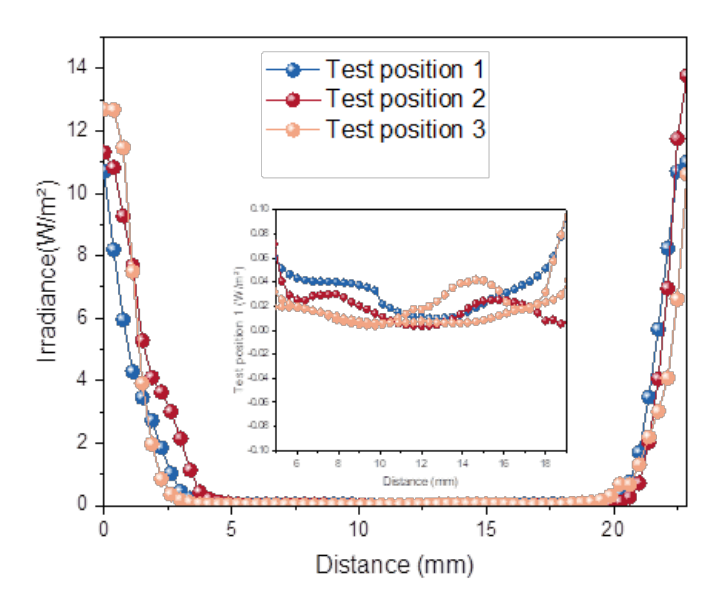


Figure 6-37. Irradiance distribution of wearable PBM (vertical).

We also measured the irradiance distribution of the wearable PBM panel across the panel. Since the wearable panel is directly in contact with the human skin, the testing distance between the panel and the detector was zero. **Figure 6-36** shows the horizontal irradiance distribution of the wearable PBM at three positions. **Figure 6-37** shows the vertical irradiance distribution of the wearable PBM at three positions. It was obvious that the positions between the two LEDs were only 0.05 mW/cm² in the horizontal direction. The central irradiance of the LEDs was 1.4 mW/cm².

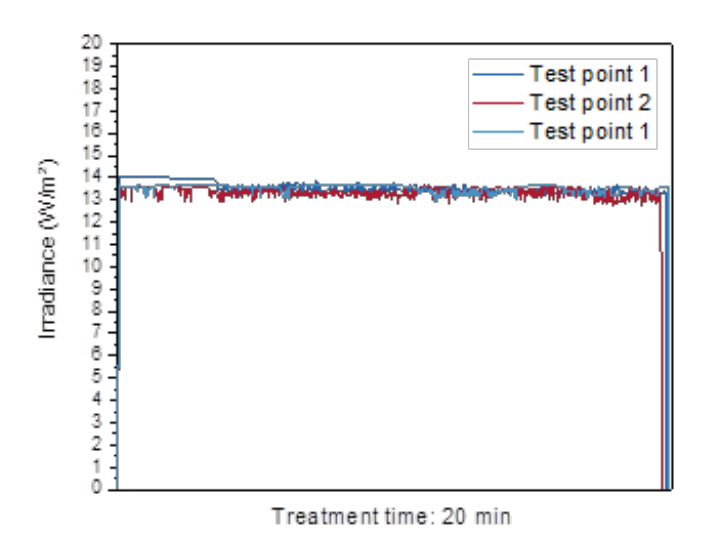


Figure 6-38. Irradiance variation of the panel throughout treatment.

In the vertical direction, the irradiance at the middle position was only around 0.002 mW/cm2 in **Figure 6-37**. Even though the interdistance between LEDs was the same, the irradiance distribution at the horizontal direction, and the vertical direction are different because the LED is a dual-mode LED containing three emitters. The interdistance between the

emitters is not the same.

We also measured the irradiance stability of the wearable PBM throughout the treatment time in **Figure 6-38**. It found out that the irradiance was kept at 1.35 mW/cm², and the standard deviation of the irradiance was 0.696.

6.4.4.1. Temperature measurement

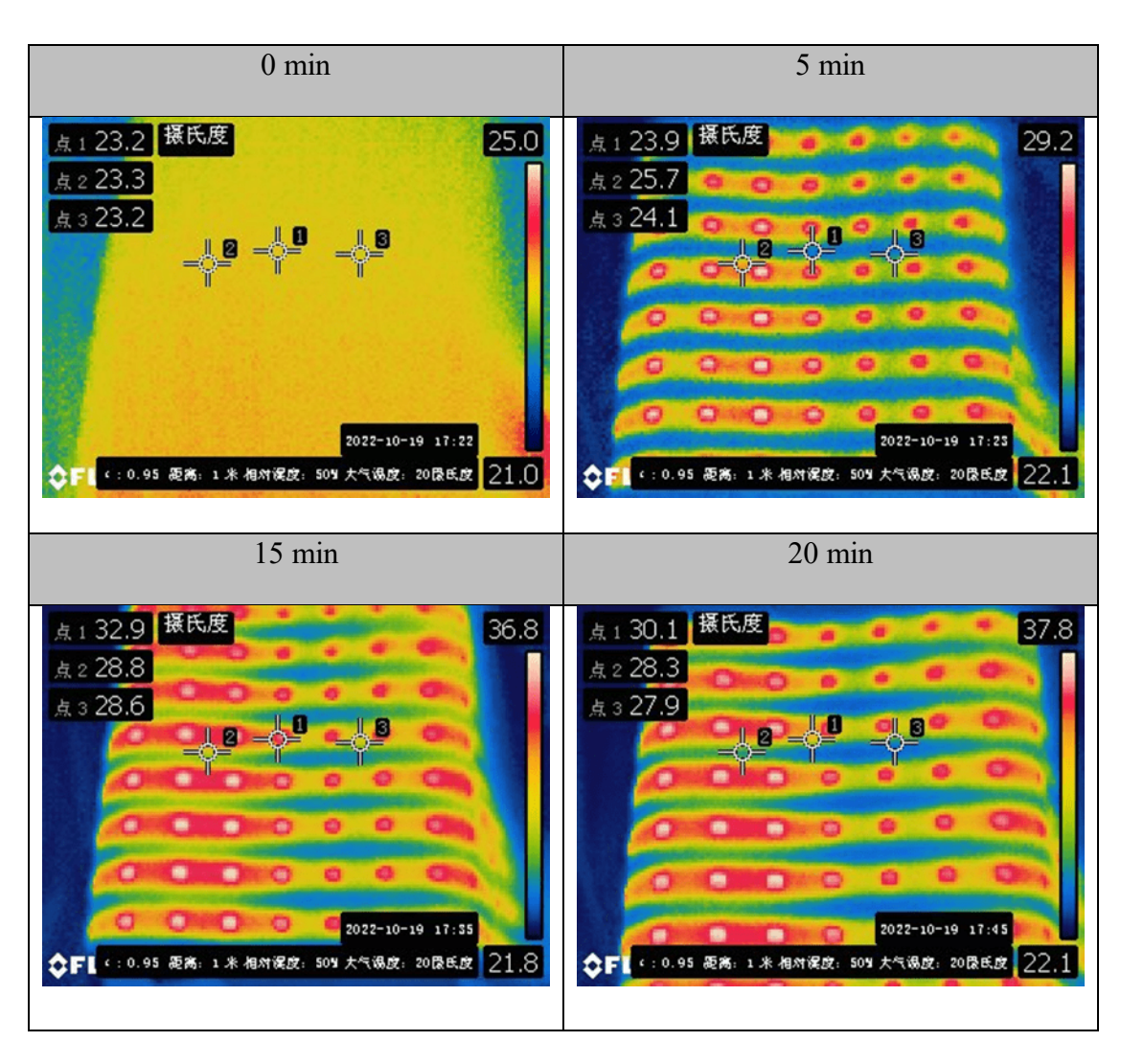


Table 6-5. Temperature measurement of wearable PBM.

For the wearable PBM panel, the temperature was monitored by the infrared red camera

at different treatment times (**Table 6-5**). For the panel, all LEDs including both 660 nm and 850 nm were worked in continuous mode. At the initial, the panel temperature was 23.2°C, similar to the room temperature. After 5 mins, the temperature of the panel slightly increased. The increase of the temperature is uneven. The highest temperature is the center of LEDS, around 29.2°C. The flexible circuit covered with fabric was around 25.7°C. The pure fabric part was around 23.9°C, which is not different from the initial. After 10 mins, the temperature of the center of LEDs raised to 36.8°C. The circuit temperature was increased to 28.8°C. At the end of treatment (20 mins), the LED surface temperature was 37.8°C. The circuit temperature was around 30.1°C. The area of the highest temperature is larger than that at 5 mins and 10 mins. The temperature of the panel increased by around 62.5%, but the temperature is still below the safe threshold of the human body.

6.4.4.2. Textile properties

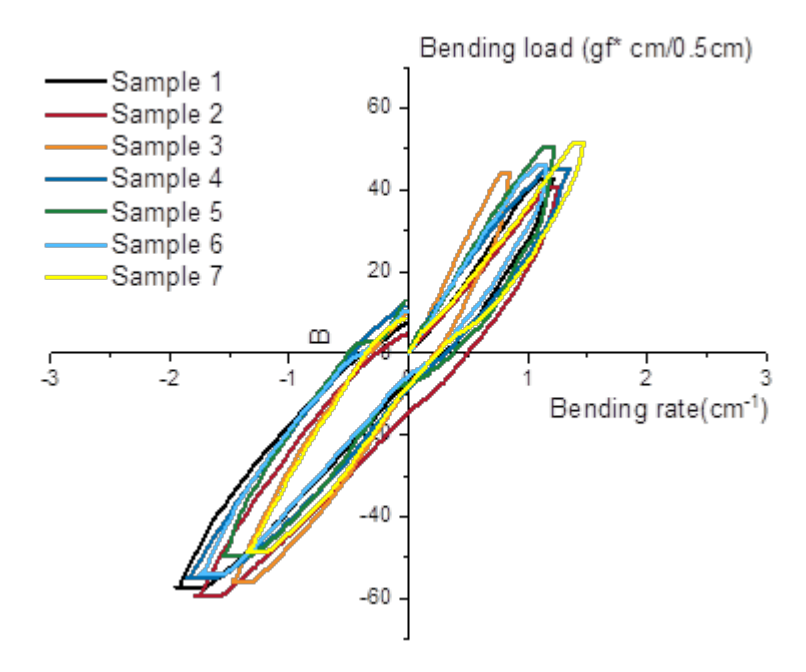


Figure 6-39. Bending rigidity of the wearable PBM circuit.

Considering the nature of the wearable PBM, we measured the flexibility of the PBM circuit. However, the circuit bending rigidity was over the upper limitation of the KES machine. We then cut the circuit into a width of 0.5 cm, and continuously measured. Figure 6-39 shows the bending performance of the circuit. The circuit requires around 45 gf to bend at the bending rate of 1 cm. The bending rigidity of this circuit is still far behind that of textile products.

The air permeability resistance of the wearable panel was 0.071 kPa*s/m (SD: 0.0174). Even adhesion was used between layers of the panel, this panel has good air permeability.

6.4.5. Comparison and conclusion

We have measured two types of PBM devices characterized by different designs, power consumption, different LEDs, and other aspects. These experiments helped us to establish an evaluation system for wearable PBM panels. Besides this, we aim to compare these two devices to study the design strength and weaknesses as the foundation for further work. The comparisons between these two devices are listed out in **Table 6-6**.

Table 6-6. Comparison between PBM panel, and wearable PBM.

	PBM _I	oanel	Wearable PBM		
System voltage	44.06 V 70.58V		12 V		
Types of power system	Constant current		Constant voltage		
Treatment distance	15-30 cm		0 cm		
LED wavelength	848.45 nm	655.96nm	854.44 nm	660.09 nm	
LED voltage	1.61	1.95	1.452	1.967	
LED current	0.65	A	0.02 A		
Central irradiance	25.89 mW/cm ²		1.35 mW/cm ²		
(Treatment distance)	(30 cm)		(0 cm)		
Irradiance distribution	Even		Uneven		
Temperature variation	54.5°C		37.8 °C		
Secondary optical	Yes		No		
design					

Through comparing the performance of these devices, several conclusions can be drawn for the further development of PBM devices:

Firstly, only one type of LED will be selected and used for the development of wearable PBM to reduce the complexity of the circuit, and power system. Both aforementioned devices use both red light and near-infrared light for PBM. However, the power difference between these two types of LEDS introduces complexity in circuit design and power control. In detail, the voltage of the red-light LED is normally higher than that of the near-infrared red LED. Based on this, the voltage requirement for red light LED will be higher, hence the power supply to the two types of LEDs needs to be different. For example, the output of the power converter

for the PBM panel needs to a cover wide range to accommodate the voltage requirement. Another key issue is that the electrical properties of LEDs also vary with types, so the appropriate voltage or current of LEDs also can be different. It is difficult to control these two types of LEDs with the same voltage, and current.

Second, LED selection is crucial to the overall performance of the PBM system in terms of power, wavelength, irradiance, and temperature variation. Several guidelines have been built up for LED selection, as follows:

- Wavelength: The peak wavelength of near-infrared light should be in the range of 845 nm to 855 nm.
- Irradiance level: The irradiance level of LED should be in the range of 1 to 25 mW/cm². The lower limit is the wearable PBM irradiance, while the upper limit is the PBM panel. This range avoids the issues related to excessive power while still providing sufficient irradiance for treatment.
- Electrical properties: The operational current of the LEDs depends on the wavelength shifting at different current levels. The current should be limited to the range of tens of milliamperes to prevent overheating and potential damage to the LEDs.

Then, it is suggested that the maximum irradiance variation across the panel should be within the range of 30%, primarily due to the LED optical variation. To achieve this, it is recommended that the wearable PBM system should not be directly in contact to the skin. The

presence of a gap between the skin, and the wearable PBM panel is advantageous to the irradiance distribution, and addresses the heat dissipation issue.

Finally, it is appropriate to use constant current for control. From the above evaluation, it found that one is using constant voltage, and another is using constant voltage. Using constant current to control the LED is advantageous in controlling the irradiance precisely because LED is a current-sensitive device. However, there is a higher requirement in power design. Additionally, the overall system voltage should be maintained at or below 12V, the same as the wearable PBM system to avoid electrical hazards.

6.5. Conclusion

This chapter presents a comprehensive evaluation of two types of PBM systems from different aspects to establish an evaluation system for wearable PBM. In addition, the results, and analysis provide a foundation in designing and fabricating wearable PBM for breast cancer patients.

6.6. References

- [1] Y.-Y. Huang, A. C.-H. Chen, J. D. Carroll, and M. R. Hamblin, "Biphasic dose response in low level light therapy," Dose-response, vol. 7, no. 4, pp. dose-response. 09-027. Hamblin, 2009.
- [2] T. C.-Y. Liu, J.-L. Jiao, X.-Y. Xu, X.-G. Liu, S.-X. Deng, and S.-H. Liu, "Photobiomodulation: Phenomenology, and its mechanism," in Optics in Health Care, and Biomedical Optics: Diagnostics, and Treatment II, 2005, vol. 5630: SPIE, pp. 185-191.
- [3] M. Cronshaw, S. Parker, O. Hamadah, J. Arnabat-Dominguez, and M. Grootveld,

- "Photobiomodulation LED Devices for Home Use: Design, Function, and Potential: A Pilot Study," Dentistry Journal, vol. 13, no. 2, p. 76, 2025.
- [4] N. Bardsley *et al.*, 'Solid-state lighting research, and development multi-year program plan', *US Dep. Energy*, 2014.
- [2] C. Cengiz, M. Azarifar, and M. Arik, 'A Critical Review on the Junction Temperature Measurement of Light Emitting Diodes', *Micromachines*, vol. 13, no. 10, Art. no. 10, Oct. 2022, doi: 10.3390/mi13101615.
- [3] M. Bürmen, F. Pernuš, and B. Likar, 'LED light sources: a survey of quality-affecting factors and methods for their assessment', *Meas. Sci. Technol.*, vol. 19, no. 12, p. 122002, 2008, doi: 10.1088/0957-0233/19/12/122002.

Chapter 7. Development of the wearable flexible photobiomodulation panel for breast cancer patients

7.1. Introduction

Chapter 6 outlines the establishment of an evaluation system for the wearable photobiomodulation system, aimed at establishing the interrelationship between effective photobiomodulation treatment, and the device setup, and corresponding parameter requirements. Two different types of commercial photobiomodulation devices were evaluated using this system, considering various aspects such as LED performance (electrical, and optical), electronic system, irradiance distribution, irradiance level, temperature, and others. These assessments serve to bridge the research gap between efficient photobiomodulation treatment, and the corresponding device requirements, and can also be utilized as a benchmark for future studies.

From previous literature review and studies, it was found that there are limited photobiomodulation devices that conform to the human contour providing relative uniform irradiance for treatment. This limitation poses a challenge to the widespread adoption of remote photobiomodulation. This chapter aims to develop a wearable flexible photobiomodulation panel, which can conform to the shape of the breast for the treatment of radioactive dermatitis. In the details of the study, we have evaluated the LED parameters, and configurations to select the appropriate one that ensures conformability, comfort, efficiency, and safety for use. Additionally, a fabric pattern-making approach was developed for the PBM panel shape,

designed with an appropriate array setting, providing a good conformability to the breast shape for the comfort, and precision of the photobiomodulation. An initial evaluation of the flexible PBM panel was conducted to understand the developed panel's performance. The irradiance level of the current PBM panel can be over 2 mW/cm², surpassing the performance of commercial wearable PBM devices. However, improvements are needed in the irradiance distribution, and temperature control of the panel for precise dose control, and user safety. This evaluation serves as a foundation for further studies, including the optical design, and integration of the PBM panel to tackle the above issues.

7.2. Experiment design

Based on the findings from previous chapters, it found that the LED chip as the light source is the critical component of the treatment parameters of the PBM. There are numerous LED chips available in the difference of wavelength, size, power, viewing angle, materials, and other characteristics. Considering this, the first step is selecting an appropriate LED as a light source for the PBM. Previous evaluation has confirmed that low-power LEDs with higher irradiance are preferred for wearable PBM. In addition, the optical properties, especially peak wavelength, will be influenced by the electrical properties of the LEDs. The stability of the LED on the electrical, and optical aspects also needs to be assessed. A comprehensive evaluation will be conducted to select the appropriate LED for the development of flexible PBM.

Consequently, the arrangement of LEDs, including the interdistance, and the layout, is

also critical to the overall performance of the array, especially for the irradiance, and irradiance distribution of the panel. This will be studied through simulation and verification experiments. It proposed to confirm the interdistance, and layout of the LEDs across the panel.

In the case of the panel shape design, conformability to the human contour is the first priority, and then in combination with the circuit design with a focus on electrical safety. The panel shape design will be investigated to allow good conformability. Additionally, sizing also needs to be considered to accommodate the body shape of different users in this process.

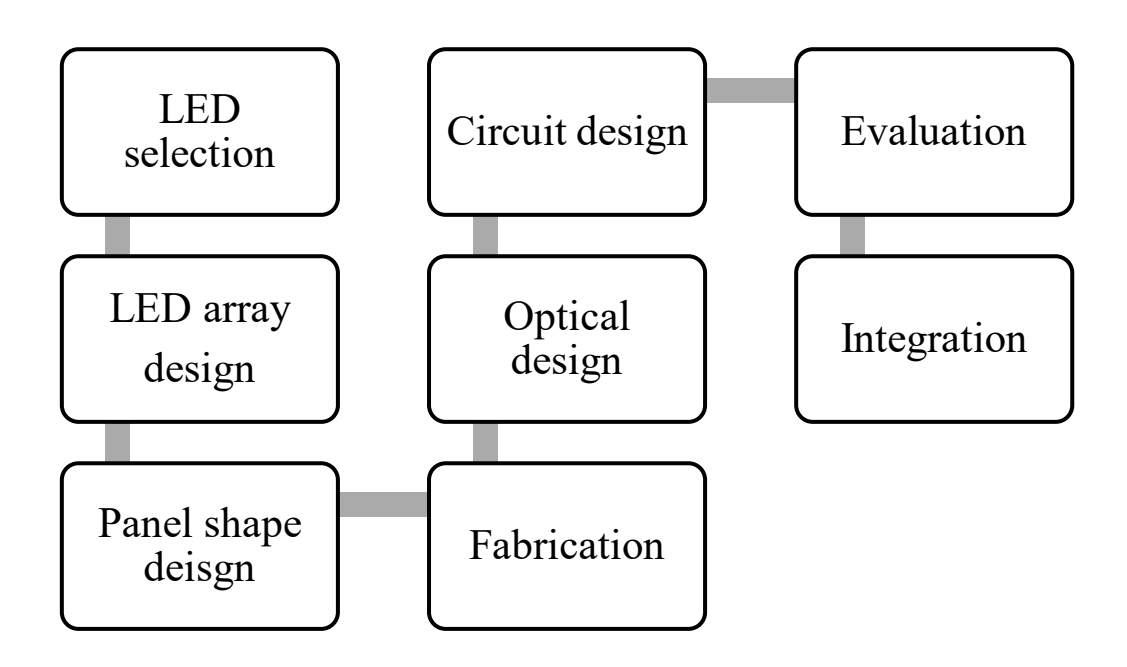


Figure 7-1. Research framework of the wearable PBM panel

Then, a secondary optical system will be considered for the panel from the design of the lens, and the light diffusion materials to maximize the light efficiency. Finally, the integration of the panel will be designed, followed by evaluation. The research framework for this chapter is demonstrated in **Figure 7-1**.

7.3. Experiment

Following the research framework, the experiments can be divided into several steps: Firstly, we are going to test the LEDs from different aspects to select the appropriate one for the wearable applications. In addition, the LED array design will be studied from the interdistance between LEDs, and the arrangement of LEDs. Then, we will design, and fabricate the shape, and circuit of the panel conforming to the breast shape for further studies.

7.3.1. Material

Table 7-1. Parameter of the LEDs

	LED type	Size of	Wavelength	Angle	Current
		LEDs			
1	1080-1553-1-ND	0603	850nm	145	65
2	1080-1347-1-ND	0603	850nm	145	65
3	1516-1269-1-ND	1206	850 nm	140	50
4	1516-1266-1ND	0805	850 nm	140	50
5	15406085BA400A	0603	850 nm	140	70
6	B170IR20C000214U930	0805	850 nm	140	70
7	1080-1346-1-ND	1206	850 nm	75	65
8	1080-1634-1-ND	1414	850nm	150°	1500
9	VSMY1850	0805	850nm	120°	100

For the studies of this chapter, different types of LEDs were brought, and tested in the aspects of voltage, current, and irradiance. Details of the LEDs are shown in Table 7-1. A pair of electrodes was designed and fabricated on a printed circuit board. A soldering bench, and solder also were used to solder the LED onto the printed circuit boards for evaluation. Besides

different LEDs, different diffuser was used to evaluate their functionality on the irradiance distribution of the flexible PBM panel. The specifications of the diffusers are listed in Table 7-2. Different types of diffusers vary in the light permeation rate, and the degree of haze, while the thickness of the diffuser also influences the rate of light permeation.

Table 7-2. Specification of the diffusers.

	Type of diffuser	Thickness (μ)		
1	CSD	50		
2	CSD	75		
3	CSD	100		
4	CSD	125		
5	SKC	210		
6	CT	188		
7	CSW	100		
8	CSW	125		

7.4. Testing

In contrast to the previous section, we conducted testing on the LED performance, and then designed, and fabricated an array for the PBM panel based on these evaluations. The evaluation of the LEDs includes the impact of the LEDs' size on irradiance, peak wavelength of LEDs, wavelength shifting, power, irradiance, and viewing angle. Below sections are going to elaborate on these tests in detailly.

7.4.1.1. LED irradiance distribution measurement

It is crucial to measure the irradiance distribution of the LED chips for the design of the PBM device. Additionally, studying the irradiance distribution of different sizes is necessary to achieve a balance between irradiance, and the form factor of the LEDs. To address this, we investigated the irradiance distribution of different LEDs. The CAS 140D spectrometer from Instrument Systems was utilized to measure the irradiance. The detector was covered with black paper with a 2 mm diameter hole. A manual x-y-axis displacement stage from NUSDUN (HTXY 210) and a manual z-axis displacement stage from HUIKE (HTZ120) were used for positioning. A power source was used to control the LEDs. The testing distance between the LED, and the detector was set at 1 cm. In this experiment, different sizes of chips were soldered onto a printed circuit board, and the power supply was fixed at a constant current of 0.02 A. The irradiance distribution of individual LEDs was then measured.

7.4.1.2. LED wavelength measurement

CAS 140D spectrometer and a power source was used to measure the wavelength of various LED chips. The wavelength stability of the LEDs was also measured at different currents. This experiment was used to evaluate the wavelength shifting of the LEDs and determine the working current of the LEDs. Considering the previous chapters' studies, it is appropriate to use low-power LEDs in wearable applications. Based on this, the settled testing current was 0.001A, 0.005A, 0.01A, 0.02A, 0.04A,0.08A, and 0.1A. The testing distance between the detector, and the LED was 3 cm.

7.4.1.3. LED electrical, and irradiance characterization

Besides irradiance distribution and the wavelength, CAS 140D spectrometer was also used to measure the total irradiance of the LEDs, and a power source was used to measure the corresponding voltage, and current. This can help us to evaluate the power consumption, and the optical efficiency of the LED chips. Similar to the above testing, the testing distance between the detector, and the LED was 3 cm, and a power source was used to control, and measure the IV curve of the LEDs.

7.4.1.4. LED viewing angle measurement

Besides the above properties, the selected LED irradiance distribution, and corresponding LED need to be measured as the information for the study of LED arrangement. Similar to the previous experiment, a 140D spectrometer was used to measure the irradiance, and a power source was used to power the LED. A manual x-y axis displacement stage from NUSDUN (HTXY 210), and a manual z-axis displacement stage from HUIKE (HTZ120) was used to position. In details of the experiment, the detector was covered with black paper with a 2 mm diameter hole. The highest irradiance in both x, and y directions was firstly identified as a basepoint for measurement. The testing distance between the LEDs, and the detector was only 1 cm.

7.4.2. Design of the shape of the flexible PBM panel

Conforming to the human contour is the critical priority of the flexible PBM device to realize comfort and convenience. The human body shape has a complex, and varied shape, making it challenging to achieve an optimal conformation with only using flexible materials, even fabric. Moreover, accommodating the shape of the breast presents an even greater challenge because it is round, asymmetrical, and varies widely across individuals. Fabric pattern making consider the shape, and dimensions of the body contours to create, and manipulate the patterns to ensure a tailored fit. Simulating the apparel pattern-making process to design the shape of the PBM panel can realize good conformability to the human body. This also can allow seamless integration of the flexible PBM panel. Therefore, it is valuable to study body shape measurement as the basis for apparel pattern making.

For underwear of women, there are two important parameters for the sizing, and pattern making: the first one is the underbust measurement, and another is the difference between the underbust and upper bust. These two parameters help customers to select properly fitting underwear, in which the first one determines the band size of bras, and the second parameters determines the cup size. The first indicator (under bust) is typically represented by a number, and the second indicator (cup size) is normally presented in a letter. The cup size determination was listed in **Table 7-3**, as a reference. These two parameters also determine the size of the pattern and serve as guidelines for the design of the corresponding pattern.

Difference	Cup size		
cm	/		
10-12	A		
13-14	В		
15-17	С		
18-19	D		
20-22	Е		
23-24	F		

The above size charts, and information provided are used to assist the customer in selecting the underwear products. There is an interconnection between the 2D fabric patterns and underwear product sizing. We have studied the drafting of the underwear pattern, in which three more parameters influence the pattern size: bust height, inner bust arc, and outer bust arc. Furthermore, the sizes of the underwear also need to be grouped for different sizes of patterns, as demonstrated in **Table 7-4**. It is evident that there are seven sizes of patterns for a total of 20 sizes of underwear. Considering this, it is a common practice to use the same panel for a group of sizes of underwear products.

Table 7-4. Size of the bra.

		Size			Bust Height	Inner bust arc	Outer bust arc
					cm	cm	cm
70B	75A				7.9	8.4	9.4
70C	75B	80A			8.5	9	10
70D	75C	80B	85A		9.1-9.2	9.5-9.6	10.5
	75D	80C	85B	90A	9.7-9.9	10-10.1	11
		80D	85C	90B	10.3-10.6	10.5-10.7	11.5-11.6
			85D	90C	10.9-11.3	11-11.2	12-12.2
			85E	90D	11.5-12	11.5-11.8	12.5-12.8

The panel design is not only related to its physical shape, but it also needs to consider the circuit design, which is determined by the study about the LED array arrangement. Based on this, the detailed pattern, and sizing of the product will be discussed in the result section, taking into consideration both the physical design of the panel and the electrical circuitry. This comprehensive approach ensures that the final product meets both aesthetic and functional requirements.

7.4.3. Secondary optical system design

In the case of the LED divergence condition, a study about the optical design of the wearable PBM will be conducted from two different aspects. The first aspect involves the design of a secondary optic lens, and another approach is the utilization of flexible light

diffusion material. These approaches were studied and compared to investigate their applicability, and the impact on improving light efficiency. The testing set-up for the irradiance distribution is similar to the test in section 7.3.2. The testing distance between the detector, and the panel was 1 cm. This testing will provide valuable insights into the effectiveness of the optical design of the wearable PBM product.

7.5. Results and discussion

In the following section, we are going to discuss the results of the LED evaluation from different properties, the impact of the LED arrangement on irradiance distribution, and panel shape design.

7.5.1. LED selection

7.5.1.1. Irradiance distribution of LED chips at different sizes

Firstly, we need to determine the size of the LED. Considering the wearable applications, the energy consumption of the wearable device needs to be minimized to reduce the electrical risks, and the temperature risks. Hence, the energy of the device needs to be efficient. The LED light exposure area needs to be maximized to reduce numbers of LEDs. The irradiance distribution of different-sized LEDs was measured. **Figure 7-2** shows the actual irradiance value, and **Figure 7-3** shows the relative irradiance value.

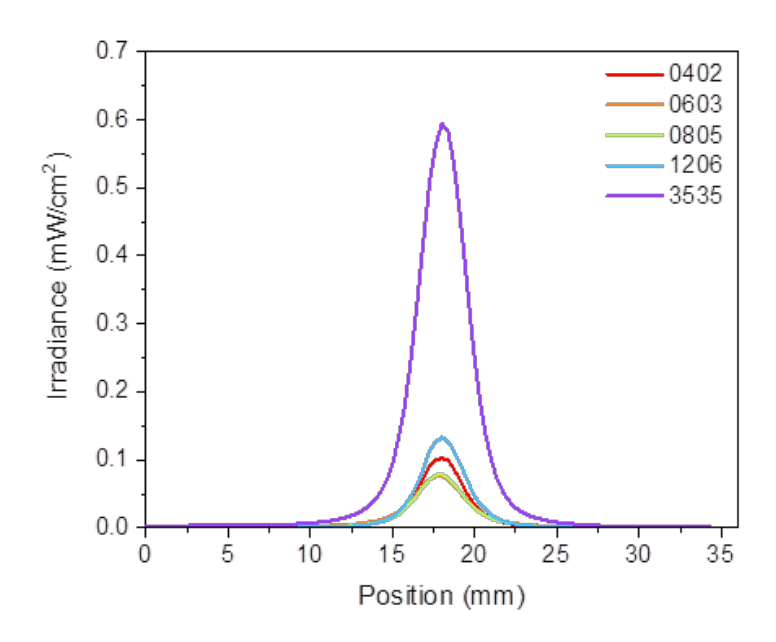


Figure 7-2. Actual irradiance distribution of different sizes of LEDs

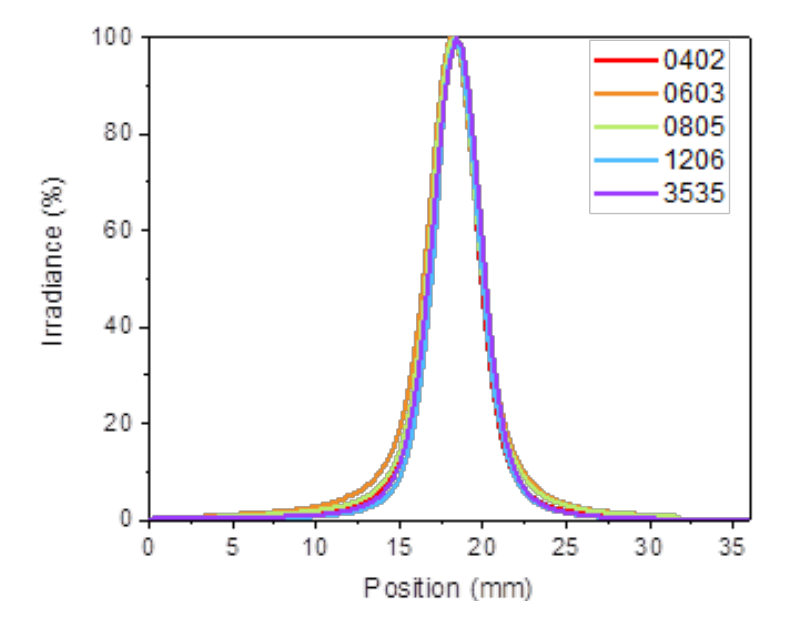


Figure 7-3. Relative irradiance distribution of different sizes of LEDs

In **Figure 7-2**, it was obvious that the LED chip in size 3535 has a relative higher center irradiance, which is around 0.6 mW/cm². For the rest of the LED, the LED chip in the size of 1206 was 0.13 mW/cm². However, LED in the chip size of 0402 irradiance (0.10 mW/cm²) at the center is higher than that of 0603 (0.076 mW/cm²), and 0805 (0.078 mW/cm²). There is a

trend that the LED chip size is larger, and the emitted irradiance is larger. However, when the LED chip size is smaller, there is no direct interrelationship between the irradiance value, and the chip size. The irradiance value of the LED chip size is more related to the quality of the LED, and the production technique, is only partially related to the LED chip.

We then calculated the relative irradiance distribution of the LED chip to evaluate whether there is a difference of the treatment area in accordance to the LED chips size, as shown in **Figure 7-3.** It found that the LED irradiance distribution among LED sizes is similar. In the case of 3535 LED, the distance between the position of 42.04% irradiance, and 46.19% was around 3.75 mm. In the case of the 0805 LED chip, the distance between the position of 46.21 %, and 41.12% was also around 3.75%. There is not a significant difference in the irradiance distribution among LED chips. In summary, the LED chip sizes only can partially influence the LED chip irradiance and not influence the LED irradiance distribution.

7.5.1.2. LED wavelength

Besides the exposure area, LED wavelength stability is also an important aspect of LED. There are two aspects of the wavelength will be evaluated. One is the peak wavelength, and the half-width. Another is the wavelength shifting at different currents, including the peak wavelength, and the half-width. The wavelength shifting at different current provide an important guide to the LED workable voltage, and current. **Table 7-5** shows the wavelength variation of the different LEDs at the different currents to evaluate the wavelength shifting of the LEDs.

Peak wavelength: We performed an analysis, and comparison of the LED peak wavelength at a constant current of 20 mA. For LED 1, the peak wavelength was 844.83 nm,, and the half-width was 31.08 nm. For LED 2, the peak wavelength was 845.25 mm, and the half-width was 32.06 nm. For LED 3, the peak wavelength was 841.17 nm, and the half-width was 34.50 nm. For LED 4, the peak wavelength was a was 844.43 nm, and the half-width was 35.86 nm. For LED 5, the peak wavelength was 852.11 nm, and half-width 50 was 33.87 nm. For LED 6, the peak wavelength was 842.75, and its width was 34.71 nm. For LED 7, the peak wavelength was 853.77 nm, and its half-width was 35.06 nm. For LED 9, the peak wavelength was 851.58 nm, and the half-width was 28.95nm. In comparison to the peak wavelength, there is no great variation in the peak wavelength among LEDs. The commercial PBM device peak wavelength was 856.57 nm, and 848.45 nm. However, the half-width of the commercial product was 28.62 nm, and 12.79 nm.

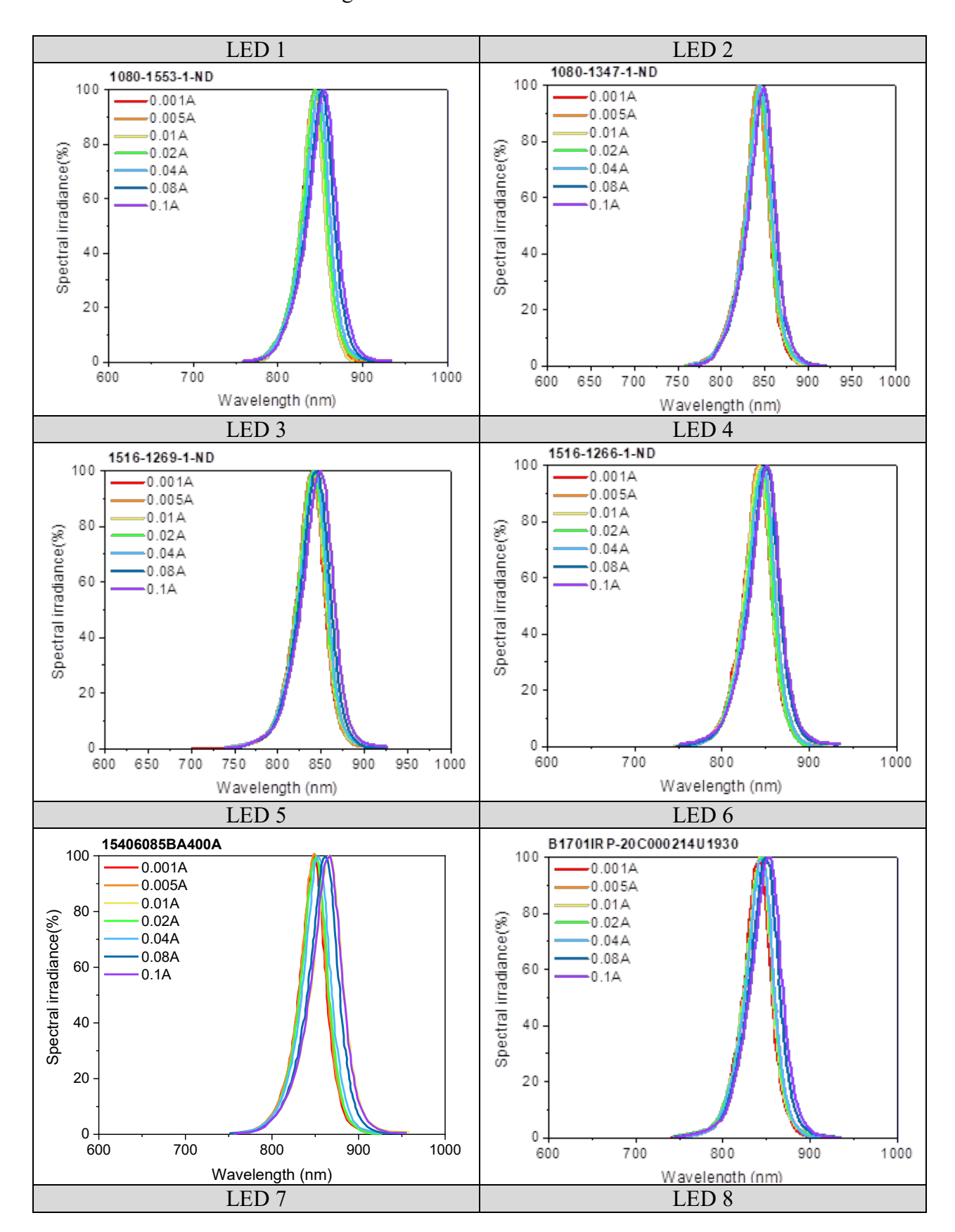
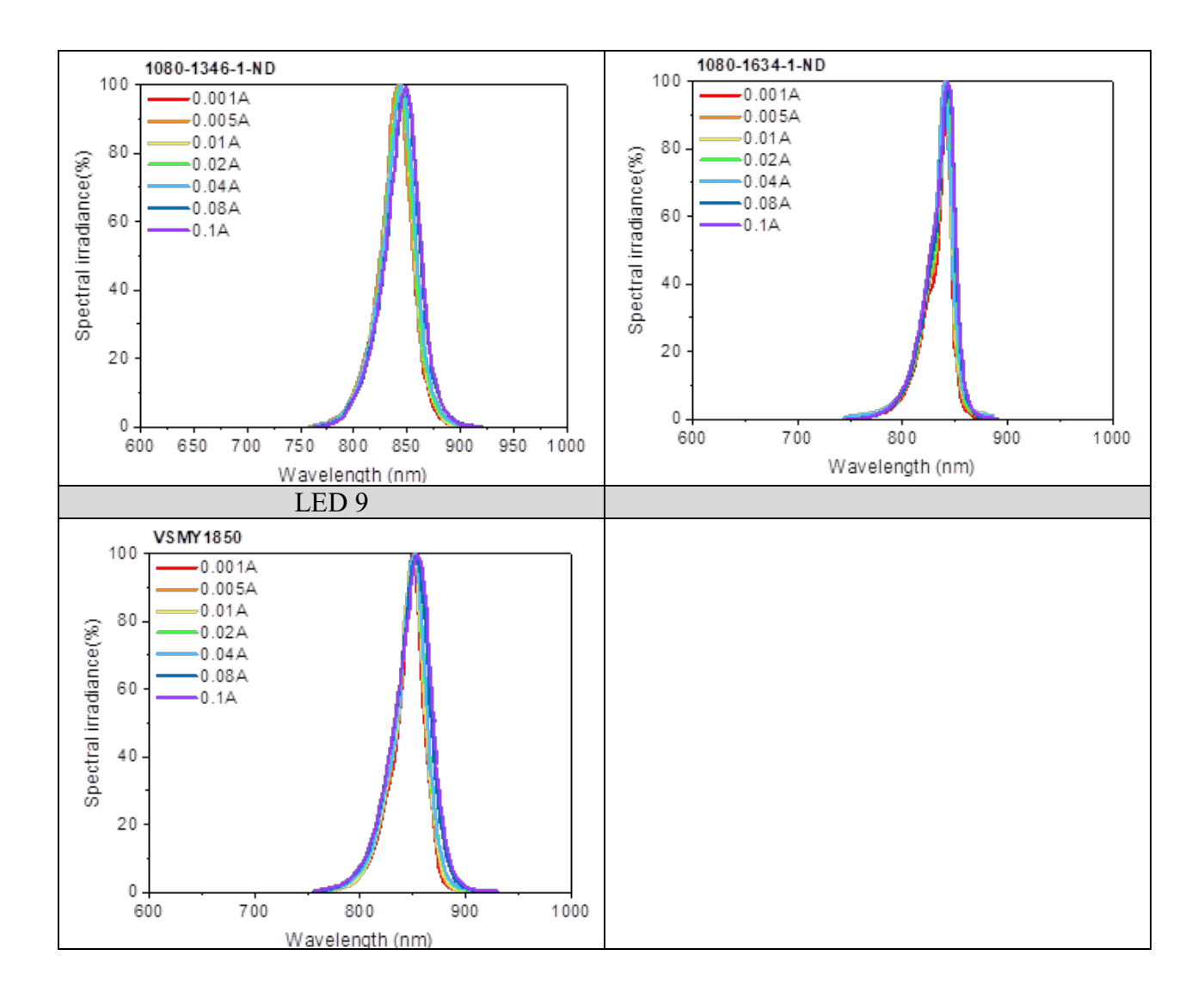


Table 7-5. Wavelength variation of the LEDs at different current



Wavelength shifting: We evaluated the wavelength shifting of the LEDs from 0.001A to 0.1A. In Table 7-5, it was evident that LED 1, LED 4, LED 5, and LED 6 have a clear shifting in the main peak wavelength. It indicates that their peak wavelength stability is not appropriate for operation within this current range. Further analysis was conducted on the performance of the other LEDs performance, in which the peak wavelength at 20 mA, and 80 mA were compared. For LED 2, the peak wavelength shifts from 845.25 nm to 854.07nm (1.04%); the peak wavelength of LED 3 shifts from 844.43 nm to 850.12 nm (0.67 %); the peak wavelength of LED 7 shifts from 843.44 nm to 848.03 nm (0.55%); the peak wavelength of LED 8 shifts from 841.22 nm to 842.76 nm (0.18 %); and the peak wavelength of LED 8

shifts from 851.58 nm to 854. 29 nm (0.32%) . The stability related to the peak wavelength of the LED was in the consequence: LED 8 > LED 9 > LED 3 > LED 2.

In terms of the half-width, the half-width of LED 8 increases from 17.41 nm to 22.28 nm(27.5 %); the half-width of LED 9 increases from 28.95 nm to 35.33 (21.30%); the half-width of LED 7 increases from 31.31 to 33.45 nm (6.83%), the half-width of LED 3 increases from 35.5 nm to 37.05 nm (4.36 %), the half-width of LED 4 increase from 32.06 nm to 37.03 nm (15.50%). The stability related to the half-width of the LEDs wavelength was in the consequence as follows: LED 3 > LED 7 > LED 4 > LED 9 > LED 8.

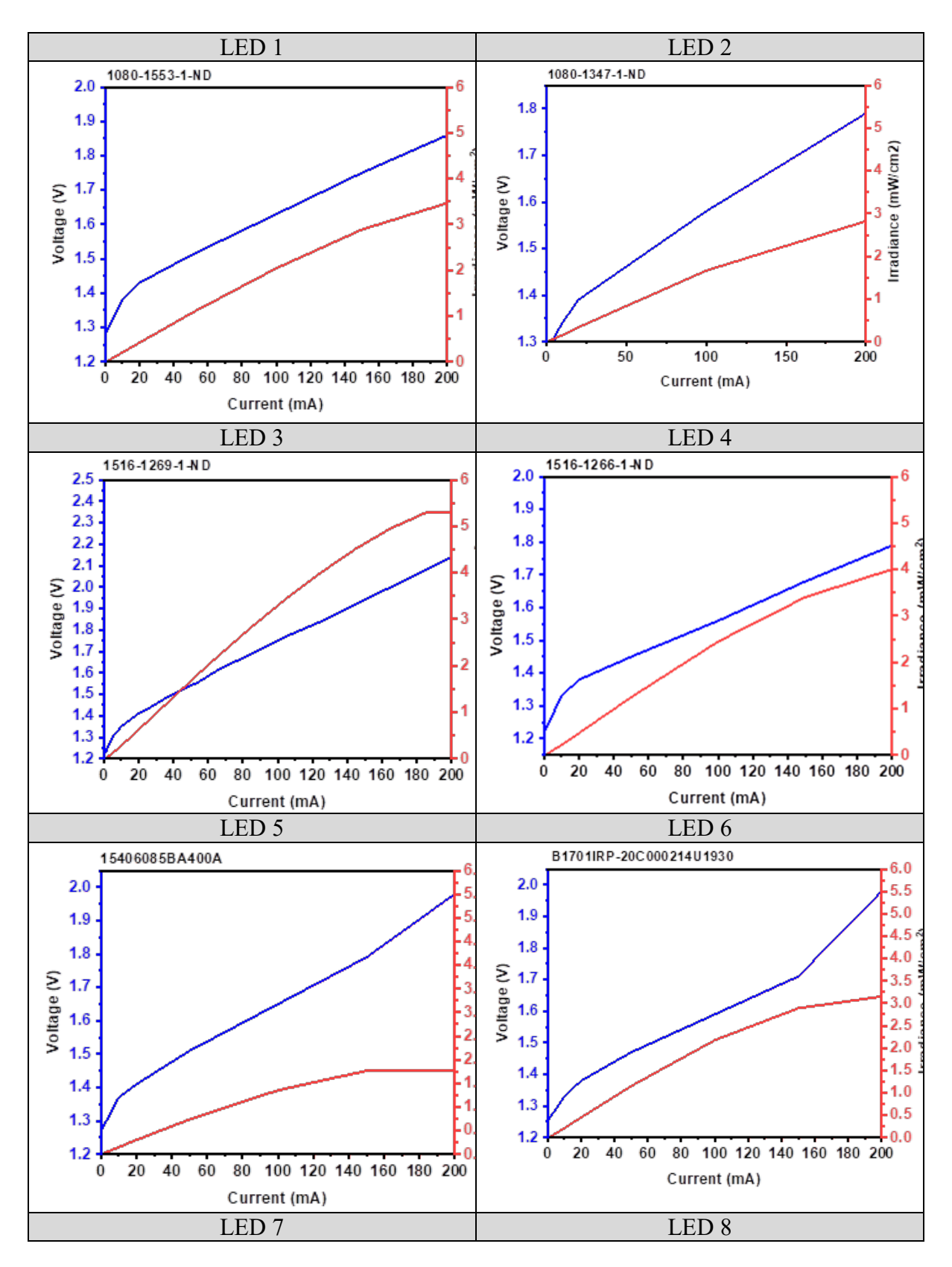
7.5.1.3. LED IV properties, and corresponding irradiance

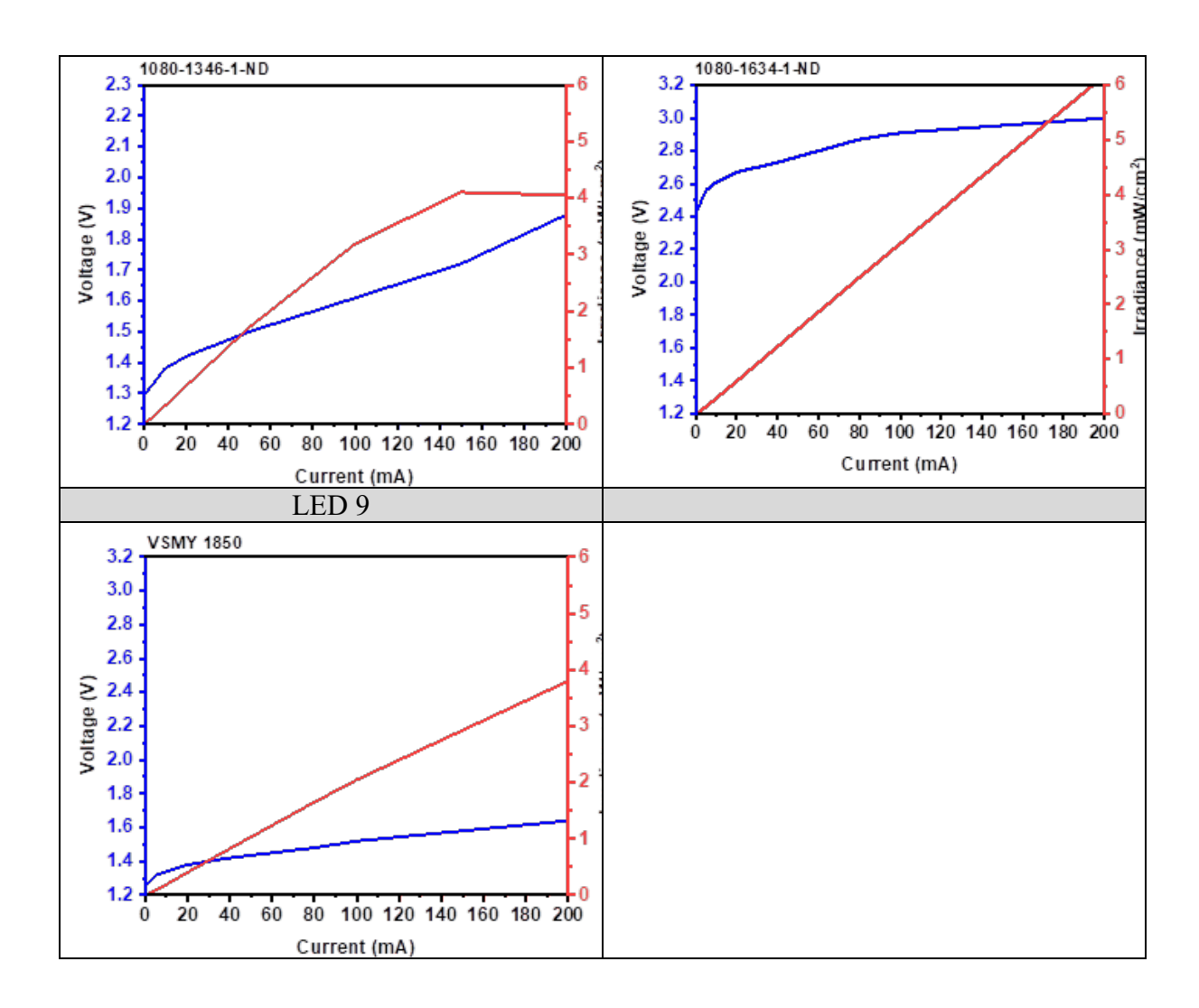
Another important consideration of the LEDs is the electrical properties and irradiance of the LEDs. We have measured the LEDs IV curve, and the corresponding irradiance, as shown in **Table 7-6**. In the details of the analysis, we focus on the irradiance, and voltage of the LED at the constant of 20 mA, and nearby. For LED 1, the irradiance at 20 mA was 0.19 mW/cm², and the voltage was 1.38V. For LED 2, the irradiance was 0.33 mW/cm², and the voltage was 1.39V. For LED 3, the irradiance was 0.62 mW/cm², and the voltage was 1.41V. For LED 4, the irradiance was 0.47 mW/cm², and the voltage was 1.51 V. For LED 5, the irradiance was 0.30 mW/cm², and the voltage was 1.41 V. For LED 6, The irradiance was 0.44 mW/cm², and the voltage was 1.38 V. For LED 7, the irradiance was 0.67 mW/cm², and the voltage was 1.42V. For LED 8, the irradiance was 0.59 mW/cm², and the voltage was 2.67 V. For LED 9, the irradiance was 0.40 mW/cm², and the voltage was 1.38 V. The irradiance of

the LEDs in consequence from large to small at 20 mA was: LED 7 > LED 3 > LED 8 > LED 4 > LED 6 > LED 9 > LED 2 > LED 5 > LED 1. The voltage requirement is in the consequence of: LED 8 > LED 4 > LED 7 > LED 5, LED 3 > LED 2 > LED 6, LED 9, LED 1.

At the current of 80 mA, the irradiance of LED 1 was 1.67 mW/cm², and the voltage was 1.58 V; the irradiance of LED 2 was 1.11 mW/cm², and the voltage was 1.59 V, the irradiance of LED 3 was 2.66 mW/cm², and the voltage was 1.66 V; the irradiance of LED 4 was 1.95 mW/cm², and the voltage was 1.52 V; the irradiance of LED 5 was 1.09 mW/cm², and the voltage was 1.59 V; the irradiance of LED 6 was 1.76 mW/cm², and the voltage was 1.54 V; the irradiance of LED 7 was 2.57 mW/cm², and the voltage was 1.56 V; the irradiance of LED 8 was 2.49 mW/cm², and the voltage was 2.87 V; the irradiance of LED 9 was 1.63 mW/cm², and the voltage was 1.47 V. The irradiance of the LEDs in consequence from large to small at 40 mA was: LED 3 > LED 7 > LED 8 > LED 4 > LED 6 > LED 1 > LED 9 > LED 2 > LED 5. The voltage requirement is the consequence of: LED 8 > LED 3 > LED 5, LED 2 > LED 1 > LED 7 > LED 6 > LED 4 > LED 9.

Table 7-6. LED IV curve, and corresponding irradiance.





Based on the above measurement and analysis, it was evident that LED 7 exhibits good irradiance with a relative lower power consumption within the current of 20 mA to 80 mA. Additionally, the peak wavelength shifting of LED 7 is also limited at these different currents. Therefore, it has been determined that LED 7 will be used for the further development of the flexible PBM panel.

7.5.2. LED viewing angle measurement

For the panel design, the LED angle needs to be measured as the basic information for the simulation. The individual LED irradiance distribution was measured, as shown in **Figure**

7-4. Then, the LED angle was calculated, as demonstrated in Figure 7-5.

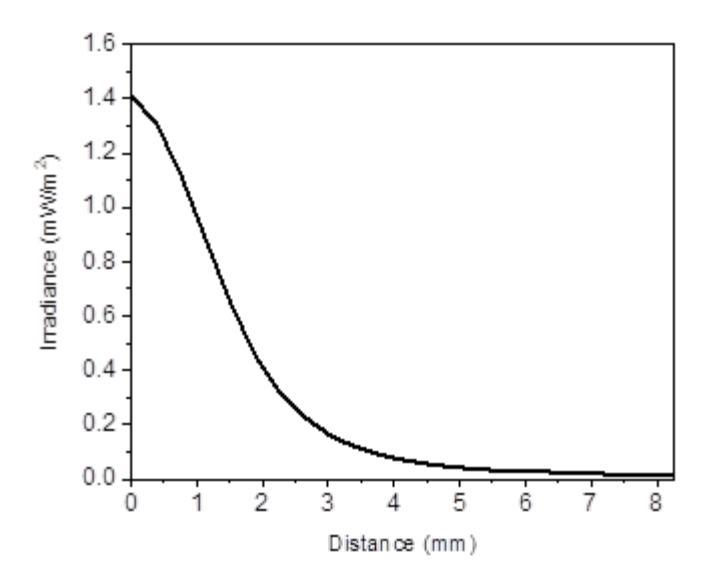


Figure 7-4. Irradiance distribution of the LEDs.

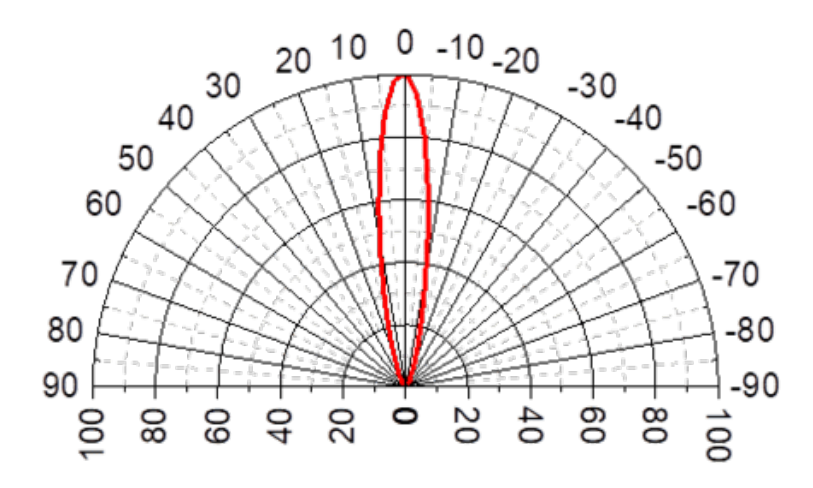


Figure 7-5. Viewing angle of the LEDs in relative intensity

From the above measurements, it was obvious that the LED irradiance decreases significantly as you move away from the center of the LEDs. At a distance of 3 mm from the center, the irradiance decreases to the level below 0.2 mW/cm². The central irradiance was around 1.7 mW/cm². The difference in the irradiance between these two positions was more

than 7 times. Additionally, the viewing angle of the LED at a distance of 1 cm is only around 18 degrees. This information suggests that the distribution of light from the LED is not uniform, with the center emitting significantly more light than the edges. The narrow viewing angle at a distance of 1 cm also indicates that the light emitted from the LED is highly directional, which may be desirable in some applications but could also limit its effectiveness in others. Based on this, a flexible PBM device requires the secondary optical design. In the following section, we consider designing an LED array as a basis for further studies.

7.5.3. LED array design

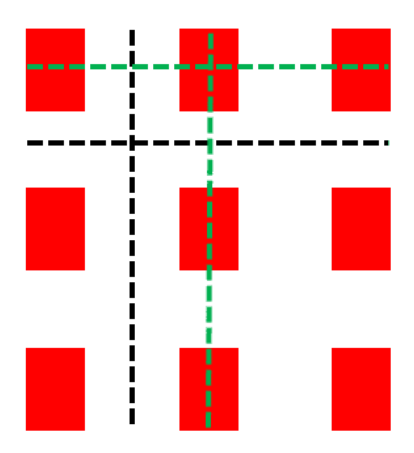


Figure 7-6. A schematic diagram of the simulated array.

We conducted an LED array light simulation based on the calculated LED viewing angle. This study aims to optimize the uniformity of irradiance distribution while minimizing the number of LEDs to reduce the energy requirement of the flexible PBM panel. There are two parameters were adopted: one is the interdistance between LEDs, and another is the arrangement of the LEDs. For the interdistance between LEDs, we have adopted different

distribution of the LEDs. In detail, a 3 *3 LED array was simulated, in which four positions of the irradiance distribution were analysed, as shown in **Figure 7-6.** The black line represents the middle horizontal, and middle vertical directions, and the green line indicates the central horizontal, and central vertical directions. It was assumed that the central positions represent the largest irradiance of the LEDs, while the middle positions represent the lowest irradiance of the array. This provides a comprehensive insight into the irradiance distribution of the LED array.

Figure 7-7 presents the simulated irradiance distribution of the LEDs at the center in both the vertical and the horizontal directions. There is no significant difference in the irradiance distribution in different directions. However, it is evident that the middle position of LED array at the distance of 15 mm starts to be overlapped, while the difference between the centre irradiance, and the middle position is still large. For instance, at the interdistance of 15 mm, the central irradiance is 0.148 mW/cm², while the middle irradiance is 0.003 mW/cm². The difference between the two positions was 49 times. When the interdistance between LEDs is only 5 mm, the central irradiance is 0.213 mW/cm², while the middle irradiance is 0.09 mW/cm². The difference between the two positions is 2.36 times. The uniformity of the irradiance can be improved by shortening the interdistance between LEDs, while there is an upper limit on the improvement. Furthermore, it found out that the LED light is overlapped, and the central irradiance also will be increased. Another drawback is that shortening the interdistance between LEDs will increase the number of LEDs across the panel, and thus

increase the energy requirement of the device. This can pose electrical, and thermal hazards to the user. Therefore, it is suggested to use other methods to improve the irradiance distribution of the flexible PBM panel, rather than solely relying on shortening the LEDs interdistance.

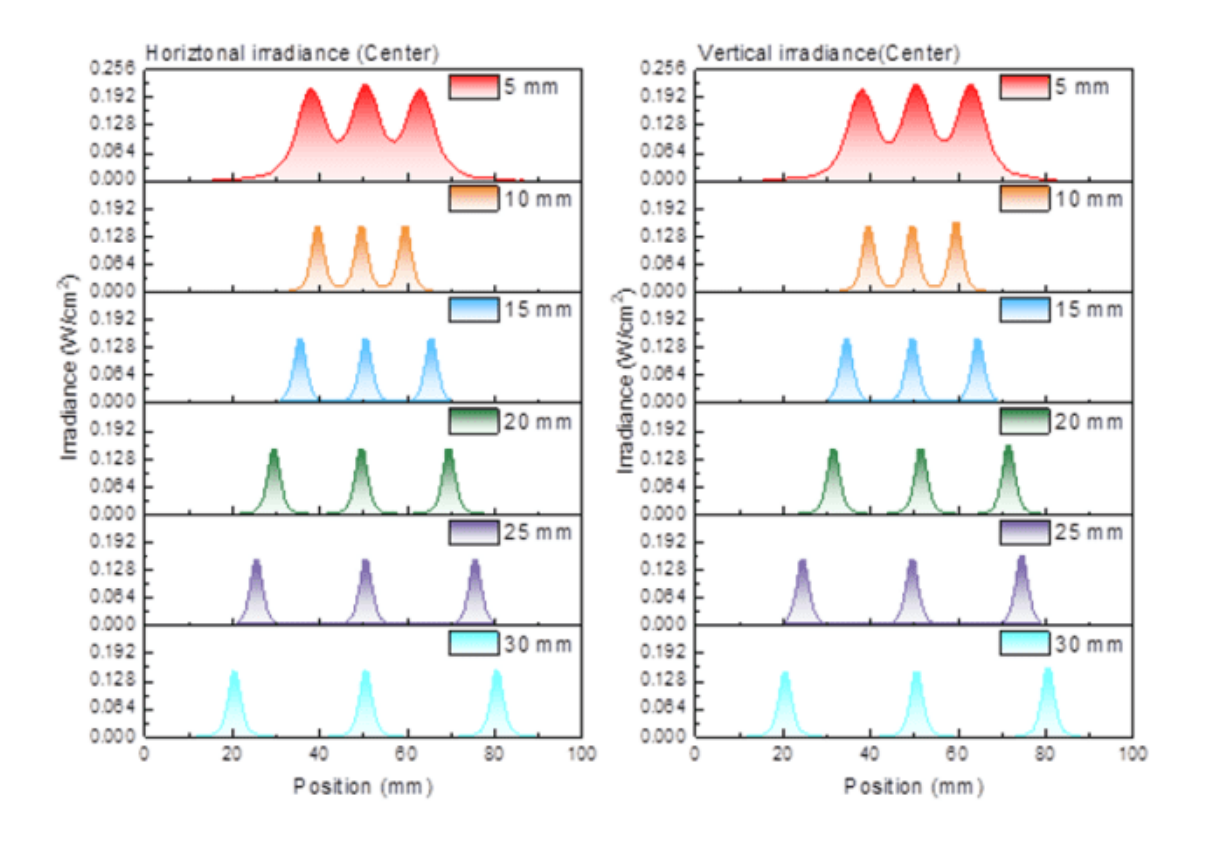


Figure 7-7. Simulated central irradiance distribution of LEDs with different distance

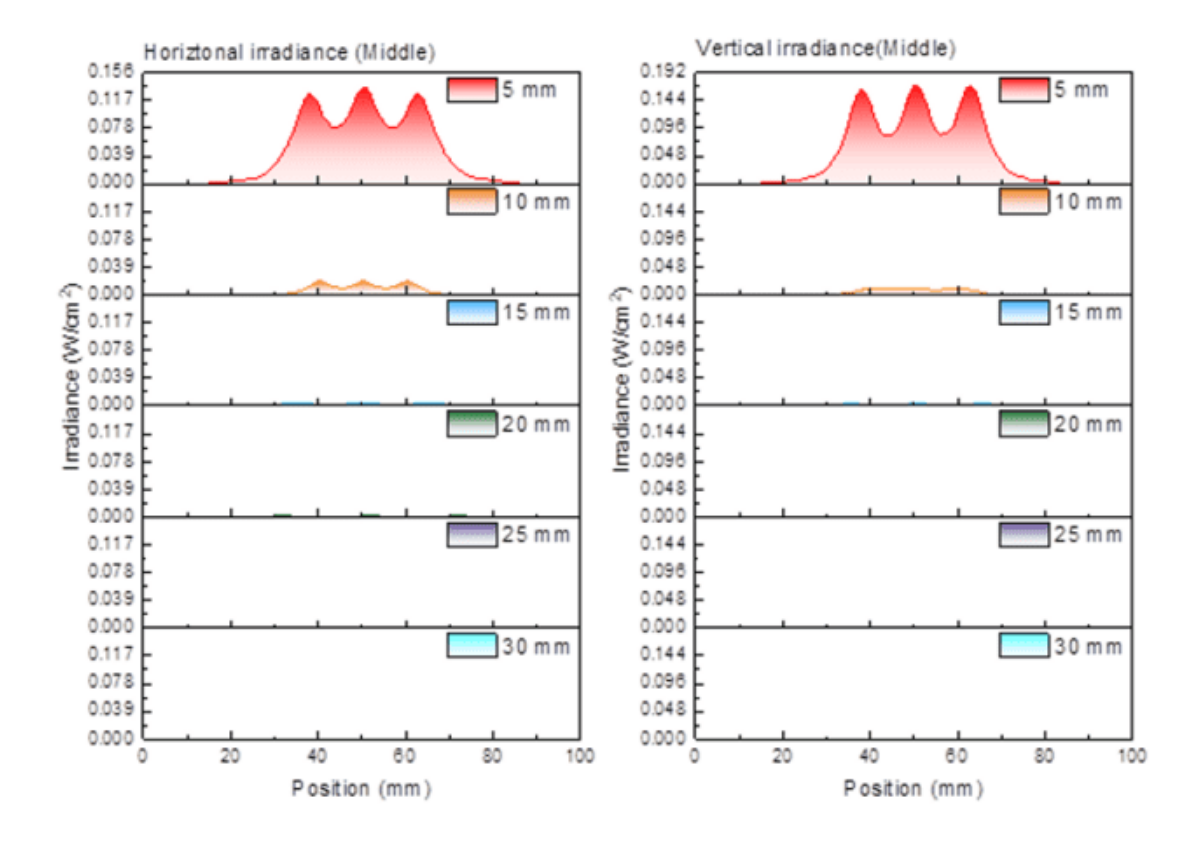


Figure 7-8. Simulated irradiance distribution of LEDs with different distances (Middle position).

Figure 7-8 shows the irradiance distribution of the LED array at the middle position in both the horizontal and the vertical direction. Compared to the central position, it was obvious that the irradiance value at the middle position is very low. The non-uniformity of the irradiance issues is very serious. The relative irradiance distribution is similar to the position at the centre. When the LED interdistance is 15 mm, the average irradiance is 0.002 mW/cm² with a standard deviation of 0.007. This proved that at 15 mm interdistance, the LED irradiance started to overlap. Otherwise, there is no any irradiance in the condition when the LED interdistance is 25 mm, and 30 mm. The critical interdistance for the LED array was 15 mm.

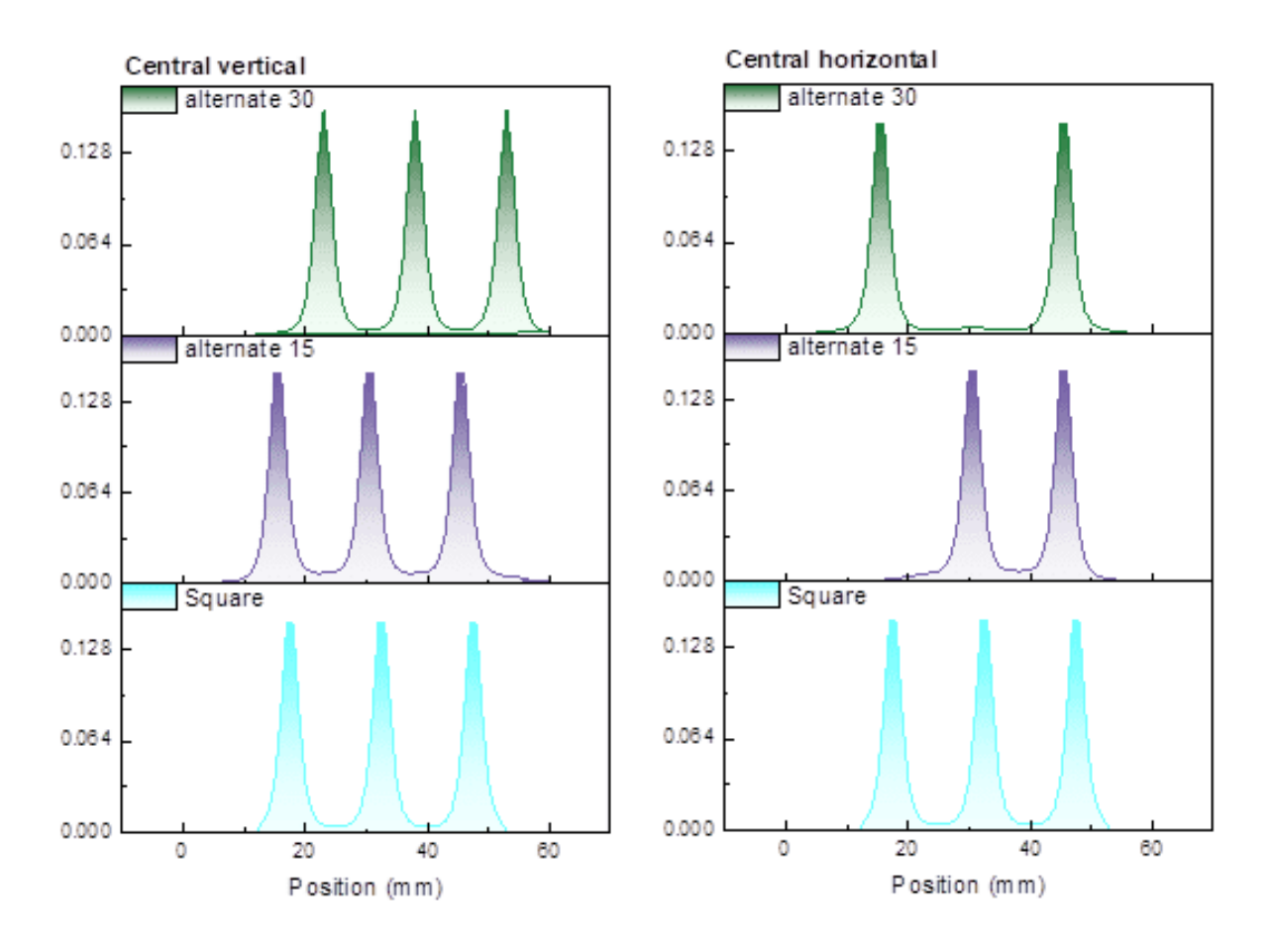


Figure 7-9. Simulated irradiance distribution of the LEDs with different arrangement.

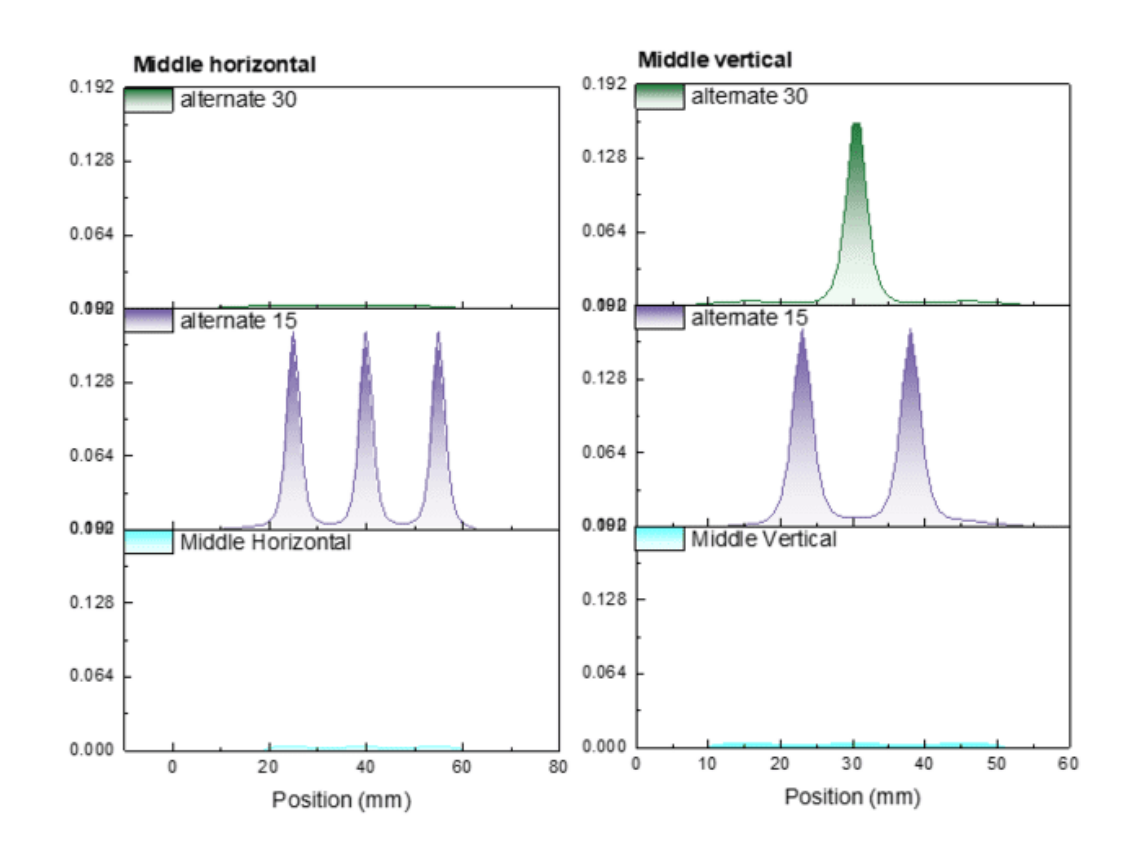
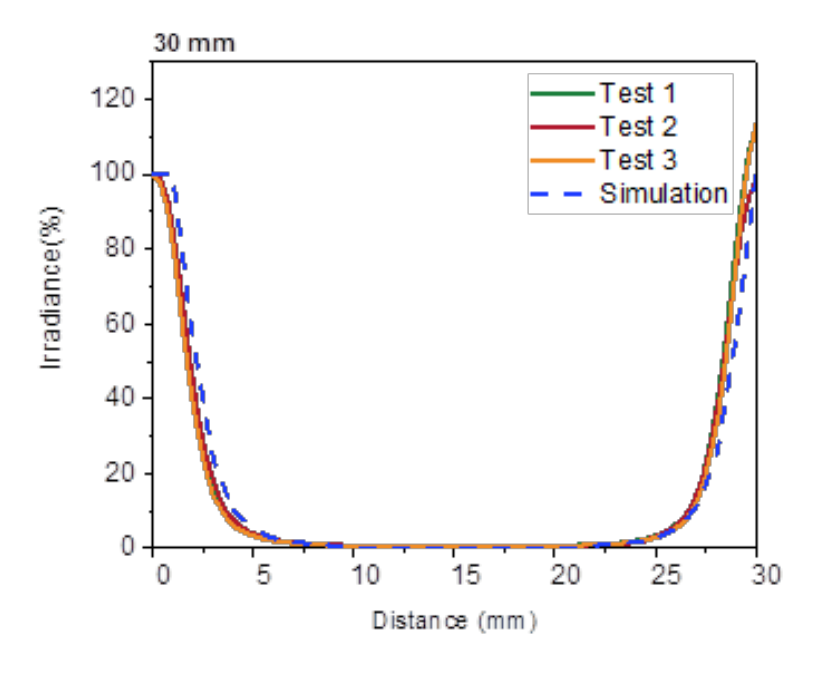


Figure 7-10. Simulated irradiance distribution of the LEDs with different arrangement.

Besides the interdistance, LED arrangement is also critical to the irradiance distribution of the array. We arrange the LED in square or staggered. 15 cm as the distance between LEDs was selected for this study. There are two staggered designs: one is that the distance between two rows is 15 mm as alternate 30, and another is 7.5 mm as alternate 15. The simulated irradiance distribution is depicted in **Figure 7-9**, and **Figure 7-10** at different positions of the LED array. The analysis revealed that changing the array to a staggered layout altered the irradiance at various positions, but did not improve the overall irradiance distribution. For example, both the square and staggered (alternate 30) arrangement have six peaks. Any improvement in the irradiance distribution was found to be contingent on reducing the distance between LED rows. There are a total of ten peaks in the alternate 15 patterns. There are four more peaks compared to square, and alternate 30 because the distance between LED rows was reduced to half.



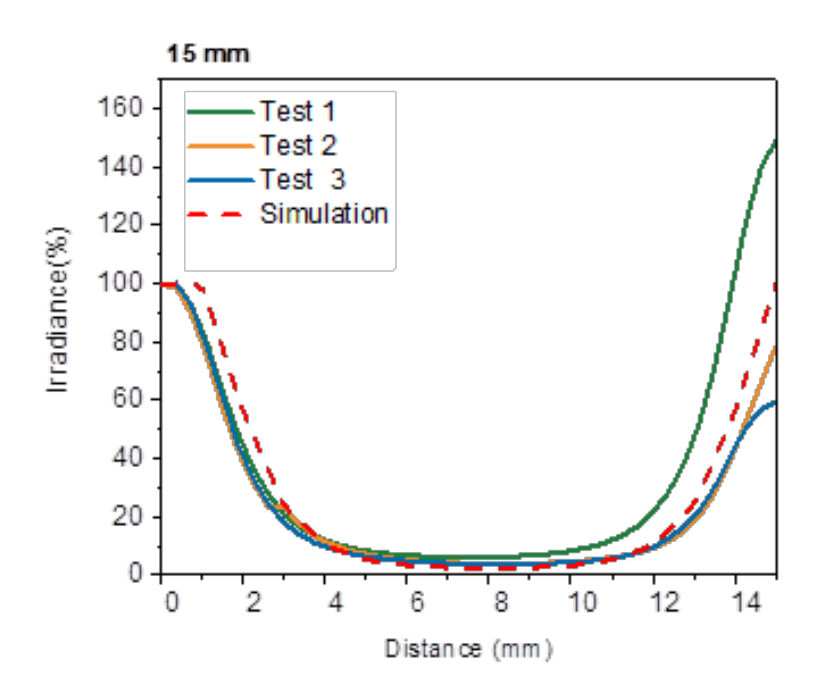


Figure 7-11. Irradiance distribution of the LED array with 30 mm interdistan5ce

Figure 7-12. Irradiance distribution of the LED array with 15 mm interdistance.

After the simulation, we conducted experiments to verify the simulated irradiance distribution. Two printed circuit boards of LED arrays with different interdistance (30 mm, and 15 mm) were fabricated, and the corresponding irradiance was measured, as shown in **Figure 7-11**, and **Figure 7-12**. We compared the simulated relative irradiance with the measurement. In these Figures, the dotted line represents the relative irradiance in the simulations, while the other lines represent the measurement. It found out that the irradiance distribution from the experiment is similar to the simulation. For a 30 mm array, there is no irradiance at the middle position between two LEDs (3 mm to 12 mm). When shortening the distance to 15 m, the irradiance in the middle was only around remained around 3.17%.

The study has led to several conclusions. Firstly, it was found that shortening the

interdistance between LEDs can indeed improve irradiance uniformity, but there are limitations to this improvement. Secondly, it was observed that alternating the LED arrangement with a shorter distance can enhance the irradiance distribution. However, considering the energy requirements of the flexible PBM panel, it is recommended to use a 15 mm interdistance between LEDs, and a staggered arrangement, with the distance between LED rows also set at 7.5 mm. This configuration strikes a balance between improving irradiance distribution, and managing energy consumption, making it a practical, and efficient choice for the flexible PBM panel.

7.5.4. Wearable panel shape design

After the LED selection, and LED array design, the shape of the panel needs to be under consideration. There are two problems that need to be considered for the panel shape design. One is the conformability of the panel to the human contour, and another is the sizing problems. For the conformability question, we have first developed the corresponding fabric pattern based on the size measurement. The fabric pattern-making procedure was referred to the book[1]. The shape of the pattern is shown in **Figure 7-13**. It found that normal underwear is composed of three pieces of fabric pattern in different pattern. The size of the lower two pieces was only around 6 to 7 cm. We decided to combine them together to reduce the complexity of the circuit connection and power control. The final pattern shape was demonstrated in **Figure 7.14**, which is the size 1. In addition, we also mark the position of LEDs, in which the circle in this Figure indicates the position of the LED.

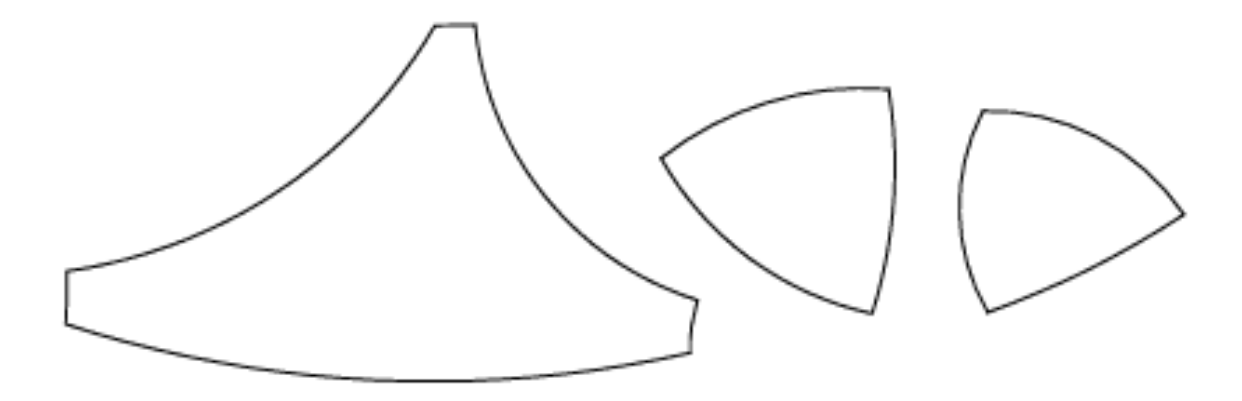


Figure 7-13. Fabric pattern of the underwear.

For the sizing issues, it is valuable to understand the fabric pattern dimensions difference among different sizes of underwear. In the grading of underwear, the dimension difference between each size of the underwear is only around 5 mm to 8.5 mm [2]. Based on the previous measurements, we used 15 mm as the interdistance between the LEDs in the design of the LEDs array. Based on this, there is no enough area to increase the number of LEDs for each additional underwear size. For instance, the edge difference between the 70B, and 70C is only around 5 mm at one edge. It is suggested to develop a size of photobiomodulation panel for two sizes of underwear. The sizes of the flexible PBM panel available for different sizes of underwear are shown in Table 7-7.

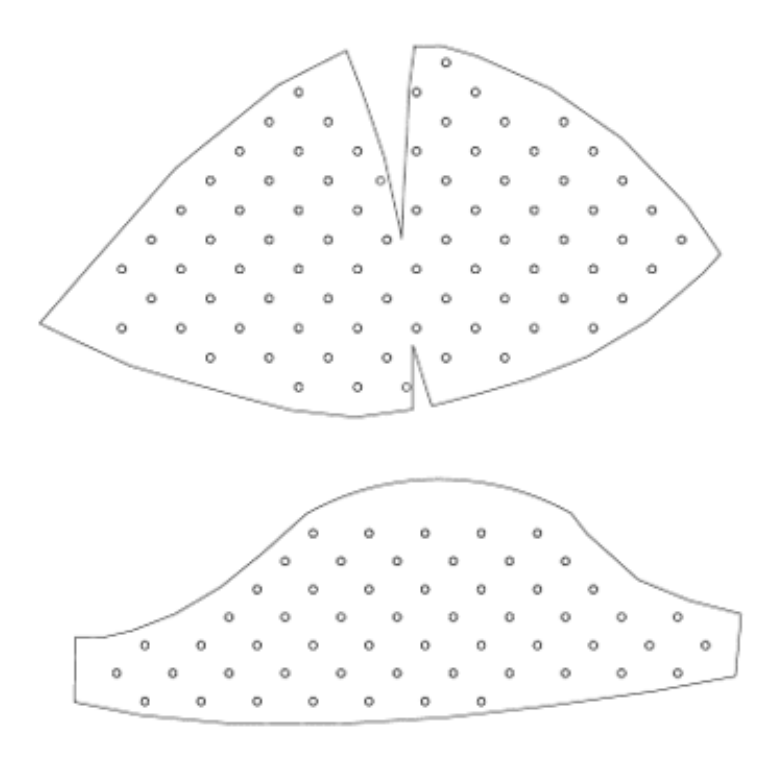


Figure 7-14. Shape of the flexible PBM panel, and corresponding LED positions.

Table 7-7. Size of the flexible PBM panel

Size					Size of panel
70B	75A				Size 1
70C	75B	80A			
70D	75C	80B	85A		Size 2
	75D	80C	85B	90A	
		80D	85C	90B	Size 3
			85D	90C	
			85E	90D	Size 4

Further exploration of the sizing issues in relation to the fabric pattern dimensions could involve conducting detailed studies on the anthropometric measurements of individuals to

understand the variations in body sizes and shapes. This could help in determining the optimal placement, and distribution of LEDs on the photobiomodulation panel to ensure effective coverage across different sizes of underwear.

7.5.5. LED array circuit design

After the shape design of the panel, the electric circuit design of the panel needs to be in combination. Considering the commercial wearable photobiomodulation panel, the voltage of the panel was designed at 12 V. We designed to parallel connect eight LEDs together, and then series the group together to control each pattern overall voltage under 12 V. **Figure 7-15** demonstrates the circuit of the pattern 1, and **Figure 7-16** pattern 2 in size 1. Pattern 1 has 56 LEDs, and Pattern 2 has 64 LEDs.

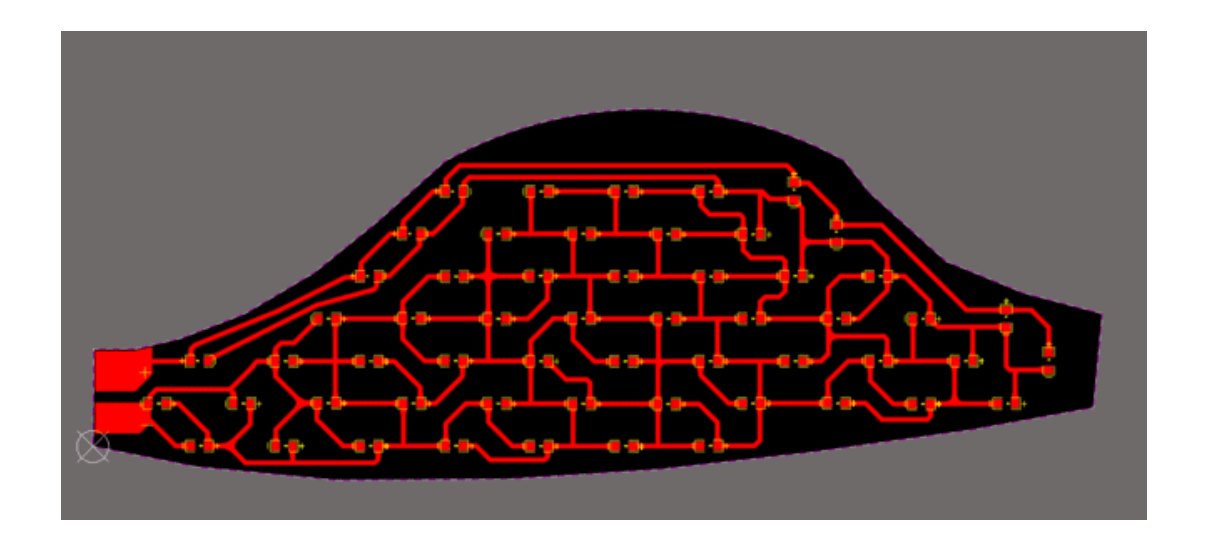


Figure 7-15. Circuit design of the PBM panel pattern 1.

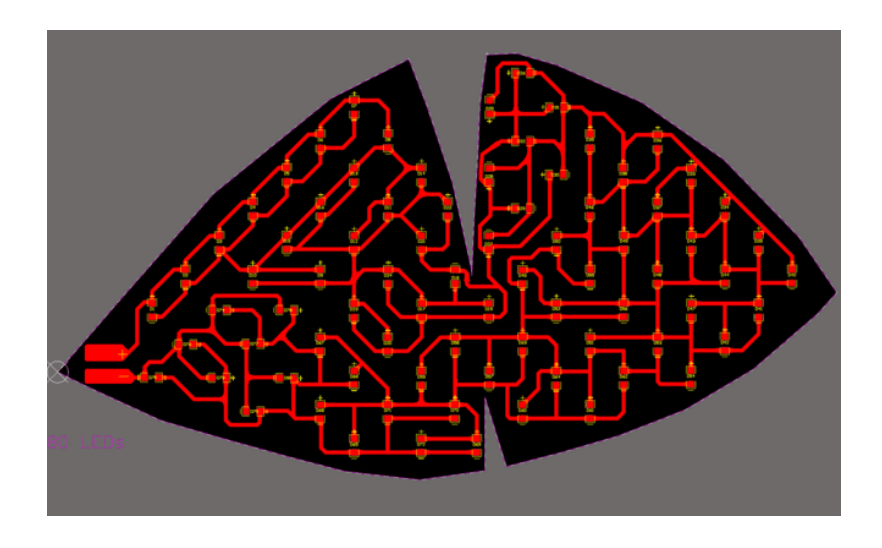


Figure 7-16. Circuit design of the PBM panel pattern 2.

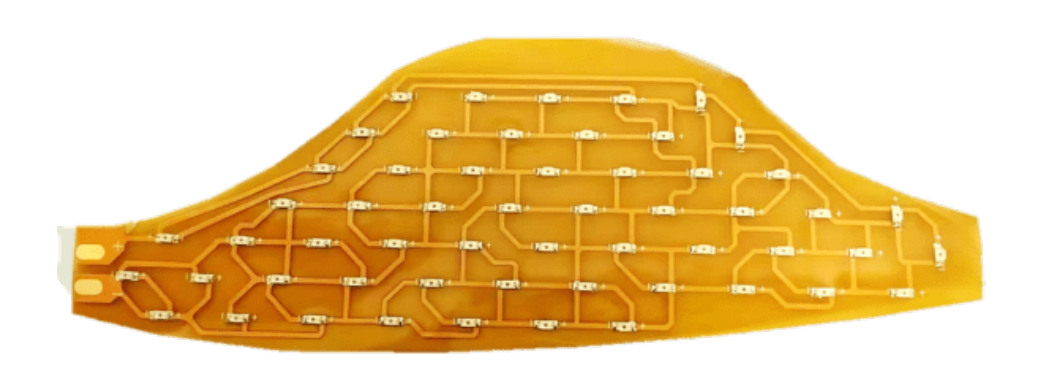


Figure 7-17. Photo of the PBM panel pattern 1.

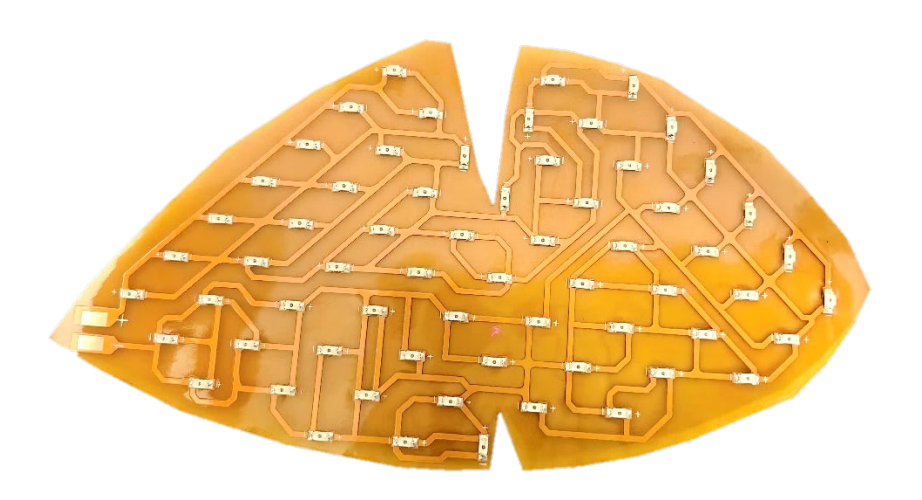


Figure 7-18. Photo of the PBM panel pattern 2.

The thickness of the copper circuit of the polyimide circuit was 35 μm to ensure the

flow of current. **Figure 7-17** shows the image of the real circuit of pattern 1, and **Figure 7-18** shows the photo of the real circuit of pattern 2. After the fabrication, we conducted a series of measurements for the flexible PBM panel to understand its performance for further studies, including the optical design, underwear design, and the corresponding integration methods.

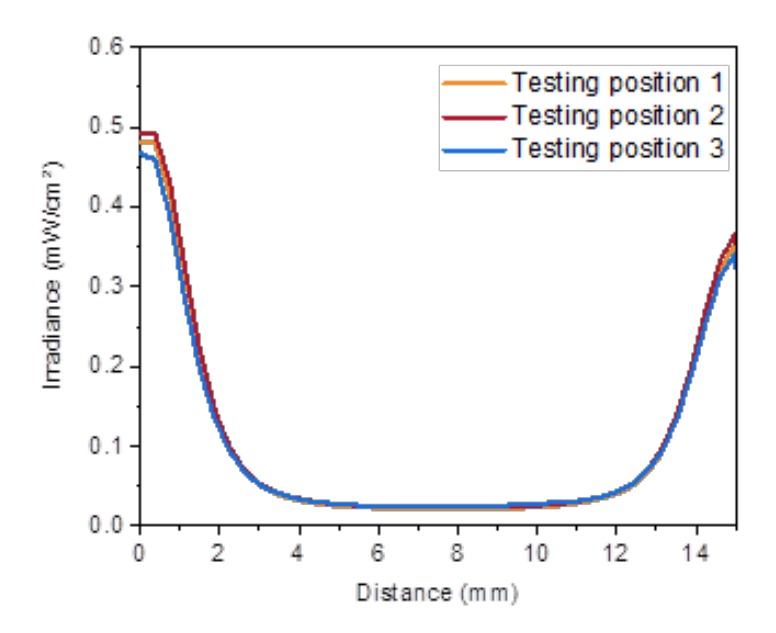


Figure 7-19. Irradiance distribution of the flexible PBM panel in horizontal direction.

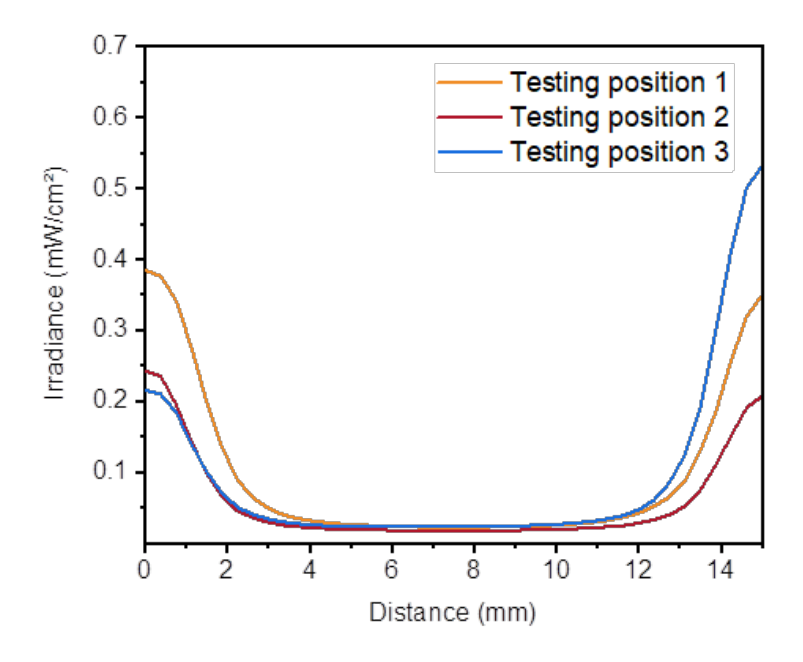


Figure 7-20. Irradiance distribution of the flexible PBM panel in vertical direction.

We measured the irradiance distribution across the panels in different directions. Figure 7-19 shows the irradiance distribution of the flexible PBM panel in the horizontal direction, and Figure 7-20 shows the irradiance distribution of the flexible PBM panel in the vertical direction. The testing position is at the center of the LED. In Figure 7-19, it can find out that the highest irradiance of the array was around 0.5 mW/cm², while the lowest irradiance was around 0.02 mW/cm². The difference between the two is around 25 times. The irradiance difference in Figure 7-20 is similar to that in Figure 7-19. However, there is a noticeable variation in the center irradiance of the LEDs. The variation of the peak irradiance can be in the range of 0.2 mW/cm² to 0.6 mW/cm². These findings highlight the need for further exploration, and potential adjustments to ensure more uniform irradiance distribution across the flexible PBM panel.

We measured the irradiance of the flexible PBM panel for around 20 mins to evaluate the performance stability of the flexible PBM panel, as illustrated in **Figure 7-21.** The average irradiance of the flexible PBM panel was around 2.075 mW/cm². The standard deviation of the irradiance was only around 0.0016. These results indicate that the flexible PBM panel can consistently provide stable treatment, demonstrating its reliability, and suitability for practical applications.

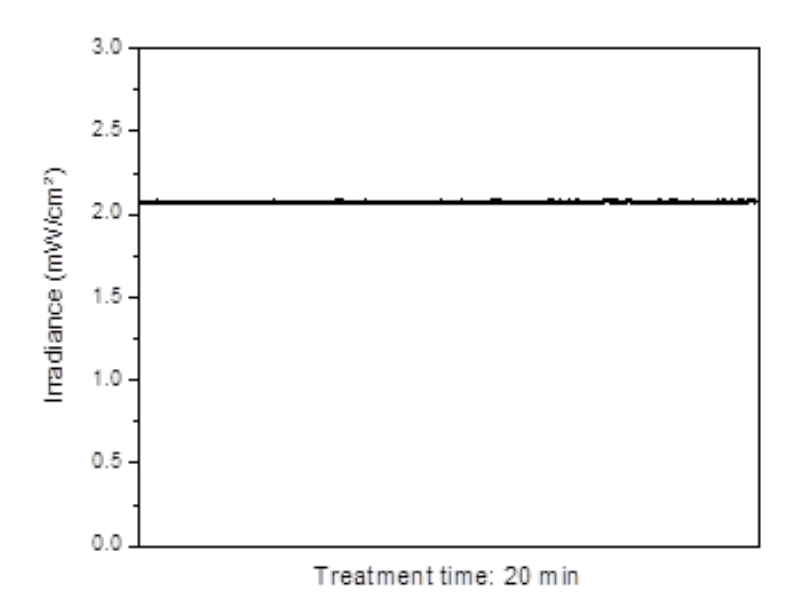


Figure 7-21. Irradiance variation of the flexible PBM panel throughout treatment.

We then evaluated whether the shape of the flexible PBM panel could conform well to the breast shape of the cancer patient in two dimensions. The two panels were connected together, and were observed to conform well to the model, as shown in **Figure 7-22**. The panels were able to fit the breast shape of the model without any folds. However, it was noted that the conformability of the flexible panel could be further improved by cutting out the extra polyimide film. This aspect will be studied in future work in combination with the integration

methods, with the aim of enhancing the overall conformability of the flexible PBM panel to better suit the specific needs of the patient.



Figure 7-22. Conformabiltiy of the flexible PBM panel

We measured the temperature of the flexible panel on the model with an infrared red camera. The results of the temperature variation at different times are shown in Table **7-8.** At initial, the panel temperature was similar to the room temperature, around 23.4 °C. After 5 mins, the temperature of the panel increases sharply. The increases in the temperature across the panel are uneven. From these figures, it was obvious that the circuit temperature was higher than that of the non-circuit area. Moreover, the temperature of the panel was stable from 5 mins to 20 mins. There is no significant difference in the temperature of the panel, and the panel position. However, the highest temperature of the panel was around 42°C. This temperature is a little bit higher than the human skin-safe temperature. Considering to this, the heat-sinking

layer or other textile material needs to be considered in the integration process of the device.

5 min 0 min 22.6 27.3 41.5 23.5 23.4 23.4 23.4 23.4 32.0 30.3 23.3 ₿ 20.0 ₿ 20.0 FLUKE . FLUKE « 22.6 2024-08-21 16:21:37 2024-08-21 16:28:51 10 min 20 min 自动 22.4 26.5 42.0 42.0 33.3 23.5 24.0 30.7 30.4 28.4 32.3 28.6 28.1 30.9 34.8 € 0.95 € 0.95 ₿ 20.0 ₿ 20.0 FLUKE . FLUKE . 2024-08-21 16:33:42

Table 7-8. Temperature measurement of the flexible PBM panel.

In summary, we have completed an initial performance evaluation of the flexible PBM panel. Through the use of an appropriate LED light source and array design, this panel demonstrates the ability to conform effectively to the shape of the breast, showcasing its potential for practical application in photobiomodulation therapy. However, there are still many

problems

7.5.6. Optical study for the flexible PBM

Based on the findings from the above studies, a significant issue identified is the uneven irradiance distribution across the panel. This non-uniform distribution may lead to challenges in determining the dose rate, potentially resulting in doses that are lower than the treatment threshold at certain positions. Conversely, it may also lead to doses that are higher at certain positions, posing a risk of harm. Addressing this non-uniformity is crucial to ensure consistent, and safe treatment delivery.

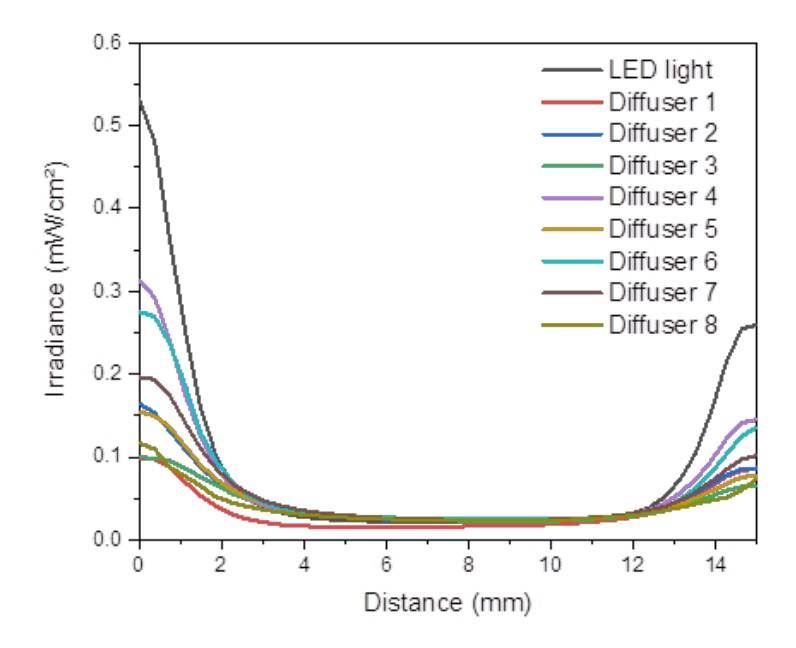


Figure 7-23. LED irradiance distribution with different light diffuser.

To improve the optical performance of the flexible PBM panel, we investigated the effects of applying different light diffusers onto the panel. The testing distance between the

panel and detector was 1 cm. We measured the irradiance distribution difference at the same position with different light diffusers, as shown in Figure 7-23. It was obvious that the central irradiance of the LED decreased sharply. The irradiance distribution of the LED array becomes more even as the central irradiance decreased. On the other hand, part of the light is wasted. Using a light diffuser to decrease the irradiance unevenness is more suitable for vision-based devices, like displays or luminous devices. For wearable devices, it is proposed to maximize light efficiency by reducing the number of LEDs to reduce the energy requirement of the devices in order to eliminate electrical, and temperature hazards. Based on this, it is better to design an appropriate flexible lens for the flexible PBM panel. Due to the time limitation, a comprehensive study of the optical design will be conducted in further work.

7.5.7. Integration of the flexible PBM



Figure 7-24. Integration of the flexible PBM panel into the underwear.

For the integration of flexible PBM, a mastectomy bra was acquired. It is characterized by its softness, lacking any rigid components such as underwire to minimize irritation. Additionally, it featured a pocket inside the underwear designed for breast prostheses or breast forms, which could facilitate the integration of the flexible PBM panel. In the study, the flexible PBM panel was attached to the inside of the mastectomy bra, as demonstrated in **Figure 7-24**. However, a challenge arose due to a mismatch between the bra, and the flexible PBM, as the cup of the bra was fabricated with molded fabric instead of a fabric pattern. As a result, it is recommended to develop a specific mastectomy bra tailored for the integration of the flexible PBM panel. This would ensure a more seamless, and effective integration of the PBM technology into the bra, enhancing comfort, and usability for individuals undergoing post-mastectomy care.

7.6. Conclusion

In this chapter, we conducted a comprehensive study on the design, and fabrication of the flexible photobiomodulation panel. This encompassed various key aspects, including LED selection, evaluation of LEDs from different perspectives such as peak wavelength, wavelength shifting, irradiance distribution, and overall irradiance. Additionally, LED array design, panel shape design, fabrication, and initial panel evaluation were thoroughly explored. Specifically, a flexible panel was designed, and fabricated using a simulated fabric pattern making technique to ensure the conformability of the panel to the shape of the breast. This approach provides a viable pathway for transforming energy treatment devices into a wearable format, offering

potential benefits for practical, and comfortable use. However, there are still some challenges that need to be addressed for practical applications, including the irradiance distribution, and temperature issues. Besides the LED panel performance limitation, the current study mainly focuses on the panel design, rather than the system design. The corresponding control system and the power system will be studied, and fabricated in future work to realize the functionality of remote photobiomodulation.

7.7. References

- [1] Shin, K. (2015). Patternmaking for underwear design (2nd edition.)
- [2] Matthews-Fairbanks, J. L. (2019). Bare essentials: bras: construction, and pattern drafting for lingerie design (Third edition.). Fairbanks Publishing LLC dba Porcelynne.

Chapter 8. Conclusions and Future work

8.1. Conclusions

This thesis presents a systematic study about a novel mechanoreceptor and flexible PBM panel. The major conclusion is summarized as follows:

- 1. A novel fabric-based mechanoreceptor with controllable pressure threshold was designed and fabricated by incorporating PDMS pillars into the insulation layer. The pressure threshold can be controlled through various parameters, including PDMS material filling rate, height of PDMS structure, PDMS material modulus, compression area, and size of the mechanoreceptors. This design allows pressure thresholds ranging from several kPa to MPa, making it adaptable to a wide range of wearable applications. Given the multiplicity of controllable dimensions, the processing requirement associated with any specific dimension can be reduced by exploiting the synergistic effects of multiple dimensions. The response time of the mechanoreceptor was only 40 ms, and it can function under 1 kHz compression frequency. Additionally, this novel structure endows the mechanoreceptors with a high on-off ratio (>10⁻⁸), and maintains good reliability under repeated compressions (>40000 compressions), and laundry cycles (20 laundry cycles).
- 2. To achieve advanced functionality, a novel mechanoreceptor spiral array containing a total of 16 mechanoreceptors, and flexible resistors for sensation positioning. The uniqueness of this array is that it only has two output electrodes, simplifying the connection between the array, and other modules, and enhancing the data processing efficiency. The identification of the mechanoreceptors can be realized through the

resistance difference between keys. The resistance of mechanoreceptors is in the range of $0.01~\text{k}\Omega$ to $48.4~\text{k}\Omega$, and the resistance difference between mechanoreceptors is around $3.226~\text{k}\Omega$. All components of this array are based on fabric or flexible substrates, with no rigid components, ensuring good flexibility, and comfort for seamless integration of e-textiles. The mechanoreceptor's on-off resistance value can be maintained stable at the high temperature (50°C for 72 hours), the low temperature (40°C for 72 hours), water immersion test (1 m), a lifespan of 10000 mins, and under maximum mechanical load (100~N).

- 3. The mechanoreceptor and the array also can be integrated into socks, and other clothing for 3D plantar pressure sensation, fall detection, and pressure sensation for various wearable applications.
- 4. A comprehensive evaluation system was established to evaluate the photobiomodulation device on the aspects of electrical properties, optical properties, and textile properties. This system was utilized to evaluate two commercial photobiomodulation devices, with a focus on how LED selection influences treatment performance, including wavelength, IV, irradiance, and system power. The evaluation successfully established the connection between the PBM treatment parameters and the device design.
- 5. A flexible wearable photobiomodulation panel was developed to conform to the human contour based on the underwear pattern. This innovation provides a guideline for transforming rigid health treatment devices into wearable formats that conform to the human contour, addressing sizing issues.

8.2. Future work

Owing to insufficient time and resources, the research remains deficient, and it also needs further work. The detailed further work is described as follows:

Wearable health monitoring device – pressure sensation:

- 1. Precision improvement on the fabrication of PDMS structure: This thesis successfully fabricated mechanoreceptors with controllable pressure thresholds, but there is a slightly large variation in the performance of pressure threshold depending on the structure variation fabrication. Further study on the viscosity of PDMS, stencil printing set-up, and solidification is valuable to minimize the structure deformation after printing. This will achieve high precision control on the pressure threshold for reliable performance.
- 2. Incomplete exploration of the control of the mechanoreceptor pressure threshold:

 The interrelationship between the pressure threshold, and the structural parameters of the mechanoreceptors was studied, including the PDMS material filling rate, height of the PDMS, material modulus, size of the compression, and the mechanoreceptor size. Furthermore, the pressure threshold also can be influenced by the bending rigidity of the composite fabric, and types of TPU as the encapsulation layer. Further study will be conducted to study the influence of the composite fabric, and TPU on the pressure threshold. This can broaden the design freedom of mechanoreceptors using different fabrics, allowing aimlessly integration into different clothing, and garments.
- 3. **Model of the mechanoreceptor:** This thesis conducted experiments to discuss the interrelationship between the pressure threshold of the mechanoreceptors and its

structural parameter. However, other factors also influence the performance of the mechanoreceptor, including the composite fabric and the TPU spacer. To enable effective mechanoreceptor design, a more comprehensive evaluation of these factors is necessary. This evaluation will inform the establishment of a robust design model. Furthermore, a systematic study specifically examining pressure threshold performance under bending conditions will be conducted to facilitate the design of mechanoreceptors functional in such states.

- 4. Study on the connection in the mechanoreceptor array: As mentioned previously, the mechanical, and electrical connection between the mechanoreceptor needs to improve for the array's lifespan, and stability. The electrical conductivity of the connection was in the range of dozens of ohms. Furthermore, this connection cannot sustain the mechanical load in the laundry. This may be attributed to the connection material- double-side conductive tape, and the flexible resistors. There is a demand to develop appropriate conductive material for the connection between the mechanoreceptor, and resistor, fitting the fabrication process of the array.
- 5. **Pressure sensation platform:** In the study, an initial pressure sensation platform was established, whose performance is still far away from human skin in the aspect of sensitivity. One approach is exploring the usage of softer material to fabricate structure in the insulation layer.

Wearable photobiomodulation device for breast cancer patient:

1. Optical design, and integration method of the flexible PBM panel: The currently developed PBM panel irradiance distribution needs to be improved for better performance. In addition, the integration method of the PBM panel also needs to be studied to increase comfort and enhance heat dissipation for safety.

- 2. Control of the wearable photobiomodulation panel: This thesis only designed, and fabricated a photobiomodulation panel, while there is a lack of a control module and power module for the remote treatment. Further study will be conducted to establish the corresponding control module, and power module integrated into the garments. The control module will manage the timing, intensity, and duration of the light therapy. The power module will ensure the working period of the device.
- 3. **Biological test:** In the study, we only evaluated commercial photobiomodulation devices' performance in designing the PBM device for breast cancer patients. The flexible panel device's optical properties are comparable to the commercial one. However, the effectiveness of the PBM need to confirmed by the biological test cellular, and animal tests. These tests will assess the device's performance in healing or reducing symptoms at a biological level. This step is crucial before moving to the clinical trials.
- 4. Clinical Trial: The effectiveness, and user experience of the PBM panel need to be evaluated by medical professionals, and breast cancer patients. Clinical trials will be conducted to assess the PBM panel's effectiveness and gather feedback on user experience.